

*Gas Turbine Laboratory
Department of Aeronautics and Astronautics
Massachusetts Institute of Technology
Cambridge, MA 02139-4307*

Final Report

NASA Grant NAG3-2179

INTRA-ENGINE TRACE SPECIES CHEMISTRY

submitted to

NASA Glenn Research Center
21000 Brookpark Road
Cleveland, OH 44135
Attn: Sandra Gage, Grants Office MS 500-315

**PRINCIPAL
INVESTIGATOR:**

Ian A. Waitz
Professor & Associate Director, Gas Turbine Lab

Final Report for NASA NAG3-2179

Ian A. Waitz, S. P. Lukachko, and A. Chobot, Massachusetts Institute of Technology
R. C. Miake-Lye and R. Brown, Aerodyne Research Incorporated

Prompted by the needs of downstream plume-wake models, the Massachusetts Institute of Technology (MIT) and Aerodyne Research Incorporated (ARI) initiated a collaborative effort, with funding from the NASA AEAP, to develop tools that would assist in understanding the fundamental drivers of chemical change within the intra-engine exhaust flow path. Efforts have been focused on the development of a modeling methodology that can adequately investigate the complex intra-engine environment. Over the history of this project, our research has increasingly pointed to the intra-engine environment as a possible site for important trace chemical activity. Modeling studies we have initiated for the turbine and exhaust nozzle have contributed several important capabilities to the atmospheric effects of aviation assessment. These include a more complete understanding of aerosol precursor production, improved initial conditions for plume-wake modeling studies, and a more comprehensive analysis of ground-based test cell and in-flight exhaust measurement data. In addition, establishing a physical understanding of important flow and chemical processes through computational investigations may eventually assist in the design of engines to reduce undesirable species.

One key area of investigation has been into the intra-engine oxidation of SO_2 to SO_3 and H_2SO_4 . The amount and nature of aircraft sulfur emissions that are deposited in the atmosphere (Fahey *et al.*, 1995; Curtius *et al.*, 1998) depend on how much fuel sulfur leaves the engine in a condensable form. The combustion process oxidizes fuel bound sulfur to mainly SO_2 , which will not condense, but post-combustor chemistry can further oxidize the SO_2 to SO_3 and H_2SO_4 , S(VI), which can participate in condensation processes as the wet exhaust gases cool. These newly formed volatile aerosols then contribute to the atmospheric aerosol loading and can lead to various potential atmospheric impacts, including direct radiative forcing, contrail formation, and cirrus cloud perturbations. In order to understand the aerosol emissions from aircraft, the conversion of fuel sulfur to condensable sulfur species is necessary. Because of the difficulty and cost of engine measurements, we have developed modeling tools to simulate the post-combustor chemistry and gain insight into the conversion processes. A list is included in Appendix A of publications and major presentations; Appendix B contains a student thesis (Chobot). Jointly these publications and the thesis that serve as a more complete account of the MIT/ARI work described below.

One-dimensional models have been used to follow both homogeneous (Brown *et al.*, 1996; Tremmel and Schumann, 1999) and heterogeneous (Brown *et al.*, 2000) chemistry along a temperature/pressure

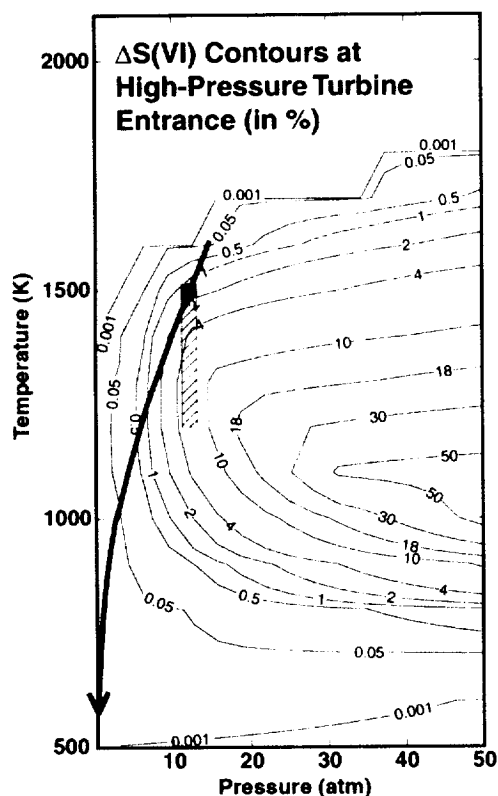


Figure 1. Characteristic Time Scale Analysis for SO_x Chemistry

trajectory through the turbine. Our effort has been to develop additional capabilities to extend such one-dimensional studies. In order to determine those regions in the turbine where trace chemistry is most active, and where more detailed multi-dimensional modeling is appropriate, a tool was developed to evaluate the potential for oxidation within trace species families. The analysis compares appropriately defined characteristic flow and chemical time scales, that, with knowledge of the thermodynamic reference state, can be used to understand conversion potential in pressure-temperature coordinates. Figure 1 shows an example space for the conversion of SO_2 to SO_3 . The contour lines represent levels of formation through a single turbine blade row. The red dot places the inlet condition to that blade row, here for the first in the high-pressure turbine, on the temperature and pressure map. The temperature and pressure flow path through the entire engine is shown as the blue line.

It is worth noting that the flow will encounter cooling as it passes through the turbine blades and the shaded region extending to lower temperatures from the high pressure turbine point on the trajectory indicates a range of temperatures associated with such cooling. Clearly, the effects of cooling move a given parcel of fluid into regions of higher conversion relative to the uncooled trajectory at the same pressure. Parallel analyses can be performed for different engine cycles, to examine the effects of engine cycle parameters, or for subsets of the complete chemical mechanism, to evaluate the relative contributions of identified chemical pathways.

Phenomena or locations in the engine to which trace chemistry is found to be sensitive can be investigated with higher-dimensional tools. For detailed investigations of the impacts of turbomachinery fluid mechanics, we employ a CFD tool developed for this program called CNEWT. CNEWT combines a well-established 3-D turbomachinery code and a chemical kinetics solver within a structure currently capable of calculating passively reacting internal flows where chemistry has no influence on the course of the

flow solution. An additional 1-D kinetics capability, used for solving along averaged profiles of relevant flow parameters, extends the CNEWT code to allow approximations at several levels of model detail. Currently, CNEWT is best used for understanding trends and influential fluid and chemical processes rather than as a predictive tool since empirical data does not presently exist to validate CNEWT for the applications of interest.

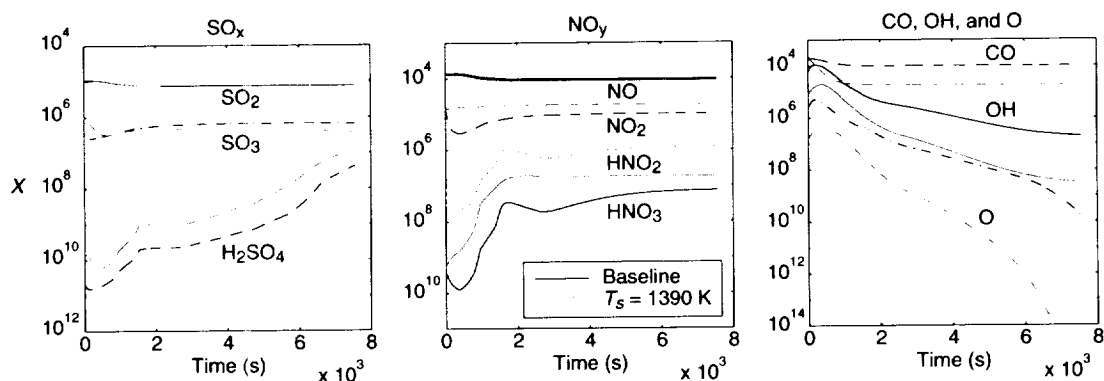


Figure 2. 1-D Parametric Analyses. Cases shown for an advanced subsonic engine cycle developed by NASA. Baseline case (black lines) initiated at a combustor exit temperature of ~1600 K and ~15 atm. Comparative case (red lines) shown for combustor exit temperature of 1390 K.

One-dimensional calculations performed with this tool constituted the first broad parametric investigations of chemical processes in the turbine and exhaust nozzle. Using a chemical mechanism developed through the work of Robert C. Brown of ARI and Fred L. Dryer of Princeton University, 1-D parametric analyses were conducted for the entire turbine and exhaust nozzle flowpath of a typical advanced subsonic engine to understand the effects of important flow and chemistry variations. An example of the results from these efforts is shown in Figure 2. These calculations were initiated at the combustor exit plane and continued to the exit plane of the exhaust nozzle. The same engine operating data and chemistry is used as in the time scale analysis of Figure 1.

It is evident that many trace species undergo significant change within the engine. Total $(\text{SO}_3 + \text{H}_2\text{SO}_4)/\text{SO}_x$ at the engine exit for a baseline case was found to be 8.3% for a representative, modern subsonic engine. Comparatively, a total of 1.2% NO_y oxidation to HNO_2 and HNO_3 was computed. A variety of combustor exit speciation prescriptions were used to illustrate the competition among NO_y , SO_x , and CO_x species for free radicals. From these studies, it was found that engine exit composition is very sensitive to the use of equilibrium versus nonequilibrium assumptions in establishing species initial conditions. Equilibrium specifications resulted in a reduced level of chemical activity through the turbine

and exhaust nozzle, a smaller amount of oxidized SO_2 as SO_3 and H_2SO_4 (5.3% versus 8.3% using non-equilibrium NO_x and CO), and a smaller amount of NO_x as HNO_2 and HNO_3 (approximately 0.2% versus 1.2%).

In response to this sensitivity, a methodology for specifying initial conditions at the combustor exit was developed. This procedure utilizes empirical information in combination with combustor fuel type, operating point, thermodynamic specifications, and 1-D kinetics to estimate trace species concentration at the combustor exit. Recent combustor measurements of various trace species supported by the NASA/DERA collaboration will be used to assess the validity of this methodology. In our effort to improve these models, we have also updated reactions for SO_x chemistry included in our analysis based on the work of the Dryer group at Princeton University. In comparison to the chemistry used for the 1-D results shown in Figure 2 as well as the 2-D results in Figure 3, which will be discussed below, SO_x production and destruction mechanisms are actually more active. In the balance, there is less oxidation than indicated by the values presented above. For the same conditions, total $(\text{SO}_3 + \text{H}_2\text{SO}_4)/\text{SO}_x$ at the engine exit is instead 4.5% rather than 8.3% for the baseline case, and 3.6% rather than 5.3% for the equilibrium initial condition case. This underscores the need for continued fundamental kinetic investigations and input as a complement to the proposed tasks.

In the 1-D calculations, flow variables were also varied to show the importance of effects such as combustor exit temperature and cooling flow mass addition on the exit plane result. Such effects were relatively less important for these 1-D, flow-averaged studies than were changes in the method by which species initial conditions were established. This is not the case if we consider the details of the combustor exit profile and turbine fluid

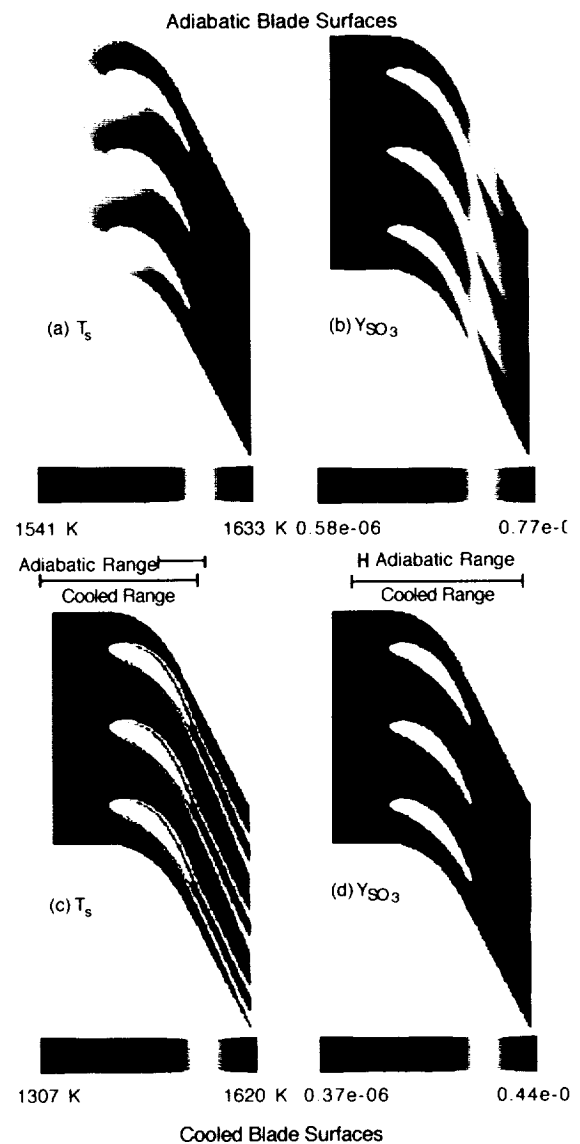


Figure 3. 2-D Steady Analysis of Trace Chemistry through a Turbine Blade Row.

mechanics. Time scale analyses make it clear that the active conversion of sulfur species to S(VI) (*i.e.* SO_3 and H_2SO_4) occurs primarily in the first stages of the high pressure turbine and can be perturbed by large temperature gradients in the flow in a nonlinear fashion. In general, the identified regions of active sulfur chemistry can be explored in more detail using the multi-dimensional code CNEWT.

Representative 2-D, single turbine blade row simulations were performed to determine the potential impact of flow non-uniformities that cannot be captured directly or modeled simply through 1-D analyses. Temperature non-uniformities that result from the use of an internal blade cooling strategy were investigated and revealed a significant impact in SO_x chemistry. A comparison of results for cooled and uncooled blades is shown in Figure 3, where it can be noted that oxidation of SO_2 to SO_3 is enhanced in the cool regions of the blade boundary layer and wake.

Comparisons of 1-D approximations to the 2-D turbine solutions were then carried out to help determine the extent to which current 1-D modeling capabilities can resolve changes in chemical composition. An example of such a 1-D reduction for the 2-D results of Figure 3 is shown in Figure 4. The results call into question the validity of 1-D averaged flow analysis for the highly non-uniform, unsteady flow fields of the turbine and exhaust nozzle. Because of the need for a high density computational grid, we have partially parallelized the CNEWT code for faster run times and have refined the calculation methodology in order to accommodate larger domains.

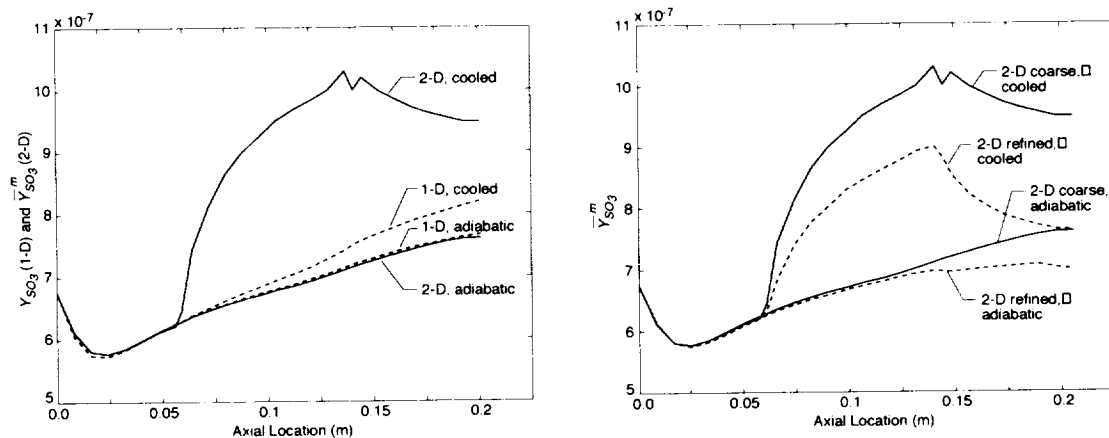


Figure 4. Comparison of 1-D and Mass-Averaged 2-D Results for Similar Calculations.

Further analyses of the impact of non-uniformities were undertaken to understand the persistence of the blade cooling impact through downstream blade rows and to determine the magnitude of that impact in

comparison to the much more significant circumferential and radial variations at the combustor exit. An unsteady, full-stage row calculation was performed for the nozzle guide vanes and rotor (together forming the first stator-rotor pair of blade rows) for a representative engine, but older and cooler than the engine example used in the discussion to this point. We used a different, older engine in support of the NASA/DERA measurement effort and expect, from our analyses as described above, that trace chemistry would be less active.

From a technical standpoint, the goal of this full-stage analysis was to capture the unsteady interaction of the cooled wakes leaving the NGV as they flow over the rotor blades. These results were compared to the corresponding steady calculation where the NGV wakes are averaged before passing on to the rotor. In the former case, we allow the mixing processes in the flow to take place without intervention. In the latter case, mixing is enforced. The impact of mixing on non-uniform cooled flow sulfur conversion can thus be investigated for this specific engine. Figure 5 shows a snapshot of the unsteady, full-stage calculation.

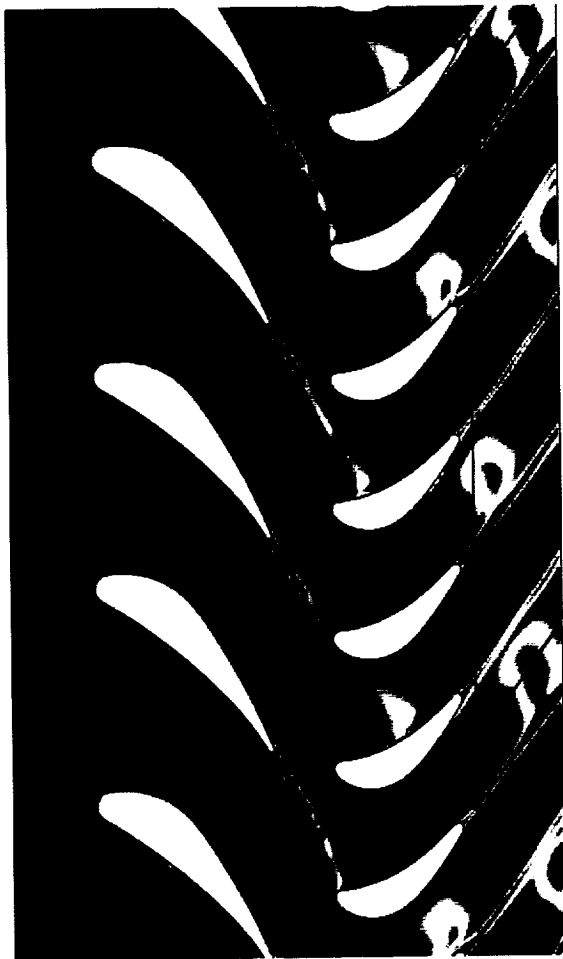


Figure 5. 2-D Unsteady Analysis of Trace Chemistry through a Turbine Stage.

We find that mixing does not have an impact on the amount of sulfur conversion for this engine operating point, a total of 0.6% at the rotor exit. However, the fact that the steady and unsteady calculations agree so closely for this engine may be due to the low overall S(VI) conversion for this engine cycle. The results may also stem from the competing effects of larger regions of enhanced SO_3 for the unsteady case being countered by mixing and dilution. For other engine cycles, these unsteady effects may impact the SO_3 formation and this is an active area of investigation for our group.

Another active area of investigation is the impact of combustor exit non-uniformities associated with the radial and circumferential temperature variability of the burner exit. Performing a similar comparison of cases as for the wake propagation investigation, this time for a higher temperature to increase conversion potential, our analysis indicates that mixing times are

long in comparison to the chemical reaction. As a result, persistent stratification of the flow originating at the combustor exit appears to inhibit S(VI) conversion. Mixing-out the flow between blade rows results in a conversion of 0.25% compared with a 0.16% conversion if the non-uniformity is allowed to propagate through the rotor. Also note that a higher conversion is realized for this higher temperature case for the same geometry and less stage flow-through residence time.

In addition to gaseous trace chemistry, research efforts have also addressed the role of heterogeneous processes. One-dimensional flow models and unity probability heterogeneous rate parameters were used to estimate the maximum effect of heterogeneous reactions on trace species evolution in aircraft gas turbines. The analysis included reactions on soot particulates and turbine/nozzle material surfaces. Results for a representative advanced subsonic engine indicated that the net change in reactant mixing ratios due to heterogeneous reactions is $< 10^{-6}$ for O_2 , CO_2 , and H_2O , and $< 10^{-10}$ for minor combustion products such as SO_2 and NO_2 . The change in the mixing ratios relative to the initial values were $< 0.01\%$. Since these estimates were based on heterogeneous reaction probabilities of unity, the actual changes will be even lower. Thus, we concluded that heterogeneous chemistry within the engine cannot explain the high conversion of SO_2 to SO_3 which some wake models require to explain the observed levels of volatile aerosols. Furthermore, turbine heterogeneous processes will not affect exhaust NO_x or NO_y levels.

From these results, we have proposed a modeling strategy for post-combustion trace species chemistry through the turbine and exhaust nozzle as defined in Figure 6. Like other gaseous chemistry, ion recombination is influenced by processes occurring through the turbine and exhaust nozzle. A one-dimensional model for aircraft turbine flows was used to estimate chemi-ion emission number densities at the engine exit plane. Results for representative subsonic and supersonic aircraft indicate that significant reductions in ion number density can occur through the turbine and exhaust nozzle. These reductions, typically a factor of 10-1000, result in chemi-ion emission indices at the engine exit that range between 10^{+16} ions kg-fuel $^{-1}$ and 10^{+18} ions kg-fuel $^{-1}$, corresponding to a typical ion number density of 10^{+8} ion cm $^{-3}$. Available ground based measurements are in line with these estimates. Aircraft wake modeling suggests that chemi-ion emissions can alter aerosol microphysical processes in such a manner as to resolve discrepancies between model predictions and in-flight observations of volatile aerosol emissions. However, we predict peak ion number densities at the engine exit that are an order of magnitude below the levels required at the onset of ion-induced nucleation in the exhaust wake to completely resolve particle size/growth discrepancies.

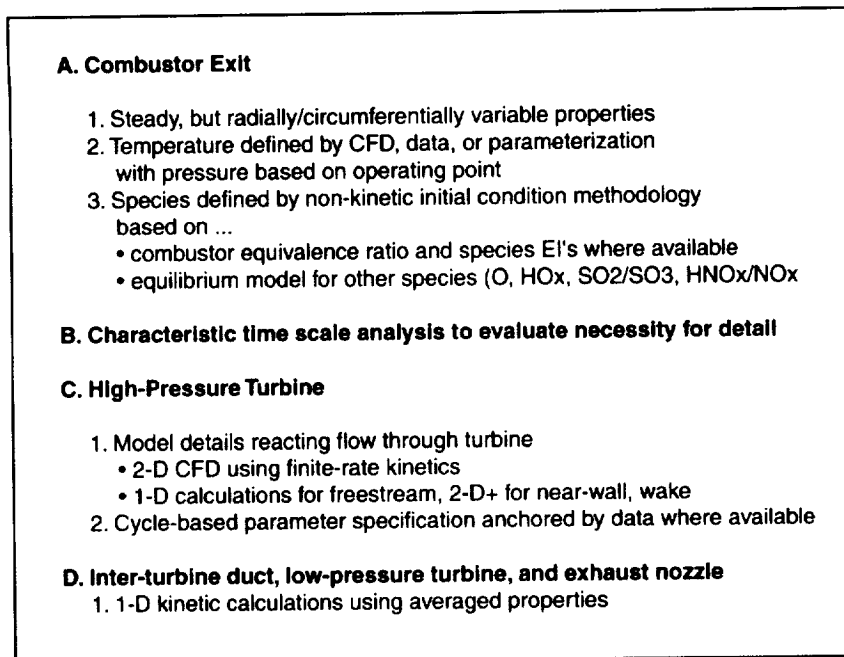


Figure 6. Proposed Modeling Strategy.

References

- Brown, R.C., R.C. Miake-Lye, S.P. Lukachko, and I.A. Waitz, Heterogeneous reactions in aircraft gas turbine engines, *Submitted to Geophysical Research Letters*, 2000.
- Brown, R.C., M.R. Anderson, R.C. Miake-Lye, C.E. Kolb, A.A. Sorokin, and Y.Y. Buriko, Aircraft exhaust sulfur emissions, *Geophys. Res. Letts.*, 23, 3603-3606, 1996.
- Curtius, J. *et al.*, First direct sulfuric acid detection in the exhaust plume of a jet aircraft in flight. *Geophysical Research Letters*. 25, 923-926, 1998.
- Fahey, D.W. *et al.*, Emission measurements of the Concorde supersonic aircraft in the lower stratosphere, *Science*, 27,. 70-74, 1995
- Tremmel, H.G. and U. Schumann, Model simulations of fuel sulfur conversion efficiencies in an aircraft engine: Dependence on reaction rate constants and initial species mixing ratios, *Aerospace Science and Technology*, 3, 417-430, 1999.

Appendix A. Publications and Major Presentations

Presentations and Conferences

- April 1995—Poster Presentation
5th Annual Meeting on the Atmospheric Effects of Aviation. Virginia Beach, VA.
- October 1996—Conference Paper and Oral Presentation
Paper: Chemical Processes in the Turbine and Exhaust Nozzle. Lukachko, Waitz, Miake-Lye, Brown, Anderson, and Dawes. Published in Proceedings, Volume 1. Comité Avion Ozone Impact of Aircraft Emissions upon the Atmosphere International Colloquium. Paris, France.
- January 1997—Oral Presentation
Particulates Round Table. NASA Glenn, Cleveland, OH.
- March 1997—Oral Presentation
1997 Conference on the Atmospheric Effects of Aviation. Virginia Beach, VA.
- May 1997—Oral Presentation
Project Review Meetings. NASA Glenn. Cleveland, OH.
- July 1997—Oral Presentation
Aerosol and Particulates Workshop. Ohio Aerospace Institute. Dayton, OH.
- April 1998—Poster Presentation
Progress in Understanding Trace Species Evolution through an Aircraft Engine
1998 Conference on the Atmospheric Effects of Aviation, Virginia Beach, VA.
- September 1998—Oral Presentation
NASA AEAP Emissions Characterization Group Kickoff Meetings, Princeton University, NJ.
- April 1999—Oral Presentation
1999 Conference on the Atmospheric Effects of Aviation, Virginia Beach, VA.
- June 2000—Oral Presentation
2000 Conference on the Atmospheric Effects of Aviation, Snowmass, CO.
- July 2000—Extended Abstract and Oral Presentation
Simulation of Post-Combustion Chemical Evolution in Gas Turbine Engines, R.C. Miake-Lye, A.T. Chobot, S.P. Lukachko, R.C. Brown, J. Zhang, and I.A. Waitz Presented at the Aviation, Aerosols, Contrails, and Cirrus Clouds (A2C3) Workshop, Seeheim, Germany.
- August 2000—Oral Presentation
Project Review Meetings. NASA Glenn. Cleveland, OH.

Publications and Theses

- January 1997—MIT S.M. Thesis
Lukachko. Research on the science and politics of the atmospheric effects of aviation debate.
- September 1997—Working Paper
Simulation of Post-Combustion Chemical Evolution in a Gas Turbine Engine. Lukachko, Waitz, Miake-Lye, Brown, Anderson, and Dawes.
- July 1998—Archival Publication
Production of Sulfate Aerosol Precursors in the Turbine and Exhaust Nozzle of an Aircraft Engine. Lukachko, Waitz, Miake-Lye, Brown, and Anderson. *Journal of Geophysical Research—Atmospheres*. 103(D13). Pp. 16159-16174. July 20, 1998.
- July 1999—Chapter Section Contribution
Chapter 7: IPCC Special Report on Aviation and the Global Atmosphere.
- July 1999—Archival Publication
Brown, Miake-Lye, Lukachko, and Waitz. Heterogeneous Chemistry in Gas Turbine Engines. Submitted to *Geophysical Research Letters*.

- September 1999—Archival Publication
Brown, Miake-Lye, Lukachko, and Waitz. Ion Recombination in Gas Turbine Engines. Submitted to Geophysical Research Letters.
- September 2000—MIT S.M. Thesis
Chobot, Modeling the Evolution of Trace Species in the Post-Combustor Flow Path of Gas Turbine Engines.

Appendix B. Chobot Thesis

MODELING THE EVOLUTION OF TRACE SPECIES IN THE POST-COMBUSTOR FLOW PATH OF GAS TURBINE ENGINES

by

ANTHONY T. CHOBOT III

B.S. Mechanical Engineering
University of Illinois at Urbana-Champaign, 1995

Submitted to the Department of Mechanical Engineering
in partial fulfillment of the requirements for the degree of

MASTER OF SCIENCE IN MECHANICAL ENGINEERING

at the

MASSACHUSETTS INSTITUTE OF TECHNOLOGY

September 2000

© 2000 Massachusetts Institute of Technology. All rights reserved.

Author: _____
Anthony T. Chobot III
Department of Mechanical Engineering
August 18, 2000

Certified by: _____
Professor Ian A. Waitz
Associate Professor of Aeronautics and Astronautics
Thesis Supervisor

Certified by: _____
Professor Ahmed F. Ghoniem
Professor of Mechanical Engineering
Thesis Reader

Accepted by: _____
Professor Ain A. Sonin
Professor of Mechanical Engineering
Chairman, Departmental Graduate Committee

MODELING THE EVOLUTION OF TRACE SPECIES IN THE POST-COMBUSTOR FLOW PATH OF GAS TURBINE ENGINES

by

Anthony T. Chobot III

Submitted to the Department of Mechanical Engineering
on August 18, 2000 in Partial Fulfillment of the
Requirements for the Degree of Master of Science in
Mechanical Engineering

ABSTRACT

A consensus among scientists has formed that human activities have an influence on the atmosphere and are contributing to global warming. Recently, aviation has garnered a significant amount of attention since it is the fastest growing sector of transportation and it is thought to be an important component of such impacts. Trace species emitted by aircraft directly into the upper atmosphere are believed to have an enhanced influence relative to other common emissions generated by human activity near the surface of the earth. Prior work has concluded that trace species can change significantly in the engine post-combustor gas path. Research efforts to understand the role of aircraft gas turbine engine emissions in global climate change and the mechanisms by which their emissions are produced have been intensified.

A modeling methodology was developed which can be used to predict the evolution of trace species in the post-combustor flow path of gas turbine engines. The modeling methodology incorporates various levels of detail to accurately and efficiently predict levels of intra-engine trace species by considering the key parameters affecting their evolution, specifically temperature, pressure, residence time, and species concentration. The core of the model is a computer code which performs a numerical solution to the fluid mechanics and chemical kinetics problems. The model is intended to improve the overall understanding of the fundamental physical processes that affect trace species evolution and to serve as a predictive design tool which can direct the development of new engine technologies which reduce undesirable aviation emissions.

The development effort consisted of several refinements aimed at increasing the accuracy and usability of the model. The improvements included an improved species initial condition specification procedure, improved grid generation, capability for multiple inlet/exit planes, addition of parallel chemistry subroutines, revision of chemistry convergence criteria, addition of circumferentially-varying unsteady inlet conditions, and incorporation of a new chemical mechanism.

Several validation exercises were performed which benchmark the capabilities of the model and test the added features. Past simulations of a duct and rotor were used as a baseline to verify several of the improvements. These simulations were used to improve the chemistry convergence criteria, perform a comparative study of several chemical mechanisms, and verify the periodic boundary conditions. The Princeton University Variable Pressure Flow Reactor was also simulated as a validation exercise in an attempt to evaluate the overall effectiveness of the model in predicting the flow field, mixing, and species concentrations in a well known and controlled environment.

The model was used to perform the first complete post-combustor engine simulation in support of an engine measurement campaign. The results provided guidance for test parameters and measurement strategies. This simulation was further used to assess the effects of flow non-uniformity on the evolution of trace species in a typical aircraft engine and to refine the current modeling practice. Engine operating conditions, multi-dimensional non-uniformities, and the unsteady interaction of non-uniformities with subsequent blade rows were all found to influence trace species evolution.

Thesis Supervisor: Professor Ian A. Waitz

Title: Associate Professor of Aeronautics and Astronautics

ACKNOWLEDGEMENTS

I would first like to thank my thesis advisor, Professor Ian Waitz, for his leadership, guidance, support, and encouragement throughout my academic career which was invaluable to my learning experience. I would also like to thank Steve Lukachko for his constant advice and assistance during my work on this project. I am also grateful to the remainder of the research team at Aerodyne Research Inc., Dr. Richard Miake-Lye, Dr. Robert Brown, and Dr. John Zhang who also provided substantial guidance and advice throughout this work. Thanks to Chowen Wey and Nan-Suey Liu at NASA for their support in our research endeavors.

Thanks to Professor Dawes, Caleb Dhanasekaran, Albert Demarnge, and the staff at the Whittle Laboratory at Cambridge University for their cooperation, generous hospitality during my visits, and assistance with my research questions. I am also indebted to Chris Wilson, Michel Whiteman, and Andrew Clague at DERA for answering numerous requests for data and providing considerable advice. I also owe thanks to Professor Fred Dryer and Mark Mueller at Princeton University for contributing data and being supportive during the course of this work. Of course, thanks to the staff of the Gas Turbine Laboratory, especially Paul Warren and Lori Martinez.

I appreciate the time and consideration offered by my thesis reader, Professor Ahmed Ghoniem. Also, thanks to Leslie Regan for her support and who has been especially helpful throughout my stay as a graduate student.

I am very grateful to Electro-Motive Division of General Motors, especially Ed Cryer, Kelly Jones, Jim Korenchan, Paula McGhee, Tom Savage, John Zagone, and the people I have worked with in the Turbocharger Design Group and Mechanical and Analytical Group for the support and encouragement they have given me. I would especially like to thank Jim Heilenbach for being a mentor throughout my studies.

The friends I have made during my stay in Boston will never be forgotten. I would like to thank all my friends at the GTL, including Dongwon Choi, Taek-Jin Choi, Keith Dalbey, Rick Francis, Jeff Freedman, Yifang Gong, Joe Lee, Shengfang Liao, Hyung-Soo Moon, Nick Savoulides, Brian Schuler, Patrick Shum, Bobby Sirakov, Chris Spadaccini, Zolti Spakovszky, Jessica Townsend, Yang Tzeng, Bret Van Poppel, Sanith Wijesinghe, and Duc Vo. It has been great working and having fun with all of you. Special thanks to Dan Kirk, Jin-Wook Lee, Sumita, Jon Protz, Chris Protz, and Chris Spadaccini for all the great times we have had together.

Also, thanks to all the other friends I have made in Boston, especially Sylwia Daniszewska, Leonard Dvorson, Randal Guendel, Olivier Kahwati, Alexandra Porter, and Nora Sasz.

TABLE OF CONTENTS

Abstract	3
Acknowledgements	5
Table of Contents	7
List of Tables	11
List of Figures	13
Nomenclature	17
1 Introduction.....	19
1.1 Chapter Overview	19
1.2 Atmospheric Effects Of Aviation.....	21
1.2.1 Aircraft Exhaust Emissions.....	22
1.2.2 Altitude Deposition Process.....	23
1.2.3 Climatic and Ozone Effects	24
1.2.3.1 Subsonic Aircraft Effects	26
1.2.3.2 Supersonic Aircraft Effects.....	27
1.3 Prior Work	28
1.3.1 General Trace Emissions Characterization	28
1.3.2 Near Field Plume And Wake Modeling	29
1.3.3 Turbine And Exhaust Nozzle Modeling.....	30
1.4 Motivation	31
1.4.1 Objectives And Contributions.....	32
1.4.2 Thesis Overview	32
1.4.2.1 Modeling Methodology.....	33
1.4.2.2 Modeling Tools	33
1.4.2.3 Validation	33
1.4.2.4 Modeling The NASA/DERA Engine Test	33
1.5 Chapter Summary	34
2 Modeling Methodology.....	37
2.1 Chapter Overview	37
2.2 Modeling Elements.....	38
2.3 Procedure.....	39
2.3.1 Time Scale Analysis.....	40
2.3.1.1 Basic Procedure	41
2.3.1.2 Further Examples Of the Utility Of Time Scale Analyses	44

5.4.2.2	Flow Features And Analysis	107
5.4.2.3	Flow-Chemistry Results.....	112
5.5	Low Fidelity Modeling	121
5.5.1	Low Fidelity Modeling Set Up	121
5.5.2	Low Fidelity Modeling Results.....	126
5.5.2.1	Calculation Description and Execution.....	126
5.5.2.2	Flow-Chemistry Results.....	127
5.6	Implications of Results	129
5.6.1	Effects Of Engine Operating Conditions	129
5.6.2	Effects Of Multi-Dimensional Non-Uniformities	130
5.6.3	Effects Of The Unsteady Interaction Of Non-Uniformities With Downstream Stations	131
5.7	Chapter Summary	132
6	Thesis Summary And Contributions	137
6.1	Thesis Summary	137
6.2	Contributions	138
Appendix A.....		143
Appendix B.....		165
Appendix C.....		169
Appendix D.....		177
Appendix E.....		199
Appendix F		213
References.....		215

LIST OF TABLES

Table 1.1 Typical emission index levels (g/kg fuel) [3]	23
Table 1.2 Effects of species contributing to climate change [2]	24
Table 2.1 Some possible modeling elements influencing intra-engine chemistry	39
Table 2.2 Input parameters to initial conditions code	47
Table 3.1 Run time stastics for parallel code test case.....	62
Table 4.1 Summary of results from chemical mechanism study case 1.....	75
Table 4.2 Summary of results from chemical mechanism study case 2.....	75
Table 4.3 Summary of results from chemical mechanism study case 8.....	75
Table 4.4 Summary of results from chemical mechanism study case 15.....	76
Table 4.5 Summary of results from periodic boundary condition study.....	85
Table 5.1 Nominal NASA/DERA test engine description.....	92
Table 5.2 Summary of conditions modeled for NASA/DERA engine test [34]	93
Table 5.3 Chemistry inlet condition code inputs for NASA/DERA engine test.....	101
Table 5.4 Comparison of fluid quantities for HPT1 at max power.....	108
Table 5.5 Summary of results from HPT1 high fidelity modeling at cruise condition	119
Table 5.6 Summary of results from HPT1 high fidelity modeling at max power condition.....	120
Table 5.7 Summary of results from HPT1 high fidelity modeling at max power condition.....	121
Table A.1 Summary of selected results for VPFR validation runs	152
Table A.2 Summary of Reynolds number matching study	155
Table A.3 Summary of boundary layer grid refinement study.....	156
Table C.1 Data for the maximum power 2° deviation velocity triangle diagram of Figure C.	174

LIST OF FIGURES

Figure 1.1 Summary of combustion products [3]	22
Figure 1.2 Radiative forcing of various trace species [2]	25
Figure 1.3 Variation of ozone concentration with altitude [7].....	27
Figure 2.1 Intra-engine trace chemistry modeling methodology	40
Figure 2.2 Typical thermodynamic potential and chemical time scale plot underlying a time scale analysis for S O ₃ (courtesy of Stephen Lukachko)	41
Figure 2.3 Severity parameter for SO ₃ from typical time scale analysis at two engine stations (courtesy of Stephen Lukachko)	43
Figure 2.4 Investigating the impact of blade cooling on SO ₃ chemistry using time scale analysis (courtesy of Stephen Lukachko)	44
Figure 2.5 Investing the effects of operating condition on chemistry using time scale analysis (courtesy of Stephen Lukachko)	45
Figure 2.6 Investing the effects of various chemistry using time scale analysis (courtesy of Stephen Lukachko)	46
Figure 2.7 Overview of chemistry initial condition specification.....	47
Figure 2.8 Representative constant temperature and pressure kinetics calculations for selected species for initial conditions formulation.....	49
Figure 2.9 Change in selected EI's during kinetics calculation for initial conditions formulation	50
Figure 3.1 Examples of a pseudo-unstructured (left) and fully unstructured (right) grid	58
Figure 3.2 Volume mesh stage dumps.....	59
Figure 3.3 Multiple inlet/exit test case, X direction velocity on streamlines	61
Figure 3.4 Run time stastics for parallel CNEWTON	63
Figure 3.5 Wake model validation case, total temperature change over 600 iterations.....	64
Figure 4.1 1D profile data for ASE engine [1]	72
Figure 4.2 Chemical mechanism study for Case 1.....	73
Figure 4.3 Chemical mechanism study for Case 2.....	73
Figure 4.4 Chemical mechanism study for case 8	74
Figure 4.5 Chemical mechanism study for case 15	74
Figure 4.6 Example result of 2D calculation on Cambridge No 2 turbine rotor with Lukachko et al (1998) mechanism	77
Figure 4.7 Original CNEWTON fluid and chemistry convergence indicators	79
Figure 4.8 Convergence of O mass fraction by visual time evolution.....	81
Figure 4.9 Maximum and minimum species mass fraction versus iteration	82

Figure 5.29 Example low fidelity modeling results, NOy species evolution in the HPT1 and from the HPT1 exit to nozzle exit for the non-uniform max power condition	129
Figure A.1 Cut-away view of Princeton VPFR [26].....	144
Figure A.2 VPFR solid model and grid detail near baffle and injector assembly	145
Figure A.3 Pressure recovery maps for constant dA/dx diffusers [41]	148
Figure A.4 Diffuser flow regime map [39].....	149
Figure A.5 Typical velocity profiles from Power Law [38]	150
Figure A.6 Experimental velocity profiles for Princeton VPFR [26]	150
Figure A.7 General velocity profiles in diffusers [40].....	151
Figure A.8 Axial position X (cm) for flow reactor modeling	152
Figure A.9 Flow reactor Run 1 convergence history	153
Figure A.10 Axial velocity from -85 to 11 m/s (note: contours clipped for presentation).....	153
Figure A.11 Velocity profiles at nine axial stations.....	154
Figure A.12 Velocity profiles for 50x viscosity case (Run 4).....	155
Figure A.13 Mesh refinement in flow reactor test section.....	157
Figure A.14 Velocity profiles for case with refined boundary layer grid (Run 6).....	158
Figure A.15 Axial velocity from -452 to 163 m/s at 10,000 (top) and 35,000 (bottom) iterations (note: contours clipped for presentation)	159
Figure A.16 Axial velocity profiles at nine axial stations for 10,000 and 35,000 iteration solutions	159
Figure A.17 Mach number contours near diffuser throat showing subsonic to supersonic transition	160
Figure A.18 Z direction velocity component near injectors	161
Figure A.19 Axial velocity just before 60,000 iterations.....	162
Figure A.20 Velocity profiles for unsteady Run 12 at 100,000 iterations (not time averaged)	163
Figure A.21 Streamlines with axial velocity contours for unsteady Run 12 showing one cycle of the periodic vortex shedding.....	163
Figure C.1 Velocity triangle diagram for maximum power condition with 2° deviation	173

NOMENCLATURE

ACRONYMS:

AEAP	Atmospheric Effects on Aviation Project
AR	Area Ratio
ASE	Advanced Subsonic Engine
ATOL	Absolute Tolerance
CAD	Computer Aided Design
CIAP	Climatic Impact Assessment Program
CFD	Computational Fluid Dynamics
DERA	Defence Evaluation and Research Agency
DOT	Department of Transportation
EI	Emissions Index
HPT1	High Pressure Turbine – Stage 1
HPT2	High Pressure Turbine - Stage 2
HSCT	High Speed Civil Transport
$h\nu$	photoelectric energy
<i>in-situ</i>	in-flight
IPCC	Intergovernmental Panel on Climate Change
L/D	Length to Diameter Ratio
LPT1	Low Pressure Turbine – Stage 1
LPT2	Low Pressure Turbine – Stage 2
MIT/ARI	MIT and Aerodyne Research Inc. team
NASA	National Aeronautics and Space Administration
NGV	Nozzle Guide Vanes
ODE	Ordinary Differential Equation
R-K	Runge-Kutta
RMS	Root Mean Square
RTOL	Relative Tolerance
SST	Supersonic Transport
TE	Trailing Edge
UARP	Upper Atmosphere Research Program
UMR	University of Missouri – Raleigh Team
VPFR	Variable Pressure Flow Reactor

ROMAN:

c	Chord
c_p	Specific heat at constant pressure
D	Diameter
ds	Differential length along curve
L	Length
M	Mach number
\dot{m}	Mass flow rate

1 INTRODUCTION

Aviation is currently the fastest growing transportation sector. Trace species emitted by aircraft directly into the upper atmosphere are believed to have an enhanced influence relative to other common emissions generated by human activity near the surface of the earth. Therefore, research efforts to understand the role of aircraft gas turbine engine emissions in global climate change and the mechanisms by which these emissions are produced have been amplified. Of particular interest are trace chemical constituents, which are understood to be particularly influential in affecting local air quality and the global atmosphere. The Atmospheric Effects of Aviation Project (AEAP), created by NASA to study the influence of aviation on the global atmosphere, initiated the effort to develop a model to predict the evolution of trace species in the post-combustor flow path of gas turbine engines. The work contained in this thesis is part of an ongoing research effort aimed at gaining accurate and informative data on these trace chemical species. Ultimately, a modeling methodology was developed and applied to a research engine in support of an engine test program being conducted for the project. A computational model which can predict the evolution of trace species within gas turbine engines is an essential tool which can be used to help understand intra-engine trace species evolution. The model can be used to investigate how the operating parameters and design characteristics of gas turbine engines affect their emissions. It can also help provide a physical understanding of trace species evolution and could be used to direct the development of new engine technologies that reduce aviation emissions.

1.1 CHAPTER OVERVIEW

The purpose of this chapter is to give a short introduction to aircraft emissions and their potential impacts on the local and global atmosphere. A brief history of the research on atmospheric effects of aviation is described. The composition of aircraft exhaust emissions is explained, the origins of a few trace species are presented, and a description of the exhaust deposition process is given. A few climatic and ozone effects are highlighted, with further details for subsonic and supersonic aircraft given. An overview of prior work to characterize trace species emissions is presented, including work done in near field plume and wake modeling and turbine and exhaust nozzle modeling. The importance of trace species modeling in the turbine and exhaust nozzle is established by several previous studies, which gives motivation for the current research. This chapter also lists the overall objectives and contributions of the current research effort which serves as a thesis roadmap.

Section 1.2 gives an overview of aircraft exhaust emissions, where these emissions are deposited, and the effects of both subsonic and supersonic aircraft exhaust emissions on the environment. Section 1.3 reviews some prior work on emissions characterization, specifically near field plume and wake modeling and turbine and exhaust nozzle modeling. Section 1.4 discusses the motivation for the work and lists the contributions of this thesis. Section 1.5 is the chapter summary.

1.2 ATMOSPHERIC EFFECTS OF AVIATION

Aircraft emissions can impact the environment both locally and globally. The aviation industry is becoming a more significant part of the world economy, in terms of both commercial and military activity, and it contributes to these atmospheric effects primarily via the emissions released from gas turbine engines. Future growth in aircraft fleets is expected to increase these effects [3]. Therefore, a complete understanding of aircraft emissions and effects of these emissions on the atmosphere is necessary in assessing the current and possible future effects of aircraft. The need to characterize trace species evolution has been heightened because trace species concentrations are known to change through the post-combustor gas path of the engine (turbine and exhaust nozzle), exhaust plume, and aircraft wake prior to deposition in the atmosphere. These processes collectively govern the impact of engine exhaust which can affect the global climate. Although there is still uncertainty surrounding the effects of emissions impacts on the global climate, a number of scientific and technological investigations have helped clarify the issue. The following sections discuss the reasons for focusing on aviation emissions, provide a brief overview of potentially influential aircraft emissions, describe atmospheric deposition, and highlight impacts of both subsonic and supersonic aircraft on the atmosphere.

The history of research on this issue dates back to the 1972, when the US Department of Transportation commissioned the Climatic Impact Assessment Program (CIAP) to record all the scientific research on the effects of aviation on the atmosphere up to that date. After CIAP was completed in 1975, NASA became the primary agent for atmospheric research and its Upper Atmosphere Research Program has been active ever since. NASA's research has also been incorporated into reports of the Intergovernmental Panel on Climate Change (IPCC) [2]. In 1988, the AEAP was established to comprehensively predict the atmospheric impacts of future aircraft. The program is a collaborative effort between several government agencies, academic institutions, and industry which was created to study the influence of aviation on the global atmosphere.

The IPCC report [2], entitled "Aviation And The Global Atmosphere," is the most comprehensive source of detailed background information related to this thesis topic. This chapter highlights a few of the relevant topics, refer to the original report for more information.

Species	Operating Condition		
	Idle	Take-Off	Cruise
CO ₂	3160	3160	3160
H ₂ O	1230	1230	1230
CO	25 (10-65)	< 1	1-3.5
HC (as CH ₄)	4 (0-12)	< 0.5	0.2-1.3
NO _x (as NO ₂)	3-6	10-65	7.9-15.4
SO _x (as SO ₂)	1	1	1

Table 1.1 Typical emission index levels (g/kg fuel) [3]

The exact concentrations of the species emitted from the engine are difficult to determine since each combustor behaves differently, and an efficient scheme for collecting accurate data is yet to be established. The levels of the trace species NO_y and SO_x emitted at the engine exit plane are kinetically determined by the amount of time spent in each section of the flow path and the time variability of the temperature and pressure histories realized through the engine (from combustor to the exhaust nozzle). Therefore, the engine specifications and thermodynamic cycle have a direct effect on the emissions. For example, higher temperatures result in greater radical concentrations at the engine exit [1].

1.2.2 ALTITUDE DEPOSITION PROCESS

The area of the atmosphere in which emissions are deposited determines the effects they have upon the atmosphere. Aircraft emissions are released at altitudes ranging from the lower troposphere into the middle stratosphere. The troposphere is the region of the atmosphere located between the ground and about 10 to 15 km (thinner in polar regions and thicker of the equator), the stratosphere is located between the altitudes of 10 to 15 km to about 50 km, and the tropopause is the area dividing these regions. Typical subsonic aircraft operate primarily in the upper troposphere and the lower stratosphere, while supersonic aircraft, such as the Concorde or military aircraft, fly in the middle stratosphere, the exact height being a function of the design Mach number.

When exhaust first exits an aircraft engine, it enters a region termed the near-field plume region, where the engine plume and the aircraft wake do not interact. The initial, turbulent shear induced dispersion of the exhaust jet is more important than any aerodynamic perturbation from the aircraft. Eventually, as the momentum of the exhaust plume is diffused, the vorticity shed from the aircraft wings begins to influence the jet plume. In this wake vortex region, the plumes are entrained and confined in the two counter-rotating tip vortices formed by the self-induced vortex sheet roll-up of the aircraft wake. This structure, at cruise altitude, sinks about 100 m for subsonic aircraft and several hundred meters for supersonic aircraft through a self-induced downwash. After a certain amount of time, the structure begins to deteriorate and break up due to

Radiative forcing is a measure of the importance of a potential climate change mechanism. It expresses the perturbation or change to the energy balance of the earth-atmosphere system in watts per square meter (W/m^2). Positive values of radiative forcing imply a net warming, while negative values imply cooling. Figure 1.2 shows the radiative forcing from different aircraft emissions in 1992 and a projection for 2050.

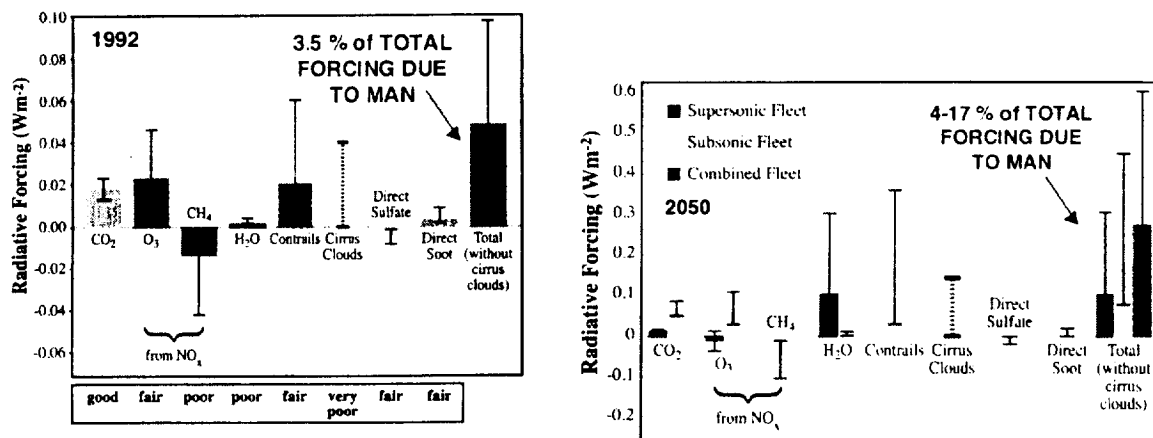


Figure 1.2 Radiative forcing of various trace species [2]

The impacts of CO₂ are well known due to its long atmospheric residence time (~100 years). It becomes well mixed throughout the atmosphere and thus the effects of its emission from aircraft are impossible to differentiate from the same quantity of carbon dioxide emitted by any other source [3]. Emissions such as NO_x, SO_x, and water vapor have shorter residence times and remain concentrated near the aircraft. Thus they lead to changes in radiative forcing localized near the flight route as opposed to emissions that are globally mixed.

Increases in particles emitted from aircraft have mixed effects: soot tends to warm the earth's surface, while sulfate particles tend to cool it. While direct effects of these particles are believed to be small, increases in their emissions by jet aircraft may potentially influence the formation of clouds and contrails, thin white-line clouds seen behind jet aircraft in the upper atmosphere, which may contribute to future climate change [4].

It is difficult to discern the impact of aircraft emissions upon changes in ozone concentration since a decrease in the ozone in the upper and middle stratosphere lead to global warming whereas decreases in ozone in the upper troposphere/lower stratosphere lead to global cooling. In addition, supersonic aircraft, flying in the middle stratosphere, emit species that lead to the destruction of ozone whereas subsonic aircraft, flying in the upper troposphere/lower stratosphere, emit species that lead to the formation of ozone. This formation and destruction of ozone along with emission of species such as CO₂ and H₂O impact the radiative balance of the earth-atmosphere system in the direction of global warming [1].

Global warming due to ozone and water vapor in the upper troposphere/lower stratosphere altitudes is greater than at the surface due to low background concentrations, longer residence times, and large radiative efficiency near the tropopause as compared to the surface.

1.2.3.2 SUPERSONIC AIRCRAFT EFFECTS

Supersonic aircraft fly in the middle stratosphere, near the peak concentration of atmospheric ozone, the exact height being a function of the design Mach number. Figure 1.3 shows the variation of ozone concentration with altitude. The peak ozone range of Mach 2.4 to 4 is where the most recently proposed US high speed-speed civil transport (HSCT) designs operate.

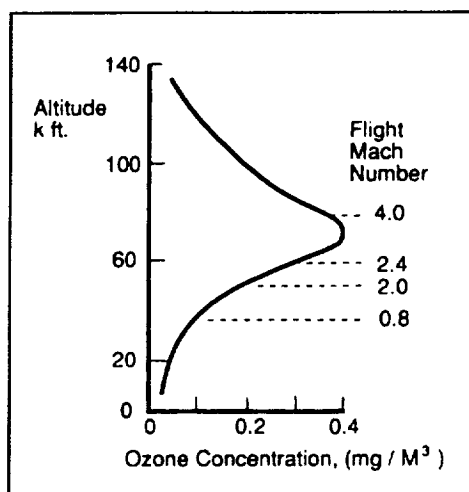
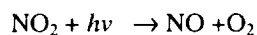
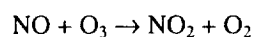
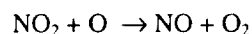


Figure 1.3 Variation of ozone concentration with altitude [7]

NO_x is the trace species that is the most significant contributor to the reduction of ozone, by the following catalytic cycle [7]:

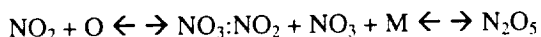
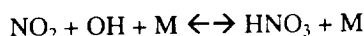
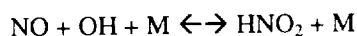


and

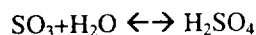
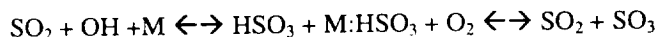
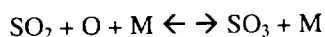


In this cycle, no NO is destroyed, but O₃ is combined with O to form O₂. This problem was first publicized in 1971, when Johnston (1971) calculated that emissions of oxides of nitrogen from a fleet of five hundred supersonic transport aircraft flying at an altitude of 20 kilometers could reduce stratospheric ozone by a global average of 10 to 20 percent [8].

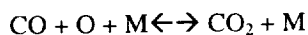
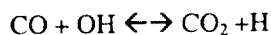
The chemistry that occurs during the deposition process in the plume and wake regions occurs at higher temperatures (500 to 600 K) than atmospheric (200 to 300 K), but lower than the temperatures encountered during the combustion process. At these temperatures, the inclusion of heterogeneous chemistry and dynamics for aerosol formation within the overall processing mechanism is necessary. Primary pollutant and trace species are highly active in the atmosphere, involving both gas-phase and heterogeneous chemistry. The hydroxyl (OH) radical, emitted either with the exhaust stream or formed by photochemical breakdown of atmospheric or exhaust constituents (O_3 , H_2O) initiates and propagates several reactions including gas phase conversions of NO_x to NO_y which occur in general through the reactions:



Water vapor also has an important role. The primary SO_2 gas phase oxidation reactions are:



Competition for the O and OH radical also occurs with the conversion of CO to CO_2 via the reactions:



The gas phase chemistry consists of other conversion processes, most notably the inevitable conversion of NO to NO_2 . Oxidation with the HO_x family can occur in many different ways including reactions with O and H.

Oxidation of SO_2 to SO_3 and H_2SO_4 is of greater interest to modeling and exhaust sampling now since studies have shown that increases in SO_3 concentration lead to higher total aerosol surface area, and greater activation of soot particles. The enhancement of aerosols, as mentioned before, can have important consequences for ozone and climatic impacts. Gas phase species such as N_2O_5 and NO_3 and SO_3 are readily converted in the presence of water containing aerosols to form aqueous HNO_3 and H_2SO_4 .

1.3.2 NEAR FIELD PLUME AND WAKE MODELING

Most in-situ and stationary measurements have been done for subsonic aircraft. These efforts concentrated on chemical activity occurring outside the engine, while only a limited understanding could be gained about the

The research by Lukachko [1], entitled “Research on the Science And Politics of the Atmospheric Effects of Aviation Debate,” is a primary source of work on turbine and exhaust nozzle modeling. The research performed in this thesis is an extension of the work by Lukachko. Lukachko also presents a more detailed summary of other prior work on intra-engine modeling. Refer to the original document for more information related to this section.

1.4 MOTIVATION

As discussed in Section 1.2, important chemical reactions occur in the post combustor flow path which potentially alter the trace species concentration at the nozzle exit plane. Trace species play an important role in the problem of emissions characterization because SO_x and NO_y families have acids and radicals that influence aerosol formation and oxidation processes, which effect the processes that occur outside the aircraft and on a global scale.

The two principal components in the efforts to characterize aircraft emission are physical tests and analytical modeling. Combustor emissions data is gathered using uninstalled combustor-only and full-scale engine tests. Full-scale engine tests at altitude conditions are the most relevant, so some tests have been performed in-flight (in situ). However, in-flight experiments are limited in accuracy due to the distances that must remain between the two aircraft. From combustor-only tests and full-scale engine tests, useful data can be gathered to determine the products that travel through the turbine and exhaust nozzle. There has been few stationary tests performed to measure NO_x , CO and HC [10], [11]. Corrections such as those for humidity and other ambient conditions must be applied to make the test results comparable to each other.

All the above approaches are valid, but there are even more complexities within a combustor. A diversity of both reactants and products of combustion are involved in hundreds of simultaneous reactions. So while the aforementioned species are the majority of the resulting compounds, there are many minor constituents that exist in very small, trace amounts. These species form because of the non-equilibrium chemical state of the exhaust gas and include the hydroxy family (HO_x), nitrogen compounds (NO_y), and the sulfur oxide family (SO_x). These species are emitted at the engine exit plane in levels that are kinetically determined, governed by the time variability of temperature and pressure histories realized within the combustor and through the turbine and exhaust nozzle of the engine as well as the amount of time spent in any particular section of flow path. Therefore, the thermodynamic cycle on which a particular engine is based will have a direct effect on these emissions. Higher temperatures generally result in greater radical speciations and less oxidation progress at the engine exit.

Due to lack of suitable test opportunities and adequate instrumentation only limited data has been acquired. Since experimental testing is expensive and time consuming, computer modeling is an efficient method for trace

1.4.2.1 MODELING METHODOLOGY

A modeling methodology was developed to simulate trace species evolution in the post-combustor flow path of a gas turbine engine. The methodology involves a fundamental time scale analysis which can help guide the overall modeling strategy and provide insight into the mechanisms influencing trace species evolution. The methodology includes specifying chemical initial conditions, fluid boundary conditions, and performing numerical solutions to the fluid mechanics and chemical kinetics problems at various levels of detail using either high fidelity, low fidelity, or a combination of modeling techniques. Key parameters affecting levels of intra-engine trace species were identified and incorporated into the model thereby improving the accuracy and increasing the efficiency of the model.

1.4.2.2 MODELING TOOLS

Usability and modeling accuracy improvements to the existing modeling tools were made, which included:

- incorporating a 3D fully unstructured grid generation tool which allows simulations of complex arbitrary geometries
- adding multiple inlet/exit capability which allows simulation of mixing flows
- adding parallel chemistry routines to improve execution time
- refining circumferentially varying unsteady inlet conditions to improve modeling accuracy and further investigate the effects of flow non-uniformity on chemistry
- improving chemistry initial condition specification procedure
- adopting improved chemistry convergence criteria
- selecting a new chemical mechanism which incorporates new kinetic data for sulfur chemistry provided by Princeton University

1.4.2.3 VALIDATION

Some model limitations were established through a validation exercise that attempted to model the Princeton University Variable Pressure Flow Reactor. The new grid generator and multiple inlet/exit modifications were demonstrated, but the fluid, mixing, and chemistry modeling could not be validated due to compressibility limits of the code, as well as, the possible unsteady flow regime of the reactor.

Further validation efforts were performed on a representative 1D engine cycle and 2D turbine geometry. They included evaluation of various chemical mechanisms, species convergence criteria, periodic boundary conditions, and the parallel code modifications.

1.4.2.4 MODELING THE NASA/DERA ENGINE TEST

The modeling methodology was applied to an engine to perform the first complete post-combustor engine simulation. Trace species concentrations were predicted at the nozzle exit for several test cases based on an

- The region of the atmosphere where emissions are deposited determines their effects on the atmosphere. A decrease in the ozone concentration in the upper and middle stratosphere leads to global warming whereas a decrease in ozone in the upper troposphere/lower stratosphere leads to global cooling. Overall, this formation and destruction of ozone impact the earth-atmosphere system in the direction of global warming.
- Subsonic aircraft affect chemical and radiative processes mainly through emission of NO_x , but also H_2O , SO_x , and soot. These emissions lead to the formation of ozone in the upper troposphere/lower stratosphere.
- Supersonic aircraft fly in the middle stratosphere near the peak concentration of atmospheric ozone. Through NO_x emissions they lead to the destruction of ozone
- Prior work has involved modeling and measuring trace species in the near field plume and wake of an aircraft and computational fluid-chemical modeling in the intra-engine environment. Results suggest that most trace species chemistry occurs early, thus there is a need for better characterization of trace species in the intra-engine environment.
- See the thesis by Lukachko [1], "Research on the Science And Politics of the Atmospheric Effects of Aviation Debate," for more background and preliminary work on intra-engine modeling.
- Computational modeling is an efficient means to acquire detailed information about intra-engine trace species chemistry since experimental techniques are complicated, time consuming, and expensive.
- The contributions of this thesis include:
 - Continued development the post-combustor trace species modeling methodology
 - Improvements to modeling tools
 - Continued validation of the model and improvements to the modeling tools
 - Performed the first complete post-combustor engine simulation to support an engine test campaign
 - Investigation of a few physical phenomena which influence trace species evolution

They are aimed at further characterization of aircraft emissions, in particular modeling the evolution of trace species in the post-combustor flow path of gas turbine engines.

2 MODELING METHODOLOGY

The outcomes of this work are several tools which can be used to evaluate and improve the design of gas turbine engines with respect to trace species emissions as well as investigate the effects of various fluid or chemical parameters on the evolution of trace species. Section 1.4 detailed the motivation and advantages of modeling the evolution of species in the post-combustor flow path. In many cases, the numerical tools can be used as a fast and inexpensive means to evaluate potential designs or to probe specific research questions. The procedure developed is adaptable to several levels of modeling detail (or accuracy) and its capability can easily be extended beyond its current state. Many aspects of the models have been previously validated. The flow solver itself is a well-established turbomachinery code [51]. Validation exercises done by Lukachko [1] verified proper calculation of kinetics as specified in the chemical mechanism, species convection, species diffusion, mixing, influence of heat transfer or boundary layers, and some numerical issues on the chemistry solution. The validation efforts are ongoing, with several code improvements verified through test cases in this thesis (see Section 4) and the ensuing effort to benchmark the code against actual engine test data in the NASA/DERA engine test simulation. The modeling methodology is a collaboration of work from many researchers [3], in particular it is a continuation of work by Lukachko [1].

2.1 CHAPTER OVERVIEW

The purpose of this chapter is to provide an overview of the intra-engine species evolution modeling methodology presented in this thesis. Various physical processes that can be incorporated into the models, as well as their potential effects, are listed. The basic procedure for a time scale analysis is defined. The relevance and advantages of performing a preliminary time scale analysis are presented, using several examples to demonstrate the utility of the time scale analysis. This chapter also discusses some of the details associated with the specification of the initial chemical conditions at the combustor exit plane. Finally, a broad overview of both the low and high fidelity modeling techniques is presented.

Modeling Element Or Physical Process	Potential Effects On Species Evolution
Chemical mechanism	Important to capture appropriate reactions for accuracy [Section 4.3]
Boundary layers and wakes	Changes residence time and thermodynamic state
Engine operating condition	Higher combustor exit temperatures enhance SO ₃ conversion [3], [Section 5.6.1]
Combustor temperature non-uniformities	Induces large scale non-uniformity [Section 5.6.2]
Downstream persistence of non-uniformities	Various implications [Section 5.6.3]
Blade cooling (thermal)	Enhances SO ₃ conversion [1], [Section 5.6.2]
Heat release or secondary reactions	Can be important locally, details unknown [65]
Chemilions	Negligible effect [58]
Heterogeneous chemistry	Negligible effect [58]
Blade cooling (mass addition)	Unknown
Turbulence	Unknown

Table 2.1 Some possible modeling elements influencing intra-engine chemistry

Table 2.1 is not meant to be a comprehensive list of all physical processes and modeling elements which can impact intra-engine chemistry and their effects, but rather a list of a few items which were brought out in the course of this research. It is important to note that the effects of many of the modeling elements or physical processes are often inter-related and may not be important in all situations. Hence, the term “potential effects” meaning that the effect was observed for a given set of conditions modeled, however, is not necessarily always the case nor the only possible effect. The modeling methodology and tools developed in this thesis incorporate many of the elements listed in Table 2.1 or can be readily adapted to include them. The modeling exercises in Section 4, Validation, and Section 5, Modeling the NASA/DERA Engine Test, explore the impacts of several these modeling elements and physical processes. The exercises were used to investigate the magnitude of the impacts and develop appropriate models that can be used to simulate the relevant processes.

The main effects typically derive from the interaction of fluid mechanics and chemistry. The fluid mechanical phenomena can alter the chemistry through parameters involved in the Law of Mass Action or Arrhenius Equation, specifically through the temperature, pressure, residence time, or chemical composition which will be discussed in more detail in Section 3. The scale (i.e. size) of the fluid mechanical phenomena can have an impact on the magnitude of the effects.

2.3 PROCEDURE

The steps outlined in Sections 2.3.1 through 2.3.3 constitute the modeling methodology for studying the trace species evolution in the post-combustor flow path of gas turbine engines. Figure 2.1 is a graphical depiction of the procedure.

analysis is beneficial. Furthermore, the time scale analysis can be used to assess the impact of detailed flow processes and influence of various chemistries. The time scale analysis includes three fundamental controls on chemical evolution; thermodynamic potential, chemical kinetics, and residence time.

The concept and method of the time scale analysis were developed by Lukachko [31] and are further detailed in unpublished internal research documentation. An endeavor to formally publish the work is planned in the near future.

2.3.1.1 BASIC PROCEDURE

The thermodynamic potential is the difference between a given composition and the equilibrium composition. This potential change in a given species and the chemical time scale required for the change can be mapped out over a large temperature and pressure parameter space using only the key reactions of interest. Figure 2.2 shows a typical plot of the thermodynamic potential, expressed as % SO_3/SO_x at equilibrium, over a parameter space relevant to gas turbine engines. Several additional simplifying assumptions about the chemistry can be made in this preliminary analysis. In this case, SO_3 chemistry is being investigated using only the O and OH pathways from [28], using only forward reactions, and assuming equilibrium radical levels.

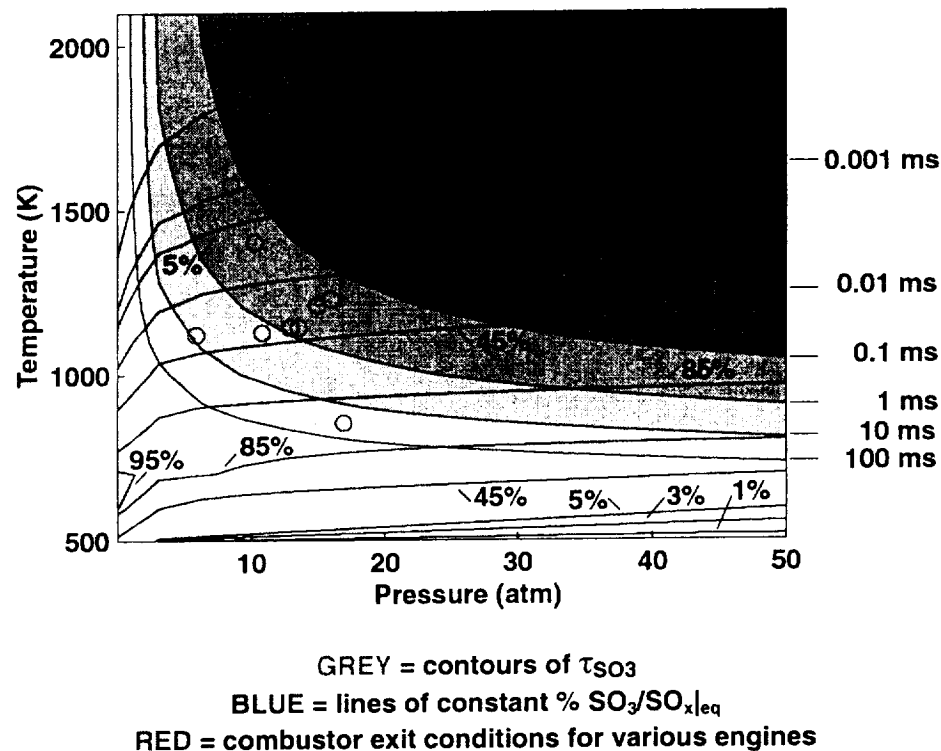


Figure 2.2 Typical thermodynamic potential and chemical time scale plot underlying a time scale analysis for SO_3 (courtesy of Stephen Lukachko)

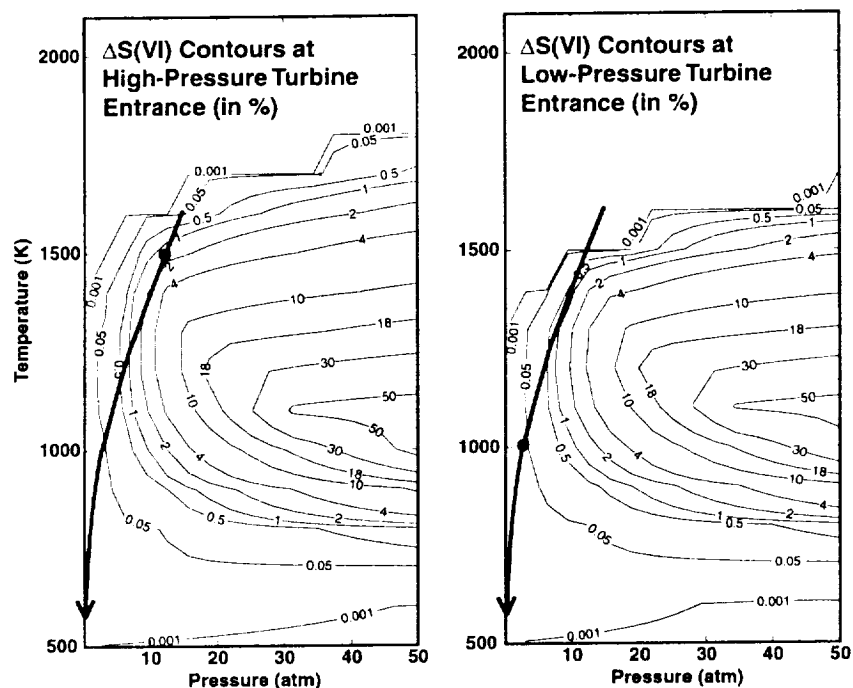


Figure 2.3 Severity parameter for SO_3 from typical time scale analysis at two engine stations (courtesy of Stephen Lukachko)

A curve representing the post-combustor flow path can be plotted on the map. The example in Figure 2.3 shows a curve (blue) for a representative engine at cruise. The severity parameter plot can be used to point out several aspects of the selected chemistry. First, notice that the contours of constant $\Delta S(\text{VI})$ shift as one traverses through the engine. The shift is due to the amount of conversion which previously occurred, the new thermodynamic state, and to a lesser extent the change in residence time at the specific engine station. Second, the contours indicate a zone of maximum SO_3 formation. In this case, there is more than 10% conversion for temperatures of 1,000-1,300K and pressures over 20 atm. Finally, the severity parameter plot at the low pressure turbine entrance indicates that there is a negligible amount of further conversion possible (i.e. the active chemistry has completed in the high pressure turbine). This would suggest that the need for higher fidelity modeling should be concentrated in the high pressure turbine region.

Finally, by integrating along the path shown in the figure preliminary estimates can be made for the evolution of the species. The simplifying assumptions inherent in the time scale analysis must be considered when making quantitative estimates. Thus, the time scale analyses are primarily used as a guide for further modeling.

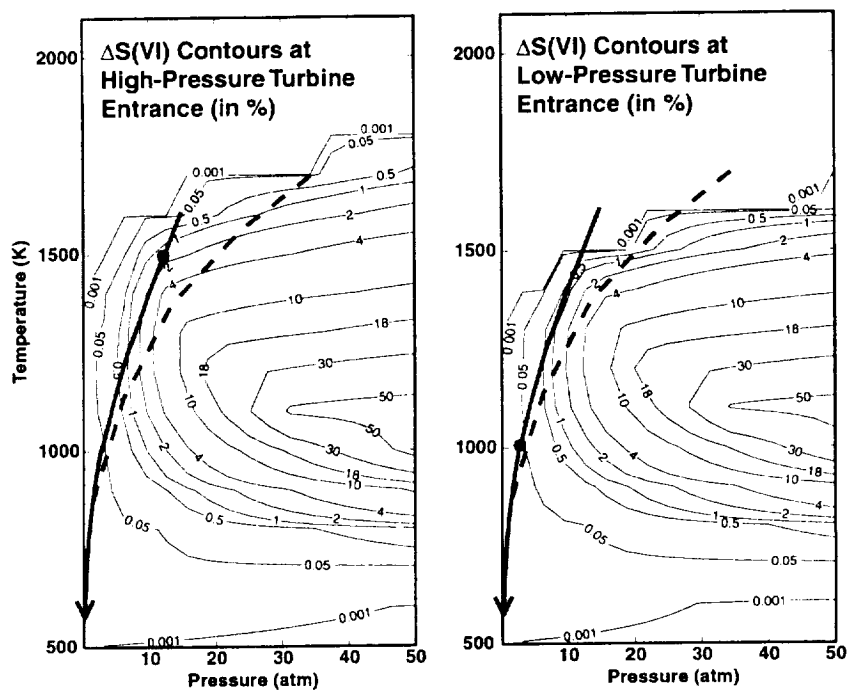


Figure 2.5 Investigating the effects of operating condition on chemistry using time scale analysis (courtesy of Stephen Lukachko)

As a final example of the utility of the time scale analysis, the influences of different chemistries can be assessed. Figure 2.6 shows a comparison of two time scale analyses, one using only the $\text{SO}_2 + \text{O}$ pathway for SO_3 formation, and the second using both $\text{SO}_2 + \text{O}$ and $\text{SO}_2 + \text{OH}$ pathways. In this situation, which assumes an equilibrium level of OH/O of about 10, it is evident that the OH route is more active than the O route. Thus, the time scale analysis can give insight as to which chemical pathways are most important for the species subset being studied.

Some minor improvements to the code were made to address the rapid initial shift in some species found in past simulations. A overview of the initial conditions code procedure is given in Figure 2.7.

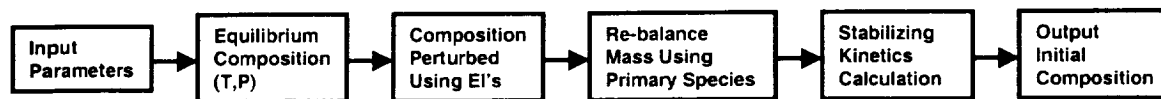


Figure 2.7 Overview of chemistry initial condition specification

The code starts with the equilibrium composition at the combustor exit conditions. The composition is then perturbed using specified emissions indices or species ratios. The addition of the trace species is balanced by adjusting the levels of the primary combustion products. Finally, a constant temperature and pressure kinetics calculation is run for a very short time to reach a stable non-equilibrium composition. Table 2.2 lists the input parameters for the code.

Initial Conditions Code Input Parameters
Temperature (K)
Pressure (atm)
ϕ (equivalence ratio)
η (combustion efficiency)
CO/H ₂ /HC ratio
EI(NO _x) (g/kg fuel)
NO/NO _x ratio
EI(S) (g/kg fuel)
SO ₂ /SO _x ratio
EI(CO) (g/kg fuel)

Table 2.2 Input parameters to initial conditions code

The improvements to the technique in [1] were made by changing some of the input parameters used to perturb the equilibrium composition and also in performing the kinetics calculation to stabilize the composition, see Section 2.3.2 for more details. The non-equilibrium solution initially output from the code is inherently unstable. Although some attempt is made to redistribute the mixture to a “stable non-equilibrium state” when applying the EI’s, the entire set of reactions in the mechanism can not be considered easily. Running the kinetics calculation for a short time allows the species to make the initial rapid re-adjustment to a “stable non-equilibrium state” with a negligible change to the overall composition. The duration of the kinetics calculation was chosen by plotting each species versus time for the constant temperature and pressure calculation and then moving back to the point where each species was deemed to be outside of the “initial shift region.” Figure 2.8 and Figure 2.9 show the mole fraction of a few species and several of the EI’s versus time during the stabilizing kinetics calculation. The left column of graphs show the result of the entire calculation, which was chosen as 5 ms to exceed a typical blade passage flow-through time. The green lines indicate 0.30 ms, and the graphs on the right column are an enlarged detail of the 0 to 0.3 ms region. For this case, the red line at 0.02 ms was

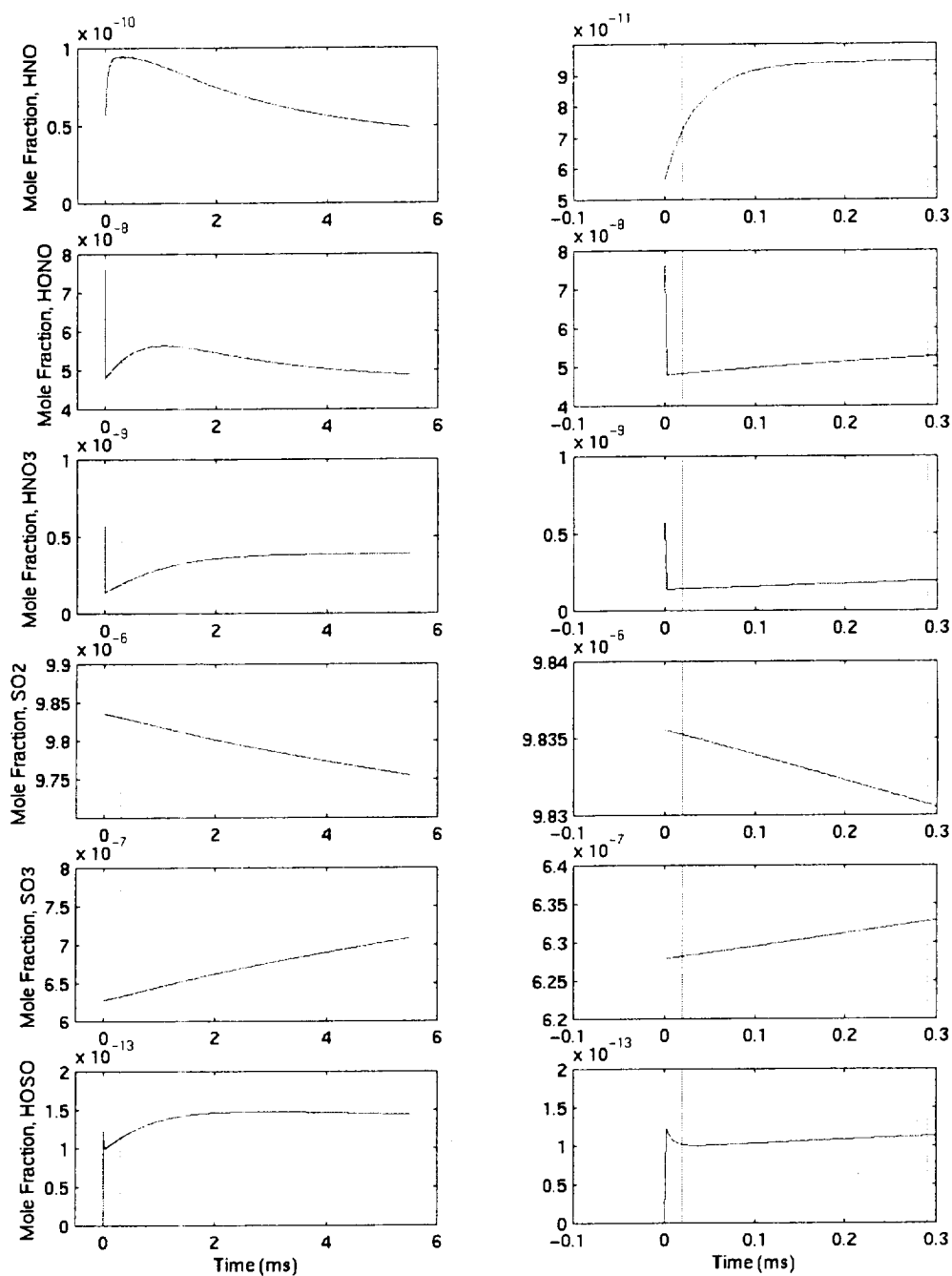


Figure 2.8 Representative constant temperature and pressure kinetics calculations for selected species for initial conditions formulation

2.3.3 HIGH AND LOW FIDELITY MODELING

The modeling techniques are divided up into two categories, high fidelity and low fidelity. The word fidelity can mean accuracy in details or exactness, and high or low fidelity represents the degree to which a reproduction is faithful to the original. In the sense of the modeling methodology being described here, a low fidelity model is a simple 1D simulation which can in general only track average quantities. A high fidelity model is any model which can directly simulate more detailed multi-dimensional flow features and thus account for chemical or flow non-uniformities. The high fidelity model, containing more details of the actual system being modeled is expected to be more accurate, although, the accuracy of the high fidelity model is also based on its ability to accurately represent the details being simulated.

In contrast to a simplified time scale analysis which is based on chemical kinetics alone, the low and high fidelity models are based on integrating the equations of mass, momentum, and energy over a discrete domain (see Section 3.2) coupled with the chemical kinetics solution. For a low fidelity model the integration occurs over a 1D profile and for a high fidelity model it occurs over a 2D or 3D grid.

A time scale analysis can be used as a guide to map out the modeling strategy. It is desirable to concentrate modeling resources on areas of the engine which have a high degree of chemical activity for the species of interest. A 2D or 3D reacting fluid-chemical simulation can be done on the regions of the engine flow path targeted for higher fidelity models. A suite of numerical tools to be discussed in more detail in Section 3 was further developed in the context of this thesis. It consists of a grid generator, fluid and chemical kinetic solvers, and flow visualization codes which can be used to do such higher order modeling. The higher order modeling can include the effects of many physical phenomena typically encountered in a turbomachinery environment such as complex geometries, viscous walls, cooled surfaces, and unsteadiness (see Section 2.2). These phenomena can cause local temperature, pressure, or species gradients, which can influence the subsequent evolution of chemical species. Higher fidelity modeling requires more user effort to set up and post-process and is more computationally intensive. These simulations take roughly 10 to 100 times an investment in resources compared to a low fidelity model. A typical high fidelity simulation may take several days to weeks to setup and run whereas a low fidelity simulation can be completed in a matter of hours or days (see Section 3.3.3 for more details). However, the high fidelity models can increase the predictive capability of the modeling methodology and help provide insight into the mechanisms responsible for altering chemical evolution if applied in regions where chemistry is suspected to be more reactive.

The complete details of the procedure needed to perform a higher fidelity simulation are numerous and highly dependent on the particular modeling situation. Many of these details are discussed further elsewhere in this thesis (especially Section 3) or in several external references such as [1], [48], and [49]. The basic process

- Time scale analyses are useful in formulating a overall modeling strategy by indicating the critical areas of the engine flow path to investigate with higher fidelity modeling.
- A time scale analysis is a simple parametric study which incorporates thermodynamic potential, chemical kinetics, and residence time. The output is a plot of severity parameter for a given species of interest, although, a preliminary estimate of species evolution can be obtained.
- Time scale analyses can also be used to provide insight into the physical phenomena influencing trace species evolution. A few example time scale analyses were used to show:
 - Blade cooling can enhance sulfur conversion.
 - Engine operating condition can influence sulfur conversion, take-off conditions can have higher sulfur conversion than cruise conditions.
 - The OH pathway to SO_3 can be more active than the O pathway.
- A simple method for specifying chemistry initial conditions involves perturbing an equilibrium composition, re-balancing the species based on mass, and doing a stabilizing kinetics calculation.
- High and low fidelity models involve integrating the equations of mass, momentum, and energy over a discrete domain coupled with chemical kinetics to simulate intra-engine chemistry. A high fidelity model can incorporate many multi-dimensional effects (i.e. non-uniformities) while a low fidelity model uses average quantities.

3 MODELING TOOLS

Underlying the modeling methodology presented in Section 2 are several computer codes which are used to generate grids, specify initial conditions, numerically solve the fluid mechanics and chemical kinetics problems, and visualize the results for geometries of interest to intra-engine chemistry.

3.1 CHAPTER OVERVIEW

The purpose of this chapter is to present a brief overview of the modeling tools and discuss the improvements made to these tools during the course of this research. The existing modeling tools consist of the PRE grid generation code, PROCESS grid pre-conditioner code, POST grid post-processor code, CNEWT and CALCHEM flow-chemistry solvers, and CNEWTVS6 flow visualization code. The improvements made to the existing tools allow for more complicated geometries, multiple inlet and exits, improved execution time for solutions with chemistry, and a specification of a pressure, temperature, and species concentration deficits associated with a wake of an upstream blade or blade row.

In summary, the following are the main points of the chapter:

- CNEWT and CALCHEM are useful modeling tools for studying intra-engine trace species flow-chemistry problems. Other supporting codes necessary for turbine chemistry modeling are PRE, PROCESS, POST, and CNEWTVS6.
- For more details on the structure and numerical mechanics of the codes, refer to “Research on the Science And Politics of the Atmospheric Effects of Aviation Debate” by Lukachko [1] as the primary source of information.
- In order to provide further insight into trace species characterization, improvements were made to existing modeling tools which include:
 - Obtaining a new grid generator
 - Adding multiple inlet/exit capability
 - Parallelizing chemistry subroutines
 - Implementing a wake model boundary condition

3.3 IMPROVEMENTS

Several improvements to the modeling tools were made during the course of this research aimed at extending the capability and improving the accuracy of the modeling tools. A few extensions are discussed elsewhere in this thesis; first, the procedure for specifying chemistry initial conditions was improved and as detailed in Section 2.3.2, next, a new chemical mechanism for turbine chemistry modeling was adopted as described in Section 4.3, finally, the chemistry convergence criteria were refined as discussed in Section 4.4. This section describes several additional improvements to the modeling tools. In particular, a new grid generator was obtained, a option for multiple inlets/exits was added, the chemistry subroutines were parallelized, and a wake model boundary condition was implemented into the codes.

3.3.1 CAD BASED FULLY UNSTRUCTURED GRID GENERATION

Grid construction is important since it determines the resolution (i.e. accuracy) of the flow solution and impacts the computational time, therefore an accurate and efficient grid construction is desired. The grid generator used for previous investigations, called PRE, is best suited to turbomachinery blade passages. The grids typically had four sides, with a blade form either entirely within the domain (block 5 input format) or on the side boundaries (block 3 input format). The grids are initiated as a structured mesh composed of hexahedral cells and are transformed into tetrahedral grids simply by dividing the hexahedrons. Hence they were “pseudo-unstructured,” since although being tetrahedral, the cells were still in an orderly arrangement based on the initial hexahedral grid. By piecing together several blocks, a more complicated grid can be obtained, such as a blade with tip clearance.

The structured or “pseudo-unstructured” grid is less flexible in the types of geometry it can mesh and it may cause some numerical issues. In previous work, of validation runs using a PRE meshed geometries, the temperature and velocity exit plane contour plots showed an undesirable result of hotter, slower flow in the corners perpendicular to the mesh diagonal and grid scale oscillations in solution variables which could be linked to the structure of the grid [1].

New grid generation tools developed at Cambridge University were implemented to overcome these potential problems and extend the codes to more complex arbitrary geometries [35] and [66]. This set of grid tools requires an initial CAD-generated geometry, which can be created with typical commercial solid modeling software. Thus, virtually any arbitrary geometry can be created and meshed. There are essentially three main aspects that comprise the new grid generation tools; the solid model, the surface mesh, and the volume mesh. Figure 3.1 shows the difference between a pseudo-unstructured grid made with PRE and fully unstructured grid made with the new grid generator.

Volume Mesh

The volume meshing routine uses the binary surface mesh file to create the final 3D grid. There are no grid controls which can be applied during volume meshing, except for specification of viscous layers. Rather, the volume grid generator attempts to make an isotropic mesh with cells that are a uniform size. There are three stages involved in the volume meshing which perform the following basic steps:

Stage 1:

- creates 8 construction nodes encompassing the surface mesh
- starts with the initial construction cell and connects surface nodes into tetrahedrons using 3D Delauney triangularization by marching across domain, grabbing, and constraining each surface node

Stage 2:

- generates viscous layers by extruding nodes near walls flagged as viscous
- moving front

Stage 3:

- in-fills domain by inserting new nodes into cells that fail quality measures
- locates tetrahedral cell that the new node is in, then divides into many new tetrahedral cells
- edge swapping based on 3D Delauney to improve local mesh quality

Figure 3.2 shows a mesh after a stage 1 dump and two meshes, one without viscous layers and one with viscous layers, after a stage 3 dump.

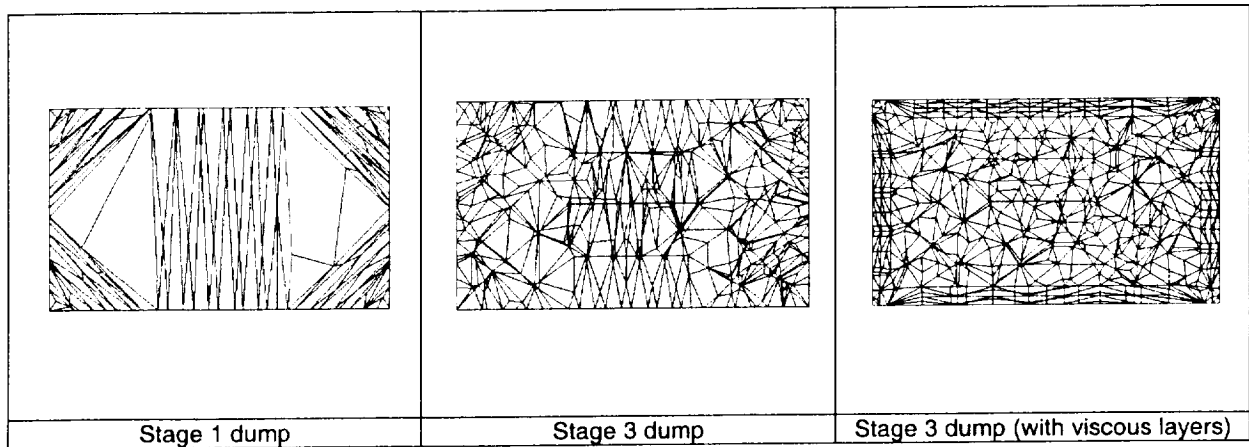


Figure 3.2 Volume mesh stage dumps

Note that the cells in the cross-section may not look uniform, because the cutting plane intersects some cells near a vertex (giving the appearance of a very small cell), some cells near an edge (giving the appearance of a sliver shaped cell), as well as some near the center of the cell. The volume mesh routine outputs a mesh connectivity variable file (.mcv) which contains the 3D mesh in NEWT format. More details of the new grid generation tools can be found in [66].

During the period of work on this thesis, the new grid generation tools were in a developmental stage. They worked well for simpler geometries, however, some difficulties were encountered for more complex

case demonstrated that the multiple inlet/exit code additions to CNEWT work properly, however, further validation should be pursued.

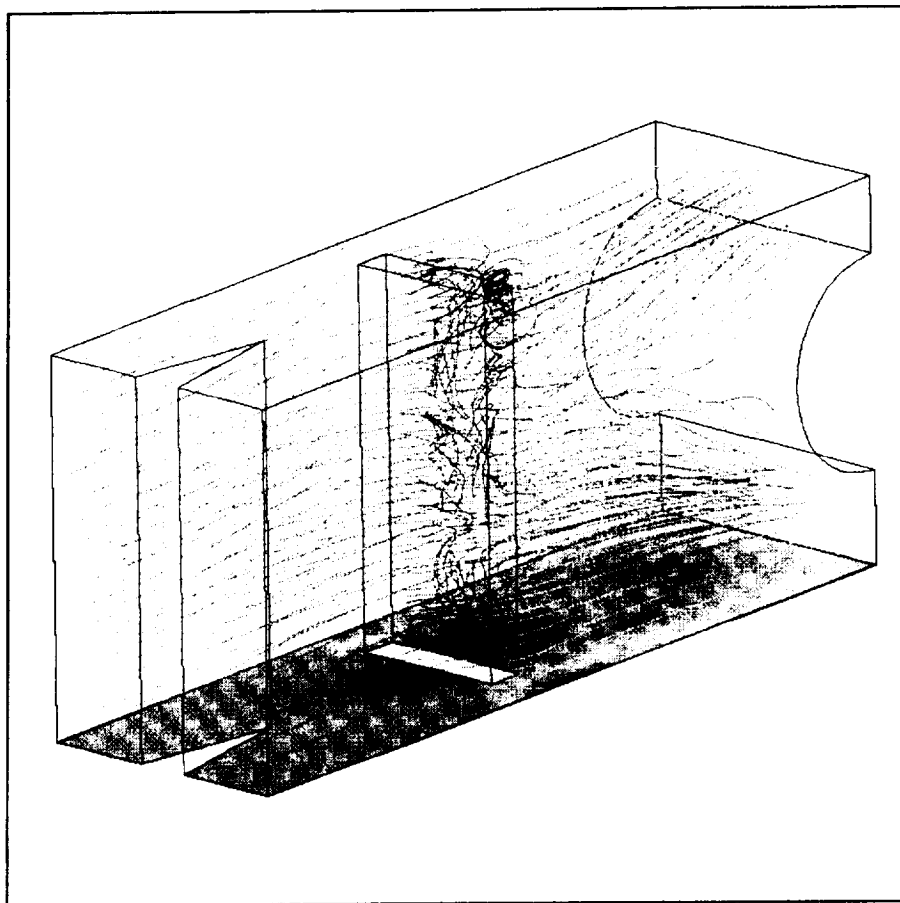


Figure 3.3 Multiple inlet/exit test case, X direction velocity on streamlines

Another implementation of the multiple inlet/exit feature is the Princeton VPFR validation exercise presented in Section 4.2 where flow reactor injector inlets are shown in Figure A.18.

3.3.3 PARALLEL CHEMISTRY SUBROUTINES

A high fidelity model of a coupled fluid and chemistry problem can require a large amount of computational resources. For a typical problem, the chemistry solution requires about 90% of the computational time. The desire to improve accuracy by resolving geometries with more detailed grids and through the use of broader chemical mechanisms, as well as, the desire to increase the turn-around time for high fidelity models prompted the exploration of methods to improve execution time. The structure of the CNEWT code, with the explicit operator-splitting algorithm in which the fluid and chemistry solutions are decoupled lends itself to a

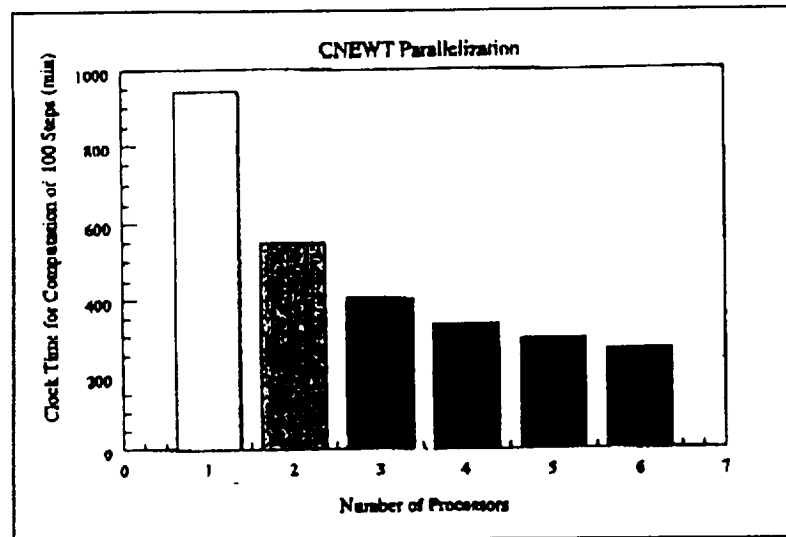


Figure 3.4 Run time statistics for parallel CNEWT

The solutions were also checked for accuracy by comparing a few maximum and minimum flow and species variables for the original code and the parallel version across several nodes. The fluid solutions for the original and parallel version (any number of processors) of the code were identical. The difference between the original and parallel version of the code with regard to the chemistry solution was found to be less than 0.2% in all of the species quantities checked. Also, the chemistry solutions from the parallel code were identical when the number of nodes was varied. Further instructions on how to compile and run the parallel version of the code are given in the README.TXT file included with the CNEWT code.

3.3.4 SPECIES AND TEMPERATURE WAKE MODEL

The original CNEWT code employs a wake model which allowed the specification of a rotating, circumferentially varying inlet profile for total pressure. The main purpose of this wake model was to allow the specification of a pressure deficit associated with the wake(s) of an upstream blade or blade row without the need to do a full unsteady calculation with both blade rows using, for example, a sliding plane technique. Thus the code could be run in unsteady mode, with a fixed timestep, and the unsteady effects of the wakes could be captured using a single blade row.

This wake model was extended to include total temperature and chemical species mass fractions. With these modifications, the capability of the code was increased by allowing a more accurate specification of the inlet conditions and enabling the investigation of the unsteady interaction of chemical and temperature non-uniformities with downstream blade rows.

3.4 CHAPTER SUMMARY

The purpose of this chapter was to present a brief overview of the modeling tools and discuss the improvements made to these tools during the course of this research. The existing modeling tools consist of the PRE grid generation code, PROCESS grid pre-conditioner code, POST grid post-processor code, CNEWT and CALCHEM flow-chemistry solvers, and CNEWTVS6 flow visualization code. The improvements made to the existing tools allow for more complicated geometries, multiple inlet and exits, improved execution time for solutions with chemistry, and a specification of a pressure, temperature, and species concentration deficits associated with a wake of an upstream blade or blade row.

In summary, the following is a list of all relevant points presented in this chapter:

- CNEWT and CALCHEM have been useful modeling tools for studying intra-engine trace species flow-chemistry problems. CNEWT is a code created by Lukachko [1] which was built upon the NEWT turbomachinery CFD code from Dawes [51]. CALCHEM is a simple, 1D version of CNEWT.
- Other supporting codes necessary for turbine chemistry modeling are PRE, PROCESS, POST, and CNEWTVS6.
- For more details on the structure and numerical mechanics of the codes, refer to "Research on the Science And Politics of the Atmospheric Effects of Aviation Debate" by Lukachko [1] as the primary source of information.
- In order to provide further insight into trace species characterization, improvements were made to existing modeling tools which include:
 - A new CAD solid model based grid generator which allows for the simulation of more complicated, arbitrary geometries. The output is a truly unstructured grid. The tools were in a developmental stage and a few difficulties were encountered with the translation step and numerical issues in the volume mesher. The VPFR was successfully meshed with the new grid generator.
 - Addition of multiple inlet/exit capability which allows for simulation of mixing flows. A test case and the Princeton VPFR were used to validate the multiple inlet/exit code modifications.
 - Addition of parallel chemistry subroutines. A test case showed a factor of 3.4 improvement in time on 6 compute nodes. The accuracy of the parallel chemistry modifications was verified.
 - Implemented and tested a wake model boundary condition for temperature and chemical species which allows for the investigation of unsteady effects including flow-chemistry interactions.

4 VALIDATION

Validation of the modeling tools is essential to provide confidence in the results obtained using the modeling methodology and verify new features or modifications. A validation exercise using the Princeton Variable Pressure Flow Reactor (VPFR) was pursued in order to prove the accuracy of the analysis tools and modeling methodology, in particular the new grid generator and multiple inlet/exit modifications. The chemical mechanism is a fundamental element underlying the intra-engine chemistry model. Thus the selection of an appropriate chemical mechanism for intra-engine chemistry modeling must also be justified. The convergence criteria and periodic boundary conditions are also important aspects of the model that must be proved accurate. All of the validation exercise presented help add to the knowledge base available to improve the modeling of intra-engine post-combustor chemistry.

4.1 CHAPTER OVERVIEW

The purpose of this chapter is to describe the validation exercises performed during the current research period. An attempt to benchmark the modeling tools through simulation of a flow reactor experiment is presented. Although it was not completely successful, it provided the opportunity to test several code improvements, investigate the limitations of the modeling tools, and analyze flow features of the reactor. A chemical mechanism study which investigated the effects of the chemical mechanism on intra-engine chemistry modeling and selected a mechanism for use in the NASA/DERA engine test modeling is detailed. This chapter also discusses a convergence criteria study which resulted in improved chemistry convergence indicators. Finally, a periodic boundary condition study is presented.

In summary, the following is a list of the main points of the chapter:

- An attempt was made to model a VPFR experiment to benchmark the accuracy of the modeling tools, however, a limitation to the flow solver prevented this ultimate objective. The flow features from the simulation did not match those expected from experimental data and empirical correlations.
- The VPFR validation exercise proved useful in validating some improvements to the modeling tools, namely the new fully unstructured grid generator and the multiple inlet/exit improvement.

This validation effort was conducted in collaboration with Princeton University. Professor Fred Dryer and Mark Mueller made important contributions to the work presented in this section.

4.2.1 OBJECTIVES

The VPFR is ideally suited to evaluate the capability of the modeling tools to represent many flow features of interest, mixing, and passively reacting flow. The specific objectives of the VPFR modeling effort were to:

- Model a VPFR reacting flow experiment in order to benchmark the accuracy of the modeling tools
- Identify the capabilities and limitations of the analysis tools, specifically with regard to characterizing the flow features, mixing, and chemistry
- Help expand the modeling techniques by evaluating several new code features, in particular, the new grid generator, multiple inlet and exit planes, and parallel chemistry subroutines
- Help establish the modeling methodology applicable to studying intra-engine trace chemistry
- Provide an analysis that can identify potential improvements to the flow reactor facilities or experimental protocol

The approach was to model a published flow reactor experiment and compare the simulation data to the experimental data. The plan was to first simulate the flow-only, then flow with inert species, and finally passively reacting flow. In the end, the objectives of the flow reactor were reduced due to the restriction of the code to simulation of compressible flows.

4.2.2 SUMMARY OF RESULTS

Limitations of the flow solver hampered the ultimate objective of validating the modeling tools through a successful reacting flow simulation of the Princeton VPFR. Although the validation exercise was not completed, many code improvements were tested, a considerable amount was learned about the limitations of the tools, and some potential issues with the flow reactor design were identified.

The new fully unstructured CAD based grid generator was successfully used to mesh the complex VPFR geometry. At the time of the work in this thesis, the new grid generation tools were in a developmental state. A significant amount of geometry repair was required to obtain a surface mesh and the volume mesh routine had trouble with large aspect ratio geometries. The multiple inlet/exit improvement was qualitatively validated. It was found that the VPFR grid had to be initialized to a zero initial guess for the velocity to achieve a solution due to the complicated geometry.

Several experimental conditions were considered when applying the modeling tools. The assumptions for passively reacting flow, steady or unsteady flow, and compressible or incompressible flow need to be addressed prior to embarking on a modeling effort. Two cases were presented to illustrate the major findings of the VPFR validation efforts, a low Re case (Run 1) and a high Re case (Run 12). The results were evaluated by

4.3 CHEMICAL MECHANISM STUDY

An important element of the modeling methodology is the chemical mechanism, which describes the reactions among the species set. Previous work [1] on intra-engine chemistry modeling used a chemical mechanism that was published in [28] and was developed by Aerodyne Research, Inc. [67]. The mechanism was created by doing a survey of the chemical kinetic literature and piecing together various reactions and sub mechanisms which were of interest to intra-engine trace species chemistry. The main species of interest to intra-engine modeling are HNO_2 , HNO_3 , SO_2 , SO_3 , H_2SO_4 , OH , H_2O_2 , HO_2 , O , and NO_x [67]. However, the task of assembling literature data into a mechanism is not easy since much of the chemical kinetics data available is not applicable to the ranges of pressure and temperature experienced in gas turbine engines. As the current research was being conducted, a new chemical mechanism was developed at Princeton University based on flow reactor experimental data. This section contains a study of chemical mechanisms which was conducted to validate the prior intra-engine chemistry work [1] and possibly improve the chemical mechanism used in the modeling methodology.

4.3.1 OBJECTIVES

The main objective of this study is to investigate the sensitivity of the modeling methodology to the selection of chemical mechanism. In essence, the effects of chemical kinetics on trace species evolution were studied. The results of this study were used to validate prior work and to select the chemical mechanism for the NASA/DERA engine test modeling. The selected mechanism is also recommended for future intra-engine trace chemistry modeling.

4.3.2 APPROACH

The approach was to repeat prior calculations done by Lukachko [1] using variations of a mechanism which was based on recent experimental data. A comparative study was done on the following four turbine chemistry mechanisms:

- Lukachko et al. (1998) [28] (26 species and 74 reactions)
- Glarborg et al. (1996) [24] (56 species and 169 reactions)
- Mueller et al. (2000) – full [23] (56 species and 169 reactions)
- Mueller et al. (2000) – truncated [23] (29 species and 73 reactions)

The Glarborg et al. (1996) and Mueller et al. (2000) mechanisms were based on experimental data and contain similar species subsets as Lukachko et al. (1998). The Mueller et al. (2000) mechanism is based on the Glarborg et al. (1996) mechanism with modifications in the SO_x chemistry at higher pressures. The Mueller et al. (2000) mechanism is split into a full and truncated version. The full mechanism contains the complete set of

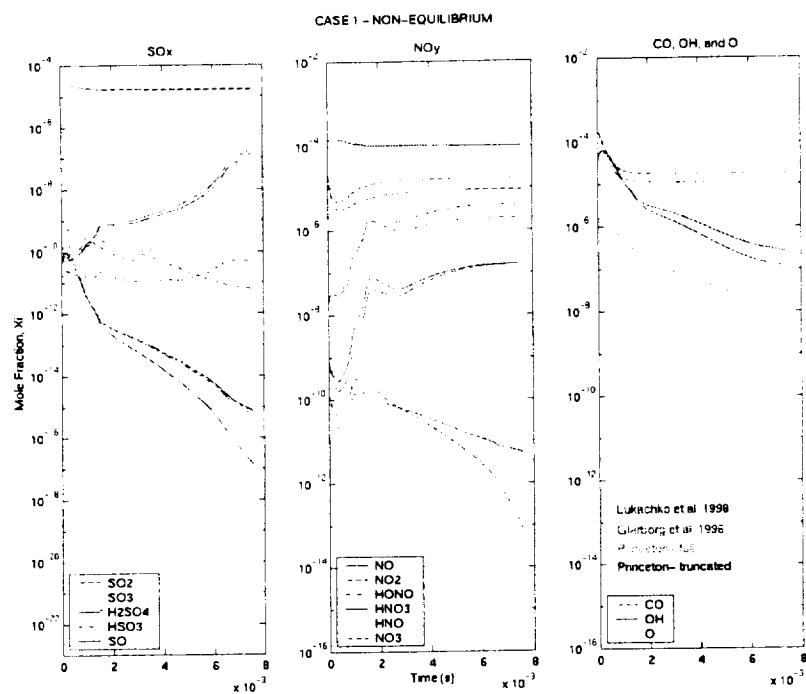


Figure 4.2 Chemical mechanism study for Case 1

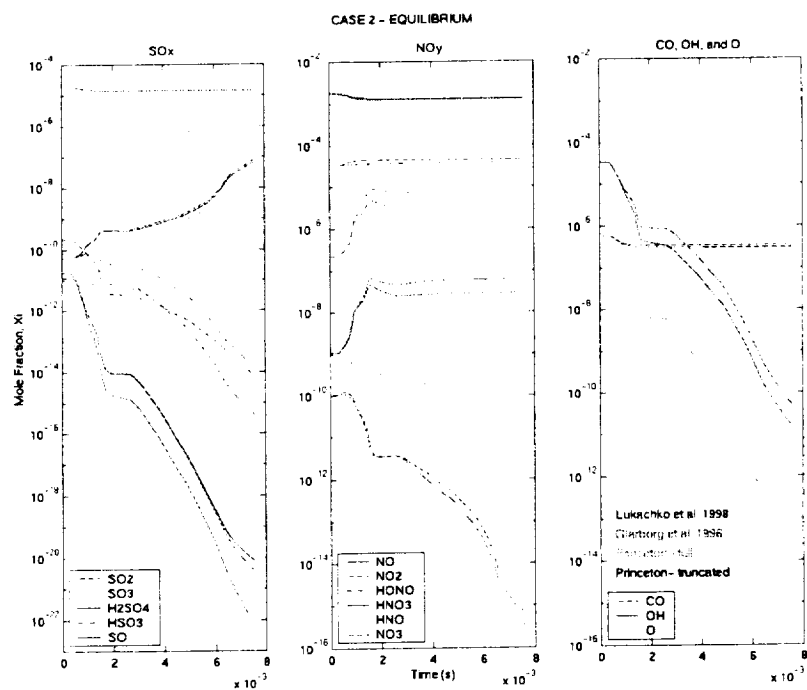


Figure 4.3 Chemical mechanism study for Case 2

Nozzle Exit (cmv) - Case 1: Non-Equilibrium IC's											
JGR paper			Lukachko			Glarborg			Princeton - full		
comb exit	nozzle exit	noz/comb	comb exit	nozzle exit	noz/comb	comb exit	nozzle exit	noz/comb	comb exit	nozzle exit	noz/comb
NO	130	95.6	0.74	129.68	95.58	0.74	129.68	95.32	0.78	129.68	99.03
NO2	14.5	10.4	0.72	14.47	10.38	0.72	14.47	5.79	0.40	14.47	5.63
HNO	0.012			0.011989	0.000284	0.024	0.011989	0.000098	0.008	0.011989	0.000099
HNO2	0.14	1.21	8.64	0.140	1.207	8.60	0.140	2.451	0.140	2.503	17.82
HNO3	0.000471	0.0737	158.48	0.0004712	0.0737322	156.49	0.0004712	0.0717786	152.34	0.0004712	0.0720485
NO3	0.000432			4.319E-05	3.847E-08	0.00089	4.319E-05	2.384E-06	0.05521	4.319E-05	2.489E-08
OH	60	0.196	0.0033	59.9970	0.1959	0.0033	59.9970	0.4364	0.0073	59.9970	0.4488
O	1.47	0.000157	0.00011	1.4737146	0.0001573	0.00011	1.4737146	0.0292526	0.01985	1.4737146	0.0314803
SO	0.000136			1.355E-05	8.225E-12	6.070E-07	1.355E-05	3.274E-10	2.416E-05	1.355E-05	3.815E-10
SO2	10.9	7.46	0.70	10.819	7.461	0.70	10.819	7.178	0.68	10.819	7.768
SO3	0.332	0.635	1.91	0.3316	0.6346	1.91	0.3318	0.9020	2.72	0.3318	0.3487
H2SO4	0.0000985			9.849E-05	2.151E-06	0.022	9.849E-05	3.695E-05	0.375	9.849E-05	1.818E-05
CO	0.000209	0.0416	1990.43	0.000209	0.0415417	1988.02	0.000209	0.0583012	2790.06	0.000209	0.0223709
CO2	50300			50300.71	37507.40	0.75	50300.71	37514.09	0.75	50300.71	37514.13
NOx	144.88	107.28	0.74	144.87	107.28	0.74	144.87	107.28	0.74	144.87	107.28
SOx	10.83	8.14	0.74	10.83	8.14	0.74	10.83	8.14	0.74	10.83	8.14
COx	50600.83			50600.83	37507.40	0.74	50600.83	37507.40	0.74	50600.83	37507.40
(SO3+H2SO4)/SOx	3.04%	8.32%		3.03%	8.31%		3.03%	11.80%		3.03%	4.54%
(HNO2+HNO3)/NOx	0.10%	1.20%		0.10%	1.19%		0.10%	2.35%		0.10%	2.40%
CO/COx	0.40%			0.40%	0.05%		0.40%	0.03%		0.40%	0.03%

Table 4.1 Summary of results from chemical mechanism study case 1

Nozzle Exit (cmv) - Case 2: Equilibrium IC's											
JGR paper			Lukachko			Glarborg			Princeton - full		
comb exit	nozzle exit	noz/comb	comb exit	nozzle exit	noz/comb	comb exit	nozzle exit	noz/comb	comb exit	nozzle exit	noz/comb
NO	1670	1230	0.74	1655.80	1215.82	0.73	1765.51	1302.51	0.74	1765.51	1299.06
NO2	19	28.3	1.51	20.94	28.45	1.36	21.05	23.78	1.12	21.05	23.62
HNO	0.000650			0.000650	0.000099	0.152	0.001140	0.000140	0.123	0.001140	0.000139
HNO2	0.141	1.95	13.83	0.141	1.922	13.65	0.141	5.103	0.141	5.111	36.33
HNO3	0.000471	0.0131	27.81	0.0004951	0.0129257	26.11	0.0004948	0.0275126	55.60	0.0004948	0.0274081
NO3				5.034E-05	2.952E-10	0.00001	5.031E-05	1.617E-10	0.00000	5.031E-05	1.602E-10
OH	60	0.000244	0.0000	57.2072	0.0000	0.0000	57.2072	0.0000	0.0000	57.2072	0.0000
O	1.47	0.00000		1.5547043	0.0000000	0.00000	1.5544046	0.0000002	0.00000	1.5544052	0.0000002
SO				1.075E-05	3.682E-17	3.408E-12	1.059E-05	2.027E-15	1.915E-10	1.059E-05	2.132E-15
SO2	10.6	7.71	0.73	8.713	8.324	0.73	8.712	8.275	0.72	8.712	8.464
SO3	0.332	0.402	1.21	0.2853	0.3440	1.21	0.2858	0.4072	1.42	0.2858	0.2283
H2SO4				7.859E-05	1.458E-10	0.000	2.790E-05	5.698E-09	0.000	2.790E-05	2.745E-09
H2SO4	0.0000209	0.0263	1258.37	0.0000153	0.0193242	1261.53	0.0000152	0.0227225	1496.97	0.0000152	0.0173787
CO				0.62	0.35	0.575	0.62	0.32	0.521	0.62	0.32
CO2				41134.12	30569.60	0.74	41134.12	30652.89	0.75	41134.12	30652.89
NOx	1688.14	1280.80	0.75	1676.80	1268.21	0.74	1768.00	1381.48	0.75	1768.00	1287.91
SOx	10.93	8.14	0.74	10.93	8.14	0.74	10.93	8.14	0.75	10.93	8.14
COx				41134.73	30569.60	0.74	41134.74	30652.89	0.75	41134.74	30652.89
(SO3+H2SO4)/SOx	3.04%	5.26%		3.17%	5.43%		3.18%	6.41%		3.18%	3.81%
(HNO2+HNO3)/NOx	0.01%	0.16%		0.01%	0.16%		0.01%	0.39%		0.01%	0.39%
CO/COx				0.00%	0.00%		0.00%	0.00%		0.00%	0.00%

Table 4.2 Summary of results from chemical mechanism study case 2

Nozzle Exit (cmv) - Case 8: Combustor Exit T=1450K											
JGR paper (BASELINE Case 1)			Lukachko			Glarborg			Princeton - full		
comb exit	nozzle exit	noz/comb	comb exit	nozzle exit	noz/comb	comb exit	nozzle exit	noz/comb	comb exit	nozzle exit	noz/comb
NO	130	95.6	0.74	129.89	90.76	0.70	129.89	94.55	0.73	129.89	94.53
NO2	14.5	10.4	0.72	14.47	14.80	1.02	14.47	9.95	0.67	14.47	9.53
HNO	0.012			0.000220	0.000684	3.013	0.000220	0.000312	1.419	0.000220	0.000312
HNO2	0.14	1.21	8.64	0.097	1.519	15.87	0.097	29.59	0.097	2.906	30.00
HNO3	0.000471	0.0737	156.48	0.0004941	0.1152097	233.19	0.0004941	0.1202412	243.37	0.0004941	0.1210178
NO3	0.000432			2.408E-05	2.226E-10	0.00001	2.408E-05	1.858E-07	0.00772	2.408E-05	1.953E-07
OH	60	0.196	0.0033	17.4575	0.0147	0.0008	17.4575	0.0465	0.0027	17.4575	0.0487
O	1.47	0.000157	0.00011	0.2125991	0.0000001	0.00000	0.2125991	0.001180	0.00525	0.2125991	0.0011912
SO	0.000136			1.313E-06	1.431E-14	1.090E-08	1.313E-06	5.344E-12	4.526E-06	1.313E-06	6.550E-12
SO2	10.6	7.46	0.70	10.259	7.562	0.74	10.259	7.367	0.72	10.259	7.585
SO3	0.332	0.635	1.91	0.6661	0.4658	0.70	0.6661	0.5303	0.96	0.6661	0.4473
H2SO4	0.0000985			5.618E-05	2.931E-07	0.005	5.618E-05	5.067E-06	0.090	5.618E-05	2.378E-06
H2SO4	0.0000209	0.0416	1990.43	0.0000779	0.0897012	1151.70	0.0000779	0.1203958	1545.79	0.0000779	0.0854637
CO	201			200.88	68.34	0.341	200.88	81.89	0.308	200.88	61.89
CO2	50300			50302.96	37457.52	0.74	50302.96	37484.05	0.74	50302.96	37484.11
NOx	144.88	107.28	0.74	144.28	107.19	0.74	144.28	107.19	0.74	144.28	107.19
SOx	10.83	8.14	0.74	10.83	8.12	0.74	10.83	8.12	0.74	10.83	8.12
COx				50600.83	37507.40	0.74	50600.83	37507.40	0.74	50600.83	37507.40
(SO3+H2SO4)/SOx	3.04%	8.32%		6.10%	6.84%		6.10%	9.25%		6.10%	6.46%
(HNO2+HNO3)/NOx	0.10%	1.20%		0.07%	1.52%		0.07%	2.79%		0.07%	2.82%
CO/COx				0.40%	0.18%		0.40%	0.16%		0.40%	0.16%

Table 4.3 Summary of results from chemical mechanism study case 8

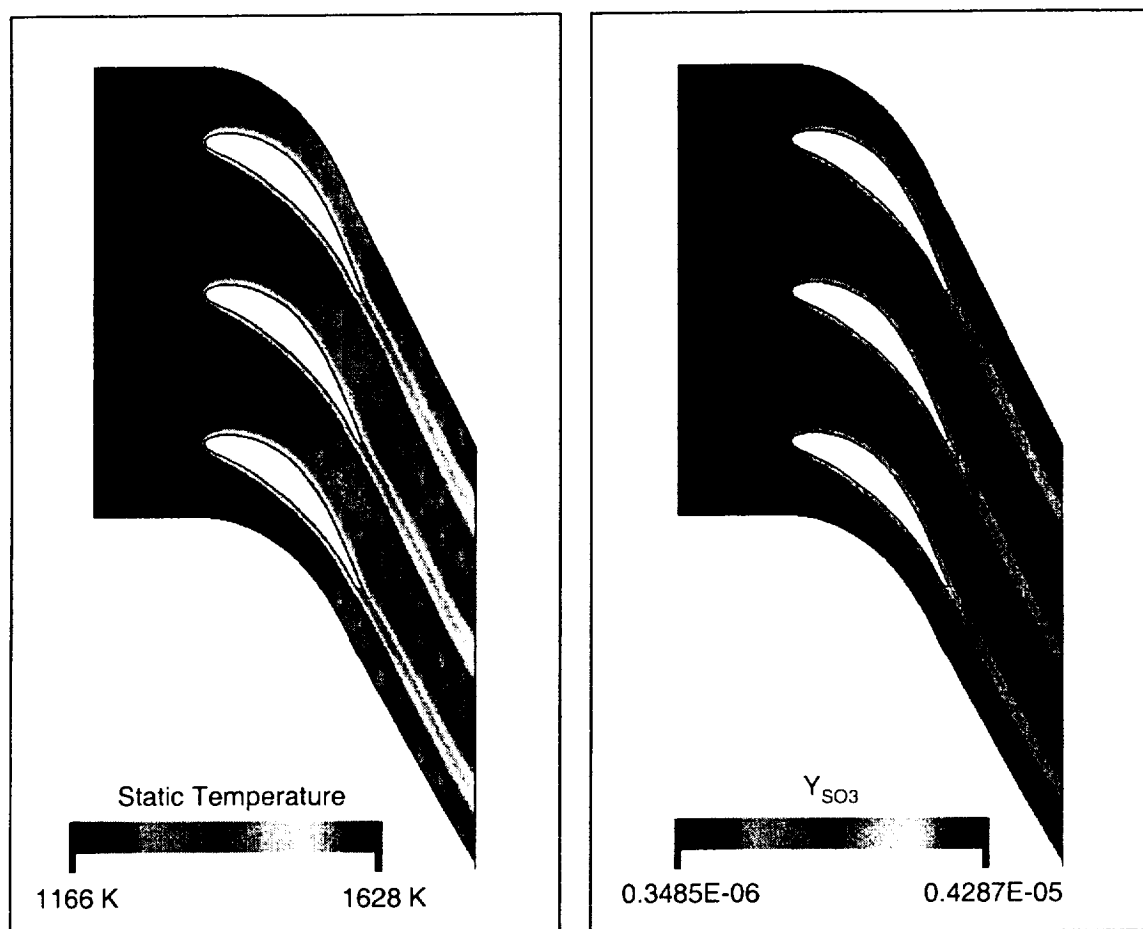


Figure 4.6 Example result of 2D calculation on Cambridge No 2 turbine rotor with Lukachko et al (1998) mechanism

4.3.5 CONCLUSIONS

Overall, the 1D ASE engine cycle and 2D Cambridge No 2 turbine rotor blade row calculations both show that the species concentration trends are the same and in particular the range of SO_x conversion for a given case was 2.7% to 7.3% for all the mechanisms. This result would imply that the chemical mechanism does have some impact on the results of the modeling effort. However, as long as the key reactions are included in the mechanism the results are in fairly good agreement. Therefore, the prior calculations [1] were substantiated by new experimentally-derived kinetic data.

The modifications to the SO_x chemistry at high pressures in the Mueller et al. (2000) mechanisms were based on experimental data and are considered an improvement with respect to the turbine chemistry mechanism previously employed. Therefore, the Mueller et al. (2000)-truncated mechanism was selected as the best option

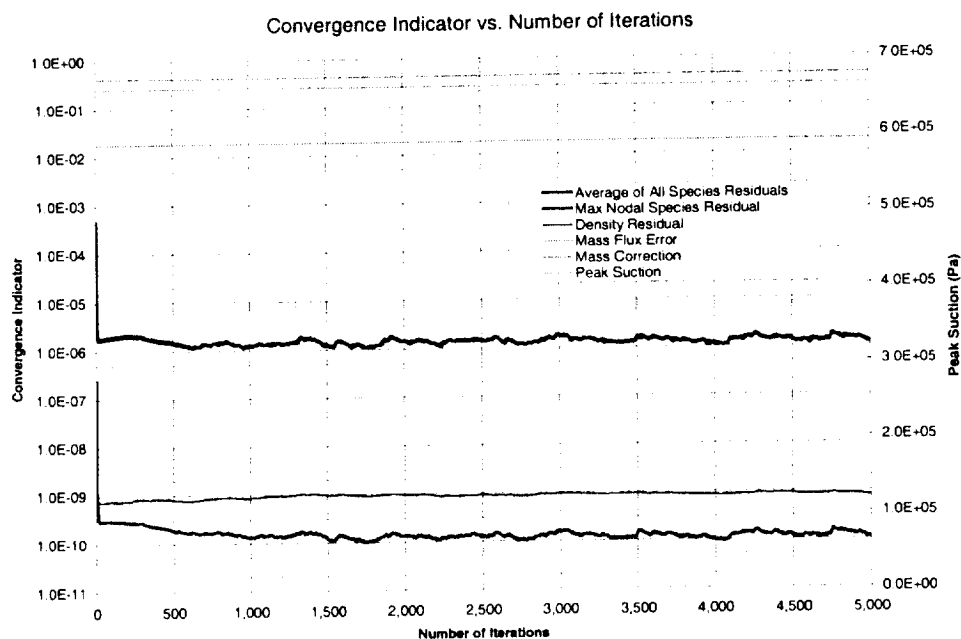


Figure 4.7 Original CNEWT fluid and chemistry convergence indicators

From the figure, it appears that the maximum nodal species residual converged by 600 iterations and the combined average converged by 1,000 iterations for the test case. The fluid solution was already converged at the start of this solution. It was suspected that the trace species could still be changing after the average and maximum criteria had converged since the trace species would play a minor roll in the average calculation and would not necessarily be the maximum residual. In other words, the average and maximum quantities could mask the actual changes in the chemistry solution since large portions of the domain could be converged while small portions could be changing significantly. Several potentially improved convergence criteria were proposed, including monitoring the maximum nodal mass fraction for individual species of interest, the RMS average for individual species of interest, or the maximum nodal residual divided by that species mass fraction.

4.4.3 RESULTS

First, a straightforward visual approach was employed to determine the actual convergence for a few trace species of interest. The chemical variables were re-initialized for the test case and it was set-up to re-run with a solution file dumped every 100 iterations. Time history plots for the species evolution of O, OH, and SO₃ mass fraction were generated for 5,000 iterations. As an example, the mass fraction of O is plotted at several points during the solution in Figure 4.8. Also, animations for all three species are included in Appendix F.

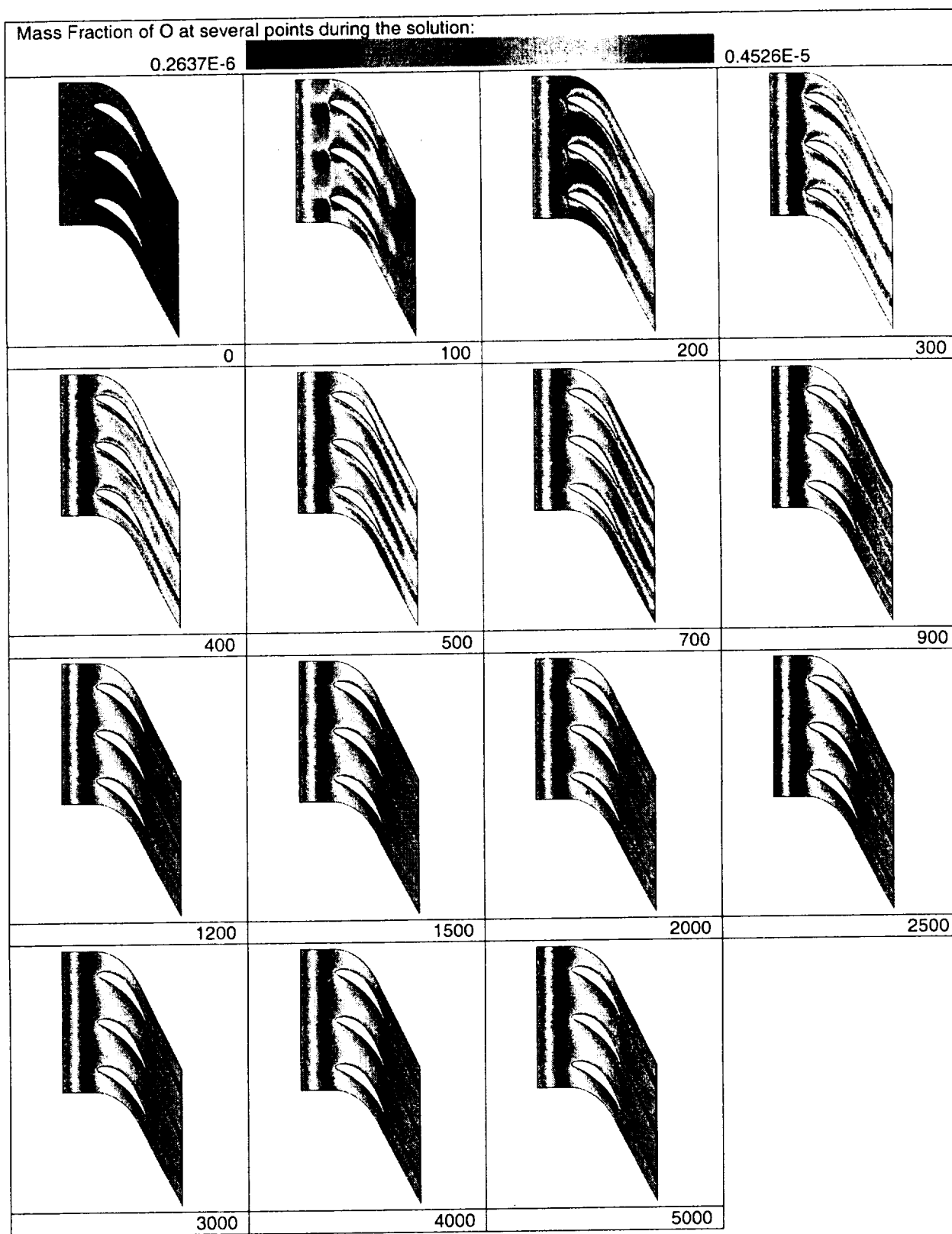


Figure 4.8 Convergence of O mass fraction by visual time evolution

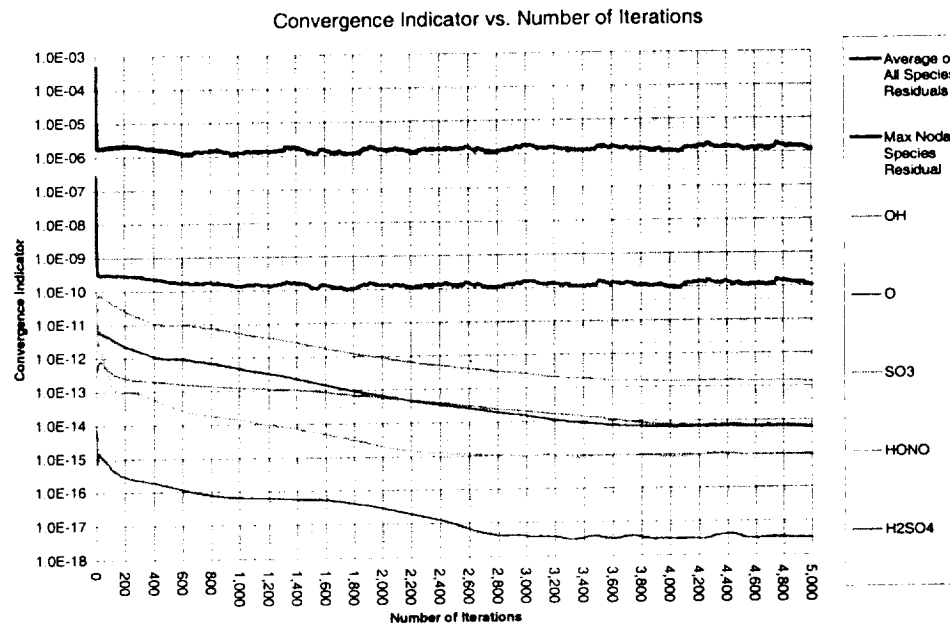
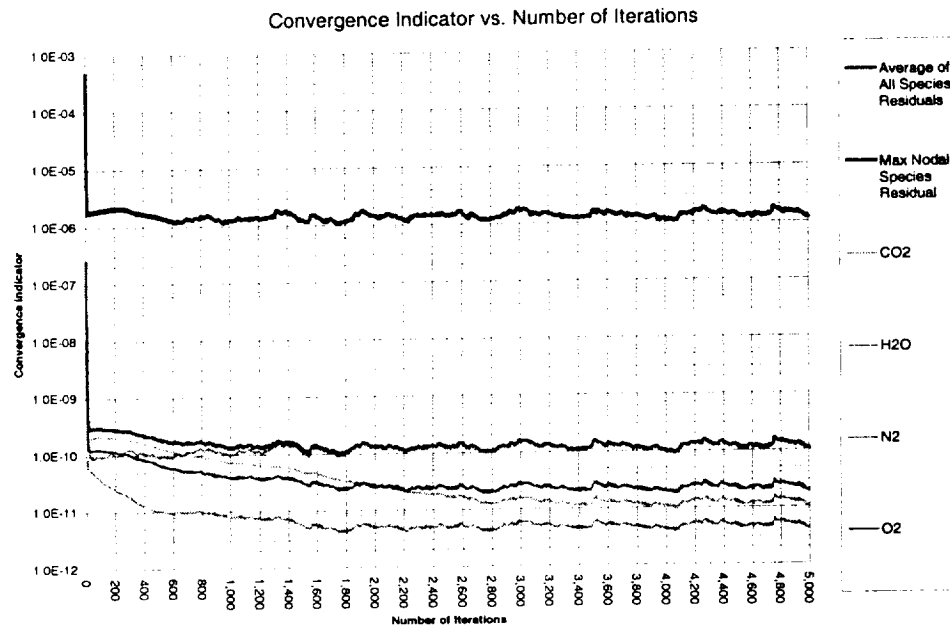


Figure 4.10 Comparison of original and new chemistry convergence indicators for major species (top) and trace species (bottom)

4.5.2 RESULTS

The results of the periodic boundary condition study are summarized in Table 4.5. Excluding V_r , the maximum error relative to the value at the 0% location was found to be 1.6%. The pseudo-2D grid had only two cells in the radial direction, and thus V_r had a very small value and was not resolved.

Summary of Results

(Error in % relative to 0% distance)

%	Distance	Y (O)	Y (OH)	Y (SO3)	Va	Vt	Vr	P	T	density
Station 1 (X = -0.090m)										
0	0.00616	0.00000	0.00000	0.00000	0.00000	0.00000	0.00000	0.00000	0.00000	0.00000
33	0.08647	1.57524	0.96817	0.51614	0.02657	0.04238	21.92809	0.00036	0.00000	0.00000
66	0.16677	1.58134	0.97314	0.51746	0.04114	0.00618	21.91245	0.00238	0.00062	0.00164
100	0.24707	0.00000	0.00019	0.00000	0.00000	0.00000	0.00344	0.00000	0.00000	0.00000
Station 2 (X = -0.050m)										
0	0.00616	0.00000	0.00000	0.00000	0.00000	0.00000	0.00000	0.00000	0.00000	0.00000
33	0.08647	0.09475	0.03310	0.07752	0.18508	0.47438	91.24584	0.00071	0.00000	0.00055
66	0.16677	0.09502	0.03194	0.07935	0.18861	0.47544	90.37488	0.00227	0.00062	0.00165
100	0.24707	0.00000	0.00000	0.00000	0.00000	0.00028	0.00307	0.00000	0.00000	0.00000
Station 3 (X = -0.030m)										
0	0.00781	0.00000	0.00000	0.00000	0.00000	0.00000	0.00000	0.00000	0.00000	0.00000
33	0.08811	0.11467	0.05943	0.08596	0.22545	0.73558	739.78837	0.00333	0.00312	0.00055
66	0.16841	0.11525	0.05820	0.08581	0.22115	0.80782	737.42081	0.00166	0.00249	0.00055
100	0.24872	0.00000	0.00000	0.00000	0.00000	0.00000	0.00467	0.00000	0.00000	0.00000
Station 4 (X = 0.000m)										
0	0.02329	0.00000	0.00000	0.00000	0.00000	0.00000	0.00000	0.00000	0.00000	0.00000
33	0.10359	0.00517	0.00145	0.04530	0.19617	0.38102	75.09076	0.00542	0.00629	0.01164
66	0.18389	0.00443	0.00022	0.04252	0.18115	0.37651	75.08537	0.00698	0.00564	0.01227
100	0.26420	0.00000	0.00000	0.00000	0.00000	0.00000	0.00287	0.00000	0.00000	0.00000
Station 5 (X = 0.025m)										
0	0.05418	0.00000	0.00000	0.00000	0.00000	0.00000	0.00000	0.00000	0.00000	0.00000
33	0.13449	0.00965	0.00695	0.02860	0.34149	0.38984	1680.61424	0.02638	0.00254	0.02429
66	0.21479	0.01210	0.00568	0.03716	0.34277	0.40235	1652.06698	0.02850	0.00320	0.02550
100	0.29510	0.00000	0.00017	0.00000	0.00000	0.00000	0.02222	0.00000	0.00000	0.00000
Station 6 (X = 0.050m)										
0	0.10459	0.00000	0.00000	0.00000	0.00000	0.00000	0.00000	0.00000	0.00000	0.00000
33	0.18490	0.04068	0.02562	0.01014	0.04683	0.04216	8.03507	0.00963	0.00445	0.00521
66	0.26521	0.05485	0.04277	0.05292	0.05177	0.03763	12.48811	0.01476	0.00763	0.00637
100	0.34551	0.00000	0.00000	0.00000	0.00000	0.00000	0.00286	0.00000	0.00000	0.00000
Station 7 (X = 0.090m)										
0	0.18742	0.00000	0.00000	0.00000	0.00000	0.00000	0.00000	0.00000	0.00000	0.00000
33	0.26773	1.19668	0.74615	0.45025	0.17822	0.01676	74.16898	0.03101	0.06989	0.10071
66	0.34804	1.17737	0.73834	0.45198	0.18307	0.01829	74.76751	0.02947	0.07052	0.10014
100	0.42835	0.02716	0.01392	0.01195	0.00321	0.00686	0.71326	0.00000	0.00127	0.00116
Maximum Error (%)		1.58	0.97	0.52	0.34	0.81	1680.61	0.03	0.07	0.10

Table 4.5 Summary of results from periodic boundary condition study

The detailed results for station 3 are given in Figure 4.12 as an example. The blue circle symbols in the figure are the 0%, 33%, 66%, and 100% circumferential locations.

presented. Although it was not completely successful, it provided the opportunity to test several code improvements, investigate the limitations of the modeling tools, and analyze flow features of the reactor. A chemical mechanism study which investigated the effects of the chemical mechanism on intra-engine chemistry modeling and selected a mechanism for use in the NASA/DERA engine test modeling was detailed. This chapter also discussed a convergence criteria study which resulted in improved chemistry convergence indicators. Finally, a periodic boundary condition study was presented.

In summary, the following is a list of all relevant points presented in this chapter:

- An attempt was made to model a VPFR experiment to benchmark the accuracy of the modeling tools, however, a limitation to the flow solver prevented this ultimate objective. The flow features from the simulation did not correlate well with those expected from experimental and empirical data.
- The VPFR validation exercise proved useful in validating some improvements to the modeling tools.
 - The new fully unstructured grid generator was successfully used to mesh the VPFR geometry
 - The multiple inlet/exit improvement was qualitatively validated.
- The modeling tools are limited to simulations of compressible flow and should be restricted to situations when the bulk of the flow field is above a Mach number of 0.2, an estimate for the compressibility limit of the code.
- The Princeton VPFR may operate with large scale unsteady stall.
- A comparative study was performed on four chemical mechanisms by repeating a 1D and 2D computation from prior work.
 - The species concentration trends were the same for all mechanisms studied.
 - The SO_x conversion ranged from 2.7% to 7.3% for a given case, which implies that the selection of chemical mechanism does impact intra-engine chemistry modeling.
 - Accurately representing key reactions in the mechanism produced reasonable results, thus prior work using Lukachko et al. (1998) was supported.
 - The Mueller et al. (2000)-truncated mechanism was selected for use intra-engine chemistry modeling. It is based on experimental data and is within 1% of the Mueller et al. (2000)-full mechanism.
- The original chemistry convergence criteria did not represent convergence of trace species well. They were improved by using the RMS average of individual species residuals for the species of interest to determine solution convergence.
- Periodic boundary conditions did not introduce any significant error into the computation, selected fluid and species variables at the boundary were within 1.6% of their corresponding value with no boundary present.

5 MODELING THE NASA/DERA ENGINE TEST

This chapter presents the first complete analysis which applies the intra-engine trace chemistry modeling methodology to a real engine. The goal of the simulation is to characterize the evolution of trace species in the post combustor flow path in order to provide engine exit plane emissions predictions, help guide the engine test plan, and research a few physical mechanisms thought to affect trace species chemistry.

5.1 CHAPTER OVERVIEW

The purpose of this chapter is to describe the modeling effort to simulate trace species evolution in the post-combustor gas path of an engine in support of the NASA/DERA engine test. The objective of the test is to provide measurements to help characterize aviation emissions and benchmark the models. The model is used to inform the test effort by providing pre-test predictions which were used to help formulate the test plan and to research a few fundamental mechanisms thought to influence trace species chemistry.

Three conditions are investigated: cruise, max power, and non-uniform max power. Details of the grid generation, fluid boundary condition specification, and species initial conditions specification are discussed. A time scale analysis is used to guide the modeling efforts. Two types of high fidelity models are used for the HPT1; a mixed-out case and a wake model case. Several properties of the solution are discussed, including: convergence, overall flow features, grid resolution, deviation angle, and flow-through times. A sample set of detailed flow-chemistry results from the high fidelity model is presented. Low fidelity models are used for HPT1 and HPT1 exit to nozzle exit. Low fidelity models for averaged and high and low temperature profiles in the HPT1 are compared to the high fidelity average. A HPT1 exit to nozzle exit profile is used to obtain a prediction of engine exit gas composition. A sample set of flow-chemistry results from the low fidelity model is presented.

This chapter also highlights several implications of the modeling results. Specifically, engine operating conditions, multi-dimensional non-uniformities, and the unsteady interaction of non-uniformities with downstream stations were all found to influence trace species evolution. They can all impact temperature,

- The unsteady interaction non-uniformities with downstream blade-rows has a significant impact on intra-engine post-combustor chemistry.
- Local regions of flow or species non-uniformity persist through the subsequent blade rows.

Section 5.2 outlines the objectives of the engine test and modeling effort, provides some background information related to the engine test, and lists the modeling scenarios considered. Section 5.3 gives a time scale analysis for the engine test and gives an outline for the presentation of the details of the modeling effort. Section 5.4 details the set up and results of the high fidelity analysis. Section 5.5 details the set up and results of the low fidelity analysis. Section 5.6 describes the implications of the results from modeling effort. Section 5.7 is the chapter summary.

5.2 OBJECTIVES, BACKGROUND, AND MODELING SCENARIOS

NASA/DERA Engine Test Objectives

One of the project objectives outlined in Section 1.4 was a validation of engine modeling results through measurement studies. A collaboration of many research groups consisting mainly of teams from DERA, NASA, MIT/ARI, and UMR have formulated an engine test to address several emissions related phenomena. The main objective of the measurement campaign is to carry out ground-based simulation and measurement of chemical and physical processes relevant to aviation emissions characterization [8]. The NASA/DERA engine test aims to measure the emissions of a typical engine, evaluate the effects of various fuels and operating conditions on engine emissions, develop and evaluate various species measurement techniques, investigate intra-engine species evolution, and provide inputs to emissions models through characterizing the composition of the gas at the combustor and nozzle planes.

Modeling Objectives

The NASA/DERA engine test provides a unique opportunity to demonstrate the modeling methodology described in Section 2. The models were used to inform the test efforts by providing pre-test predictions for intra-engine species evolution. The pre-test predictions assisted in formulating the test plan by helping to ensure that operating conditions are selected so as to provide useful information about the intra-engine environment. The pre-test predictions are also useful in directing the measurement efforts by indicating the important species to monitor and providing estimates for the instrumentation requirements. Modeling of the engine test also provides the opportunity to benchmark the accuracy of the modeling methodology against measured data. A matched set (i.e. same engine and operating condition) of combustor and nozzle exit plane species data is required to evaluate the predictive capability of the intra-engine modeling tools. To date no such

Modeling Scenarios

The engine modeling scenarios that were simulated in the context of this thesis were based on the nominal operating points for cruise and max power. Table 5.2 overviews the three simulations conducted which cover a range of combustor exit temperatures pertinent to many modern civil aircraft engines.

Summary of NASA/DERA Engine Test Conditions			
Label	Cruise	Max power	Non-uniform max power
Description	Nominal cruise power setting	Nominal maximum power setting	Maximum power setting with a combustor exit temperature profile (nominally 1,600K)
Engine speed (rpm)	7,821	8,864	8,864
Ts at combustor exit (K)	1,123	1,357	1,430-1,840 (average~1,600)
Ps at combustor exit (Pa)	687,000	1,594,000	1,594,000
Ts at HPT1 exit (K)	983	1,186	1,186
Ps at HPT1 exit (Pa)	428,000	986,000	986,000
HPT1 rotor metal temperature (K)	826	999	999
HPT1 stator metal temperature (K)	791	956	956

Table 5.2 Summary of conditions modeled for NASA/DERA engine test [34]

These three test conditions provide a basis for investigating the effects of operating conditions on trace species evolution. As discussed previously in this section, the modeling strategy used for the NASA/DERA engine simulations called for high fidelity modeling of the first stage of the high pressure turbine followed by low fidelity modeling for the remainder of the post-combustor flow path. These computational simulations were extended to investigate the effects of several physical phenomena suspected to influence the evolution of trace species, namely circumferential non-uniformities and the unsteady interaction of the non-uniformities on downstream stations.

Two of the simulated conditions were used to investigate two types of circumferential non-uniformity. The HPT1 rotor calculation for the max power and non-uniform max power conditions were run both using a steady mixed-out initial condition and an unsteady wake model profile initial condition to investigate the effects of unsteady interaction of the non-uniformities on downstream stations (see Section 3.3.4 for more details on the wake model). Figure 5.1 gives a overview of all the modeling scenarios explored.

The profile was clocked such that the peak temperature, corresponding approximately to the injector locations, was aligned with a blade. This was considered a worst case scenario since the temperature difference between the combustor gas and the cooled blade would be greatest. Given the number of injectors and stator blades it is likely that this would occur somewhere within the circumference. The derived profile was then fit to the three NGV blade passages as shown in Figure 5.3 (0 to 18 degrees).

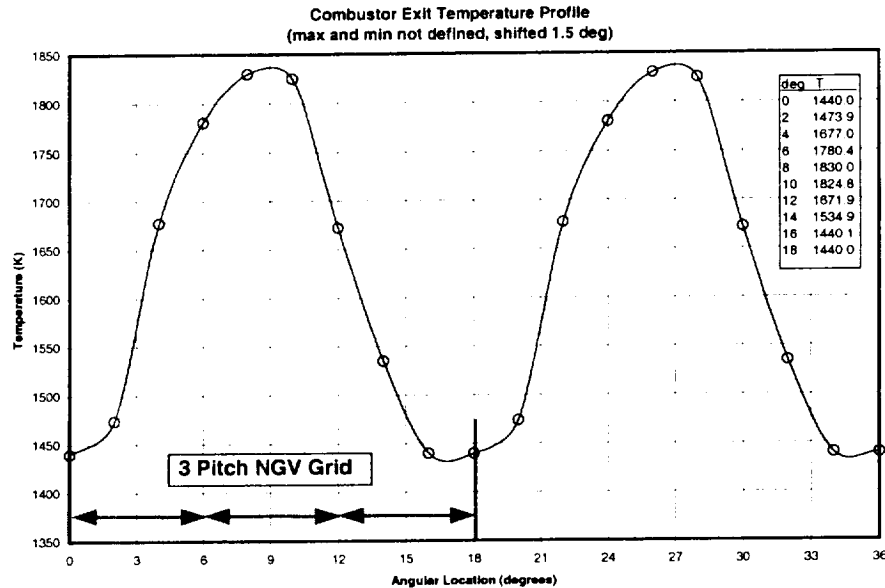


Figure 5.3 Combustor temperature profile used as initial condition for non-uniform max power case

Species of importance to evaluating the SO_x and NO_y evolution are SO_3 , SO_2 , H_2SO_4 , O, OH, NO, NO_2 , NO_3 and HONO. Several instrumentation teams will measure a multitude of primary and trace combustion products such as O_2 , CO_2 , CO, H_2O , unburned hydrocarbons, and soot particles. Initially, measurements were focused on SO_3 evolution, however, pre-test simulations showed that majority of the SO_2 conversion was completed in the combustor for the operating conditions considered (more so for the cruise condition). These results suggested concentrating the test efforts on the highest power setting attainable such that the combustor exit temperature is highest and the magnitude of change is greatest along the post-combustor gas path (i.e. between the measurement stations). Also, the focus was broadened to include HONO evolution which exhibits a greater change between the measurement stations for the planned test conditions. Furthermore, since NO_y chemistry remains active over this range of power settings it was still advantageous to explore multiple operating points. These modifications to the test plan would help to magnify the changes in HONO concentration through the measurement stations and provide the potential for comparison between two operating conditions.

Integration along the path from the combustor exit to the HPT1 exit indicates that there will be less than 4% sulfur conversion in that stage. Integration along the path subsequent to this conversion, the severity parameter suggests several orders of magnitude less potential for sulfur conversion after the HPT1. Using these findings it was decided to use a high fidelity 2D model for the HPT1 combined with a low fidelity 1D model from the HPT1 exit to the nozzle exit to perform the pre-test modeling for the NASA/DERA engine test.

5.3.2 PRESENTATION OF MODELING EFFORT

A complete set of all the specific results accumulated during the course of this research would be overwhelming and not add much to the value to this thesis. In order to keep the write-up concise and not to obscure the key findings, the specific results were divided into two main parts with two subsections each. The two parts are: Section 5.4 High Fidelity Modeling and Section 5.5 Low Fidelity Modeling. The subsections are Set Up and Results. Finally, Section 5.6 Implications of Results contains an analysis of the results with regard to their impact on the research of intra-engine trace species evolution. The presentation layout gives a representative case for each distinct case without listing or plotting every chemical species or fluid variable for each operating condition and analysis technique. A diagram showing the important topics in the presentation layout is given in Figure 5.5.

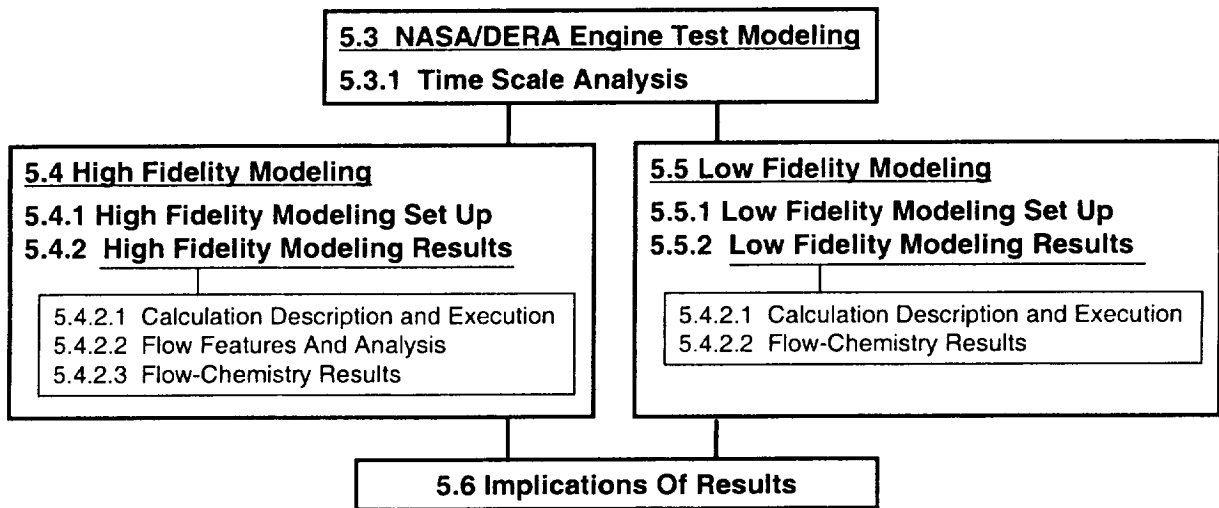


Figure 5.5 Presentation layout of NASA/DERA engine test modeling

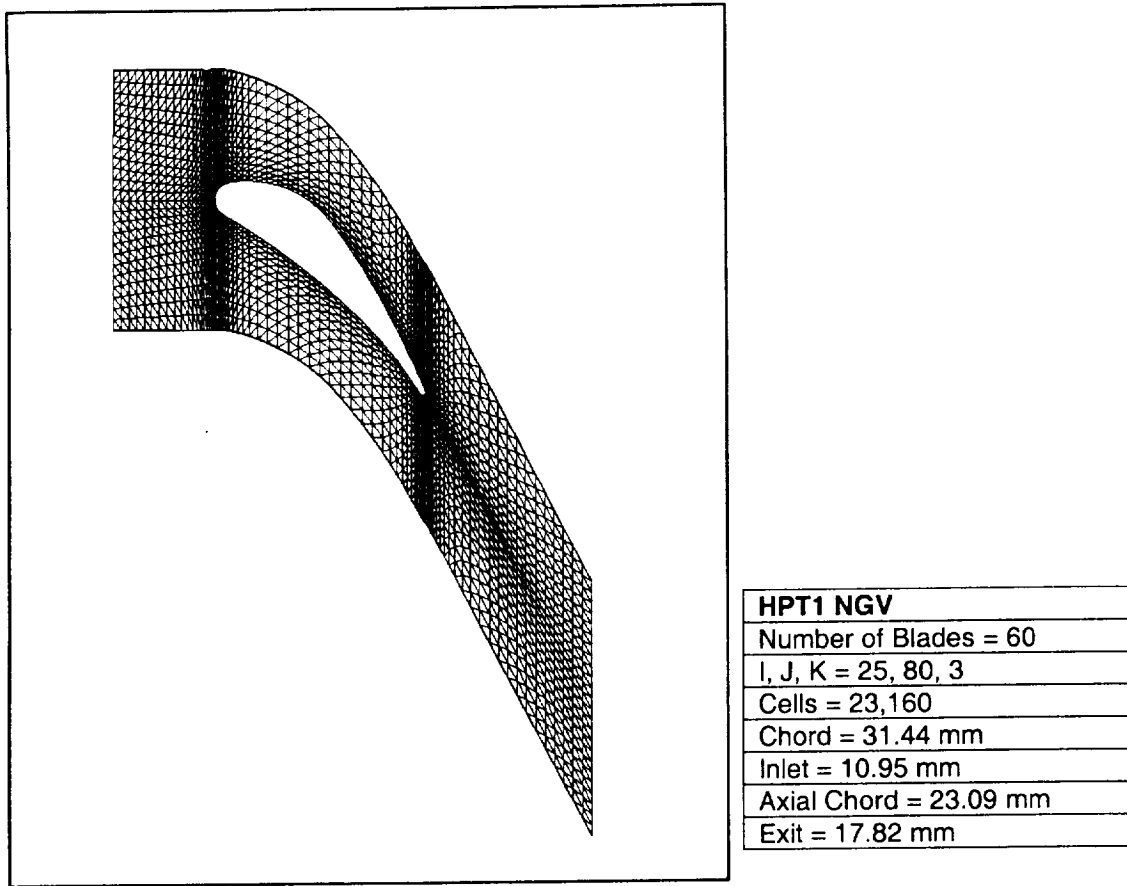


Figure 5.6 Single pitch HPT1 NGV grid

Figure 5.7 shows the rotor grid. The inlet length for the rotor was set as half of the distance from the NGV trailing edge to the rotor leading edge. The inlet conditions for the high fidelity rotor calculations were extracted from the NGV solution at that plane. Again, the exit length was extended roughly 0.8 axial chords downstream.

and pressure was derived for each of the three operating conditions investigated. The important input parameters used in the initial conditions code are listed in the table below:

Condition	Chemistry Initial Condition Code Inputs		
	Cruise	Max power	Non-uniform max power
T (K)	1,122.8	1,356.6	1,440-1,830
P (atm)	6.78	15.732	15.732
ϕ (equiv ratio)	0.35	0.35	0.35
η (comb eff)	0.9988	0.99988	0.99988
CO/H ₂ /HC ratio	100/0/0	100/0/0	100/0/0
EI(NO _x) (g/kg fuel)	21.0	21.0	21.0
NO/NO _x ratio	0.99	0.99	0.99
EI(S) (g/kg fuel)	0.5	0.5	0.5
SO ₃ /SO _x ratio	0.06	0.06	various equilibrium (about 0.03 average)
EI(CO) (g/kg fuel)	5.09	0.51	0.51

Table 5.3 Chemistry inlet condition code inputs for NASA/DERA engine test

The main differences in the chemistry inlet specification technique relative to prior work in [1] and the Cambridge No 2 turbine rotor calculations discussed previously are that the CO/H₂/HC ratio was changed from 78/22/0 to 100/0/0, the NO/NO_x ratio was changed from 0.90 to 0.99, and a kinetics calculation was used to resolve rapid numerical changes in the initial conditions due to inconsistencies in the resulting speciations. Due to lack of emissions data, the EI's represent a best estimate for an engine typical of this make and era. The EI(NO_x) was adjusted to obtain approximately 300 ppm of NO_x to coincide with a rough visual average of NO_x contours of a similar gas turbine engine (see Figure 5.8). The EI(CO) was set by adjusting the combustion efficiency to achieve a value close to one interpolated from an emissions data base for a 1970's era engine with a pressure ratio of about 16 at the appropriate power setting [11]. The selected EI(NO) was also similar to the ones listed in the data base. The SO₃/SO_x was fixed at 6% for the cruise and max power setting based on experience from prior work [30] which showed that sulfur conversion in the combustor was limited. In contrast, the equilibrium level for these two cases resulted in a SO₃/SO_x ratio of about 38%. The temperature for the non-uniform max power condition spanned 1,440-1,830K which gave an equilibrium SO₃/SO_x ranging from about 1-8%, thus the equilibrium sulfur ratio was used in this case.

5.4.2.1 CALCULATION DESCRIPTION AND EXECUTION

Overview Of Analysis Types For Rotor Calculation

Figure 5.9 depicts the two types of high fidelity analysis were used for the HPT1 rotor in the current research. The first analysis uses the mass-averaged fluid and species quantities at the NGV exit plane as inlet conditions to the rotor domain and is called the “mixed-out case.” The second analysis uses the wake model described in Section 3.3.4 to apply a rotating, circumferentially-varying fluid and species profile from the NGV exit plane as the inlet condition to the rotor domain and is called the “wake model case.” These two techniques were used to evaluate the effects of non-uniformities on downstream blade rows.

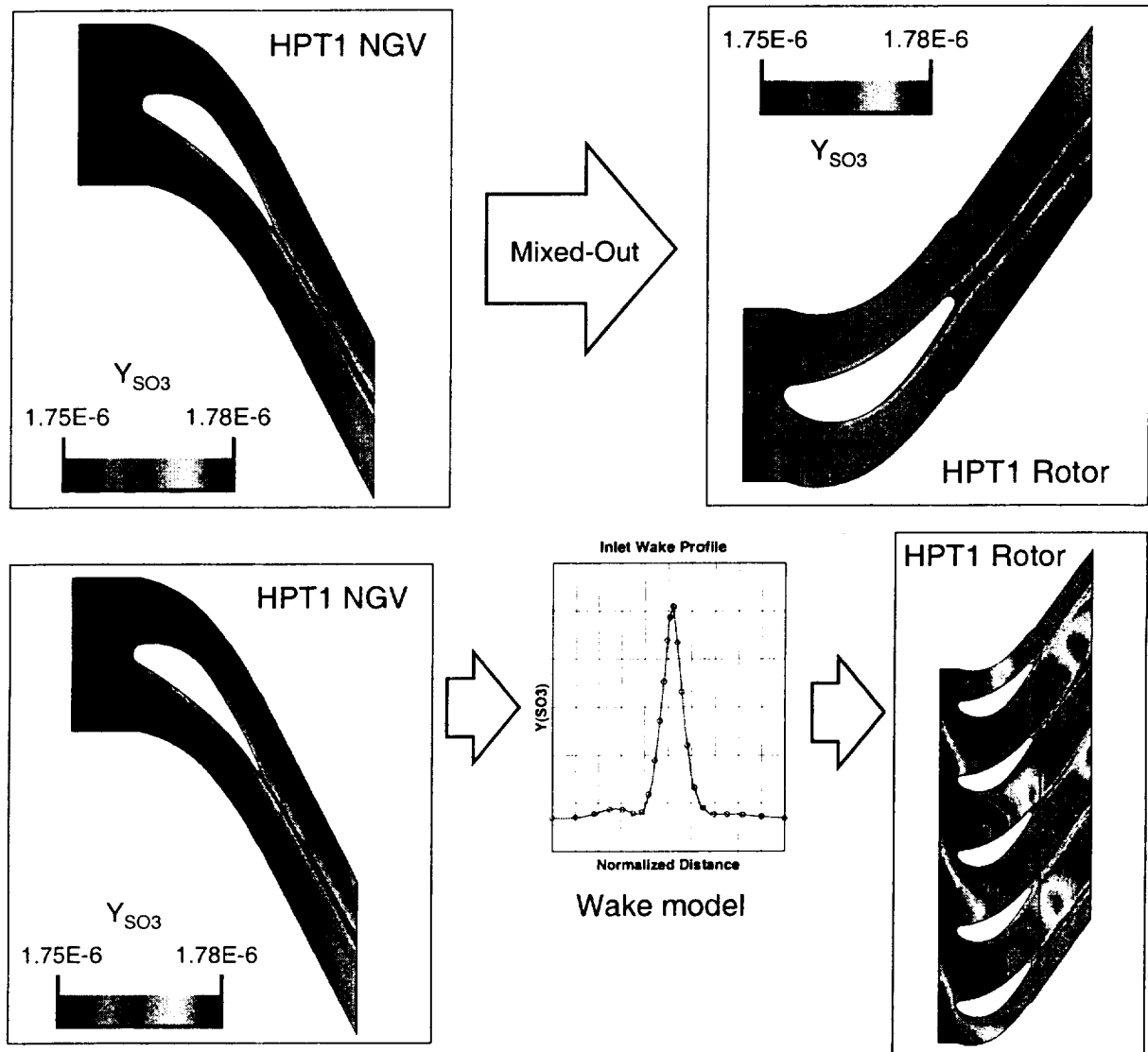


Figure 5.9 Two high fidelity analysis types, mixed-out (top) and wake model (bottom)

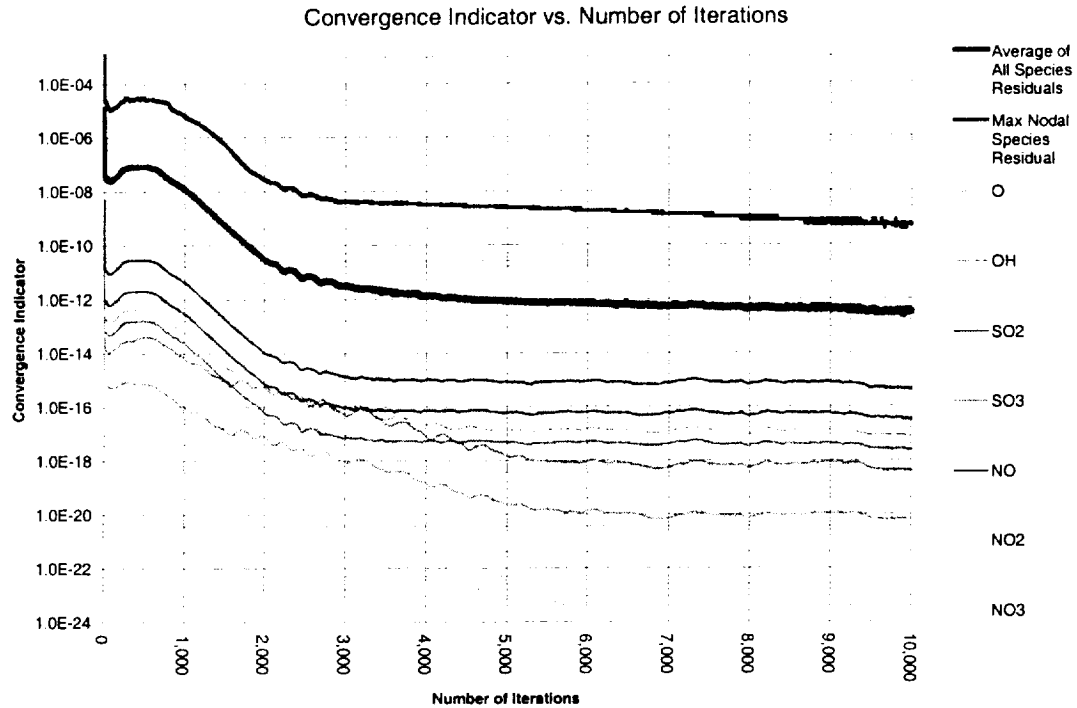


Figure 5.11 Selected species convergence indications for NGV calculation at cruise condition

The unsteady HPT1 rotor solutions were deemed to be converged when the convergence criteria became periodic about a constant value. Figure 5.12 and Figure 5.13 show example convergence histories for the HPT1 rotor calculation at the max power conditions. The unsteady solutions converge faster, although to higher residuals than the steady solutions. The higher residuals are due the need to resolve the fluid and chemistry variables in time (with a finite time-step) as well as the spatial domain.

An full unsteady solution consists of the set of one complete cycle after convergence. Figure 5.14 shows the locations of a set of solution output files for an example unsteady rotor run at max power. In this case, ten evenly distributed locations in time were chosen for output over 275 iterations. All later runs spanned a minimum of 400 iterations per cycle for better resolution and typically consisted of 10 to 15 output locations per cycle.

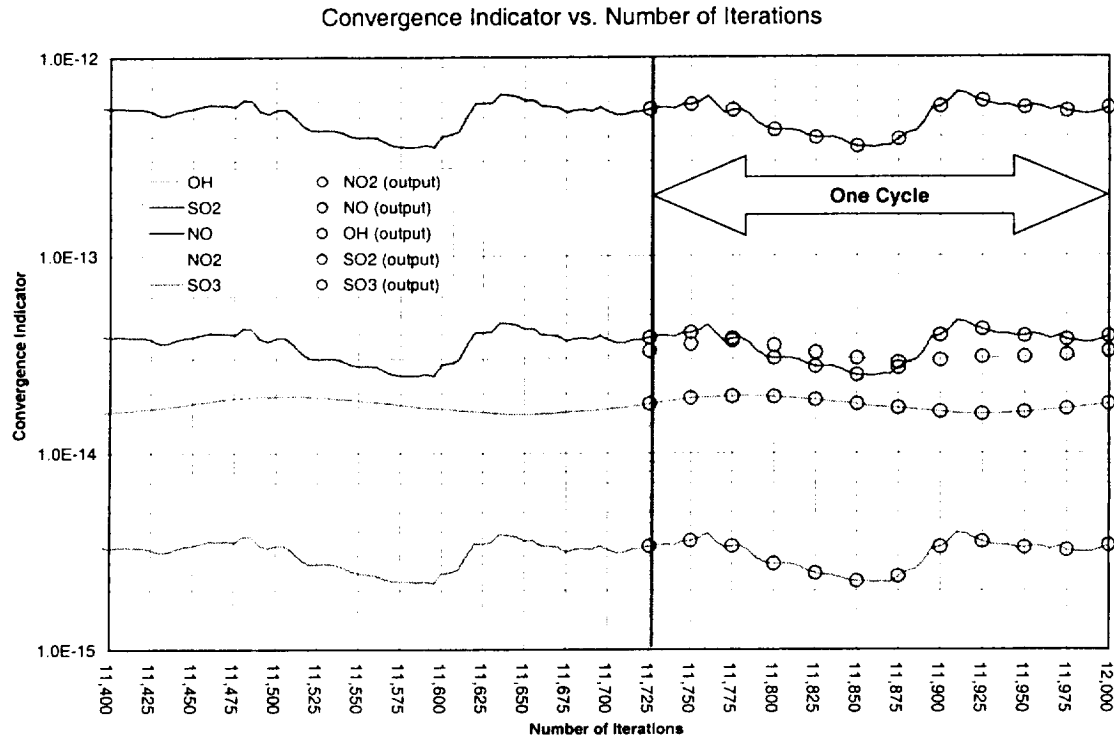


Figure 5.14 An example set of solution output files making up one cycle of a full unsteady solution

5.4.2.2 FLOW FEATURES AND ANALYSIS

Overall

In general, all of the solutions obtained in the high fidelity modeling phase were resonable. The features of the flow field and values of the fluid state variables were as expected. Table 5.4 contains a summary of the fluid quantities from the velocity triangle analysis and the high fidelity modeling.

analysis, the deviation angle is reasonable, and the inlet/exit conditions are as specified. In general, all of the solutions from the high fidelity models were probed in a similar manner and the flow results were found to be similar.

Trailing Edge Resolution

One peculiar feature of the flow field was a very small region near the trailing edge which had a significantly higher Mach number. Upon close inspection, it appears that the high speed flow is caused by the tendency of the fluid to accelerate around the TE from the pressure side to the suction side of the blade prior to the point of separation. The phenomena is magnified by the faceted shape of the TE and the limited grid resolution. This phenomena was much less pronounced in the prior calculations of the Cambridge No 2 turbine rotor because the TE was modeled as squared off which fixed the point of separation at the corners. Plots of the Mach number and total pressure for both cases are shown in Figure 5.16 for comparison. By modeling the true curvature of the TE, the point of separation and flow field in this region are not well resolved for the given grid spacing. The effect of this deficiency in the representation of the flow field is likely to be minimal on chemical species evolution. Two possibilities to improve the situation would be to cut ("square off") the TE or to enhance the mesh in this region, however, both methods have drawbacks. Cutting the TE is in essence fixing the point of separation and thus dictates the shape of the wake. Reducing the initial grid spacing would start to skew the cells in that region and simply enhancing the grid using the boundary layer technique in POST will increase the number of cells drastically.

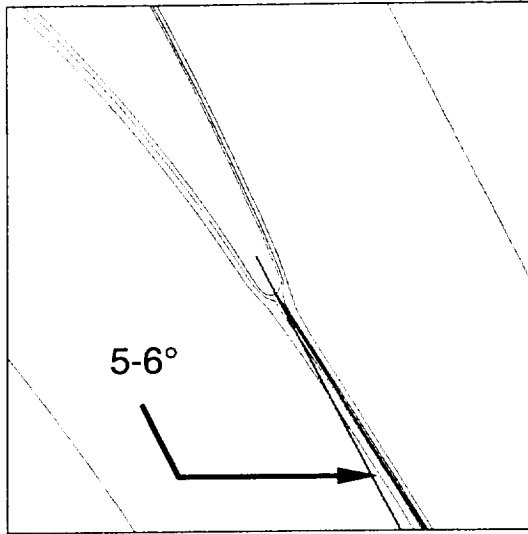


Figure 5.17 Streamlines near the trailing edge used to estimate the deviation angle

The deviation measured from the high fidelity model was between the estimate from Carter's Rule (7.5°) and the assumed value (2°). As mentioned, the flow parameters (including velocity vectors) from the high fidelity models at station B were used as input to the rotor high fidelity models, therefore, the assumed deviation of 2° was considered adequate to make the initial estimate of fluid boundary conditions.

Blade-Row Flow-through Time

The flow-through time for the HPT1 blade rows at cruise condition was estimated by integrating the total velocity along three streamlines as follows:

$$t = \int \frac{1}{V_T} ds \quad (5.23)$$

To give a feel for the range of flow-through times for various parcels of fluid, streamlines were chosen near the pressure and suction sides of the blade as well as one at mid passage. Figure 5.18 shows the streamlines and velocity profiles used for the calculation.

rotor leading edge (at $X = 0.04515$ m in the NGV grid). As an example, the mass-averaged total pressure was computed as follows:

$$\overline{P}_i^m = \frac{\int \left(P + \frac{1}{2} \rho u^2 \right) d\dot{m}}{\int d\dot{m}} \quad (5.24)$$

The column labeled “HPT1 Rotor Exit” is divided into two parts. The “mixed-out steady” column is the mass-averaged species concentration at the plane midway between the rotor trailing edge and the leading edge from the NGV on the following turbine stage, HPT2, for a mixed-out case (at $X = 0.0106$ m in the rotor grid). In the mixed-out case, the inlet condition for the rotor was simply specified as a constant value equal to the mass-averaged species concentration from the “HPT1 NGV Exit” for each species and also the mass-averaged temperature and pressure. In effect, all of the quantities were instantaneously mixed-out at the rotor inlet plane and thus all non-uniformities were removed. The “time ave. unsteady” column is the time-average of the mass-averaged species concentration at the same plane for the unsteady wake model case. As an example, the time-averaged mass-averaged total pressure was computed as follows:

$$\overline{P}_i^{tm} = \frac{\int \left(\overline{P}_i^m \cdot \dot{m} \right) dt}{\int \dot{m} dt} \quad (5.25)$$

In the unsteady wake model case, the actual 2D non-uniform species, temperature, and pressure profiles were applied to the rotor inlet using the wake model. The wake model which was discussed in detail in Section 3.3.4 preserves the upstream circumferential non-uniformities. Some example profiles for the max power case are given in the graphs on the third row of results in Figure 5.19 and Figure 5.20. The blue symbols on the graphs represent the data points input into the wake model.

Figure 5.19 and Figure 5.20 give example results for total temperature, total pressure, and a few selected species mass fractions from the high fidelity modeling for the NGV and mixed-out rotor cases. The first row is a spanwise view of the contour plot for the particular quantity where the black vertical line represents the blade-row exit plane. The second row is an axial view contour plot on that plane. The third row of the NGV plots is a plot of species mass fraction versus circumferential location at the center of that plane. And the last row lists the range for the contour plot and the mass averaged value on that plane.

The total temperature deficit in the NGV wake is about 9%. Also, notice that the SO_3 and HONO mass fraction profiles are inverse to the temperature wake profile, suggesting that the temperature gradients have the strongest influence on their local concentration and that blade cooling enhances their production.

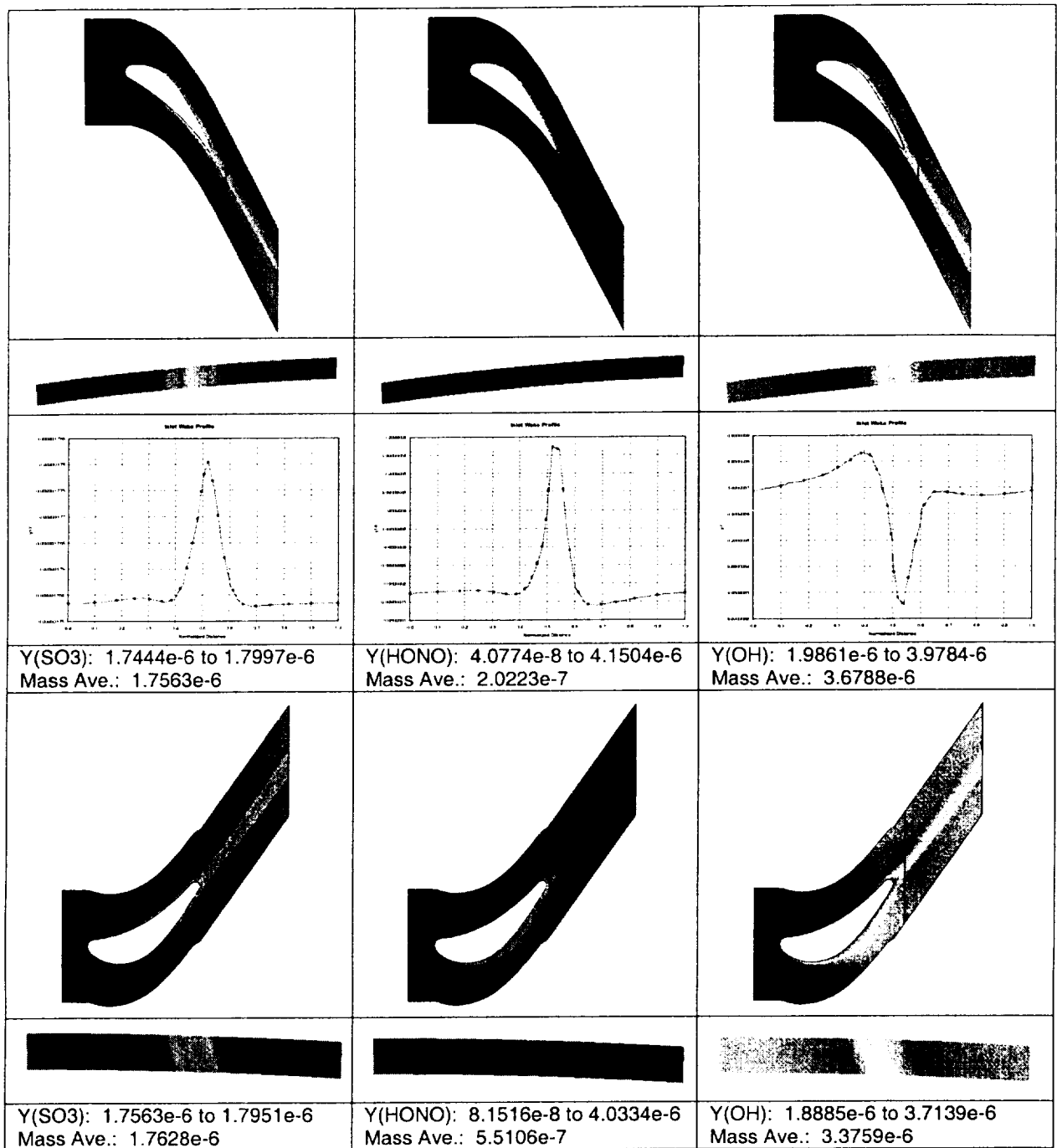


Figure 5.20 SO₃, HONO, and OH at NGV and rotor exit for max power case

The wake model rotor cases are unsteady (i.e. time varying) solutions due to the rotation of the upstream stator wakes and combustor profile relative to the rotor blades. Therefore, the specific results consist of a series of plots equally spaced out over a time interval equal to one cycle. An example result of the wake model case is shown in Figure 5.22 for the non-uniform max-power case. A similar result for the max power case is given in Appendix C. The time dependent results can also be viewed in the animations contained in the attached media detailed in Appendix E.

From the figure, it is evident that the localized regions of non-uniform SO_3 mass fraction persist downstream past the exit of the blade row. Also, notice that the non-uniformity from the combustor temperature profile is much larger than the non-uniformity from the wakes of the cooled blades (i.e. more of the flow is subject to the larger scale combustor non-uniformity).

A summary of all the key results is given in Table 5.5, Table 5.6, and Table 5.7 for the cruise, max power, and non-uniform max power conditions, respectively. The species quantities are given in mole fraction. The unsteady wake model case and HPT1 exit to nozzle exit was not run for the cruise condition. Again, for a complete set of detailed results for the max power conditions see Appendix C.

Summary of 2-D Simulation Results: Cruise Condition						
Number	Species	Combusor Exit Initial Condition	HPT1 NGV Exit	HPT1 Rotor Exit		Nozzle Exit
				mixed-out steady	time ave. unsteady	
1	CO	1.21890E-04	1.21772E-04	1.21739E-04	N/A	N/A
2	CO ₂	4.76468E-02	4.76469E-02	4.76469E-02	N/A	N/A
3	O ₂	1.33217E-01	1.33217E-01	1.33217E-01	N/A	N/A
4	H ₂ O	4.78257E-02	4.78257E-02	4.78257E-02	N/A	N/A
5	H	1.68680E-10	1.64263E-10	1.52266E-10	N/A	N/A
6	O	4.88767E-09	4.92741E-09	4.53878E-09	N/A	N/A
7	OH	3.68109E-07	3.16391E-07	2.65419E-07	N/A	N/A
8	HO ₂	9.90554E-09	8.70358E-09	7.39922E-09	N/A	N/A
9	H ₂ O ₂	4.64661E-10	6.84852E-10	7.97481E-10	N/A	N/A
10	NO	3.02737E-04	3.02550E-04	3.02462E-04	N/A	N/A
11	NO ₂	3.10783E-06	3.20137E-06	3.23082E-06	N/A	N/A
12	NO ₃	5.26957E-13	4.23230E-13	3.37662E-13	N/A	N/A
13	HNO	5.33968E-11	1.38233E-10	1.63320E-10	N/A	N/A
14	HONO	5.32214E-08	1.45864E-07	2.04203E-07	N/A	N/A
15	HNO ₃	1.50489E-10	5.45819E-10	8.45071E-10	N/A	N/A
16	SO ₂	9.83418E-06	9.83378E-06	9.83355E-06	N/A	N/A
17	SO ₃	6.29053E-07	6.29292E-07	6.29353E-07	N/A	N/A
18	HOSO	1.02269E-14	6.53196E-15	4.32394E-15	N/A	N/A
19	HSO ₃	3.29192E-13	4.87219E-13	6.07823E-13	N/A	N/A
20	HSO ₂	5.81476E-17	7.31318E-17	8.16752E-17	N/A	N/A
21	SO	1.24025E-14	7.82809E-15	4.90596E-15	N/A	N/A
22	HCO	2.09232E-16	1.78302E-16	1.45277E-16	N/A	N/A
23	H ₂	5.76045E-10	1.35492E-09	1.49002E-09	N/A	N/A
24	N ₂	7.70872E-01	7.70873E-01	7.70872E-01	N/A	N/A
25	AR	0.00000E+00	0.00000E+00	0.00000E+00	N/A	N/A
26	C(S)	0.00000E+00	0.00000E+00	0.00000E+00	N/A	N/A
27	N	0.00000E+00	0.00000E+00	0.00000E+00	N/A	N/A
28	H ₂ SO ₄	2.71298E-10	4.32577E-10	5.97855E-10	N/A	N/A
29	S	8.93357E-26	8.93358E-26	8.93357E-26	N/A	N/A

Note: All quantities are species mole fractions

(SO ₃ +H ₂ SO ₄)/SO _x	6.014627%	6.017002%	6.017683%	N/A	N/A
Δ from comb exit	0.000000%	0.002375%	0.003057%	N/A	N/A
(HNO ₂ +HNO ₃)/NO _y	0.017448%	0.047862%	0.067032%	N/A	N/A
Δ from comb exit	0.000000%	0.030415%	0.049584%	N/A	N/A
CO/CO _x	0.255167%	0.254920%	0.254850%	N/A	N/A
Δ from comb exit	0.000000%	-0.000247%	-0.000317%	N/A	N/A

Table 5.5 Summary of results from HPT1 high fidelity modeling at cruise condition

Summary of 2-D Simulation Results: Non-Uniform Max Power Condition						
Number	Species	Combustor Exit Initial Condition	HPT1 NGV Exit	HPT1 Rotor Exit		Nozzle Exit
				mixed-out steady	time ave. unsteady	
1	CO	1.15329E-05	8.35163E-06	7.38236E-06	7.79052E-06	5.03788E-06
2	CO2	4.78104E-02	4.78135E-02	4.78145E-02	4.78109E-02	4.78168E-02
3	O2	1.34160E-01	1.34167E-01	1.34172E-01	1.34181E-01	1.34182E-01
4	H2O	4.77659E-02	4.77844E-02	4.77958E-02	4.78122E-02	4.78231E-02
5	H	5.91935E-08	3.13144E-08	1.90711E-08	2.65527E-08	5.39530E-12
6	O	5.61601E-06	3.61282E-06	2.78809E-06	3.09000E-06	2.26319E-09
7	OH	1.20450E-04	8.40250E-05	6.14268E-05	6.45515E-05	1.76425E-07
8	HO2	6.76771E-07	4.43111E-07	4.21141E-07	4.71472E-07	1.12166E-09
9	H2O2	3.81133E-08	4.82831E-08	1.07656E-07	8.13361E-08	2.56225E-07
10	NO	3.03484E-04	3.02503E-04	3.01528E-04	2.98333E-04	2.87829E-04
11	NO2	2.88219E-06	3.83386E-06	4.75487E-06	1.05940E-05	1.09828E-05
12	NO3	7.33999E-12	1.97938E-11	6.09685E-11	9.39380E-11	5.28522E-13
13	HNO	3.88249E-10	3.50353E-10	6.70221E-10	4.79792E-10	3.15691E-10
14	HONO	2.62278E-08	5.56272E-08	1.09335E-07	1.20774E-07	7.47313E-06
15	HNO3	7.55054E-11	2.47416E-10	5.20103E-10	1.41816E-09	1.07858E-07
16	SO2	1.01206E-05	1.01041E-05	1.00939E-05	1.01001E-05	1.00311E-05
17	SO3	3.41779E-07	3.58292E-07	3.68528E-07	3.58658E-07	4.29548E-07
18	HOSO	3.87086E-12	2.08593E-12	1.28268E-12	1.62738E-12	1.92871E-16
19	HSO3	6.59378E-12	6.38182E-12	8.06975E-12	6.88370E-12	2.11402E-12
20	HSO2	3.77560E-15	2.22706E-15	2.10835E-15	2.05852E-15	7.21925E-18
21	SO	6.86930E-11	3.42928E-11	1.46333E-11	2.15939E-11	6.72918E-16
22	HCO	6.08598E-15	1.91539E-15	1.19428E-15	1.27618E-15	1.44639E-19
23	H2	8.14864E-07	5.79348E-07	4.34916E-07	5.26470E-07	1.09997E-07
24	N2	7.69808E-01	7.69809E-01	7.69810E-01	7.69761E-01	7.69810E-01
25	AR	0.00000E+00	0.00000E+00	0.00000E+00	0.00000E+00	0.00000E+00
26	C(S)	0.00000E+00	0.00000E+00	0.00000E+00	0.00000E+00	0.00000E+00
27	N	4.01390E-12	4.00640E-12	4.00640E-12	3.86511E-12	4.00640E-12
28	H2SO4	3.05830E-11	4.19789E-11	3.13587E-11	5.12671E-11	1.80619E-09
29	S	4.11071E-16	4.10394E-16	4.10395E-16	3.99506E-16	4.10395E-16

Note: All quantities are species mole fractions

(SO3+H2SO4)/SOx	3.267025%	3.424855%	3.522683%	3.429555%	4.106721%
Δ from comb exit	0.000000%	0.157831%	0.255658%	0.162531%	0.839697%
(HNO2+HNO3)/NOy	0.008585%	0.018236%	0.035854%	0.039538%	2.474273%
Δ from comb exit	0.000000%	0.009651%	0.027269%	0.030953%	2.465688%
CO/COx	0.024116%	0.017464%	0.015437%	0.016292%	0.010535%
Δ from comb exit	0.000000%	-0.006652%	-0.008679%	-0.007825%	-0.013582%

Table 5.7 Summary of results from HPT1 high fidelity modeling at max power condition

5.5 LOW FIDELITY MODELING

5.5.1 LOW FIDELITY MODELING SET UP

Low fidelity models were used to model both the HPT1 and the HPT1 exit to nozzle exit flow paths. Several steps were required to prepare for these runs. First, the 1D temperature, pressure, and velocity profiles were extracted from the high fidelity models of the HPT1 NGV and rotor blade rows. A mass-averaged profile as well as profiles along several streamlines were investigated. Next, the available engine performance data was used to generate similar 1D profiles for the HPT1 exit to nozzle exit. A set of input files to CALCHEM for the max power condition is given in Appendix D as an example.

Streamlines

Representative low and high temperature streamlines were also selected at the exit of the NGV and rotor domains. Flow and species quantities were extracted along those streamlines for both the max power and non-uniform max power cases. The high temperature streamline was between the blades near the pressure surface and the low temperature streamline was in the boundary layer near the suction surface for both the NGV and rotor. Figure 5.24 shows the streamlines selected for the max power case. The corresponding high and low temperature 1D profiles extracted from those streamlines are shown in Figure 5.25. The streamline profiles were used to perform a 1D analysis which would be expected to show the range in magnitude of species change due to 2D non-uniformity.

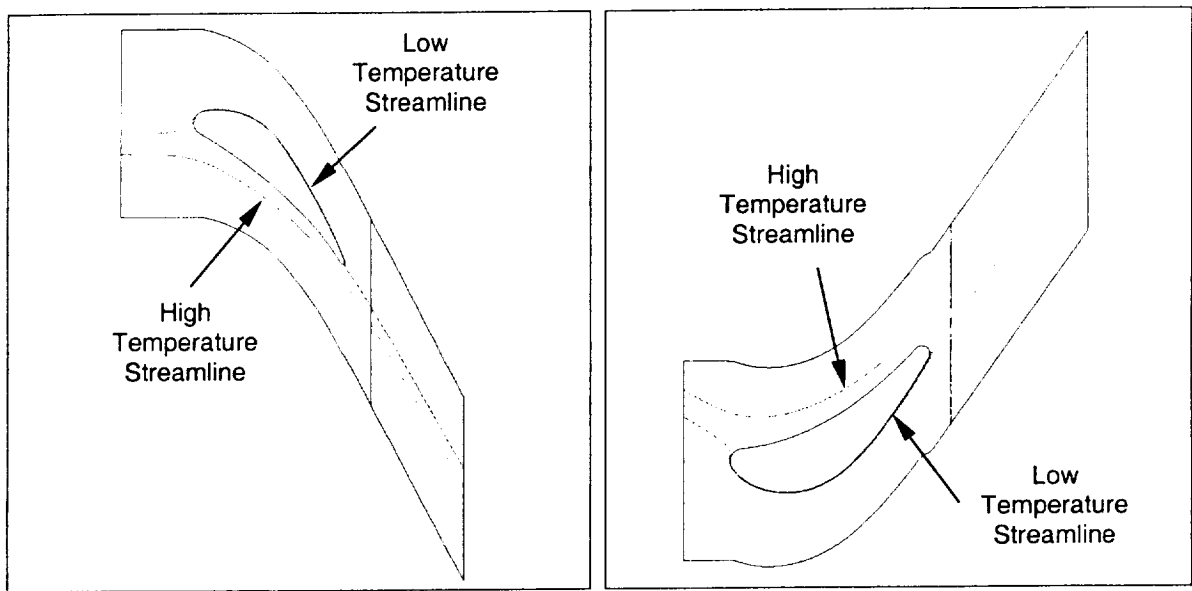


Figure 5.24 High and low temperature streamlines selected for 1D profiles

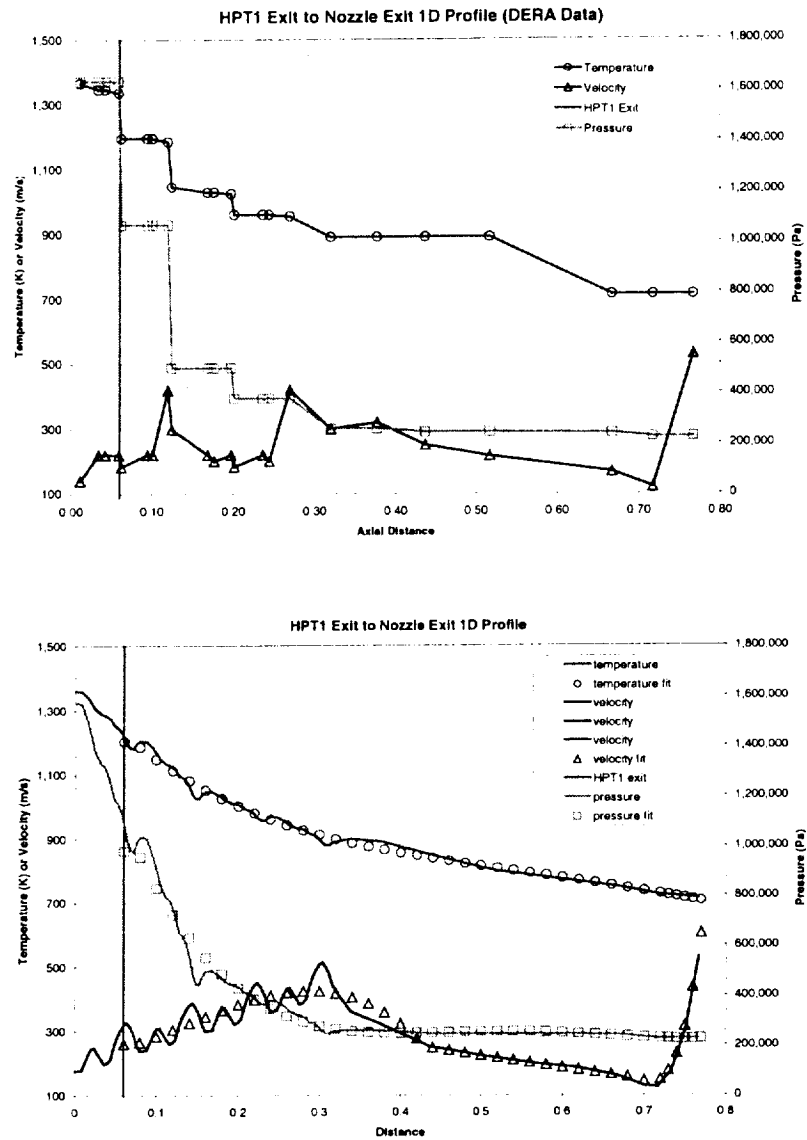


Figure 5.26 HPT1 exit to nozzle exit 1D profile, available data (top) and curve fit (bottom)

Figure 5.27 shows the final normalized HPT1 exit to nozzle exit 1D profiles used for the low fidelity modeling. The magenta lines approximate the locations of the inlet and exit planes for the HPT2, LPT1, and LPT2 turbine stages.

HPT1 and Engine Flow-Through Time

The flow-through times ranged from 0.24 ms for the mass averaged case to 0.32 ms for the high temperature streamline of the HPT1 at max power conditions. For the 1D analysis the flow-through time was computed by integrating the axial velocity along the axial distance rather than the total velocity along the actual streamline path. These estimated flow-through times for the HPT1 were consistent with those from the high fidelity modeling (see 5.4.2.2). The flow-through time for the HPT1 exit to nozzle exit was 2.77 ms for the max power condition, giving an overall flow-through time for the post-combustor gas path of about 3 ms.

5.5.2.2 FLOW-CHEMISTRY RESULTS

A summary of the important chemical species results from HPT1 low fidelity modeling is given in Table 5.6 and Table 5.7. In each table, the column labeled “Nozzle Exit” is the result of the 1D low fidelity modeling of the HPT1 exit to nozzle exit using the mixed-out HPT1 results as input to the low fidelity models.

The results from the low fidelity model were plotted as mass fraction versus time for three subsets of species. The plots are divided into two halves, the left graph shows the species evolution within the HPT1, and the right graph shows the species evolution from the HPT1 exit to the nozzle exit. Notice that the axis scales are different on both graphs. The species subsets were divided by family: SO_x (SO_2 , SO_3 , H_2SO_4 , HSO_3 , SO), NO_y (NO , NO_2 , HONO , HNO_3 , HNO , NO_3), and CO , OH , and O . The plots contain the three 1D calculations for the mass average, high temperature streamline, and low temperature streamline profiles, as well as, the mass-averaged species from the high fidelity modeling (labeled “2D Mass Average”). As an example, the NO_y plots are given in Figure 5.28 and Figure 5.29 for the max power and non-uniform max power case, respectively. For a complete set of detailed results for the max power conditions see Appendix C.

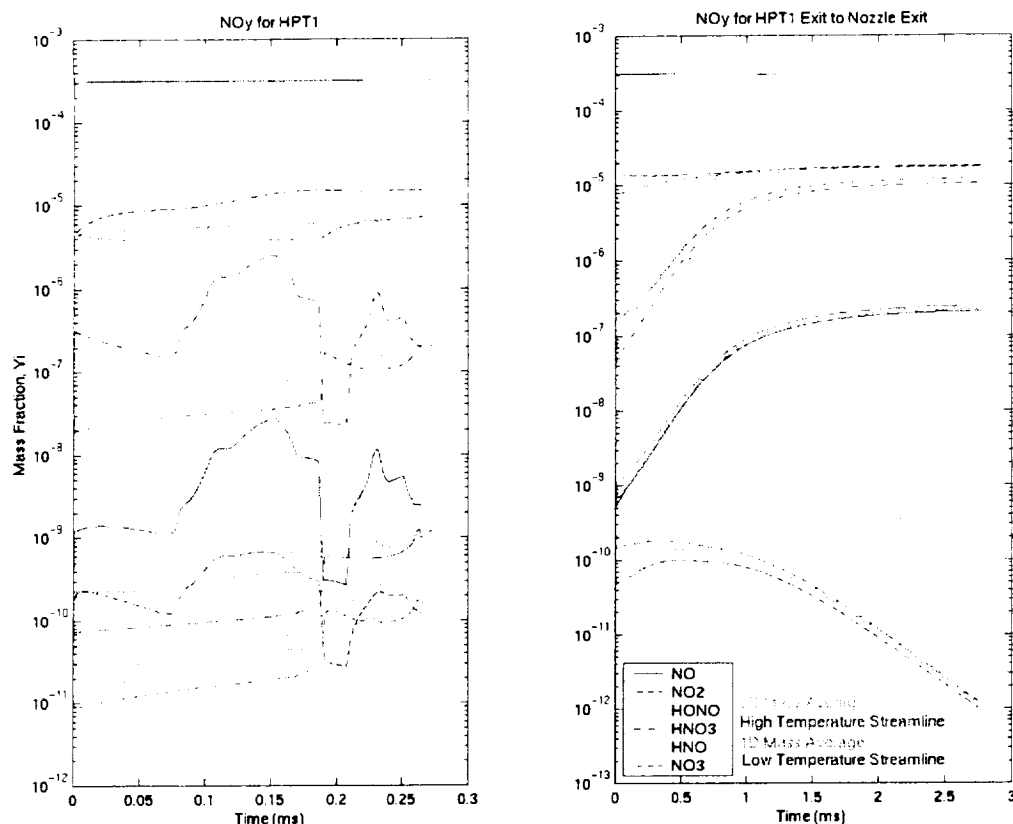


Figure 5.29 Example low fidelity modeling results, NOy species evolution in the HPT1 and from the HPT1 exit to nozzle exit for the non-uniform max power condition

NOTE: The legend on the chart lists the species in the proper sequence for the lines (top to bottom), however, the line style is not correct (dashed, dotted, solid, etc is wrong).

5.6 IMPLICATIONS OF RESULTS

5.6.1 EFFECTS OF ENGINE OPERATING CONDITIONS

The three operating points studied for the NASA/DERA engine test simulation are typical of an older, but currently in-use engine. They can be used to assess the effects of engine operating conditions on trace species evolution and engine emissions. The cruise case has a combustor exit temperature of 1120 K and pressure of 6.8 atm, while for the max power case they are 1360 K and 15.7 atm, and for the non-uniform max power case the temperature is nominally 1600 K. It was found that SO_3 and HONO concentrations increased with

the mass averaged T, P, and V_x profiles. There was a significant difference between the 1D and 2D computations. The 1D computation under-predicted the SO_3 and HONO by 0.25% and 11.25% for the max power case and 2.7% and 21.3% for the non-uniform max power case, respectively. This trend is general and the difference is expected to depend on the magnitude of the temperature, pressure, or residence time discrepancies captured in the 2D model, as well as, the scale of those non-uniformities.

Another way to look at these effects is to consider the different pressure, temperature, and velocity profiles encountered by fluid elements traveling along different streamlines. The species concentrations along a high and low temperature streamline were also plotted versus axial distance. The results from the two streamlines differ significantly from the averaged values, as well as each other. These results further support the conclusions from previous work by Lukachko [1] that multi-dimensional non-uniformities have a considerable influence on trace chemistry evolution which indicates that some important features can not be captured in 1D models. Furthermore, other non-uniformities such as endwall boundary layers/cooling (similar to blade cooling), cooling air mass addition (addition of O_2), regions of separation or re-circulation (large residence time), or afterburner duct geometry (large residence time) would also be expected to affect trace species evolution.

5.6.3 EFFECTS OF THE UNSTEADY INTERACTION OF NON-UNIFORMITIES WITH DOWNSTREAM STATIONS

The high fidelity model for the rotor of the HPT1 was used to investigate the effects of the persistence of non-uniformities on subsequent blade rows. Two cases were investigated, focusing on temperature non-uniformities; the max power case which has smaller scale non-uniformities mainly caused by the wakes from the upstream cooled stator blades, and a non-uniform combustor exit temperature profile case which has a larger scale non-uniformity caused by combustion variations from the discrete fuel injector nozzles as well as the non-uniformity from the upstream cooled stator blades. Qualitatively, local regions of non-uniformity can be seen to persist through the downstream blade row in Figure 5.22. The mass-averaged exit plane species concentrations were time averaged over one cycle for the unsteady cases. The $(\text{SO}_3 + \text{H}_2\text{SO}_4)/\text{SO}_x$ is 0.0005% higher and the $(\text{HNO}_2 + \text{HNO}_3)/\text{NO}_y$ is 0.007% higher at the rotor exit plane for the max power case with the effects of the unsteady non-uniformities relative to the mixed-out case. The low reactivity of the SO_3 chemistry for this condition makes it difficult to make a definitive statement about the unsteady effects of the non-uniformity on SO_3 , although, it appears to enhance the oxidation of both trace species. Including the unsteady non-uniformities increases the HONO ratio by 26% relative to the mixed-out case.

The $(\text{SO}_3 + \text{H}_2\text{SO}_4)/\text{SO}_x$ is 0.09% lower and the $(\text{HNO}_2 + \text{HNO}_3)/\text{NO}_y$ is 0.004% higher at the rotor exit plane for the unsteady non-uniform combustor exit temperature max power case. This case shows that the effect of the

- A first of its kind analysis was completed on the post-combustor gas path of the NASA/DERA engine to support an engine test aimed at characterizing aviation emissions.
- The engine is typical of an older, but currently in-use civil aircraft engine. Three conditions were simulated: cruise, max power, and non-uniform max power.
- Pre-test simulations were used to guide the test plan. They helped to ensure that the operating conditions selected provide useful information about intra-engine chemistry. Also, they helped direct the measurement efforts by indicating important species to monitor and giving estimates for the instrumentation requirements.
- The pre-test simulations suggested testing at the highest combustor exit temperature attainable, as well as, a lower power setting. Also, SO_3 and HOHO were selected as important species to monitor.
- A time scale analysis indicated that most SO_3 production occurs in the HPT1 at max power conditions (approximately 4%). The analysis indicated that there is several orders of magnitude less sulfur conversion after the HPT1, and modeling resources were thus concentrated on the HPT1.
- PRE was used to generate grids of the NGV and rotor. A velocity triangle analysis was used to derive necessary intra-stage fluid parameters for the high fidelity modeling. The species initial condition for each condition were derived using the technique outlined in Section 2.3.2.
- Two types of high fidelity modeling were employed, a mixed-out case and a wake model case. All solutions were deemed converged using the criteria from Section 4.4. Also, the flow features such as deviation angle, streamlines, and inlet/exit conditions were checked to ensure the quality of each solution.
- The boundary layers and trailing edge geometry were not fully resolved for the grids used, however, they are not expected to have a significant impact on the trace chemistry results.
- HPT1 NGV blade-row flow-through time ranged from 0.18 to 0.26 ms and HPT1 rotor blade-row flow-through time ranged from 0.10 to 0.15 ms. The flow-through times computed from the low fidelity modeling were similar.
- A summary of all high fidelity modeling results is contained in Table 5.5, Table 5.6, and Table 5.7. Examples of some detailed results of the high fidelity modeling can be found in Section 5.4.2.3 or Appendix C.

- Local regions of flow or species non-uniformity persist through the subsequent blade rows.
- With the small scale non-uniformities (wakes from cooled blades) in the max power case, the $(\text{SO}_3 + \text{H}_2\text{SO}_4)/\text{SO}_x$ is 0.0005% higher and the $(\text{HNO}_2 + \text{HNO}_3)/\text{NO}_y$ is 0.007% higher at the rotor exit plane with the effects of the unsteady non-uniformities relative to the mixed-out case. In other words, including the unsteady non-uniformities increases the HONO ratio by 26% relative to the mixed-out case.
- With the large scale non-uniformities (combustor temperature profile and wakes from cooled blades) in the non-uniform max power case, the $(\text{SO}_3 + \text{H}_2\text{SO}_4)/\text{SO}_x$ is 0.09% lower and the $(\text{HNO}_2 + \text{HNO}_3)/\text{NO}_y$ is 0.004% higher at the rotor exit plane with the effects of the unsteady non-uniformities relative to the mixed-out case. In other words, mixing out the non-uniformities over predicts the conversion of SO_3 by about 60%.

6 THESIS SUMMARY AND CONTRIBUTIONS

This chapter will present a summary of the research discussed in this thesis and describe specific contributions of this research.

6.1 THESIS SUMMARY

Trace species of aircraft emissions were shown to have potential impacts on the local and global atmosphere, including changes in radiative forcing and ozone depletion. A summary of prior work was provided, which has concluded that most trace species chemistry occurs early, thus the need exists for better characterization of trace species in the intra-engine environment.

This thesis presented an overview of a modeling methodology developed to simulate the evolution of trace species in the post-combustor flow path of gas turbine engines. The modeling methodology incorporates various levels of detail to accurately and efficiently predict levels of intra-engine trace species by considering key parameters affecting their evolution, specifically temperature, pressure, residence time, and species concentration. The model is intended to improve the overall understanding of the fundamental physical processes that effect trace species evolution and to serve as a predictive design tool which can direct the development of new engine technologies which reduce undesirable aviation emissions.

Modeling tools and improvements made to these tools were discussed. The existing tools consist of the PRE grid generation code, PROCESS grid pre-conditioner code, POST grid post processor code, CNEWT and CALCHEM flow chemistry solvers, and CNEWTVS6 flow visualization code. Improvements in modeling tools were made, which allow for more complicated geometries, multiple inlet and exits, improved execution time for solutions with chemistry, and a specification of a pressure, temperature, and species concentration deficits associated with a wake of an upstream blade or blade row.

Several validation exercises were performed to benchmark these modeling tools. An attempt was made to model a VPFR experiment to demonstrate the accuracy of the modeling tools, however, a limitation to the flow solver prevented this ultimate objective. The validation exercise did nonetheless provide the opportunity to test several code improvements, investigate the limitations of the modeling tools, and analyze flow features of the reactor. A chemical mechanism study which investigated the effects of the chemical mechanism on intra-

- Time scale analyses are useful in formulating a overall modeling strategy by indicating the critical areas of the engine flow path to investigate with higher fidelity modeling.
- A time scale analysis is a simple parametric study which incorporates thermodynamic potential, chemical kinetics, and residence time. The output is a plot of severity parameter for a given species of interest, although, a preliminary estimate of species evolution can be obtained.
- Time scale analyses can also be used to provide insight into the physical phenomena influencing trace species evolution. A few example time scale analyses were used to show:
 - Blade cooling can enhance sulfur conversion.
 - Engine operating condition can influence sulfur conversion, take-off conditions can have higher sulfur conversion than cruise conditions.
 - The OH pathway to SO_3 can be more active than the O pathway.
- A simple method for specifying chemistry initial conditions involves perturbing an equilibrium composition, re-balancing the species based on mass, and doing a stabilizing kinetics calculation.
- High and low fidelity models involve integrating the equations of mass, momentum, and energy over a discrete domain coupled with chemical kinetics to simulate intra-engine chemistry. A high fidelity model can incorporate many multi-dimensional effects (i.e. non-uniformities) while a low fidelity model uses average quantities.
- CNEWT and CALCHEM have been useful modeling tools for studying intra-engine trace species flow-chemistry problems. CNEWT is a code created by Lukachko [1] which was built upon the NEWT turbomachinery CFD code from Dawes [51]. CALCHEM is a simple, 1D version of CNEWT.
- Other supporting codes necessary for turbine chemistry modeling are PRE, PROCESS, POST, and CNEWTVS6.
- The improvements made to existing modeling tools include:
 - A new CAD solid model based grid generator which allows for the simulation of more complicated, arbitrary geometries. The output is a truly unstructured grid. The tools were in a developmental stage and a few difficulties were encountered with the translation step and numerical issues in the volume mesher. The VPFR was successfully meshed with the new grid generator.
 - Addition of multiple inlet/exit capability which allows for simulation of mixing flows. A test case and the Princeton VPFR were used to validate the multiple inlet/exit code modifications.
 - Addition of parallel chemistry subroutines. A test case showed a factor of 3.4 improvement in time on 6 compute nodes. The accuracy of the parallel chemistry modifications was verified.

- The pre-test simulations suggested testing at the highest combustor exit temperature attainable, as well as, a lower power setting. Also, SO_3 and HOHO were selected as important species to monitor.
- A time scale analysis indicated that most SO_3 production occurs in the HPT1 at max power conditions (approximately 4%). The analysis indicated that there is several orders of magnitude less sulfur conversion after the HPT1, and modeling resources were thus concentrated on the HPT1.
- PRE was used to generate grids of the NGV and rotor. A velocity triangle analysis was used to derive necessary intra-stage fluid parameters for the high fidelity modeling. The species initial condition for each condition were derived using the technique outlined in Section 2.3.2.
- Two types of high fidelity modeling were employed, a mixed-out case and a wake model case. All solutions were deemed converged using the criteria from Section 4.4. Also, the flow features such as deviation angle, streamlines, and inlet/exit conditions were checked to ensure the quality of each solution.
- The boundary layers and trailing edge geometry were not fully resolved for the grids used, however, they are not expected to have a significant impact on the trace chemistry results.
- HPT1 NGV blade-row flow-through time ranged from 0.18 to 0.26 ms and HPT1 rotor blade-row flow-through time ranged from 0.10 to 0.15 ms. The flow-through times computed from the low fidelity modeling were similar.
- A summary of all high fidelity modeling results is contained in Table 5.5, Table 5.6, and Table 5.7. Examples of some detailed results of the high fidelity modeling can be found in Section 5.4.2.3 or Appendix C.
- Low fidelity models were used to model the HPT1 and HPT1 exit to nozzle exit flow paths. A high and low temperature streamline, as well as the averaged profile, through the HPT1 were investigated. The HPT1 low fidelity model can be compared to the HPT1 high fidelity model to investigate the impacts of 2D versus 1D modeling.
- The HPT1 exit to nozzle exit low fidelity model profile was improved using a curve fit to results from the HPT1 high fidelity modeling and the available data.
- A summary of all low fidelity modeling results is contained in Table 5.6 and Table 5.7. Examples of some detailed results of the low fidelity modeling can be found in Section 5.5.2.2 or Appendix C.

APPENDIX A

PRINCETON VPFR VALIDATION MODELING

The Princeton University's Variable Pressure Flow Reactor (VPFR) is an experimental apparatus specifically designed to measure chemical kinetic data at the high temperatures and pressures typical of energy conversion systems. The VPFR is ideally suited to evaluate the capability of the modeling tools to represent many flow features of interest, mixing, and passively reacting flow. The approach was to model a published flow reactor experiment and compare the simulation data to the experimental data in an attempt to benchmark the accuracy of the modeling tools. The plan was to first simulate the flow-only, then flow with inert species, and finally passively reacting flow. In the end, the objectives of the flow reactor were reduced due to the restriction of the modeling tools to simulation of compressible flows since the flow-only solution did not accurately represent the actual VPFR experimental data.

The objectives of the Princeton VPFR validation modeling effort can be found in Section 4.2.1 and a summary of results can be found in Section 4.2.2.

VPFR MODELING SET UP

Grid Generation

The flow reactor is essentially a cylindrical tube with an inlet section, a baffle, an injector assembly, a diffuser, and a test section. Figure A.1 shows the basic flow reactor geometry and identifies some important features.

generation procedure are detailed in Section 3.3.1 and [66]. The solid model and final flow reactor grid are shown in Figure A.2.

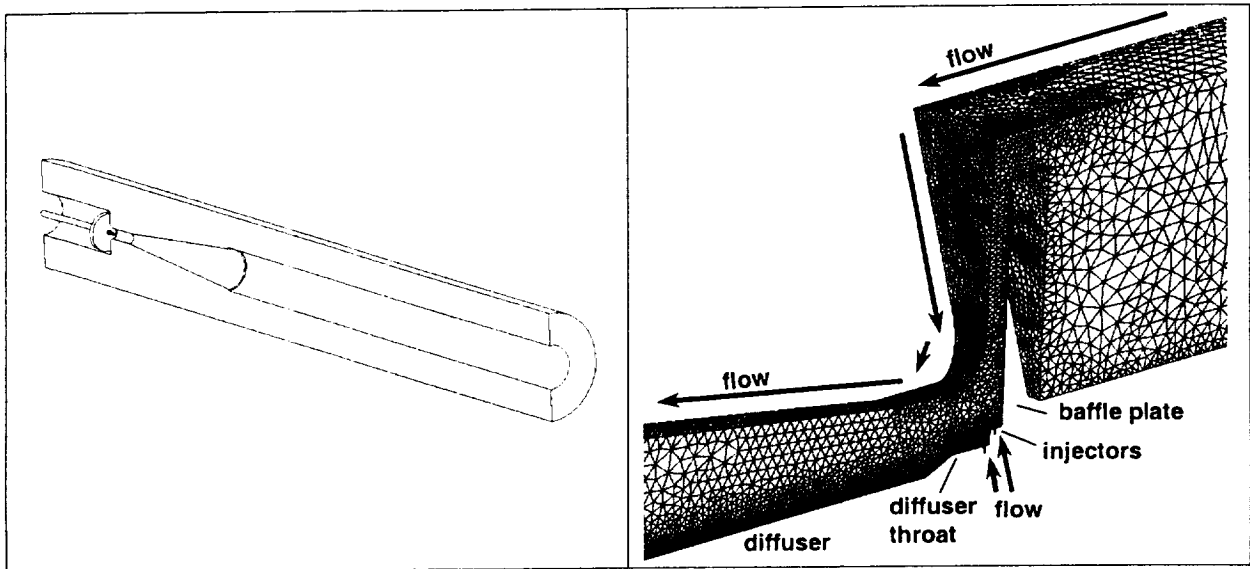


Figure A.2 VPFR solid model and grid detail near baffle and injector assembly

As mentioned in Section 3.3.1, the new grid generator had difficulty meshing geometries with large aspect ratios. This was overcome in the flow reactor grid by scaling the radial dimension in the solid model by a factor of 2 to reduce the aspect ratio then re-scaling the resultant grid back to the original aspect ratio.

To improve convergence time the grid is typically initialized with an approximate guess for the fluid variables (temperature, pressure, density, and velocity). In particular, an axial velocity in the direction of flow was estimated and used for the flow reactor. However, due to the complex nature of the flow path in the reactor it was found to be better to start with zero initial velocity. In the inlet and test section the flow is nearly axial, however, near the injection site it moves radially outward around the baffle and then radially inward into the diffuser. In other words, the baffle is perpendicular to the flow which means that the fluid near the baffle had a poor initial guess. Therefore, the grid with a prescribed axial velocity would cause the code to enter the “panic smoothing” routine which is triggered by an abnormally low pressure since the fluid on the downstream side of the baffle was moving away from the baffle causing a low pressure region. In most cases, the code would eventually crash once the pressure became very small. Initializing the grid with a zero velocity resolved this problem at the expense of having a large transient in the beginning of the solution and long convergence time.

Experimental Conditions And Modeling Assumptions

Several aspects of the experimental operating conditions need to be considered relative to the modeling assumptions inherent in CNEWT when evaluating the applicability of the code to the flow reactor problem. A

results for Mach numbers as low as 0.2 to 0.3 [69] it is in general not well suited to simulate the experimental conditions typical of the VPFR operation. Modifying the code by changing the flow variables to double precision could extend the compressibility limits of the code by helping to resolve the pressure differences [69], however, it is uncertain how much this modification would help.

In general, the error introduced by exceeding the compressibility limit was large and the fluid solution did not represent experimental or empirical features well. Initially, a similarity approach was attempted to improve the solution quality by using non-dimensional analysis. The Mach number could be increased (to $0.1 < M < 0.3$) while maintaining the incompressibility assumption by altering the numeric artificial viscosity. The Reynolds number is defined as:

$$\text{Re}_D = \frac{\rho \cdot V \cdot D}{\mu} \quad (\text{A.1})$$

Matching the Reynolds number of the simulation to the experiment is an important step to reproducing the flow features. However, it was found to be practically impossible to scale the reactor with complete similarity [59], [60]. Using the available independent variables, it is very difficult to match the non-dimensional numbers necessary to equate the various other parameters required to accomplish modeling with even partial similarity for this situation [59]. The fluid flow features, mixing, and chemical kinetics are all important to accurately represent the flow reactor, some of the difficulties encountered in the similarity approach for this situation will be detailed further in “Steady Non-Reacting Flow Solution.

Other possibilities to overcome the compressibility problem with the flow reactor modeling effort was to use the double precision fluid variables, implement a pre-conditioner to the current solution algorithm [70] or adopt a entirely new solution algorithm. Using the double precision option was not expected to resolve the problem and the other options were not easily implemented and were outside the context of the research agenda.

EXPECTED FLOW REACTOR RESULTS

Diffuser Pressure Recovery Coefficient

The pressure recovery coefficient is one method to measure the performance of a diffuser. It is defined as:

$$c_p = \frac{P_e - P_t}{P_{or} - P_t} \quad (\text{A.2})$$

There are ample data in the literature relating diffuser design parameters and operating conditions to this pressure recovery coefficient. These pressure recovery maps are useful to diffuser designers. In the context of

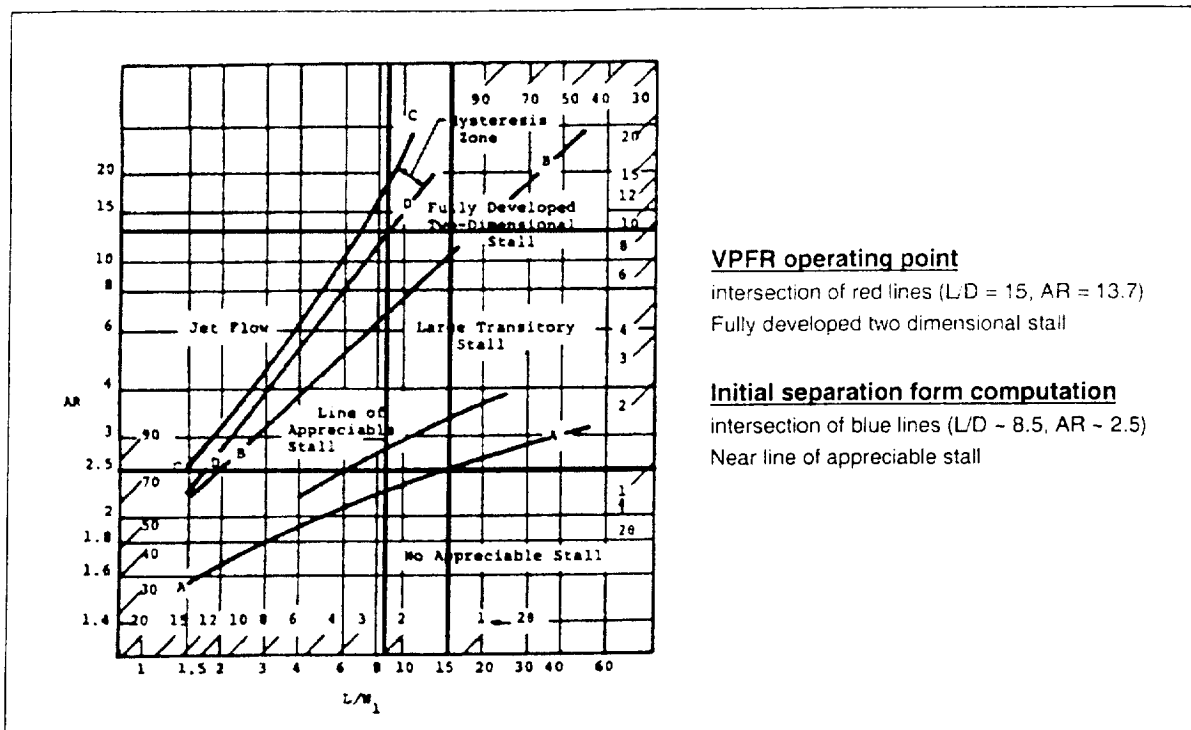


Figure A.4 Diffuser flow regime map [39]

Velocity Profiles

The most informative method to evaluate the quality of the computational solution was to compare the velocity profiles to experimental data and empirical correlations. The VPFR was designed to operate such that the velocity profiles transition quickly to fully-developed turbulent velocity profiles [26]. These profiles have a characteristic “top hat” shape (see Figure A.5 and Figure A.6).

Empirical Correlation

The Power Law is one empirical correlation commonly used to predict velocity profiles in pipe flow:

$$\frac{u}{V_c} = \left(1 - \frac{r}{R}\right)^{\frac{1}{n}} \quad (A.3)$$

Where V_c is the centerline velocity, u is the time average x component of velocity, and R is the pipe radius. For the flow reactor case, n , which is a function of Reynolds number, is about 6. Figure A.5 shows the expected velocity profile for the VPFR derived from the Power Law.

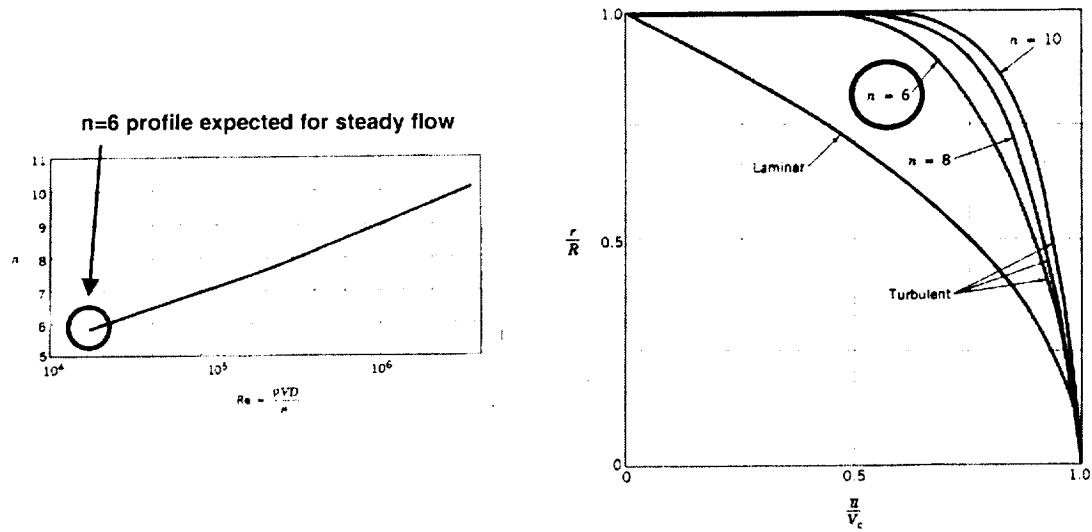


Figure A.5 Typical velocity profiles from Power Law [38]

Experimental Data

For comparison, some velocity profile data specific to the Princeton VPFR is given in Figure A.6.

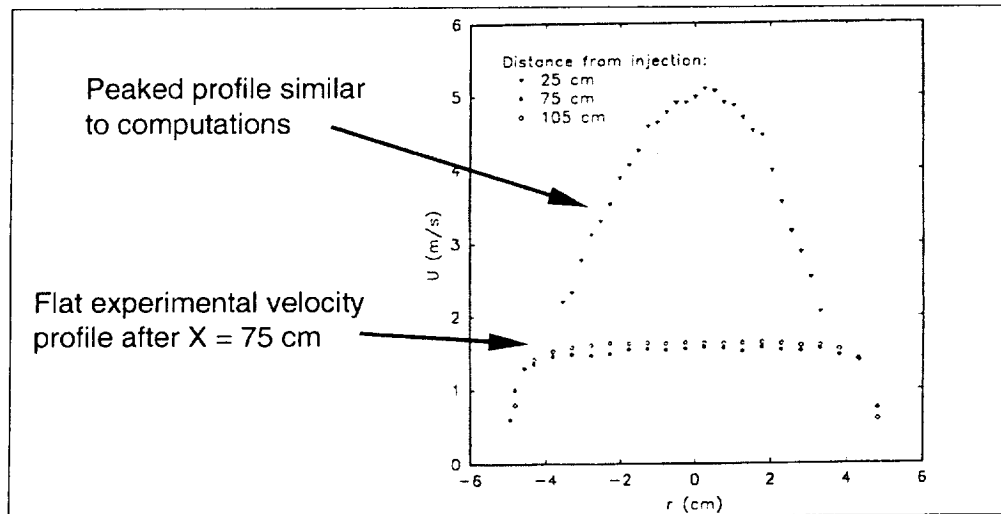


Figure A.6 Experimental velocity profiles for Princeton VPFR [26]

Another point of comparison are other experimentally measured velocity profiles for conical diffusers, such as that given in Figure A.7. The red labels in the figure indicate the profiles for diffusers with design parameters similar to those of the Princeton VPFR. This figure shows that the profiles become more asymmetric and peaked with higher AR and L/D.

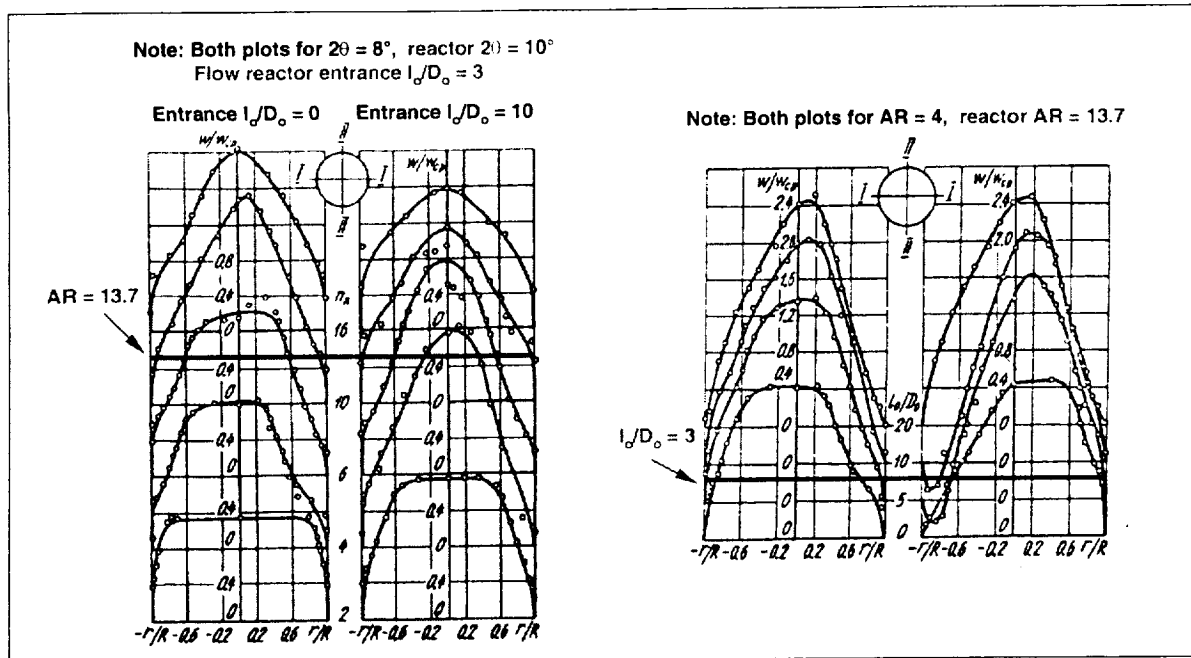


Figure A.7 General velocity profiles in diffusers [40]

STEADY NON-REACTING FLOW SOLUTIONS

Several modeling runs were made in an attempt to simulate the flow reactor and characterize the capability and limitations of the CNEWT code. Two cases were selected for presentation in this thesis to illustrate the major findings of the flow reactor validation effort. The first case, labeled "Run 1," has the lowest Reynolds number in the test section for which a converged solution could be obtained. The second case, labeled "Run 12," has a higher Reynolds number. Further differences between the cases and details of the solutions follow in "Low Reynolds Number Solution (Run 1)" and "High Reynolds Number Solution (Run 12)".

General Results

A summary of results from the two selected cases is given in Table A.1. The Reynolds number for both solutions is several times larger than the experimental conditions of the VPRF.

	Run 1	Run 12
ΔP (kPa)	1	30
V_x max (m/s)	-85	-452
V_x min (m/s)	11	163
M_{max}	0.25	1.7
P_t	93,004	55,181
P_{ot}	96,677	122,028
P_e	96,994	106,128
C_p	1.09	0.76
V_x average exit (m/s)	-4.7	-16
Re_D	31,400	116,700
Mass flow in (kg/s)	2.7e-3	8.4e-3
Mass flow out (kg/s)	2.5e-3	1.1e-2
Mass flow error	7.2%	Injectors ??
Shock position (cm)	none	5

Table A.1 Summary of selected results for VPFR validation runs

Figure A.8 shows a cross-section of the flow reactor with locations of nine axial stations from 15 to 95 cm. In the simulations presented here, the flow travels in the negative X direction (right to left in the figure).

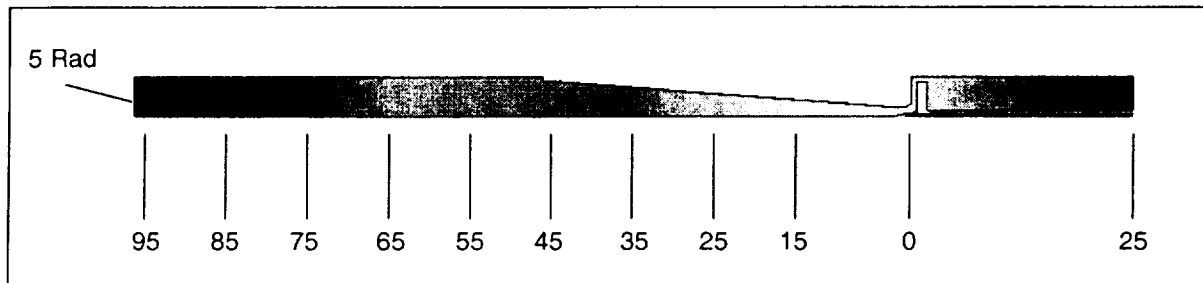


Figure A.8 Axial position X (cm) for flow reactor modeling

Low Reynolds Number Solution (Run 1)

Run 1, a low Re solution, was solved on a preliminary coarse grid which had about 60,000 cells and no injector flow. It was started with a ΔP across the reactor main inlet to exit of 30 kPa which yielded a Mach number of 1.23 at the throat of the diffuser and a Reynolds number of 82,400 in the test section. The convergence history, which was typical of most flow reactor runs, is plotted in Figure A. 9.

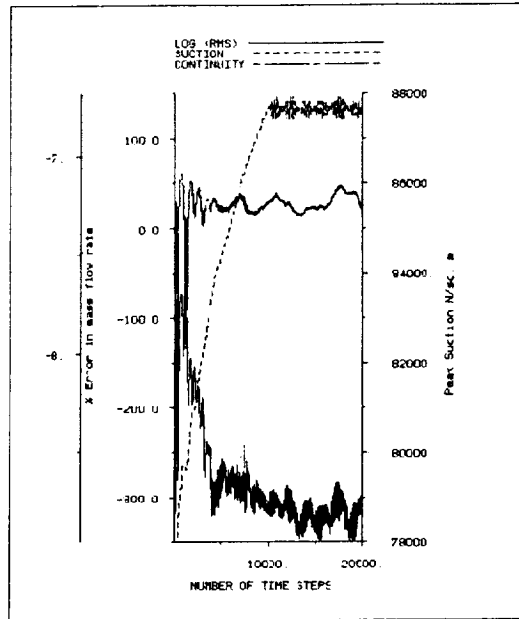


Figure A. 9 Flow reactor Run 1 convergence history

The peak suction (lowest pressure in the domain) converged to about 87 kPa, $\log(\text{RMS})$ (the root mean square residual) was below $1.0\text{E}-8$, and the continuity (mass flow error) oscillated between 10% and 60%. The mass flow error and oscillations were larger for lower Mach number flows, and Run 1 represents the edge of solution stability. The large mass flow error was eventually attributed to the codes inability to compute incompressible flows.

As mentioned previously, a similarity approach was planned as a potential method to overcome the compressibility issue and continue the flow reactor validation efforts. In an attempt to match the experimental conditions for the Princeton VPFR, the inlet pressure was sequentially reduced until the Mach number at the throat of the diffuser was less than 0.3, which occurred at a pressure difference of 1 kPa. Contours of axial velocity are given in Figure A.10. The average Mach number was 0.013 in the test section.

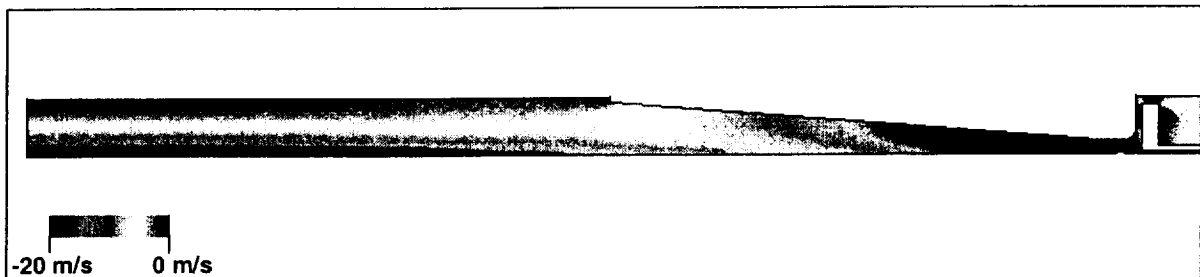


Figure A.10 Axial velocity from -85 to 11 m/s (note: contours clipped for presentation)

The diffuser and test section were divided into nine axial stations (see Figure A.8) and velocity profiles were obtained at each. The profiles are given in Figure A.11 for Run 1.

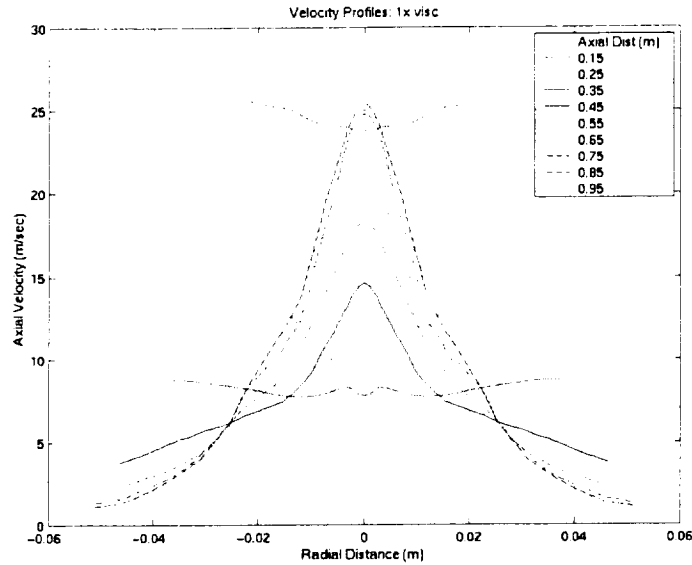


Figure A.11 Velocity profiles at nine axial stations

The velocity profiles for Run 1 are not similar to the “top hat” profiles typical of fully developed turbulent flow. They are peaked and the curvature is opposite to that which is expected. The results from Run 1 exhibit no recirculation, however the inflective velocity profiles indicate the possibility of separated jet flow. Furthermore, the pressure coefficient was unrealistically greater than unity. Considering the very low Mach number in the bulk of the test section ($M \sim 0.01 \ll 0.3$), it was suspected that the majority of the error encountered was associated with using the code beyond the compressibility limit. However, potential discrepancies caused by the mismatched Reynolds number or boundary layer grid resolution were still investigated.

Carrying on with the plan to match the Reynolds number by increasing the artificial viscosity, three additional solutions were started from Run 1. The laminar and turbulent viscosity were increased by a factor of 10, 20, and 50 for these solutions. The results of this study are summarized in the following table:

	Run 1	Run 2	Run 3	Run 4
Description	1x μ	10x μ	20x μ	50x μ
V_x max (m/s)	-85	-73	-72	-61
V_x min (m/s)	11	10	9	7
M_{max}	0.247	0.210	0.206	0.176
P_i	93,004	94,444	95,314	96,401
P_{ot}	96,677	96,898	97,018	97,211
P_e	96,994	96,999	96,999	96,999
C_p	1.09	1.04	0.99	0.74
V_x average exit (m/s)	-4.7	-3.8	-3.2	-2.3
Re_D	31,400	2,590	1,080	300
Mass flow in (kg/s)	2.7E-3	2.3E-3	1.9E-3	1.3E-3
Mass flow out (kg/s)	2.5E-3	1.8E-3	1.5E-3	1.5E-3
Mass flow error	7.2 %	25.1 %	29.8 %	12.7 %

Table A.2 Summary of Reynolds number matching study

The Reynolds number for the 10x case was already beyond the goal of reaching 3,000 to 15,000. The profiles for that case were very similar to Run 1 and are not repeated here. Instead the velocity profiles for Run 4, the extreme case with 50x viscosity, are shown in Figure A.12. As the numerical viscosity increased, the velocity profiles became more inflected and still remained peaked, thus matching the Reynolds number did not move toward a more realistic solution. In fact, increasing the viscosity lowered the flow Mach number pushing the flow more into the incompressible regime which would make the error associated with the incompressibility higher.

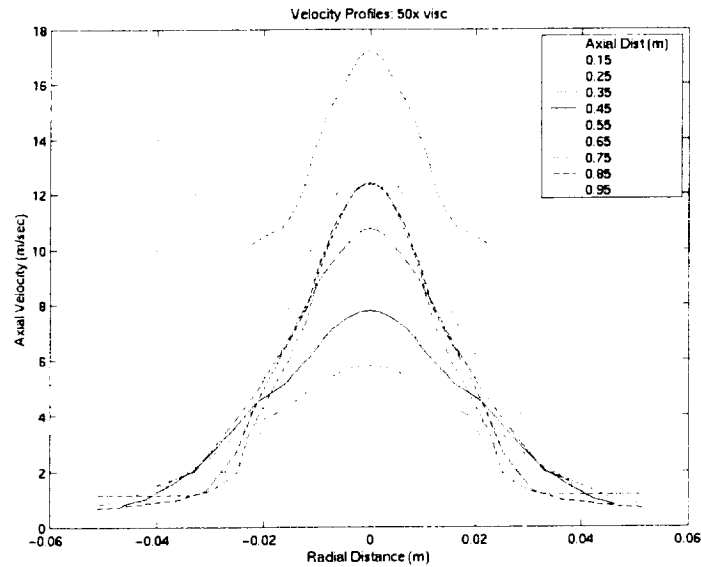


Figure A.12 Velocity profiles for 50x viscosity case (Run 4)

Also, it was initially thought that the wall functions or grid boundary layer resolution could be causing the poor solution quality. The grid post processor was used to refine the grid near the outer walls of the diffuser and test section. The first node from the outer wall for the coarse grid was 5.9 mm away. Several levels of refinement were used until a grid with nearly 670,000 cells was created with the first node located 0.6 mm from the outer wall, see Figure A.13. The results of this study are summarized in the following table:

	Run 1	Run 5	Run 6
Grid	coarse	2 level refinement	3 level refinement
Cells	60,166	205,682	668,681
V_x max (m/s)	-85	-71	-85
V_x min (m/s)	11	10	11
M_{max}	0.247	0.209	0.245
P_t	93,004	94,438	93,338
P_{ot}	96,677	96,984	96,543
P_e	96,994	97,000	97,000
C_p	1.086	1.006	1.143
V_x average exit (m/s)	-4.7	-3.9	-4.3
Re_D	31,400	26,300	28,600
Mass flow in (kg/s)	2.7E-3	2.3E-3	2.5E-3
Mass flow out (kg/s)	2.5E-3	2.2E-3	2.6E-3
Mass flow error	7.2 %	5.9 %	3.4 %

Table A.3 Summary of boundary layer grid refinement study

The velocity profiles from Run 6 with the highest degree of boundary layer refinement are shown in Figure A.14. Again, the velocity profiles did not move in the direction of resembling the experimentally or empirically derived profiles. The velocity profiles were still peaked/inflected and the pressure recovery coefficient was unreasonable, lending further evidence that the main source of error in these flow reactor simulations is due to the compressibility limits of the code.

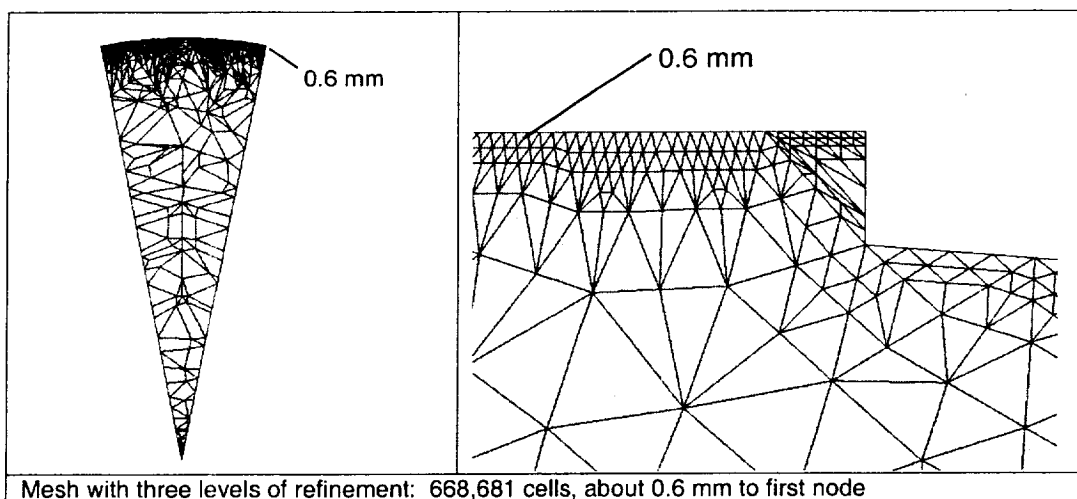
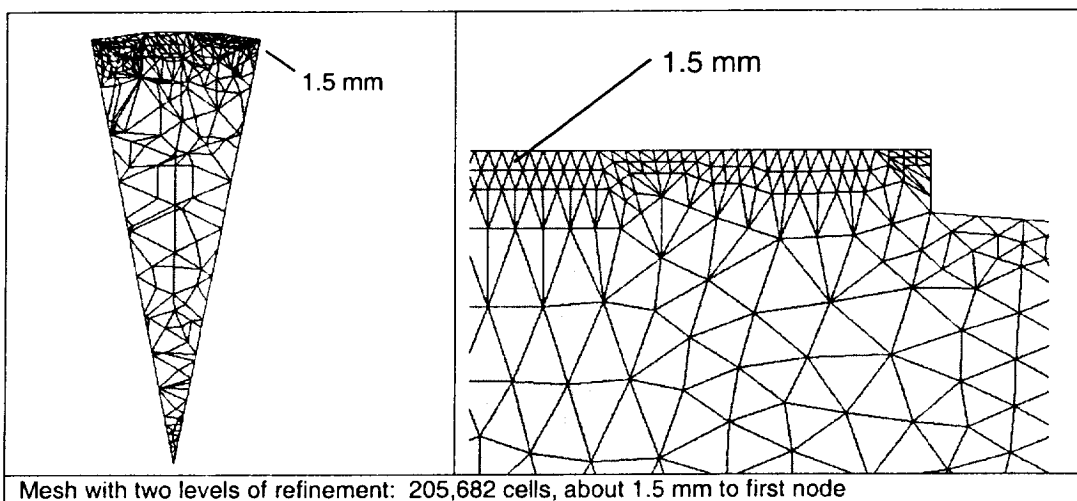
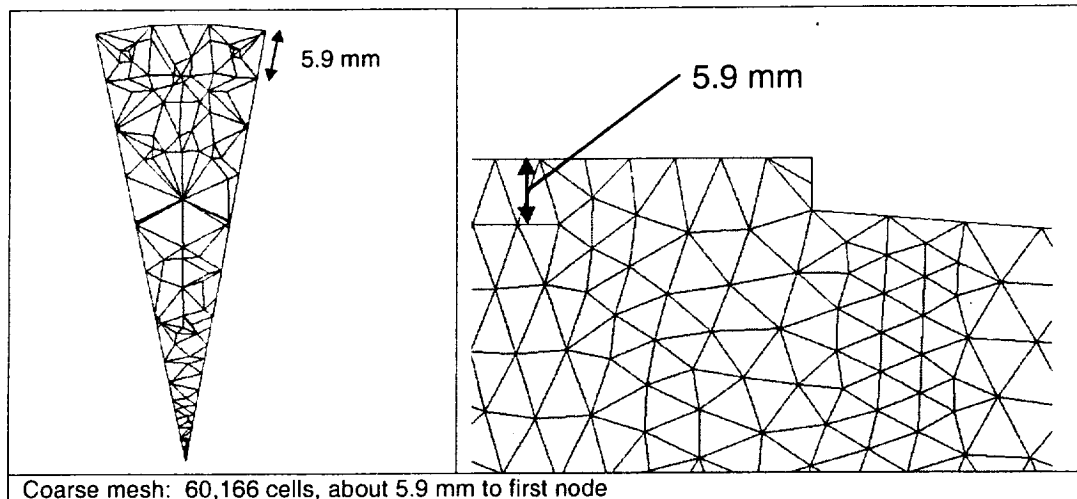


Figure A.13 Mesh refinement in flow reactor test section

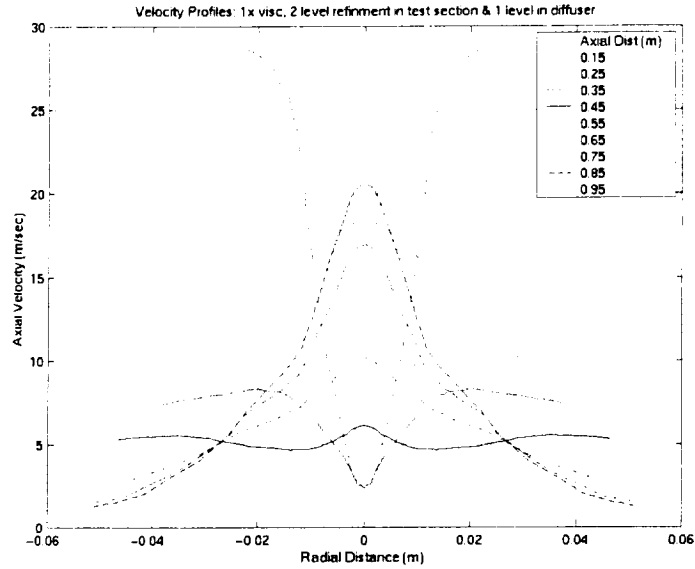
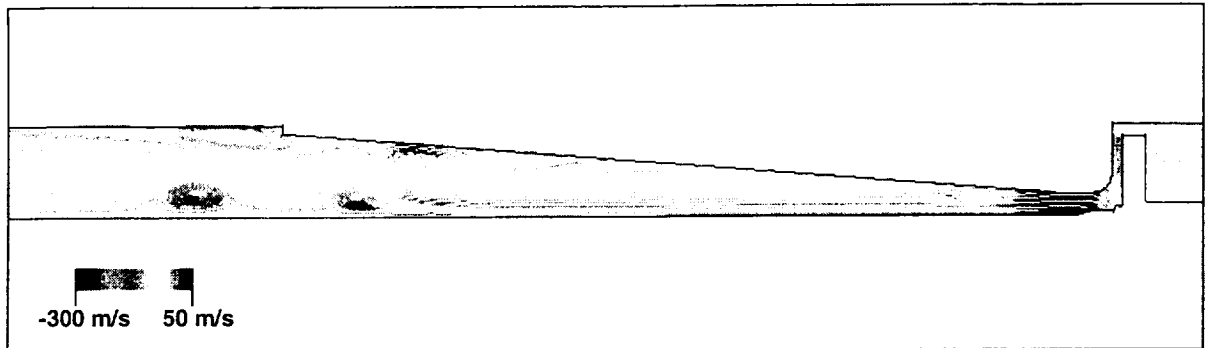


Figure A.14 Velocity profiles for case with refined boundary layer grid (Run 6)

High Reynolds Number Solution (Run 12)

The second case to be discussed in some detail, Run 12, was solved on a finer grid which had about 270,000 cells (see Figure A.2). It was maintained at a higher ΔP of 30 kPa from the main inlet to exit and had flow at the two injector inlets. The injector inlets were set at a pressure ratio of about 9 to 1 relative to the pressure at the main exit. In this case the mass flow error was not computed correctly because the injector mass flow could not be easily accounted. Figure A. 15 shows the axial velocity contours plotted on streamlines for a solution dumped at 10,000 and 35,000 iterations.

10,000 iterations:



35,000 iterations:

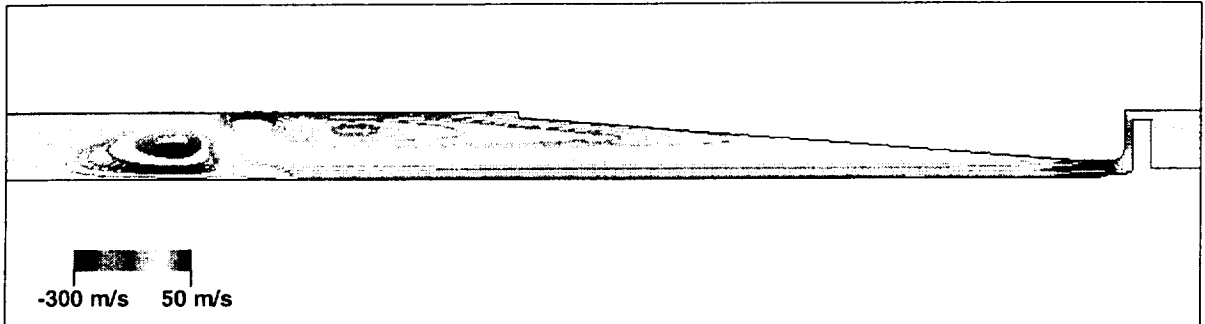


Figure A. 15 Axial velocity from -452 to 163 m/s at 10,000 (top) and 35,000 (bottom) iterations (note: contours clipped for presentation)

The average Mach number in the test section was 0.05. This solution shows that the flow separates in the diffuser and recirculation zones begin to form. The point of separation is roughly 23 cm downstream of the injection site. This point corresponds to a L/D of about 8.5 and a AR of about 2.5 and was anticipated based on the flow regime map presented in Figure A.4.

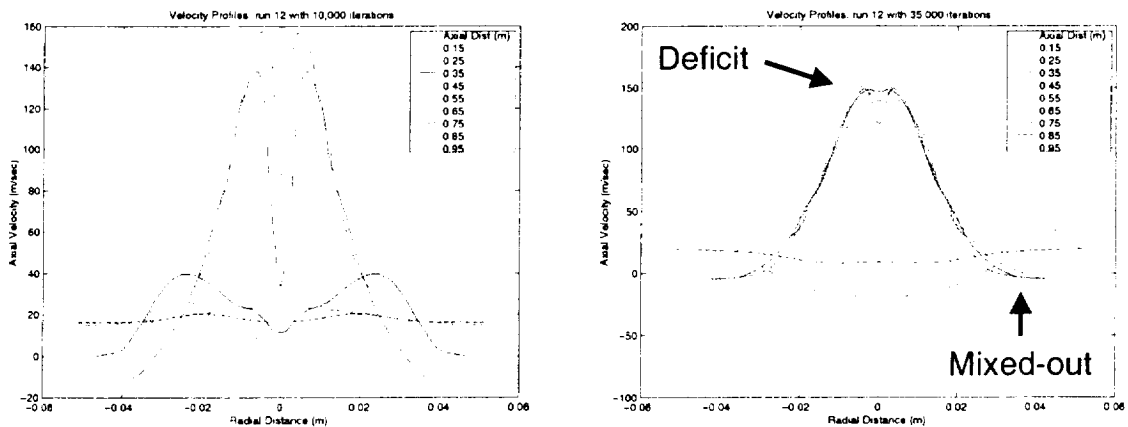


Figure A.16 Axial velocity profiles at nine axial stations for 10,000 and 35,000 iteration solutions

The velocity profiles were peaked prior to the recirculation, followed by flat profiles characteristic of the experimental data. The flat profiles after the stall cells are likely due to the large scale mixing, exchange of low momentum fluid at the wall with high momentum fluid in the core. The profiles show a deficit near the centerline which is typical of flow around a bluff body (the injector). These observations would suggest that the diffuser is operating with large scale unsteady stall similar to the expected operation based on the flow regime map. The flat experimental velocity profiles of the Princeton VPFR could be due to this averaged unsteadiness rather than high turbulence at the diffuser inlet. However, the code was being run in steady mode with a non-uniform time step, therefore, further investigation into the unsteadiness was required (see Unsteady Non-Reacting Flow Solution).

In the higher ΔP solution, Run 12, the diffuser was choked and there was a shock positioned 5 cm into the diffuser. Figure A.17 shows the supersonic region where the flow accelerates from the diffuser throat to the shock where the maximum Mach number was 1.7.

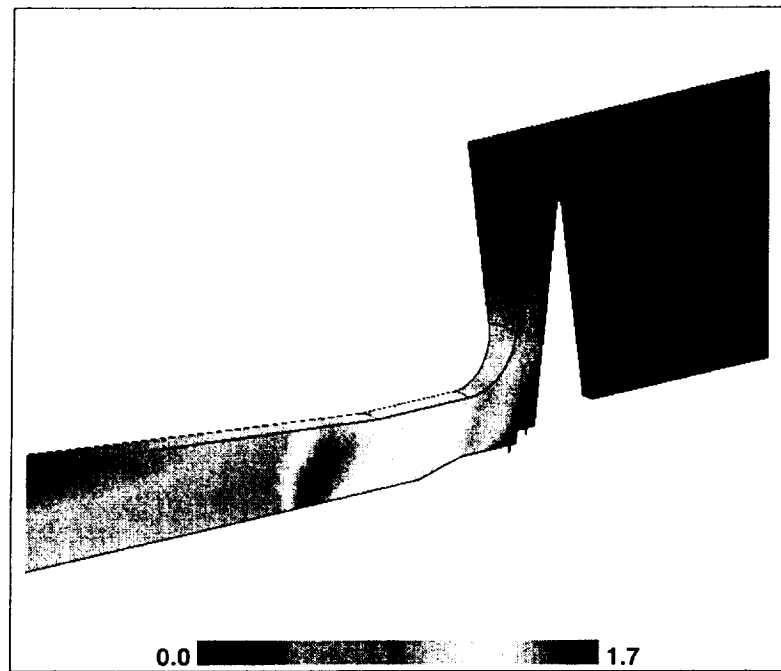


Figure A.17 Mach number contours near diffuser throat showing subsonic to supersonic transition

The pressure recovery coefficient for this case was 0.76. However, this lower value was due to the losses associated with the shock rather than a better representation of the diffuser operation at the desired flow conditions.

The presence of the shock was an additional complication when considering the plan for a similarity solution. It was apparent from Run 1 that having a Mach number of about 0.2 to 0.3 solely in the throat of the diffuser was not sufficient to overcome the compressibility limits of the code. The bulk of the flow field would have to be

above a Mach number of 0.2 to obtain an accurate solution. The flow reactor geometry is such that the throat of the diffuser chokes well before the Mach number in the test section increases to a reasonable level for the flow solver. From a compressible flow table for an ideal gas (with $\gamma = 1.4$), assuming isentropic flow with an area ratio of 13.7, the Mach number at the diffuser exit would only reach about 0.04 when the throat chokes [38]. Or in other words, to use geometric scaling and assuming a desired Mach number in the test section of less than 0.25, the maximum diffuser area ratio would be 2.4. With this Mach number and area ratio, the velocity in the test section is much higher and the length of the test section must be increased to capture the same flow reactor residence time. The test section becomes prohibitively long (about 25 m), making lab measurements difficult and the geometry harder to mesh (worse aspect ratio).

Figure A.18 shows a detail of the Z-direction velocity contours overlaid on streamlines near the injectors. This figure gives qualitative evidence that the multiple inlet/exit code modifications are functioning properly. At this point, no attempt has been made to quantitatively evaluate the ability of the code to simulate the mixing process associated with the injected fluid.

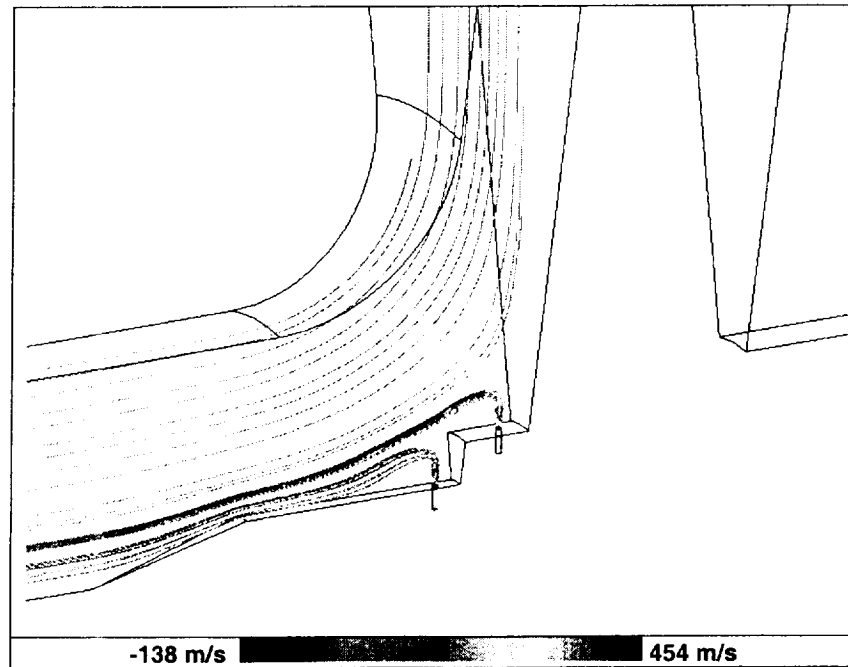


Figure A.18 Z direction velocity component near injectors

Matching the momentum ratio of the injection jet and the opposing primary flow is another complex problem with regard to performing a similarity solution.

UNSTEADY NON-REACTING FLOW SOLUTION

After discovering the flow separation in Run 12 and knowing that the diffuser may operate in a unsteady fashion, it was decided to continue Run 12 using a uniform time step to get a proper unsteady solution. The choice of time step was constrained by the size of the smallest cell. Choosing too large a time step would cause the code to crash because the flow could not be resolved on the scale of that smallest cell. The fine mesh near the injector limited the time step to 0.2455E-06 seconds per iteration.

This unsteady case gives more insight into the operating characteristics of the flow reactor and the capability of the code to simulate unsteady flow. Figure A.19 shows contours of axial velocity overlaid on streamlines at 60,000 iterations, just prior to the time when the large initial transient leaves the domain.

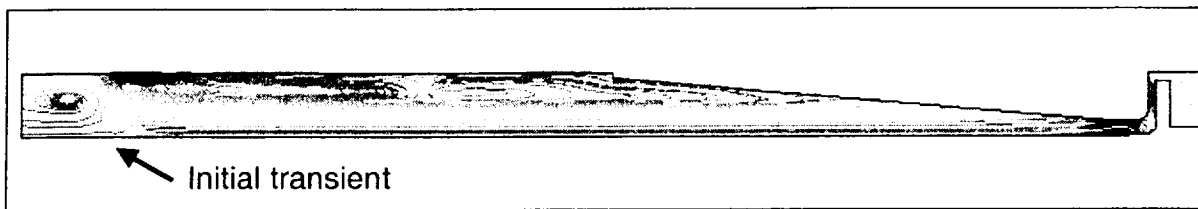


Figure A.19 Axial velocity just before 60,000 iterations

Figure A.20 shows the instantaneous velocity profiles for the unsteady Run 12 at 100,000 iterations. The shape of the velocity profiles are similar to the steady case and are no more representative of the “top hat” profiles expected of fully developed turbulent flow. The deficit near the centerline from the bluff body and inflected profile shape are still evident. In fact, the negative velocity near the outer radius is indicative of reversed flow and signifies separation.

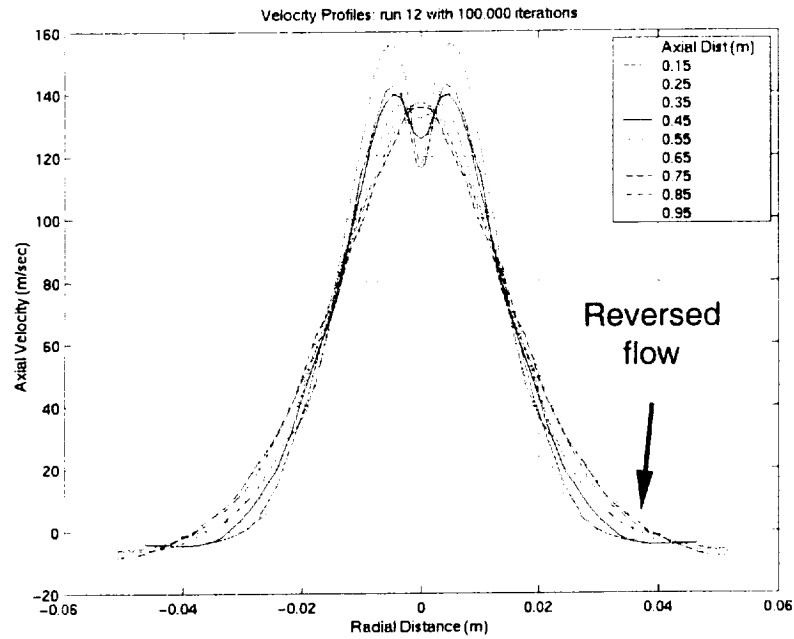


Figure A.20 Velocity profiles for unsteady Run 12 at 100,000 iterations (not time averaged)

The unsteady Run 12 solution was continued for one cycle after the initial transient left the domain. The limitations on time step meant that nearly 30 days of computational time were required to compute that one cycle. A recirculation vortex was observed to form near the outer wall at the point of first separation then travel downstream while growing in size until it is shed into the test section, see Figure A.21. The periodic vortex shedding was estimated to occur at a frequency of 151 Hz by computing the time elapsed between one cycle in the unsteady computation.

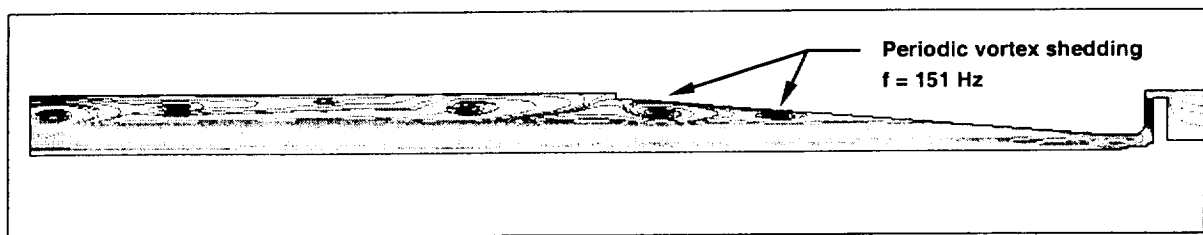


Figure A.21 Streamlines with axial velocity contours for unsteady Run 12 showing one cycle of the periodic vortex shedding

An animation of the initial transient leaving the domain and one cycle of the periodic vortex shedding can be found in Figure F.9 and Figure F.10, respectively (see Appendix F).

Acoustic Resonance Calculation

The VPFR was suspected to have an acoustic resonance at certain operating conditions [26]. It was hypothesized that these acoustic pressure waves could be linked to the vortex shedding frequency. Using the wave equation, the resonant frequency for the modeled portion of the flow reactor was estimated as:

$$f = \frac{c}{\lambda} = \frac{c}{2 \cdot L} = \frac{(340 \text{ m/s})}{2 \cdot (0.964 \text{ m})} = 176 \text{ Hz} \quad (\text{A.4})$$

This theoretical frequency compared well to the value of 151 Hz predicted in the unsteady simulation. The simulation did not include the entire length of test section of the real flow reactor. Using $L = 1.7 \text{ m}$ for the actual length from the baffle to the exit of the flow reactor, the vortex shedding frequency for the experimental facility is predicted to be about 100 Hz.

VPFR MODELING SUMMARY

Limitations of the flow solver hampered the ultimate objective of validating the modeling tools through a successful reacting flow simulation of the Princeton VPFR. Although the validation exercise was not completed, many code improvements were tested, a considerable amount was learned about the limitations of the tools, and some potential issues with the flow reactor design were identified.

Refer to Section 4.2.2 for a more detailed summary of the results from the Princeton VPFR validation modeling exercise.

APPENDIX B

TURBINE CHEMISTRY MECHANISM

Several turbine chemistry chemical mechanisms were evaluated for use in the calculations. The mechanism referred to as the "Mueller et al. (2000)-truncated mechanism" was selected for the NASA/DERA engine simulations. The mechanism has 29 species and 73 reactions. For more information regarding the selection of chemical mechanism see Section 4.3. This appendix lists the output from CHEMKIN which describes the mechanism.

CHEMKIN INTERPRETER OUTPUT: CHEMKIN-II Version 3.9 Aug. 1994
DOUBLE PRECISION

		ELEMENTS CONSIDERED		ATOMIC WEIGHT							
		1. C		12.0112							
		2. H		1.00797							
		3. O		15.9994							
		4. S		32.0640							
		5. N		14.0067							
		6. AR		39.9480							

		C									
		P H									
		H A									
		A R									
SPECIES		S G		MOLECULAR		TEMPERATURE		ELEMENT COUNT			
CONSIDERED		E E		WEIGHT		LOW HIGH		C H O S N AR			

1. CO		G	0	28.01055	300	5000	1	0	1	0	0
2. CO2		G	0	44.00995	300	5000	1	0	2	0	0
3. O2		G	0	31.99880	300	5000	0	0	2	0	0
4. H2O		G	0	18.01534	300	5000	0	2	1	0	0
5. H		G	0	1.00797	300	5000	0	1	0	0	0
6. O		G	0	15.99940	300	5000	0	0	1	0	0
7. OH		G	0	17.00737	300	5000	0	1	1	0	0
8. HO2		G	0	33.00677	200	3500	0	1	2	0	0
9. H2O2		G	0	34.01474	300	5000	0	2	2	0	0
10. NO		G	0	30.00610	300	5000	0	0	1	0	1
11. NO2		G	0	46.00550	300	5000	0	0	2	0	1
12. NO3		G	0	62.00490	300	5000	0	0	3	0	1
13. HNO		G	0	31.01407	300	5000	0	1	1	0	1
14. HONO		G	0	47.01347	300	5000	0	1	2	0	1
15. HNO3		G	0	63.01287	300	5000	0	1	3	0	1
16. SO2		G	0	64.06280	300	5000	0	0	2	1	0
17. SO3		G	0	80.06220	300	5000	0	0	3	1	0
18. HOSO		G	0	65.07077	300	5000	0	1	2	1	0

19. HOSO2	G	0	81.07017	300	5000	0	1	3	1	0	0
20. HSO2	G	0	65.07077	300	5000	0	1	2	1	0	0
21. SO	G	0	48.06340	300	5000	0	0	1	1	0	0
22. HCO	G	0	29.01852	300	5000	1	1	1	0	0	0
23. H2	G	0	2.01594	300	5000	0	2	0	0	0	0
24. N2	G	0	28.01340	300	5000	0	0	0	0	2	0
25. AR	G	0	39.94800	300	5000	0	0	0	0	0	1
26. C(S)	S	0	12.01115	300	5000	1	0	0	0	0	0
27. N	G	0	14.00670	200	6000	0	0	0	0	1	0
28. H2SO4	G	0	98.07754	300	5000	0	2	4	1	0	0
29. S	G	0	32.06400	300	5000	0	0	0	1	0	0

REACTIONS CONSIDERED				(k = A T**b exp(-E/RT))		
				A	b	E
1. H2+M=H+H+M				4.57E+19	-1.4	104400.0
H2	Enhanced by	2.500E+00				
H2O	Enhanced by	1.200E+01				
CO	Enhanced by	1.900E+00				
CO2	Enhanced by	3.800E+00				
AR	Enhanced by	7.500E-01				
2. O+H2=H+OH				5.08E+04	2.7	6290.0
3. O+O+M=O2+M				6.16E+15	-0.5	0.0
H2	Enhanced by	2.500E+00				
H2O	Enhanced by	1.200E+01				
CO	Enhanced by	1.900E+00				
CO2	Enhanced by	3.800E+00				
AR	Enhanced by	7.500E-01				
4. H+O2=O+OH				1.91E+14	0.0	16440.0
5. H+O2(+M)=HO2(+M)				1.48E+12	0.6	0.0
Low pressure limit:	0.34820E+17	-0.41100E+00		-0.11150E+04		
TROE centering:	0.50000E+00	0.10000E-29		0.10000E+31		
H2	Enhanced by	2.500E+00				
H2O	Enhanced by	1.200E+01				
CO	Enhanced by	1.900E+00				
CO2	Enhanced by	3.800E+00				
AR	Enhanced by	7.500E-01				
6. H+O+M=OH+M				4.71E+18	-1.0	0.0
H2	Enhanced by	2.500E+00				
H2O	Enhanced by	1.200E+01				
CO	Enhanced by	1.900E+00				
CO2	Enhanced by	3.800E+00				
AR	Enhanced by	7.500E-01				
7. OH+H2=H2O+H				2.16E+08	1.5	3430.0
8. H2O+O=OH+OH				2.97E+06	2.0	13400.0
9. H2O2(+M)=OH+OH(+M)				2.95E+14	0.0	48430.0
Low pressure limit:	0.12000E+18	0.00000E+00		0.45500E+05		
TROE centering:	0.50000E+00	0.10000E-89		0.10000E+91		
H2	Enhanced by	2.500E+00				
H2O	Enhanced by	1.200E+01				
CO	Enhanced by	1.900E+00				
CO2	Enhanced by	3.800E+00				
AR	Enhanced by	7.500E-01				
10. OH+H+M=H2O+M				2.21E+22	-2.0	0.0
H2	Enhanced by	2.500E+00				
H2O	Enhanced by	1.200E+01				
CO	Enhanced by	1.900E+00				
CO2	Enhanced by	3.800E+00				
AR	Enhanced by	7.500E-01				
11. HO2+O=O2+OH				3.25E+13	0.0	0.0
12. HO2+H=H2+O2				1.66E+13	0.0	823.0
13. HO2+H=OH+OH				7.08E+13	0.0	295.0
14. HO2+OH=H2O+O2				2.89E+13	0.0	-497.0
15. HO2+HO2=H2O2+O2				4.20E+14	0.0	11982.0
Declared duplicate reaction...				-		

16.	HO2+HO2=H2O2+O2		1.30E+11	0.0	-1629.0
	Declared duplicate reaction...				
17.	H2O2+O=OH+HO2		9.55E+06	2.0	3970.0
18.	H2O2+H=H2O+OH		2.41E+13	0.0	3970.0
19.	H2O2+H=HO2+H2		4.82E+13	0.0	7950.0
20.	H2O2+OH=H2O+HO2		1.00E+12	0.0	0.0
	Declared duplicate reaction...				
21.	H2O2+OH=H2O+HO2		5.80E+14	0.0	9557.0
	Declared duplicate reaction...				
22.	HNO+H=NO+H2		4.40E+11	0.7	650.0
23.	NO+O(+M)=NO2(+M)		1.30E+15	-0.8	0.0
	Low pressure limit:	0.47200E+25 -0.28700E+01	0.15510E+04		
	TROE centering:	0.95700E+00 0.10000E-89	0.83320E+04		
	AR	Enhanced by 7.500E-01			
24.	NO+H(+M)=HNO(+M)		1.52E+15	-0.4	0.0
	Low pressure limit:	0.31000E+20 -0.13200E+01	0.73520E+03		
	TROE centering:	0.82000E+00 0.10000E-89	0.10000E+91		
	AR	Enhanced by 7.500E-01			
25.	NO+OH(+M)=HONO(+M)		1.99E+12	-0.1	-721.0
	Low pressure limit:	0.50800E+24 -0.25100E+01	-0.67600E+02		
	TROE centering:	0.62000E+00 0.10000E-89	0.10000E+91		
	AR	Enhanced by 7.500E-01			
26.	NO2+H2=HONO+H		7.33E+11	0.0	28810.0
27.	NO2+O=O2+NO		1.05E+14	-0.5	0.0
28.	NO2+O(+M)=NO3(+M)		1.33E+13	0.0	0.0
	Low pressure limit:	0.14900E+29 -0.40800E+01	0.24670E+04		
	TROE centering:	0.82600E+00 0.10000E-89	0.31910E+04		
	AR	Enhanced by 7.500E-01			
29.	NO2+H=NO+OH		1.32E+14	0.0	362.0
30.	NO2+OH(+M)=HNO3(+M)		2.41E+13	0.0	0.0
	Low pressure limit:	0.64200E+33 -0.54900E+01	0.23500E+04		
	TROE centering:	0.83700E+00 0.10000E-89	0.16570E+04		
	AR	Enhanced by 7.500E-01			
31.	HO2+NO=NO2+OH		2.11E+12	0.0	-479.0
32.	NO2+NO2=NO3+NO		9.64E+09	0.7	20920.0
33.	NO2+NO2=2NO+O2		1.63E+12	0.0	26120.0
34.	HNO+O=OH+NO		1.81E+13	0.0	0.0
35.	HNO+OH=H2O+NO		1.30E+07	1.9	-956.0
36.	HNO+NO2=HONO+NO		6.02E+11	0.0	1987.0
37.	HONO+O=OH+NO2		1.20E+13	0.0	5961.0
38.	HONO+OH=H2O+NO2		1.70E+12	0.0	-520.0
39.	HCO+M=H+CO+M		1.86E+17	-1.0	17000.0
	H2	Enhanced by 2.500E+00			
	H2O	Enhanced by 1.200E+01			
	CO	Enhanced by 1.900E+00			
	CO2	Enhanced by 3.800E+00			
40.	HCO+O2=CO+HO2		7.58E+12	0.0	410.0
41.	HCO+O=CO+OH		3.02E+13	0.0	0.0
42.	HCO+H=CO+H2		7.23E+13	0.0	0.0
43.	HCO+OH=CO+H2O		3.02E+13	0.0	0.0
44.	CO+O(+M)=CO2(+M)		1.80E+10	0.0	2384.0
	Low pressure limit:	0.13500E+25 -0.27880E+01	0.41910E+04		
	H2	Enhanced by 2.500E+00			
	H2O	Enhanced by 1.200E+01			
	CO	Enhanced by 1.900E+00			
	CO2	Enhanced by 3.800E+00			
45.	CO+O2=CO2+O		2.53E+12	0.0	47700.0
46.	CO+OH=CO2+H		1.40E+05	1.9	-1347.0
47.	CO+HO2=CO2+OH		3.01E+13	0.0	23000.0
48.	NO+HCO=HNO+CO		7.23E+12	0.0	0.0
49.	NO2+HCO=CO+HONO		1.26E+23	-3.3	2354.0
50.	NO2+HCO=H+CO2+NO		8.43E+15	-0.8	1927.0
51.	NO2+CO=CO2+NO		9.03E+13	0.0	33780.0
52.	SO3+O=SO2+O2		4.40E+11	0.0	6100.0
53.	SO3+SO=SO2+SO2		1.00E+12	0.0	4000.0
54.	SO2+O(+M)=SO3(+M)		9.20E+10	0.0	2384.0
	Low pressure limit:	0.40000E+29 -0.40000E+01	0.52500E+04		
	N2	Enhanced by 1.300E+00			

	H2O	Enhanced by	1.000E+01			
55.	SO2+OH(+M)=HOSO2(+M)			1.21E+12	0.0	0.0
	Low pressure limit:	0.18700E+32	-0.46100E+01	0.20500E+04		
	TROE centering:	0.35000E+00	0.10000E-29	0.10000E+31		
	H2O	Enhanced by	1.000E+01			
56.	SO2+OH=SO3+H			4.90E+01	2.7	23800.0
57.	SO+O(+M)=SO2(+M)			3.20E+13	0.0	0.0
	Low pressure limit:	0.29000E+25	-0.29000E+01	0.00000E+00		
	TROE centering:	0.55000E+00	0.10000E-29	0.10000E+31		
	N2	Enhanced by	1.500E+00			
	H2O	Enhanced by	1.000E+01			
58.	SO+OH=SO2+H			5.20E+13	0.0	0.0
59.	SO+OH+M=HOSO+M			8.00E+21	-2.2	830.0
60.	SO+O2=SO2+O			6.20E+03	2.4	3050.0
61.	HOSO+M=SO2+H+M			5.90E+34	-5.7	50900.0
62.	HOSO+OH=SO2+H2O			1.00E+12	0.0	0.0
63.	HOSO+O2=SO2+HO2			1.00E+12	0.0	1000.0
64.	HSO2+M=SO2+H+M			1.20E+28	-4.1	18900.0
65.	HSO2+M=HOSO+M			1.10E+21	-2.0	29900.0
66.	HOSO2=HOSO+O			5.40E+18	-2.3	106300.0
67.	HOSO2+M=SO3+H+M			3.20E+16	-0.8	53700.0
68.	HOSO2+H=SO2+H2O			1.00E+12	0.0	0.0
69.	HOSO2+O=SO3+OH			5.00E+12	0.0	0.0
70.	HOSO2+OH=SO3+H2O			1.00E+12	0.0	0.0
71.	HOSO2+O2=SO3+HO2			7.80E+11	0.0	656.0
72.	SO2+NO2=SO3+NO			6.30E+12	0.0	27000.0
73.	SO3+H2O=H2SO4			7.23E+08	0.0	0.0

NOTE: A units mole-cm-sec-K, E units cal/mole

NO ERRORS FOUND ON INPUT...CHEMKIN LINKING FILE WRITTEN.

WORKING SPACE REQUIREMENTS ARE

INTEGER:	1569
REAL:	1675
CHARACTER:	35

APPENDIX C

HPT1 VELOCITY TRIANGLE ANALYSIS

Due to the limited data available for the NASA/DERA engine, a velocity triangle analysis was used to obtain the intra-stage data needed for the HPT1 high fidelity modeling. This type of analysis is common in turbomachinery textbooks, and further details can be found in [7], [36], or [37]. This appendix presents the specific procedure along with some example results for the velocity triangle analysis referred to in Section 0:

The axial stations of interest were labeled as follows:

Station A: Combustor exit (8) (numbers refer to DERA data designation)

Station B: HPT1 rotor inlet (9)

Station C: HPT1 rotor exit

Station "Overall HPT exit": HPT2 rotor exit (11)

The subscripts a, b, and c are used to designate these stations in this analysis, as well as, Figure C. and Table C.. The annulus area was calculated at each station. The properties of air $R=288.7 \text{ J/kgK}$ and $\gamma=1.34$ were assumed to be constant over the temperature range of interest, 800-1,300K.

The fluid density was calculated using the ideal gas law and the relationship between total and static pressure/temperature by using an initial guess for the Mach number as follows:

$$P_a = \frac{P_{Ta}}{\left(1 + \frac{\gamma-1}{2} M_a^2\right)^{\frac{\gamma}{\gamma-1}}} \quad (\text{C.1})$$

$$T_a = \frac{T_{Ta}}{\left(1 + \frac{\gamma-1}{2} M_a^2\right)} \quad (\text{C.2})$$

$$\rho_a = \frac{P_a}{RT_a} \quad (\text{C.3})$$

Then, the axial velocity and Mach number were calculated as follows:

$$u_{xa} = \frac{\dot{m}_a}{\rho_a A_a} \quad (C.4)$$

$$M_a = \frac{u_{xa}}{\sqrt{\gamma \cdot R \cdot T_a}} \quad (C.5)$$

An iteration was performed using equations (C.1) to (C.5) until the Mach number was consistent. The combustor exit flow was assumed to enter the NGV with zero incidence angle, thus:

$$V_a = u_{xa} \quad (C.6)$$

A similar iterative procedure was used to compute u_{xb} . However, since the total temperature and pressure were not explicitly given within the stages, negligible total pressure loss was assumed to occur through the HPT1 NGV and thus, the “Overall HPT exit” values (which were similar to the combustor exit) were used for this intra-stage station. Also, the Mach number was computed using the absolute velocity, V_b . The flow was initially assumed to have zero deviation, thus the blade metal angle at the trailing edge, β_b , and u_{xb} were used to compute V_b as follows:

$$V_b = \frac{u_{xb}}{\cos(\beta_b)} \quad (C.7)$$

$$M_b = \frac{V_b}{\sqrt{\gamma \cdot R \cdot T_b}} \quad (C.8)$$

Vector addition was used to subtract the tangential velocity of the rotor, ωr , from V_b to get the velocity, V_b' , and inlet angle, β_b' , relative to the rotor reference frame as follows:

$$v_b = \sqrt{V_b^2 - u_{xb}^2} \quad (C.9)$$

$$v_b' = v_b - \omega \cdot r \quad (C.10)$$

$$V_b' = \sqrt{u_{xb}^2 + v_b'^2} \quad (C.11)$$

$$\beta_b' = \tan^{-1} \left(\frac{v_b'}{u_{xb}} \right) \quad (C.12)$$

Again, since the HPT1 rotor exit condition was not given explicitly the turbine was assumed to have a 50% reaction, thus the work per stage was assumed to be equal. A power balance using Station A and the “Overall HPT exit” values was done assuming a polytropic efficiency of 0.90 to obtain the total temperature and pressure at station C, T_{Tc} and P_{Tc} respectively. An iteration was performed to obtain T_{Tc} and the turbine temperature and pressure ratios were computed to obtain P_{Tc} as follows:

$$\dot{m}_1 c_p (T_{Tc} - T_{Ta}) = \dot{m}_2 c_p (T_{T2} - T_{Tc}) \quad \Rightarrow \quad T_{Tc} \quad (C.13)$$

$$\tau_{t1} = \frac{T_{Tc}}{T_{Ta}} \quad (C.14)$$

$$\pi_{t1} = \frac{P_{Tc}}{P_{Ta}} = \tau_{t1}^{\left(\frac{\gamma-1}{\gamma \cdot \eta_{poly}} \right)} \quad (C.15)$$

$$P_{Tc} = \pi_{t1} \cdot P_{Ta} \quad (C.16)$$

Finally, an iterative procedure over equations (C.5) to (C.12) was used to compute the velocity vectors at the HPT1 rotor exit. Again a zero deviation was assumed ($\beta_c' =$ rotor blade metal angle at the trailing edge) and the Mach number was computed using the absolute velocity, V_c' , as follows:

$$V_c' = \frac{u_{xc}}{\cos(\beta_c')} \quad (C.17)$$

$$v_c' = \sqrt{V_c'^2 - u_{xc}^2} \quad (C.18)$$

$$v_c = v_c' - \omega \cdot r \quad (C.19)$$

$$V_c = \sqrt{u_{xc}^2 + v_c^2} \quad (C.20)$$

$$\beta_c = \tan^{-1} \left(\frac{v_c}{u_{xc}} \right) \quad (C.21)$$

$$M_c = \frac{u_{xc}}{\sqrt{\gamma \cdot R \cdot T_c}} \quad (C.22)$$

The results of this analysis were reasonable since the fluid flow angle at the exit of the stage is nearly axial as is typical in the design of a turbine stage, $\beta_c = 3.7^\circ$. However, the incidence angle to the rotor, although reasonable, was fairly large $\beta_b' = 37.1^\circ$. Therefore, a deviation of the flow from the blade metal angles was

assumed. The deviation was initially set at 2° for both blades. This lowered the rotor incidence angle to -2.2° and changed the rotor exit angle to 28.7° . As an example, the resultant velocity triangles and underlying data from this analysis for the maximum power condition with 2° assumed deviation are given in Figure C. and Table C..

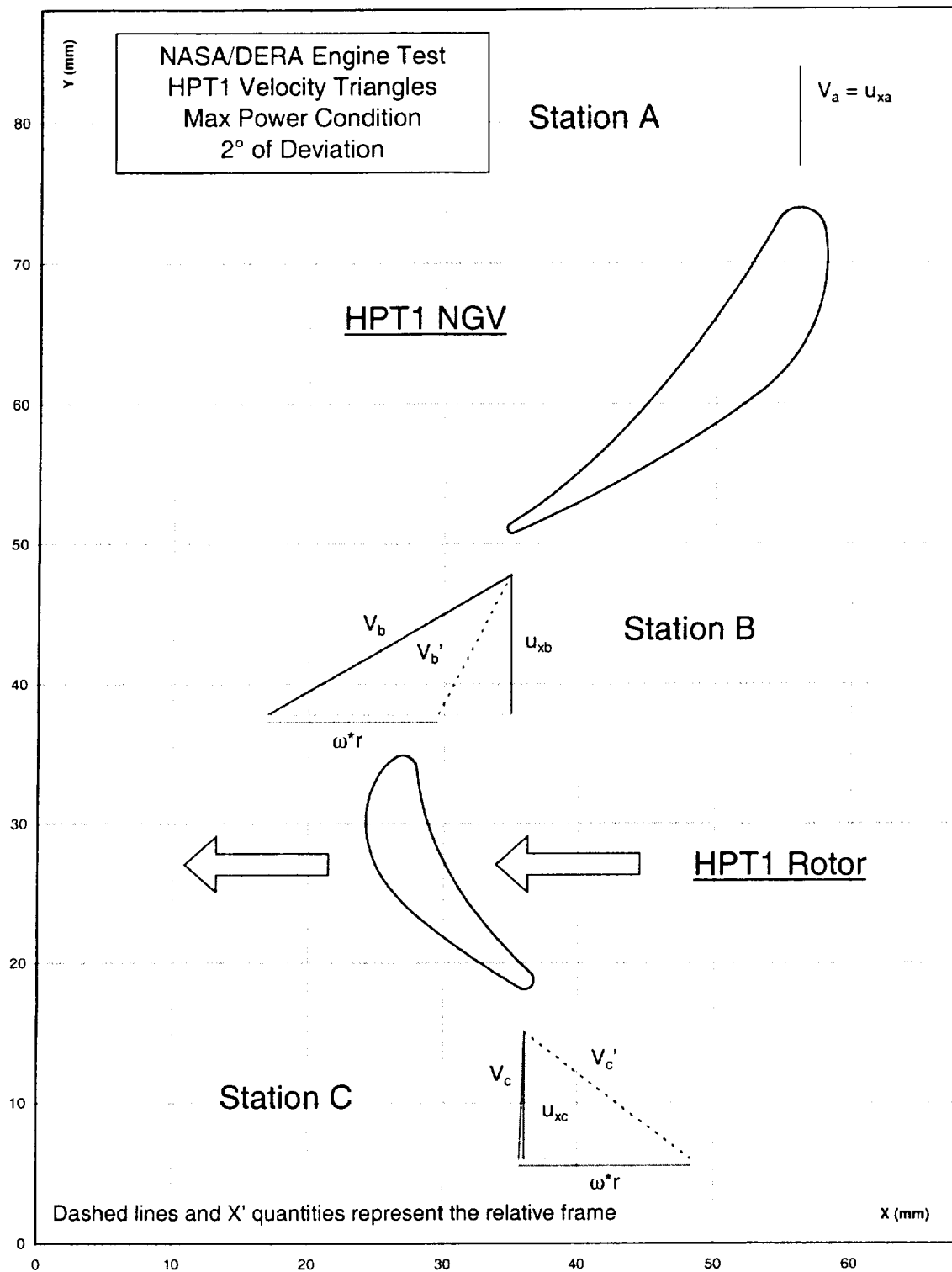


Figure C.1 Velocity triangle diagram for maximum power condition with 2° deviation

Station A Combustor exit condition (8)	Station B HT1 rotor inlet (10)	Station C HPT1 rotor exit	Station overall HPT exit HPT2 rotor exit (11)																																																						
<table> <tr><td>R =</td><td>270.38 mm</td></tr> <tr><td>Nblades =</td><td>60</td></tr> <tr><td>t =</td><td>0 mm</td></tr> <tr><td>Do =</td><td>22.86 in</td></tr> <tr><td>Di =</td><td>19.1 in</td></tr> <tr><td>delta D =</td><td>3.76 in</td></tr> <tr><td>A =</td><td>123.9119541 m² 0.079943036 m²</td></tr> </table>	R =	270.38 mm	Nblades =	60	t =	0 mm	Do =	22.86 in	Di =	19.1 in	delta D =	3.76 in	A =	123.9119541 m ² 0.079943036 m ²	<table> <tr><td>Nblades =</td><td>100</td></tr> <tr><td>t =</td><td>0 mm</td></tr> <tr><td>Do =</td><td>22.7 in</td></tr> <tr><td>Di =</td><td>19.74 in</td></tr> <tr><td>delta D =</td><td>2.96 in</td></tr> <tr><td>A =</td><td>98.66360224 m² 0.06365381 m²</td></tr> <tr><td>A ave =</td><td>0.06740622 m²</td></tr> </table>	Nblades =	100	t =	0 mm	Do =	22.7 in	Di =	19.74 in	delta D =	2.96 in	A =	98.66360224 m ² 0.06365381 m ²	A ave =	0.06740622 m ²	<table> <tr><td>t =</td><td>0 mm</td></tr> <tr><td>Do =</td><td>23.52136781 in</td></tr> <tr><td>Di =</td><td>19.25826812 in</td></tr> <tr><td>delta D =</td><td>4.263099693 in</td></tr> <tr><td>A =</td><td>143.236069 m² 0.092410195 m²</td></tr> </table>	t =	0 mm	Do =	23.52136781 in	Di =	19.25826812 in	delta D =	4.263099693 in	A =	143.236069 m ² 0.092410195 m ²																	
R =	270.38 mm																																																								
Nblades =	60																																																								
t =	0 mm																																																								
Do =	22.86 in																																																								
Di =	19.1 in																																																								
delta D =	3.76 in																																																								
A =	123.9119541 m ² 0.079943036 m ²																																																								
Nblades =	100																																																								
t =	0 mm																																																								
Do =	22.7 in																																																								
Di =	19.74 in																																																								
delta D =	2.96 in																																																								
A =	98.66360224 m ² 0.06365381 m ²																																																								
A ave =	0.06740622 m ²																																																								
t =	0 mm																																																								
Do =	23.52136781 in																																																								
Di =	19.25826812 in																																																								
delta D =	4.263099693 in																																																								
A =	143.236069 m ² 0.092410195 m ²																																																								
<table> <tr><td>Ma =</td><td>0.192940639</td></tr> <tr><td>T =</td><td>1.34</td></tr> <tr><td>Pt =</td><td>1.634.150.0 Pa</td></tr> <tr><td>Tt =</td><td>1.365.2 K</td></tr> <tr><td>Pa =</td><td>1.594.021.3 Pa</td></tr> <tr><td>Ta =</td><td>1.356.6 K</td></tr> <tr><td>R =</td><td>288.7 J/kg.K</td></tr> <tr><td>ρ =</td><td>4.070 kg/m³</td></tr> </table>	Ma =	0.192940639	T =	1.34	Pt =	1.634.150.0 Pa	Tt =	1.365.2 K	Pa =	1.594.021.3 Pa	Ta =	1.356.6 K	R =	288.7 J/kg.K	ρ =	4.070 kg/m ³	<table> <tr><td>Mb =</td><td>0.592963798</td></tr> <tr><td>Ptb =</td><td>1.634.150.0 Pa</td></tr> <tr><td>Ttb =</td><td>1.325.2 K</td></tr> <tr><td>Pb =</td><td>1.299.940.8 Pa</td></tr> <tr><td>Tb =</td><td>1.250.4 K</td></tr> <tr><td>ρb =</td><td>3.601 kg/m³</td></tr> </table>	Mb =	0.592963798	Ptb =	1.634.150.0 Pa	Ttb =	1.325.2 K	Pb =	1.299.940.8 Pa	Tb =	1.250.4 K	ρb =	3.601 kg/m ³	<table> <tr><td>Mc =</td><td>0.270039799</td></tr> <tr><td>Ptc =</td><td>1.034.667.2 Pa</td></tr> <tr><td>Ttc =</td><td>1.200.2 K</td></tr> <tr><td>Pc =</td><td>985.627.1 Pa</td></tr> <tr><td>Tc =</td><td>1.185.5 K</td></tr> <tr><td>ρc =</td><td>2.880 kg/m³</td></tr> </table>	Mc =	0.270039799	Ptc =	1.034.667.2 Pa	Ttc =	1.200.2 K	Pc =	985.627.1 Pa	Tc =	1.185.5 K	ρc =	2.880 kg/m ³	<table> <tr><td>Stage 2</td><td></td></tr> <tr><td>Pt2 =</td><td>498.714.0 Pa</td></tr> <tr><td>Tt2 =</td><td>1.045.6 K</td></tr> <tr><td>m dot =</td><td>46.6346 kg/s</td></tr> <tr><td>cp =</td><td>1137.741 J/kg.K</td></tr> <tr><td>Δt2 =</td><td>154.3 K</td></tr> <tr><td>W2 =</td><td>8540226 W</td></tr> </table>	Stage 2		Pt2 =	498.714.0 Pa	Tt2 =	1.045.6 K	m dot =	46.6346 kg/s	cp =	1137.741 J/kg.K	Δt2 =	154.3 K	W2 =	8540226 W
Ma =	0.192940639																																																								
T =	1.34																																																								
Pt =	1.634.150.0 Pa																																																								
Tt =	1.365.2 K																																																								
Pa =	1.594.021.3 Pa																																																								
Ta =	1.356.6 K																																																								
R =	288.7 J/kg.K																																																								
ρ =	4.070 kg/m ³																																																								
Mb =	0.592963798																																																								
Ptb =	1.634.150.0 Pa																																																								
Ttb =	1.325.2 K																																																								
Pb =	1.299.940.8 Pa																																																								
Tb =	1.250.4 K																																																								
ρb =	3.601 kg/m ³																																																								
Mc =	0.270039799																																																								
Ptc =	1.034.667.2 Pa																																																								
Ttc =	1.200.2 K																																																								
Pc =	985.627.1 Pa																																																								
Tc =	1.185.5 K																																																								
ρc =	2.880 kg/m ³																																																								
Stage 2																																																									
Pt2 =	498.714.0 Pa																																																								
Tt2 =	1.045.6 K																																																								
m dot =	46.6346 kg/s																																																								
cp =	1137.741 J/kg.K																																																								
Δt2 =	154.3 K																																																								
W2 =	8540226 W																																																								
<table> <tr><td>m dot =</td><td>45.479 kg/s</td></tr> <tr><td>uxa =</td><td>139.77 m/s</td></tr> </table>	m dot =	45.479 kg/s	uxa =	139.77 m/s	<table> <tr><td>m dot =</td><td>46.6346 kg/s</td></tr> <tr><td>uxb =</td><td>200.35 m/s</td></tr> </table>	m dot =	46.6346 kg/s	uxb =	200.35 m/s	<table> <tr><td>m dot =</td><td>46.6346 kg/s</td></tr> <tr><td>uxc =</td><td>182.74 m/s</td></tr> </table>	m dot =	46.6346 kg/s	uxc =	182.74 m/s	<table> <tr><td>Stage 1</td><td></td></tr> <tr><td>m dot =</td><td>45.479 kg/s</td></tr> <tr><td>cp =</td><td>1137.741 J/kg.K</td></tr> <tr><td>Δt1 =</td><td>165.0 K</td></tr> <tr><td>W1 =</td><td>8540226 W</td></tr> </table>	Stage 1		m dot =	45.479 kg/s	cp =	1137.741 J/kg.K	Δt1 =	165.0 K	W1 =	8540226 W																																
m dot =	45.479 kg/s																																																								
uxa =	139.77 m/s																																																								
m dot =	46.6346 kg/s																																																								
uxb =	200.35 m/s																																																								
m dot =	46.6346 kg/s																																																								
uxc =	182.74 m/s																																																								
Stage 1																																																									
m dot =	45.479 kg/s																																																								
cp =	1137.741 J/kg.K																																																								
Δt1 =	165.0 K																																																								
W1 =	8540226 W																																																								
<table> <tr><td>βa =</td><td>0 deg</td></tr> </table>	βa =	0 deg	<table> <tr><td>Exit Slope Ave =</td><td>-1.957070591</td></tr> <tr><td>βb =</td><td>82.93443178 deg</td></tr> <tr><td>c =</td><td>31.44 mm</td></tr> <tr><td>σ =</td><td>1.110399751</td></tr> <tr><td>Δt =</td><td>2 deg</td></tr> <tr><td>βb - Δt =</td><td>60.93443178 deg</td></tr> <tr><td>ω =</td><td>828.215 rad/s</td></tr> </table>	Exit Slope Ave =	-1.957070591	βb =	82.93443178 deg	c =	31.44 mm	σ =	1.110399751	Δt =	2 deg	βb - Δt =	60.93443178 deg	ω =	828.215 rad/s	<table> <tr><td>Exit Slope Ave =</td><td>1.437840026</td></tr> <tr><td>βc =</td><td>55.17812707 deg</td></tr> <tr><td>c =</td><td>19.18 mm</td></tr> <tr><td>σ =</td><td>1.129000595</td></tr> <tr><td>Δt =</td><td>2 deg</td></tr> <tr><td>βb - Δt =</td><td>53.17812707 deg</td></tr> </table>	Exit Slope Ave =	1.437840026	βc =	55.17812707 deg	c =	19.18 mm	σ =	1.129000595	Δt =	2 deg	βb - Δt =	53.17812707 deg	<table> <tr><td>delta(W) =</td><td>0 W</td></tr> </table>	delta(W) =	0 W																								
βa =	0 deg																																																								
Exit Slope Ave =	-1.957070591																																																								
βb =	82.93443178 deg																																																								
c =	31.44 mm																																																								
σ =	1.110399751																																																								
Δt =	2 deg																																																								
βb - Δt =	60.93443178 deg																																																								
ω =	828.215 rad/s																																																								
Exit Slope Ave =	1.437840026																																																								
βc =	55.17812707 deg																																																								
c =	19.18 mm																																																								
σ =	1.129000595																																																								
Δt =	2 deg																																																								
βb - Δt =	53.17812707 deg																																																								
delta(W) =	0 W																																																								
<table> <tr><td>Tt (HPCe) =</td><td>696.856 K</td></tr> <tr><td>T (HPCe) =</td><td>694.463 K</td></tr> <tr><td>T met ngv =</td><td>696.997 K</td></tr> <tr><td>T met rot =</td><td>696.207 K</td></tr> </table>	Tt (HPCe) =	696.856 K	T (HPCe) =	694.463 K	T met ngv =	696.997 K	T met rot =	696.207 K	<table> <tr><td>Vb =</td><td>412.40 m/s</td></tr> <tr><td>vb =</td><td>380.48 m/s</td></tr> <tr><td>Mb =</td><td>0.592963795</td></tr> <tr><td>delta Mb =</td><td>0.00000000</td></tr> </table>	Vb =	412.40 m/s	vb =	380.48 m/s	Mb =	0.592963795	delta Mb =	0.00000000	<table> <tr><td>Vc =</td><td>304.90 m/s</td></tr> <tr><td>vc =</td><td>244.08 m/s</td></tr> </table>	Vc =	304.90 m/s	vc =	244.08 m/s	<table> <tr><td>η poly =</td><td>0.9</td></tr> <tr><td>τ t1 =</td><td>0.879105</td></tr> <tr><td>κ t1 =</td><td>0.633153</td></tr> </table>	η poly =	0.9	τ t1 =	0.879105	κ t1 =	0.633153																												
Tt (HPCe) =	696.856 K																																																								
T (HPCe) =	694.463 K																																																								
T met ngv =	696.997 K																																																								
T met rot =	696.207 K																																																								
Vb =	412.40 m/s																																																								
vb =	380.48 m/s																																																								
Mb =	0.592963795																																																								
delta Mb =	0.00000000																																																								
Vc =	304.90 m/s																																																								
vc =	244.08 m/s																																																								
η poly =	0.9																																																								
τ t1 =	0.879105																																																								
κ t1 =	0.633153																																																								
<table> <tr><td>Ma =</td><td>0.192941463</td></tr> <tr><td>delta Ma =</td><td>-0.00000067</td></tr> <tr><td>Va =</td><td>139.77 m/s</td></tr> </table>	Ma =	0.192941463	delta Ma =	-0.00000067	Va =	139.77 m/s	<table> <tr><td>ω'r =</td><td>250.97 m/s</td></tr> <tr><td>vb =</td><td>109.48 m/s</td></tr> <tr><td>Vb =</td><td>228.31 m/s</td></tr> </table>	ω'r =	250.97 m/s	vb =	109.48 m/s	Vb =	228.31 m/s	<table> <tr><td>vc =</td><td>4.89 m/s</td></tr> <tr><td>Vc =</td><td>182.87 m/s</td></tr> <tr><td>Mc =</td><td>0.270039781</td></tr> <tr><td>delta Mc =</td><td>-0.00000001</td></tr> </table>	vc =	4.89 m/s	Vc =	182.87 m/s	Mc =	0.270039781	delta Mc =	-0.00000001																																			
Ma =	0.192941463																																																								
delta Ma =	-0.00000067																																																								
Va =	139.77 m/s																																																								
ω'r =	250.97 m/s																																																								
vb =	109.48 m/s																																																								
Vb =	228.31 m/s																																																								
vc =	4.89 m/s																																																								
Vc =	182.87 m/s																																																								
Mc =	0.270039781																																																								
delta Mc =	-0.00000001																																																								
<table> <tr><td>Inputs</td><td></td></tr> <tr><td>Iterate</td><td></td></tr> <tr><td>Output</td><td></td></tr> <tr><td>Solution converged</td><td></td></tr> </table>	Inputs		Iterate		Output		Solution converged		<table> <tr><td>βb =</td><td>28.88 deg</td></tr> </table>	βb =	28.88 deg	<table> <tr><td>βc =</td><td>-2.18 deg</td></tr> </table>	βc =	-2.18 deg																																											
Inputs																																																									
Iterate																																																									
Output																																																									
Solution converged																																																									
βb =	28.88 deg																																																								
βc =	-2.18 deg																																																								

Table C.1 Data for the maximum power 2° deviation velocity triangle diagram of Figure C.

In an attempt to obtain a more accurate estimate of the deviation an empirical correlation, Carter's Rule, was employed as follows [36]:

$$\phi = \beta_1 + \beta_2 \quad (C.23)$$

$$\sigma = \frac{c}{s} \quad (C.24)$$

$$\delta_i = \frac{\phi}{8 \cdot \sqrt{\sigma}} \quad (C.25)$$

This resulted in a deviation of 7.5° and 7.3° for the NGV and rotor, respectively. Using these deviation values, the rotor incidence angle was 7.0° and the rotor exit angle was -14.8°.

Another possibility to increase the accuracy of the velocity triangle analysis was investigated. A total pressure loss coefficient ("profile loss") at Station B was attempted rather than assuming a negligible total pressure loss across the NGV. However, using empirical cascade correlations for a stator which are a function of the solidity

($\sigma = c_{axial}/s$) the pressure loss coefficient was found to be $w = 0.03$ and the effect on the result for P_{Tb} and β_b was found to be less than 2% [36].

Overall, the velocity triangle analysis provided reasonable fluid property data for the high fidelity modeling. Including the profile loss had a negligible effect on the results and thus it was ignored to keep the analysis simple. Also, it is difficult to justify a particular deviation angle. The NASA/DERA engine test simulations used a deviation angle of 2° since it was thought to be a conservative approach and gave a nearly axial exit flow angle. As another point of reference, the HPT2 NGV has a chord angle of 41° versus 45° for the HPT1 NGV. This would imply that the blades are both roughly designed to have a zero inlet swirl, supporting the notion that the exit flow angle be nearly axial.

APPENDIX D

DETAILED RESULTS FROM NASA/DERA ENGINE SIMULATION OF MAX POWER CASE

This appendix contains a complete set of calculation results for the max power condition. From the high fidelity modeling effort the following items are given in order for the mixed-out case, first for the NGV and then for the rotor:

- Fluid and chemistry convergence history
- Range and mass averaged quantities of fluid and chemistry variables at exit plane
- Total temperature and total pressure contours
- Mass fraction contours of trace species

Then, for the high fidelity rotor wake model case:

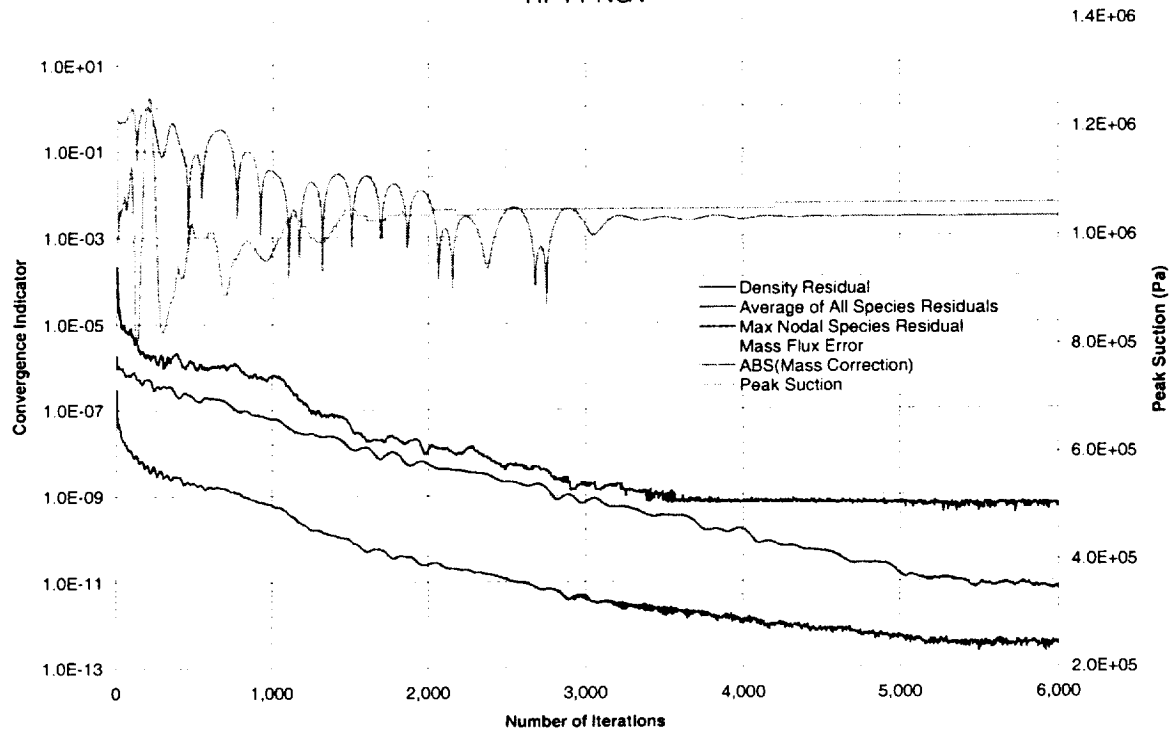
- Time series of SO_3 mass fraction for one blade passing cycle (see Appendix D for an animation)

And finally, from the low fidelity modeling effort the following items are given:

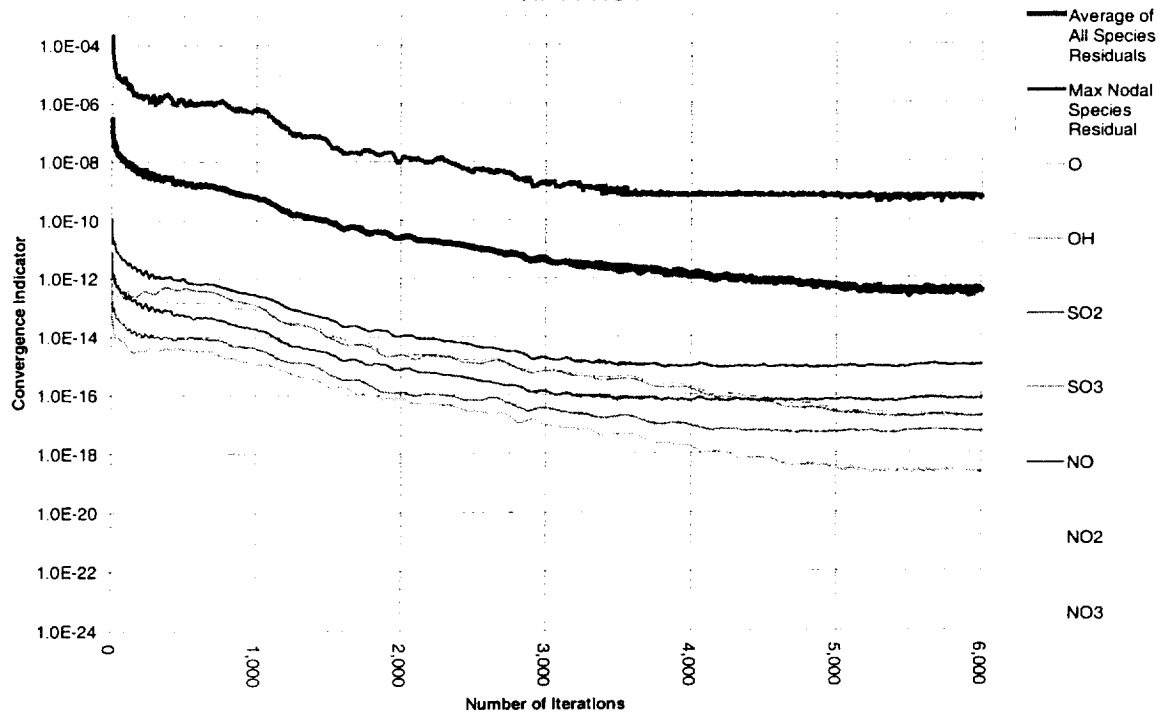
- SO_x species evolution
- NO_y species evolution
- CO, OH, and O species evolution

The CNEWT and CALCHEM input file used to obtain these results are given in Appendix E.

Convergence Indicator vs. Number of Iterations
HPT1 NGV



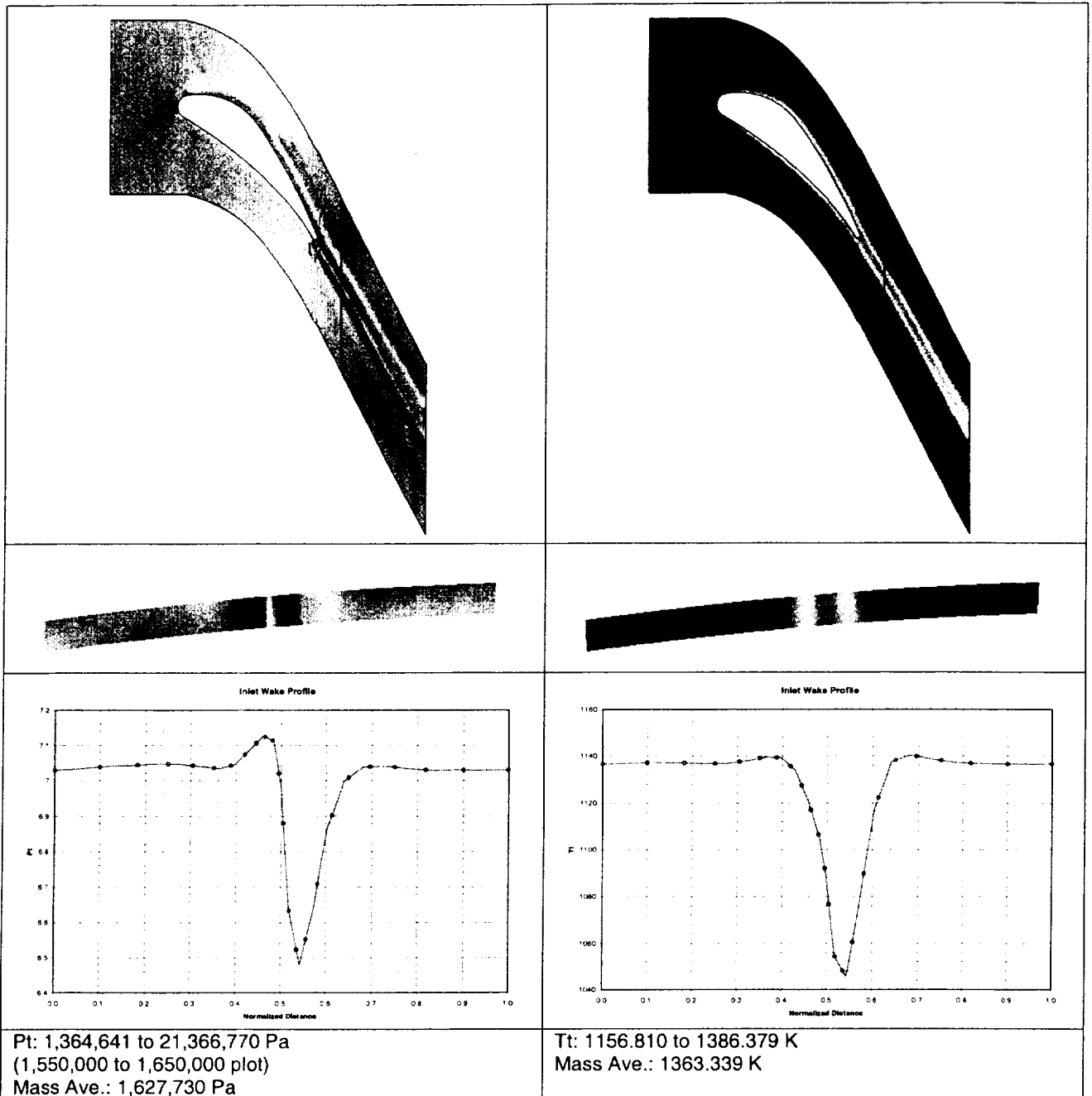
Convergence Indicator vs. Number of Iterations
HPT1 NGV

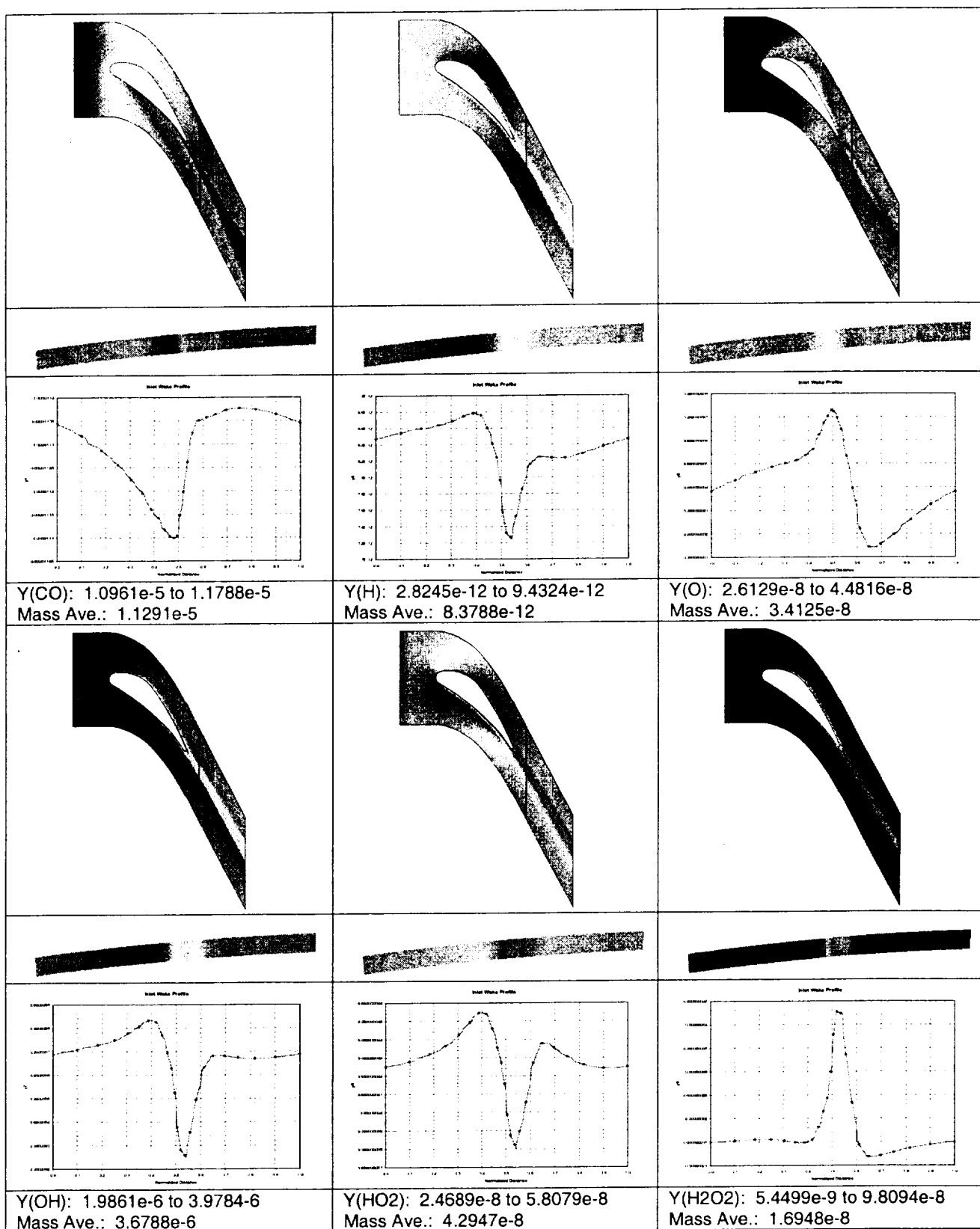


range and mass averaged quantities at cutting plane
cutting plane at 0.04515

Num	Spec	min	max	mass ave
1	CO	1.0960670E-05	1.1788260E-05	1.1291178E-05
2	CO2	7.2901480E-02	7.2902828E-02	7.2902240E-02
3	O2	0.1480127	0.1480136	0.1480131
4	H2O	2.9883171E-02	2.9883521E-02	2.9883305E-02
5	H	2.8244520E-12	9.4324088E-12	8.3788480E-12
6	O	2.6128790E-08	4.4815678E-08	3.4125186E-08
7	OH	1.9860620E-06	3.9784268E-06	3.6788304E-06
8	HO2	2.4688800E-08	5.8078822E-08	4.2947221E-08
9	H2O2	5.4499472E-09	9.8093857E-08	1.6948434E-08
10	NO	3.1216681E-04	3.1549390E-04	3.1493246E-04
11	NO2	4.9967889E-06	6.4257251E-06	5.7360417E-06
12	NO3	5.9383180E-12	3.1245451E-11	1.0588782E-11
13	HNO	7.8105612E-11	1.7963479E-10	1.2943577E-10
14	HONO	4.0774090E-08	4.1504150E-06	2.0222627E-07
15	HNO3	-1.4242200E-10	5.3347769E-08	9.1435254E-10
16	SO2	2.1805350E-05	2.1853461E-05	2.1843829E-05
17	SO3	1.7444370E-06	1.7997299E-06	1.7563391E-06
18	HOSO	2.7650279E-14	2.5342201E-13	1.4487009E-13
19	HSO3	5.0049240E-12	1.1248480E-10	8.1400182E-12
20	HSO2	1.2148050E-16	5.7409781E-16	1.5103668E-16
21	SO	9.1956160E-14	3.9928561E-13	3.4998060E-13
22	HCO	2.5679660E-17	5.7935929E-17	4.5071751E-17
23	H2	1.1504340E-10	1.0300690E-09	7.3819911E-10
24	N2	0.7488416	0.7488421	0.7488415
25	AR	0.0000000E+00	0.0000000E+00	0.0000000E+00
26	C(S)	0.0000000E+00	0.0000000E+00	0.0000000E+00
27	N	0.0000000E+00	0.0000000E+00	0.0000000E+00
28	H2SO4	3.7797829E-10	6.7893300E-09	5.7222255E-10
29	S	2.4445289E-21	2.4445451E-21	2.4445346E-21

X/X	7.1622198E-03	5.9027892E-02	
Y/R	0.2616538	0.2712400	
Z/T	-6.3572727E-02	2.0361030E-02	
Tt	1156.810	1386.379	1363.339
dens	3.119411	4.331536	
Ps	10.55461	16.76656	12.99278
Vx	-123.4683	450.0187	201.4363
Vt	-430.1193	261.4255	361.1647
Vr	-84.10556	25.99604	-5.2535836E-02
TK	0.5282233	285292.6	
TE	12.38410	6.1178208E+10	
Ts	1083.624	1374.872	1287.489
Mach	3.7381984E-03	0.9269373	
Pt	13.64641	21.36677	16.27730
Pred	10.55461	16.76656	
S	0.6861496	0.8642535	





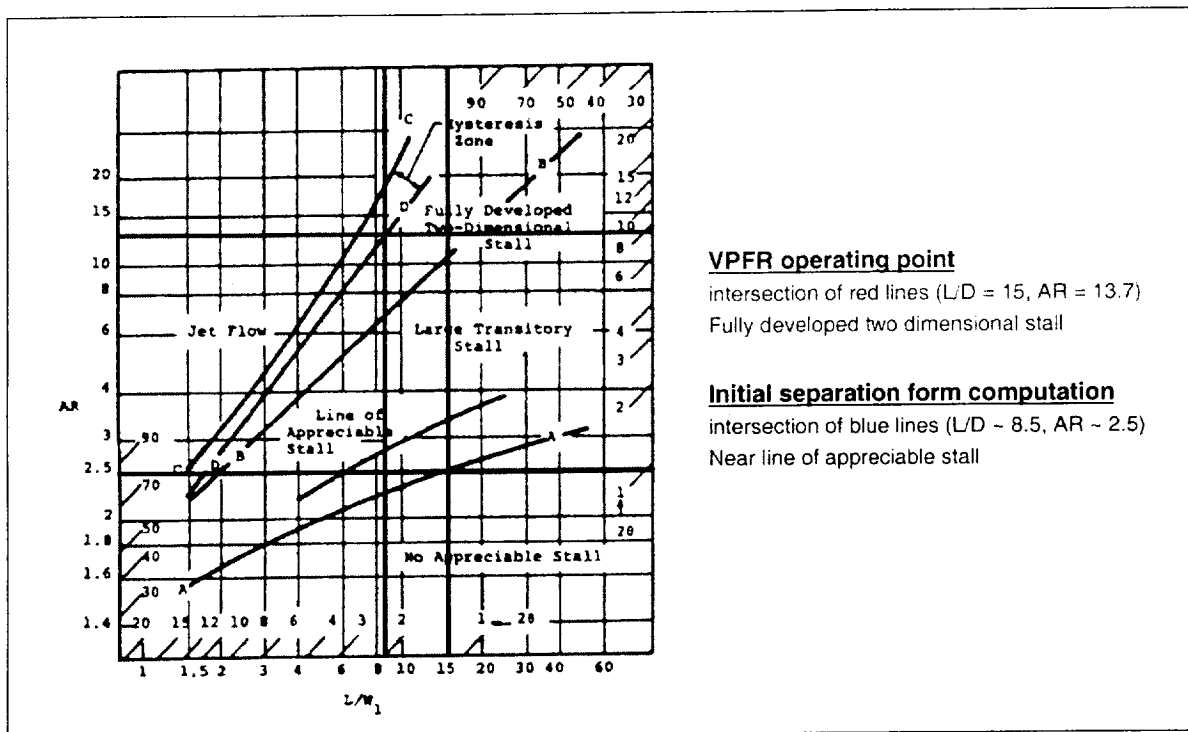


Figure A.4 Diffuser flow regime map [39]

Velocity Profiles

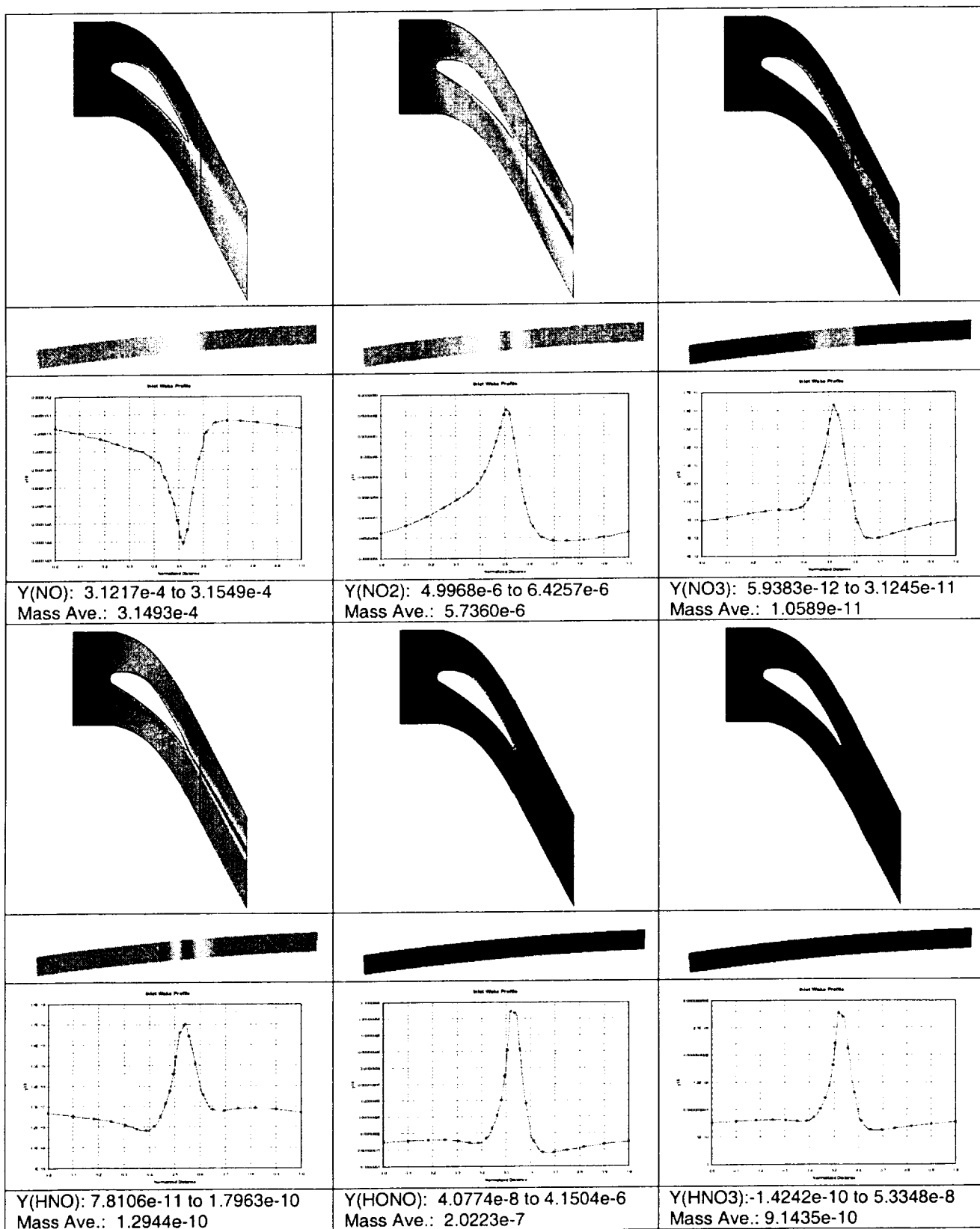
The most informative method to evaluate the quality of the computational solution was to compare the velocity profiles to experimental data and empirical correlations. The VPFR was designed to operate such that the velocity profiles transition quickly to fully-developed turbulent velocity profiles [26]. These profiles have a characteristic “top hat” shape (see Figure A.5 and Figure A.6).

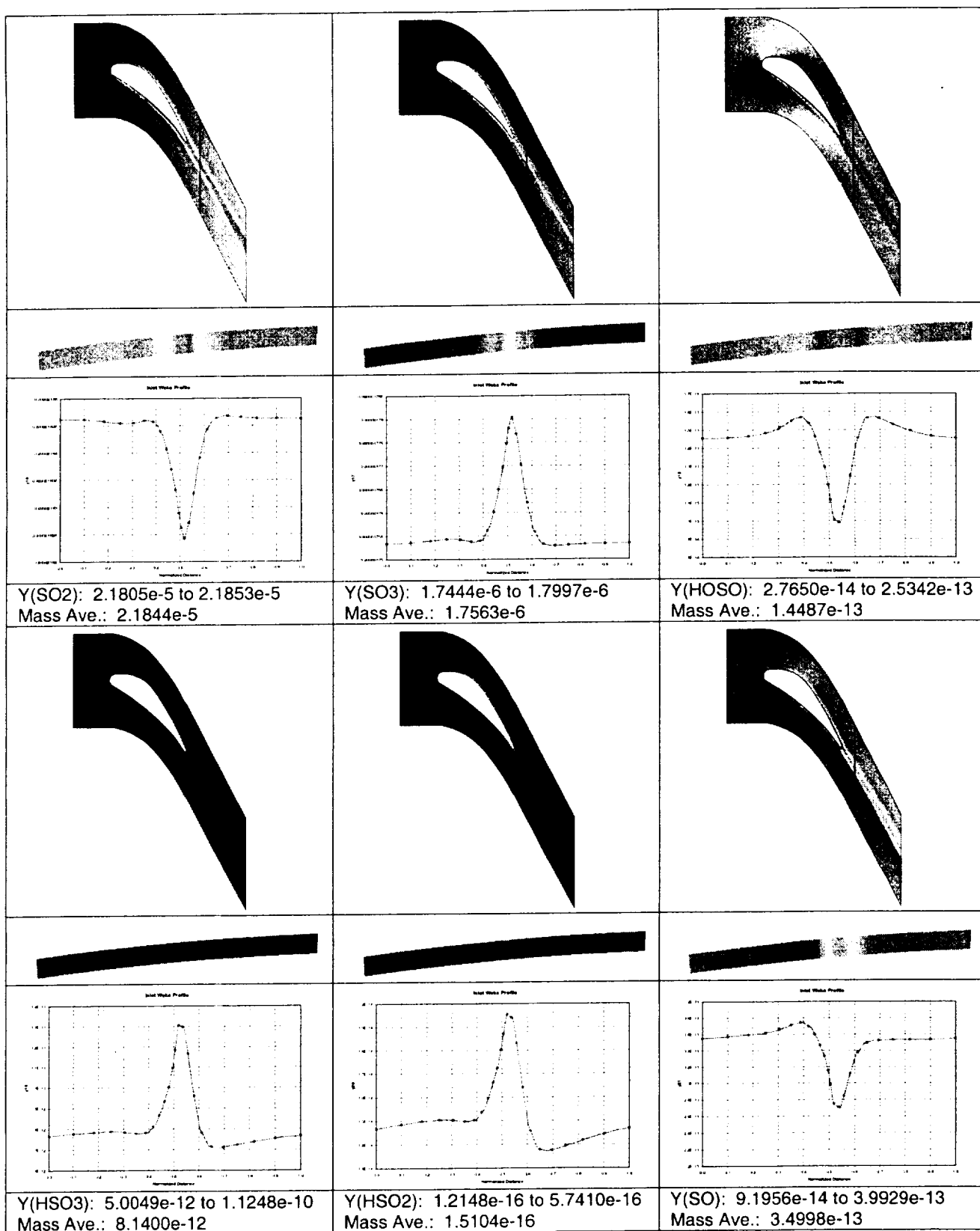
Empirical Correlation

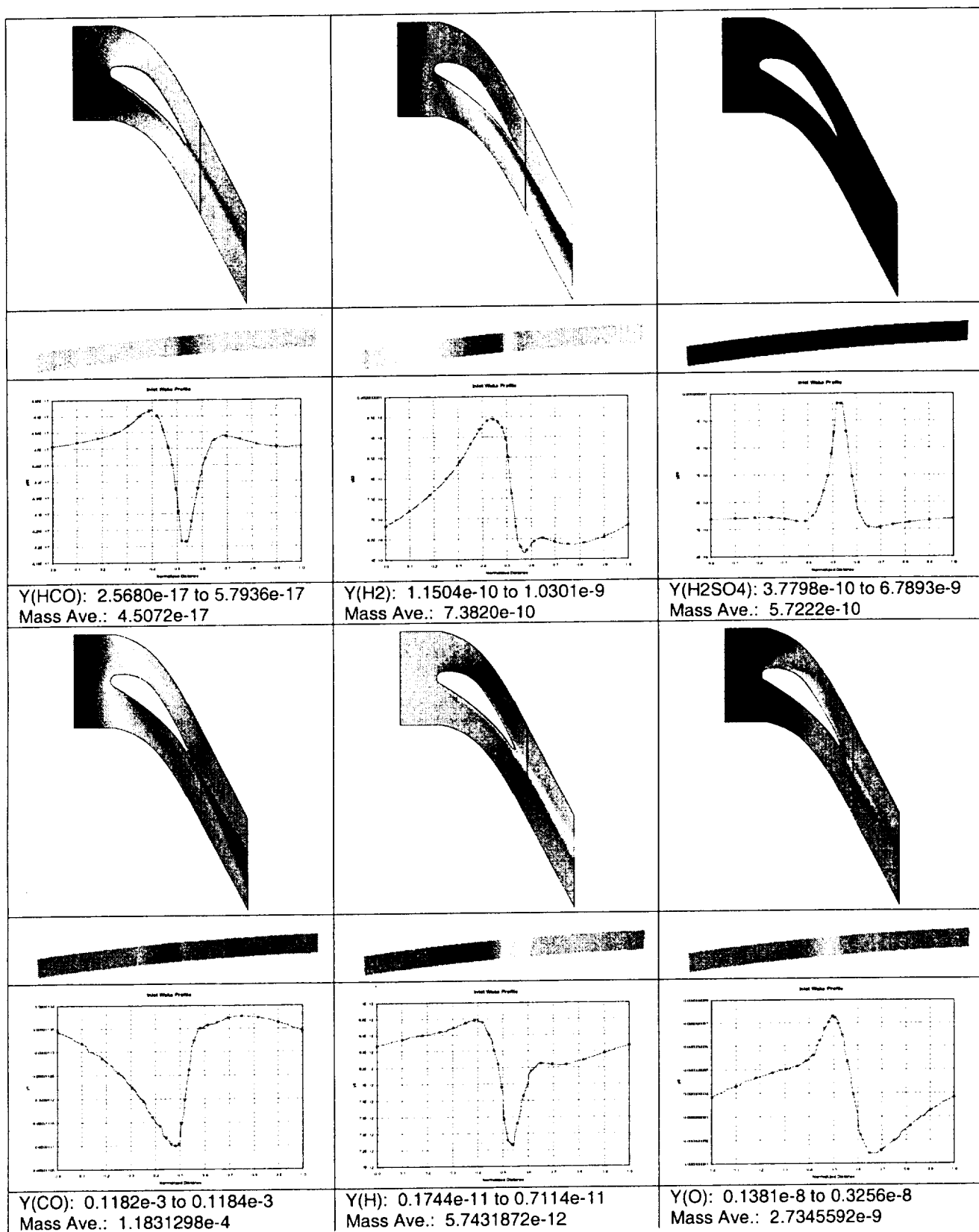
The Power Law is one empirical correlation commonly used to predict velocity profiles in pipe flow:

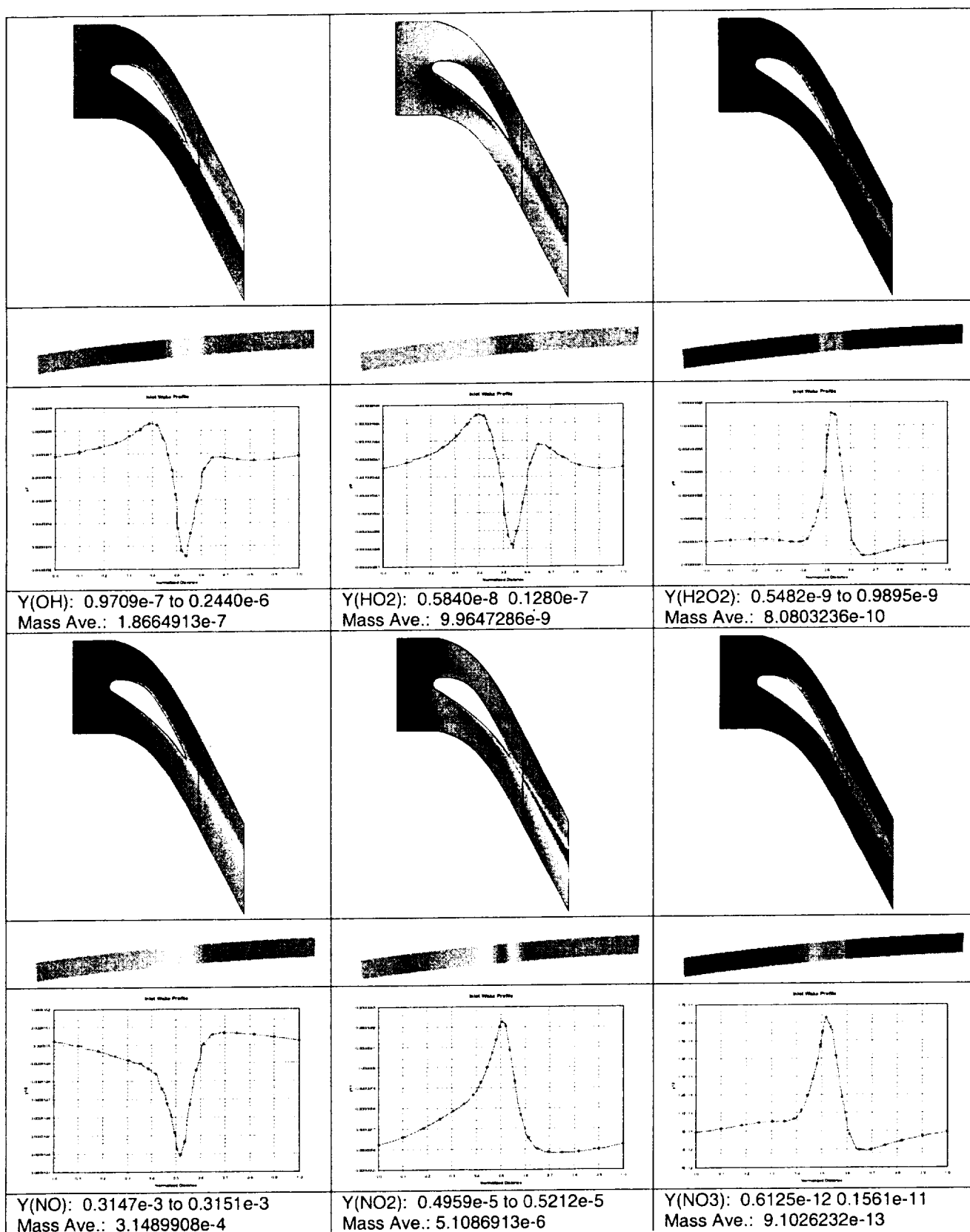
$$\frac{u}{V_c} = \left(1 - \frac{r}{R}\right)^{\frac{1}{n}} \quad (A.3)$$

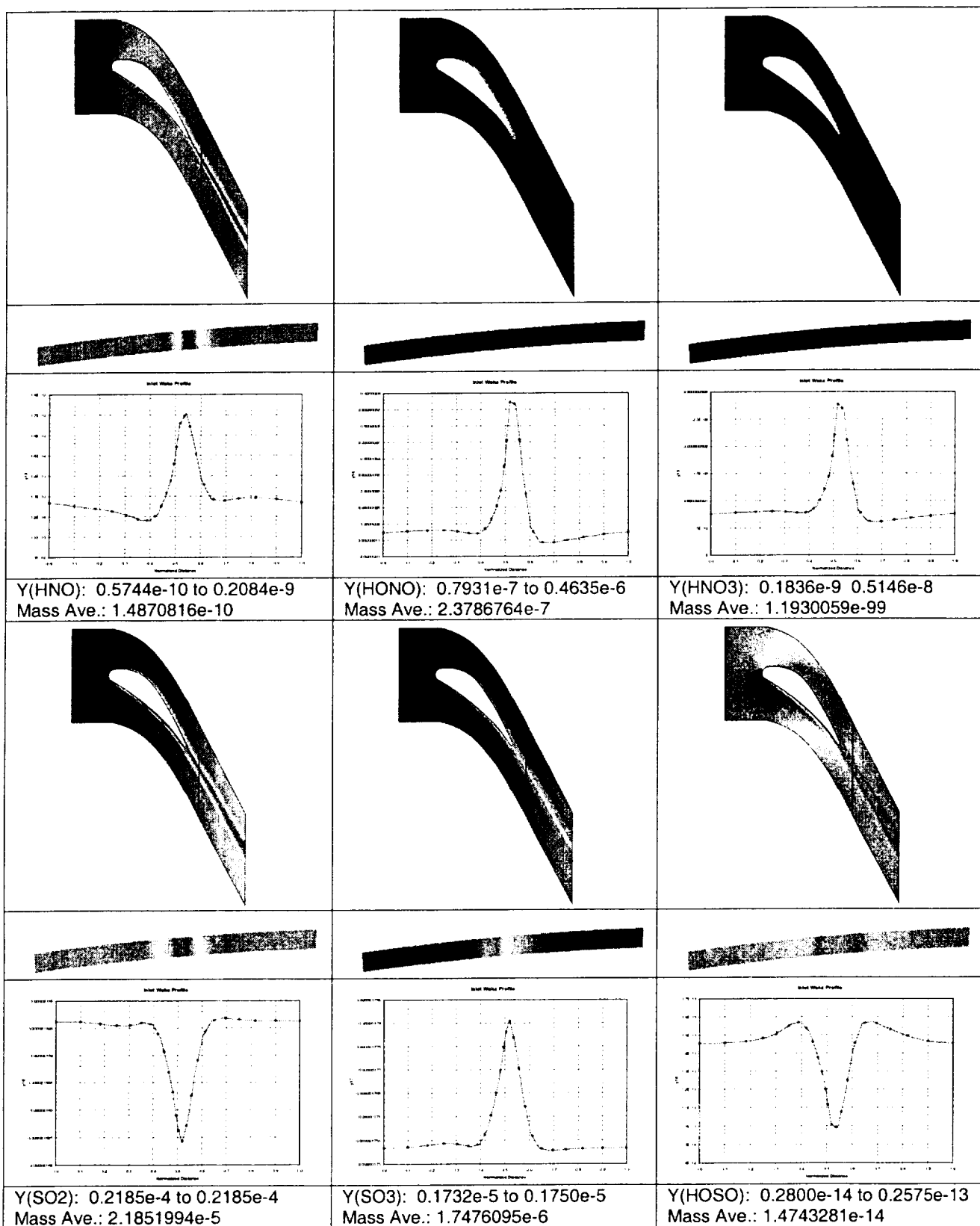
Where V_c is the centerline velocity, u is the time average x component of velocity, and R is the pipe radius. For the flow reactor case, n , which is a function of Reynolds number, is about 6. Figure A.5 shows the expected velocity profile for the VPFR derived from the Power Law.

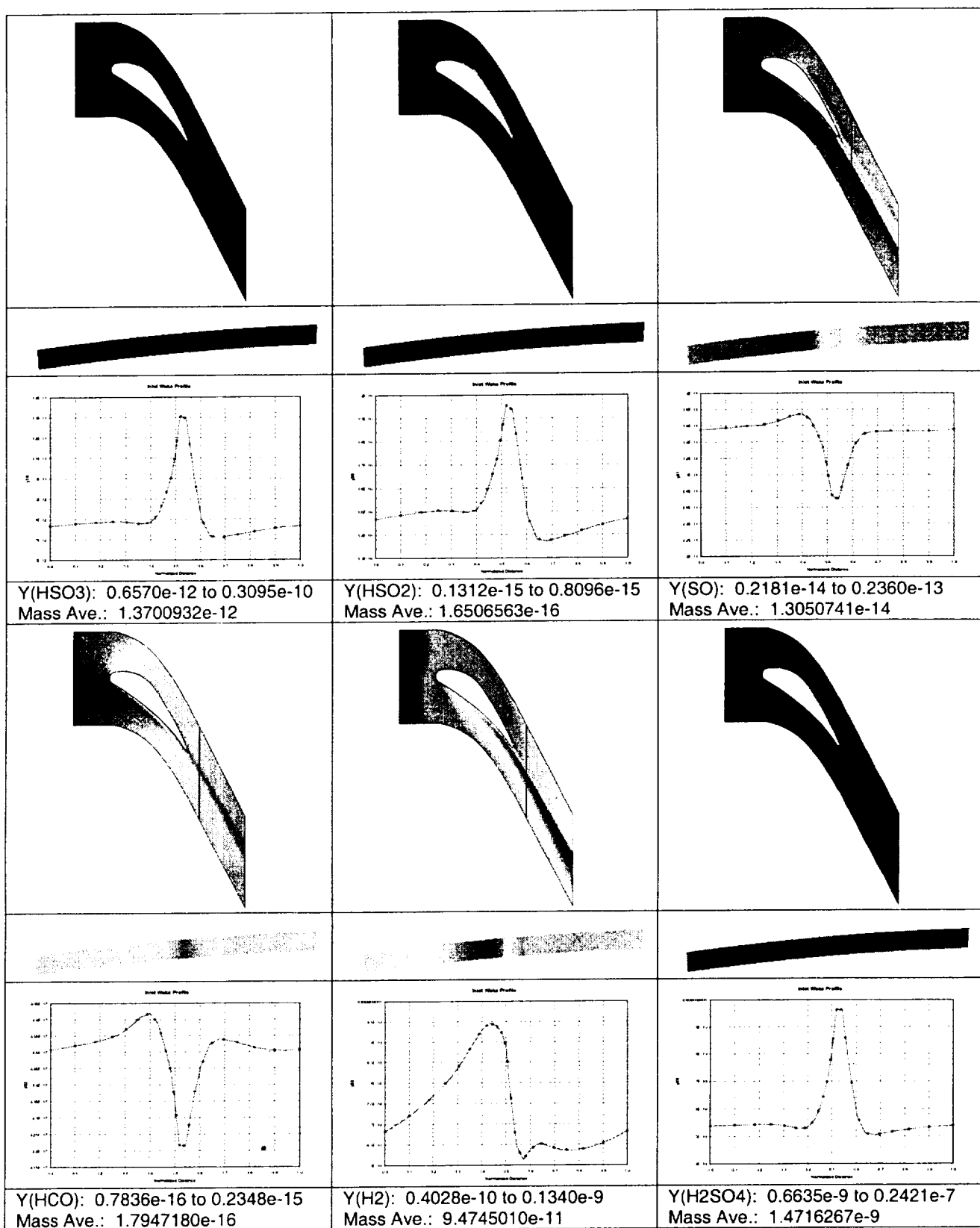


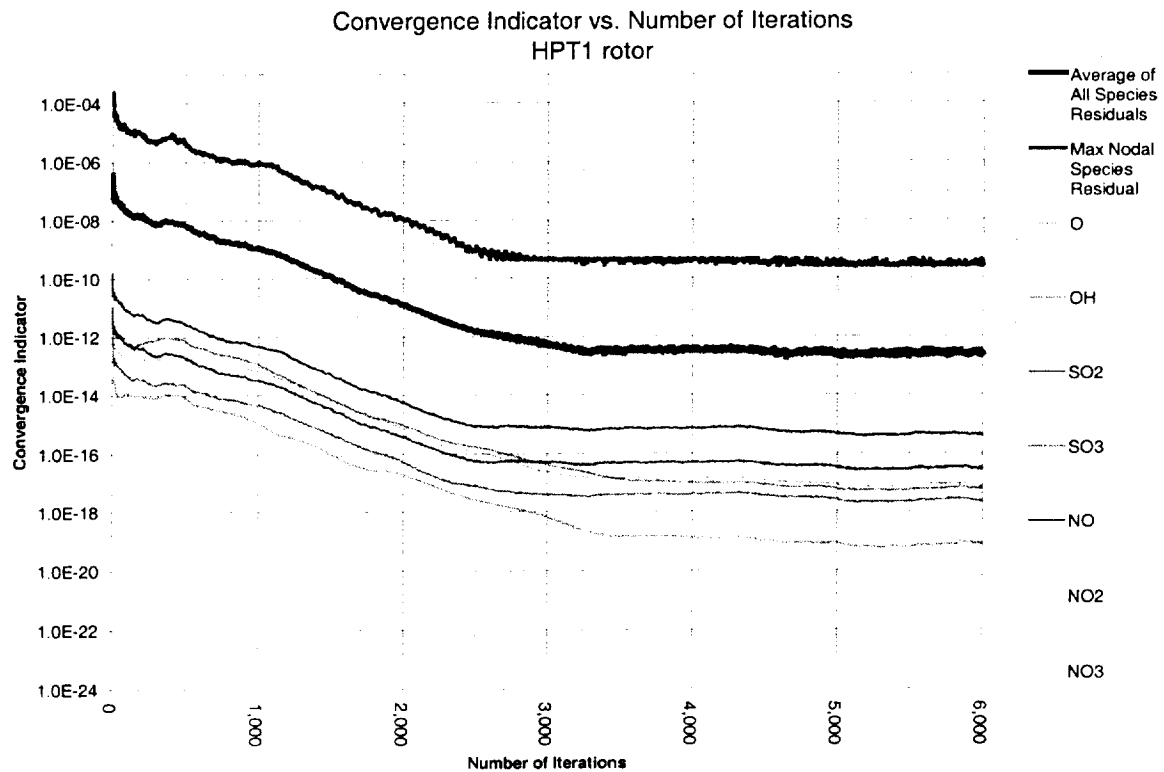
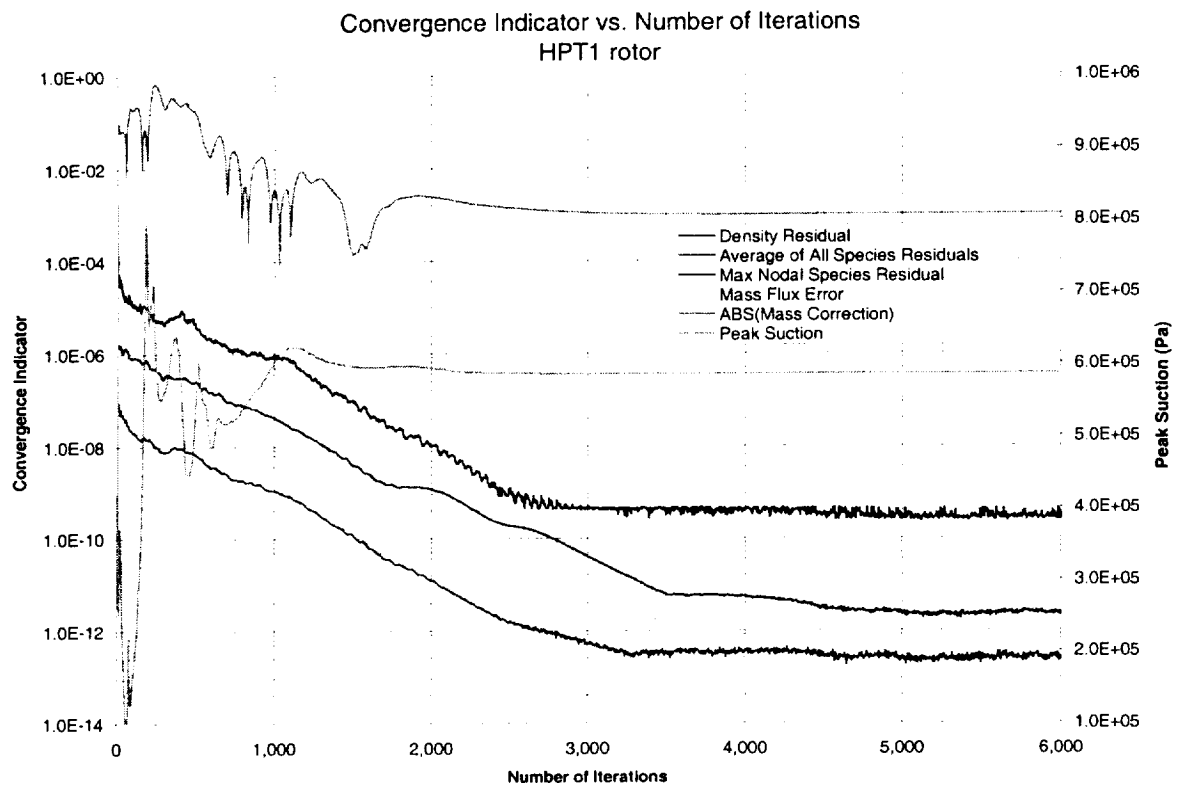








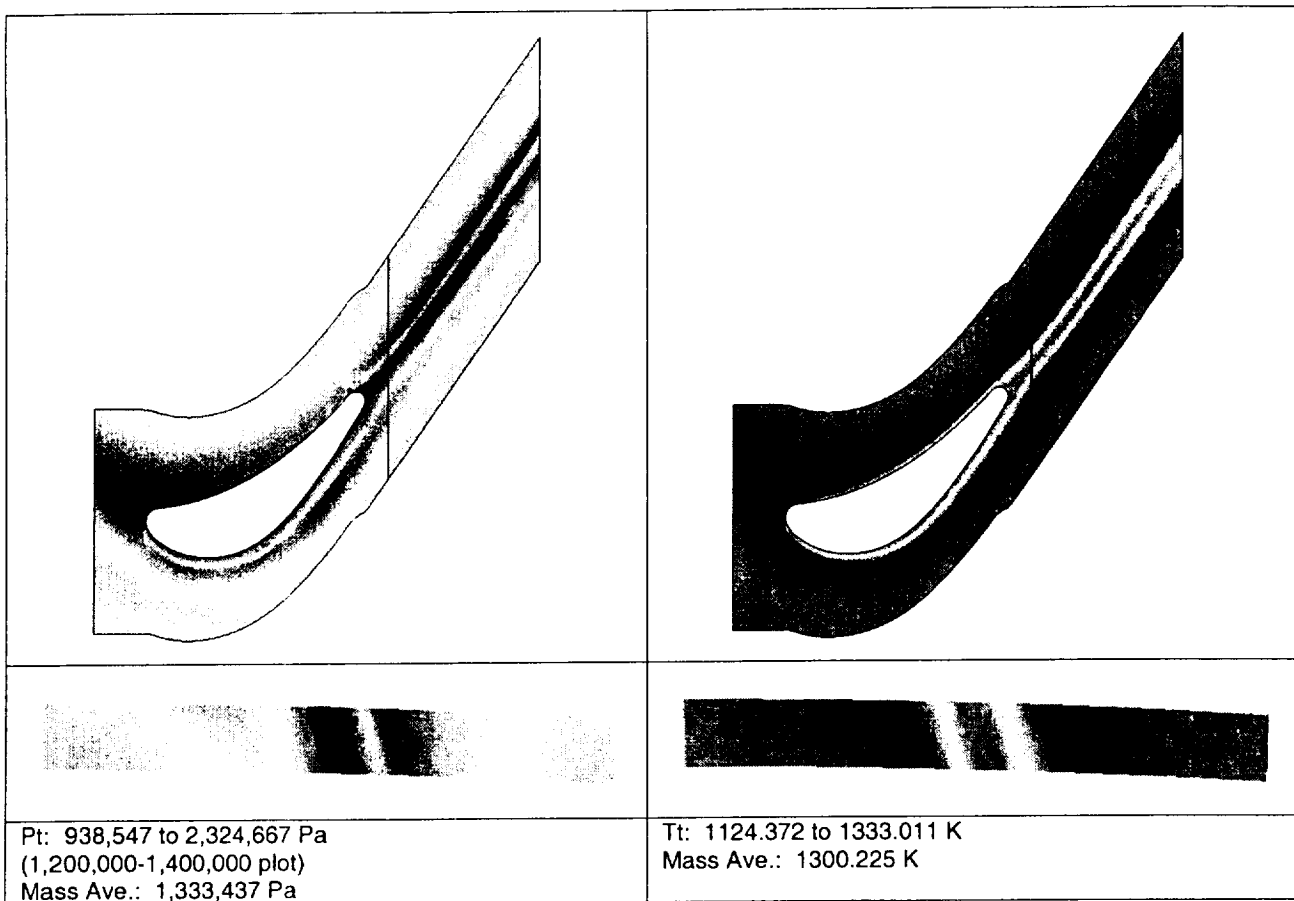


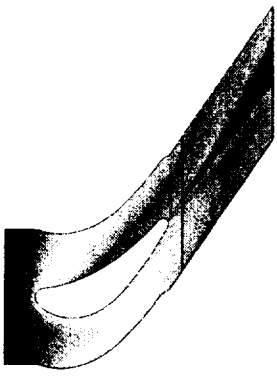
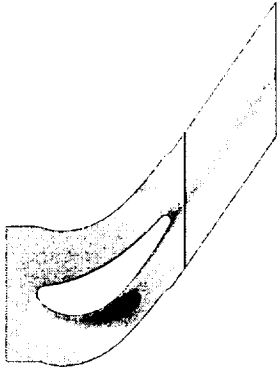
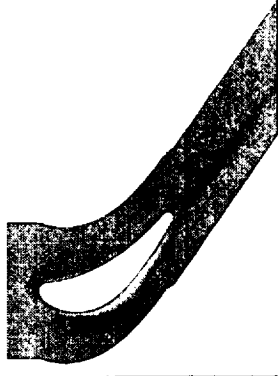



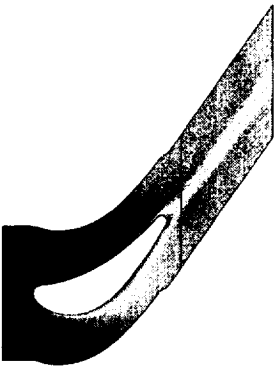
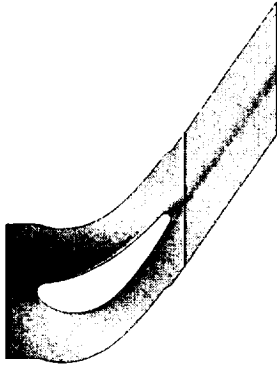
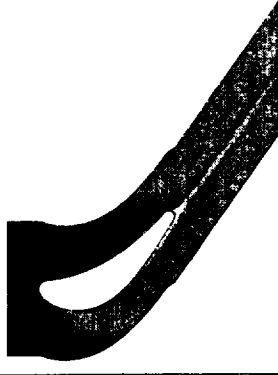



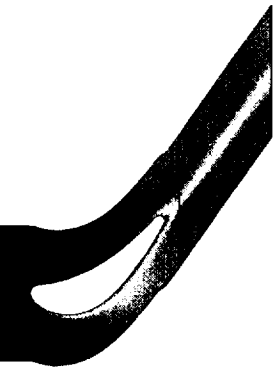
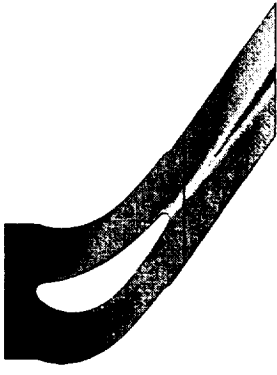






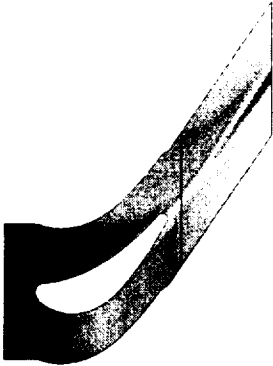
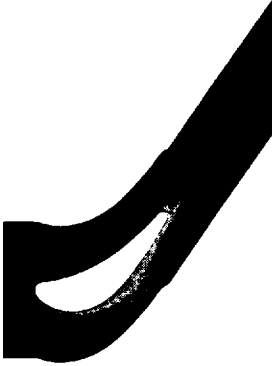




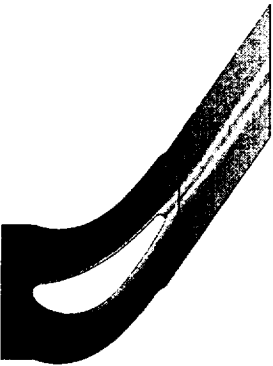
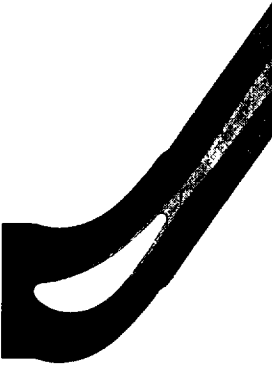
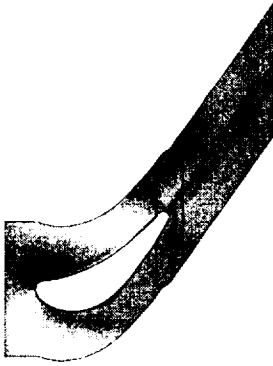




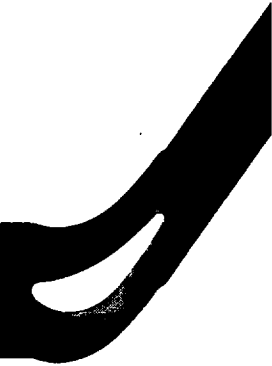
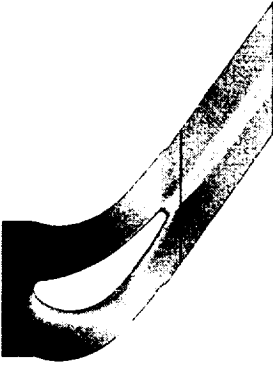



range and mass averaged quantities at cutting plane
cutting plane at 0.01060

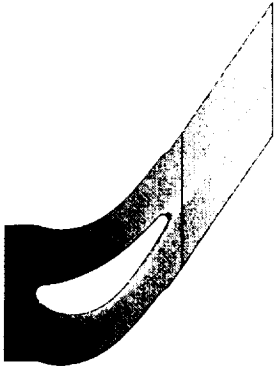
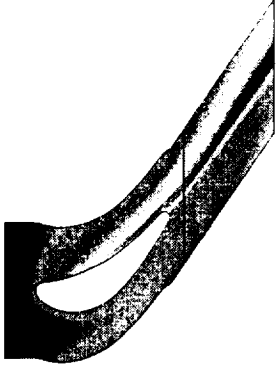




num	species	min	max	mass ave
1	CO	1.1028110E-05	1.1291180E-05	1.1155897E-05
2	CO2	7.2902203E-02	7.2902679E-02	7.2902434E-02
3	O2	0.1480128	0.1480133	0.1480130
4	H2O	2.9883269E-02	2.9883681E-02	2.9883401E-02
5	H	3.0306020E-12	1.1951770E-11	9.4046255E-12
6	O	3.0920891E-08	5.6032619E-08	4.3273968E-08
7	OH	1.8885230E-06	3.7138709E-06	3.3758893E-06
8	HO2	2.3738091E-08	4.5069211E-08	3.6882440E-08
9	H2O2	1.0050790E-08	8.7000387E-08	3.9920529E-08
10	NO	3.1211879E-04	3.1495970E-04	3.1454579E-04
11	NO2	5.7360421E-06	6.3211310E-06	5.9863410E-06
12	NO3	8.3264983E-12	3.6301271E-11	1.4460729E-11
13	HNO	1.2877401E-10	1.8293370E-10	1.5504040E-10
14	HONO	8.1516284E-08	4.0333512E-06	5.5106256E-07
15	HNO3	-3.1286479E-10	6.1903712E-08	2.4605282E-09
16	SO2	2.1808110E-05	2.1843831E-05	2.1838596E-05
17	SO3	1.7563390E-06	1.7951180E-06	1.7627525E-06
18	HOSO	2.1189459E-14	1.6339089E-13	9.3304000E-14
19	HSO3	5.8176632E-12	1.5686860E-10	1.0739637E-11
20	HSO2	1.3123580E-16	7.0853009E-16	1.9591100E-16
21	SO	8.1447761E-14	3.6073450E-13	3.1185338E-13
22	HCO	2.3288410E-17	4.5266589E-17	4.0807966E-17
23	H2	7.3819911E-10	8.7823260E-10	8.1180129E-10
24	N2	0.7488415	0.7488420	0.7488419
25	AR	0.0000000E+00	0.0000000E+00	0.0000000E+00
26	C(S)	0.0000000E+00	0.0000000E+00	0.0000000E+00
27	N	0.0000000E+00	0.0000000E+00	0.0000000E+00
28	H2SO4	4.2082671E-10	9.0190957E-09	7.5702011E-10
29	S	2.4445289E-21	2.4445469E-21	2.4445352E-21

X/X	-1.1852840E-02	2.2079229E-02	
Y/R	0.2671618	0.2712400	
T/Z	-1.2139130E-02	3.3451378E-02	
Tt	1124.372	1333.011	1300.225
dens	2.046658	3.929755	
Ps	5.856664	14.15914	9.808423
Vx	-72.06285	712.5885	271.0783
Vt	-484.9583	490.9988	-379.8698
Vr	-52.12230	43.46152	-0.2326850
TK	0.5275032	527503.2	
TE	20.16434	6.5262518E+11	
Ts	851.8360	1315.987	1202.610
Mach	3.7721284E-03	1.512067	
Pt	9.385468	23.24667	13.33437
Pred	5.856664	14.15914	
S	0.6160989	0.8636632	

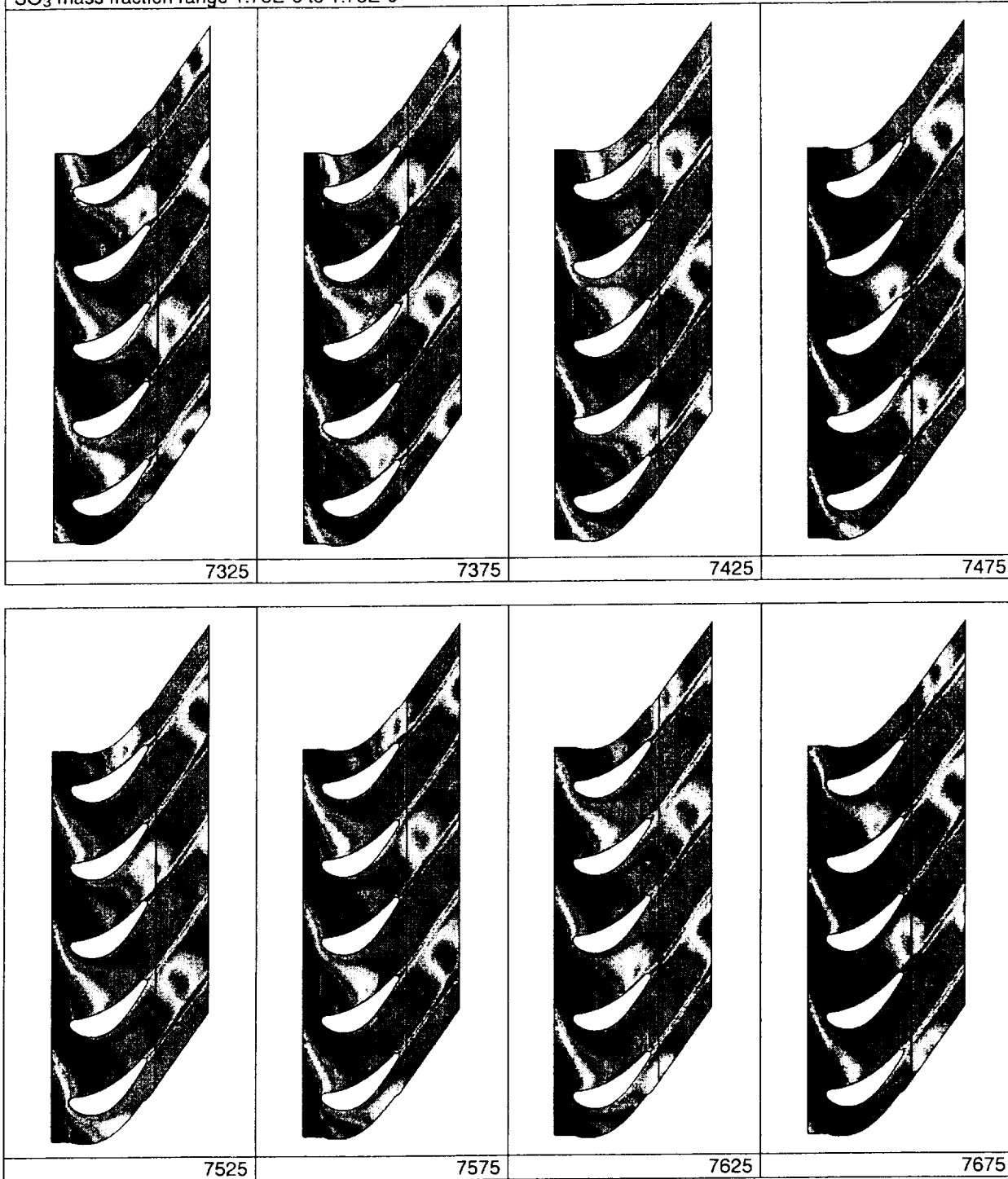


		
		
Y(CO): 1.1028e-5 to 1.1291e-5 Mass Ave.: 1.1156e-5	Y(H): 3.0306e-12 to 1.1952e-11 Mass Ave.: 9.4046e-12	Y(O): 3.0921e-8 to 5.6033e-8 Mass Ave.: 4.3274e-8
		
		
Y(OH): 1.8885e-6 to 3.7139e-6 Mass Ave.: 3.3759e-6	Y(HO2): 2.3738e-8 to 4.5069e-8 Mass Ave.: 3.6882e-8	Y(H2O2): 1.0051e-8 to 8.7000e-8 Mass Ave.: 3.9921e-8
		
		
Y(NO): 3.1212e-4 to 3.1496e-4 Mass Ave.: 3.1455e-4	Y(NO2): 5.7360e-6 to 6.3211e-6 Mass Ave.: 5.9863e-6	Y(NO3): 8.3265e-12 to 3.6301e-11 Mass Ave.: 1.4461e-11

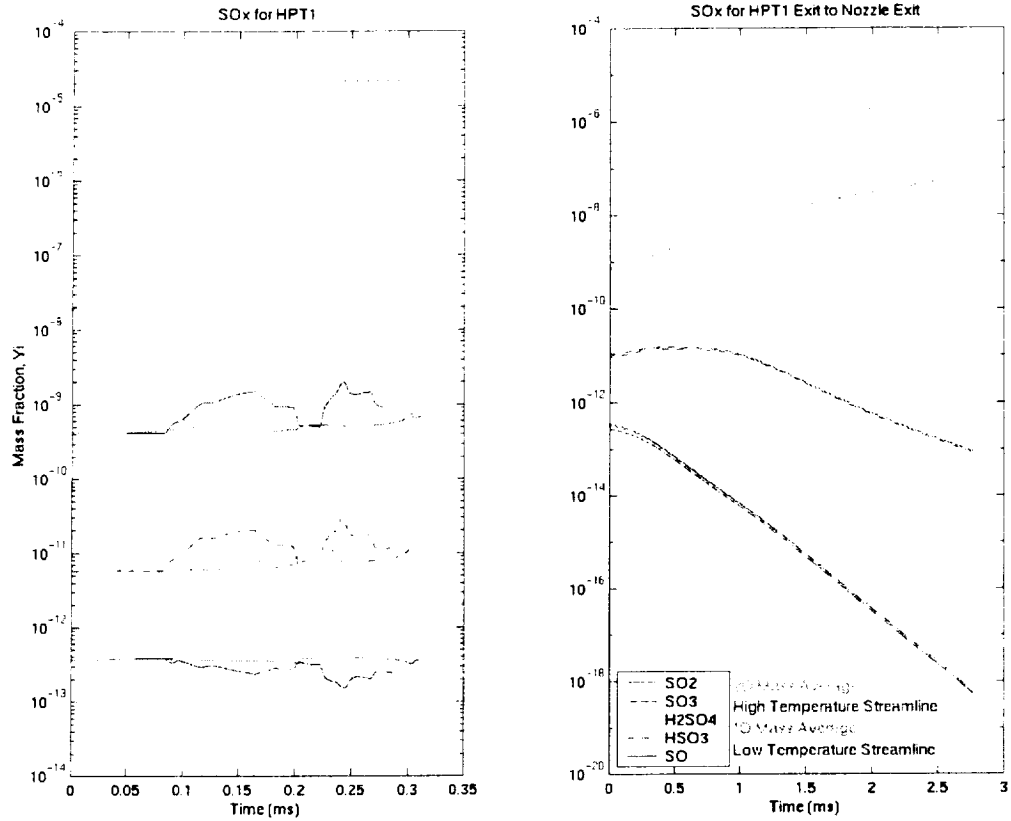
		
		
Y(HNO): 1.2877e-10 to 1.8293e-10 Mass Ave.: 1.5504e-10	Y(HONO): 8.1516e-8 to 4.0334e-6 Mass Ave.: 5.5106e-7	Y(HNO3): -3.1286e-10 to 6.1904e-8 Mass Ave.: 2.4605e-9
		
		
Y(SO2): 2.1808e-5 to 2.1844e-5 Mass Ave.: 2.1839e-5	Y(SO3): 1.7563e-6 to 1.7951e-6 Mass Ave.: 1.7628e-6	Y(HOSO): 2.1189e-14 to 1.6339e-13 Mass Ave.: 9.3304e-14
		
		
Y(HSO3): 5.8177e-12 to 1.5687e-10 Mass Ave.: 1.0740e-11	Y(HSO2): 1.3124e-16 to 7.0853e-16 Mass Ave.: 1.9591e-16	Y(SO): 8.1448e-14 to 3.6073e-13 Mass Ave.: 3.1185e-13

		
		
<p>Y(HCO): 2.3288e-17 to 4.5267e-17 Mass Ave.: 4.0808e-17</p>	<p>Y(H2): 7.3820e-10 to 8.7823e-10 Mass Ave.: 8.1180e-10</p>	<p>Y(H2SO4): 4.2083e-10 to 9.0191e-9 Mass Ave.: 7.5702e-10</p>

Rotor Wake Model Case – SO₃ Mass Fraction at selected times for one cycle
 SO₃ mass fraction range 1.75E-6 to 1.78E-6

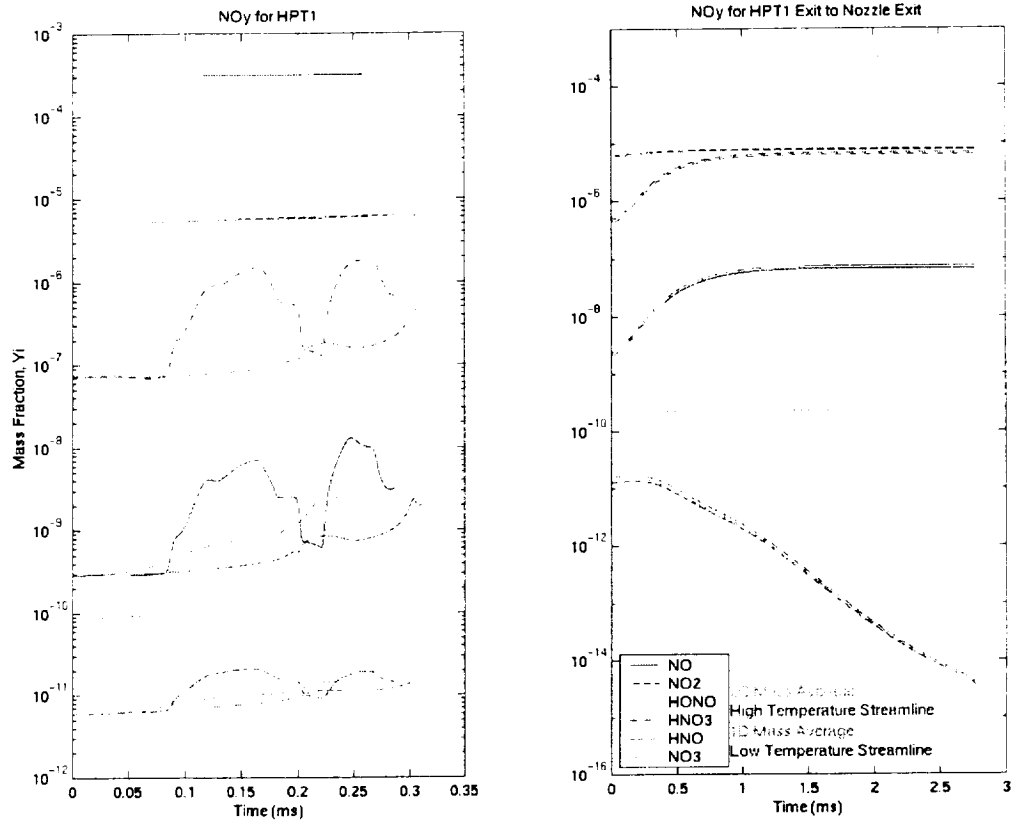


DERA Engine Exit Plane Calculation For Max Power Case



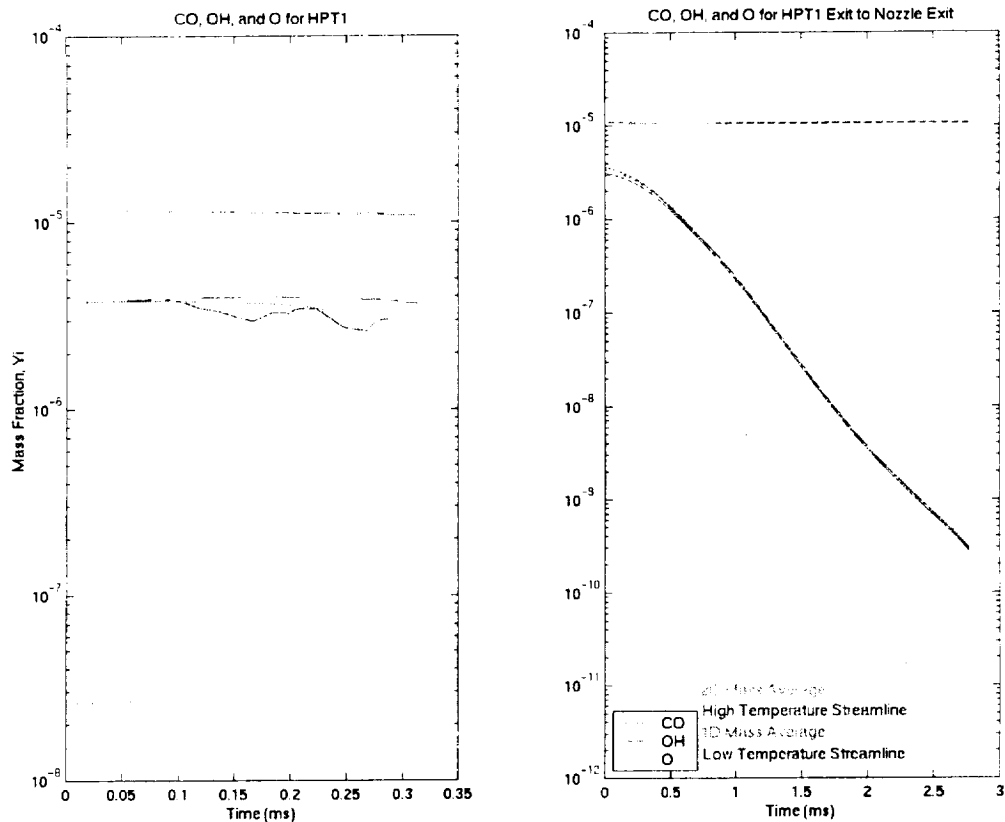
NOTE: The legend on the chart lists the species in the proper sequence for the lines (top to bottom), however, the line style is not correct (dashed, dotted, solid, etc is wrong).

DERA Engine Exit Plane Calculation For Max Power Case



NOTE: The legend on the chart lists the species in the proper sequence for the lines (top to bottom), however, the line style is not correct (dashed, dotted, solid, etc is wrong).

DERA Engine Exit Plane Calculation For Max Power Case



NOTE: The legend on the chart lists the species in the proper sequence for the lines (top to bottom), however, the line style is not correct (dashed, dotted, solid, etc is wrong).

APPENDIX E

CNEWT AND CALCHEM INPUT FILES FOR MAX POWER CONDITION

This appendix contains the CNEWT run files used for the high fidelity modeling and CALCHEM input files used for the low fidelity modeling of the NASA/DERA engine test max power condition.

There are three CNEWT run files listed in the following order:

- HPT1 NGV - Max power
- HPT1 rotor - Max power - Mixed-out
- HPT1 rotor - Max power - Unsteady wake model

Followed by four CALCHEM input files listed in the following order:

- HPT1 - Max power - Mass averaged
- HPT1 - Max power - High temperature streamline
- HPT1 - Max power - Low temperature streamline
- HPT1 exit to nozzle exit - Max power - Mass Averaged

HPT1 NGV - Max power:

```

CNEWT:mid-span of DERA HPT1 NGV:max power condition
3550 0 2 1 1 0 <--- change KNORM=1 for stronger blade bc
1.00000 0.00000 0.50000 0.00200 0.25000
1634150. 1365.20000 00.00000 0.00000 000.00000 1299940.8 1299940.8 998.99700
1138. 1.34 0.0000546 0000.0 0.031
1 2 3 3 -4
3 0 1 29 1 1 <--- MASKIN=0; code will not read lines after MIN
25 80 3
0.26924 0.27124
1634150.0 1634150.0 1634150.0
1365.2 1365.2 1365.2
0. 0. 0.
0. 0. 0.
0. 0. 0.
1. 1. 1.
1.1788260e-05 1.1788260e-05 1.1788260e-05
7.2901490e-02 7.2901490e-02 7.2901490e-02
1.4801360e-01 1.4801360e-01 1.4801360e-01
2.9883310e-02 2.9883310e-02 2.9883310e-02
7.8778370e-12 7.8778370e-12 7.8778370e-12
2.6128790e-08 2.6128790e-08 2.6128790e-08
3.7438540e-06 3.7438540e-06 3.7438540e-06
5.4143820e-08 5.4143820e-08 5.4143820e-08
6.6700590e-09 6.6700590e-09 6.6700590e-09
3.1549390e-04 3.1549390e-04 3.1549390e-04
4.9967900e-06 4.9967900e-06 4.9967900e-06
6.0388730e-12 6.0388730e-12 6.0388730e-12
7.8105610e-11 7.8105610e-11 7.8105610e-11
7.8798570e-08 7.8798570e-08 7.8798570e-08
3.0977400e-10 3.0977400e-10 3.0977400e-10
2.1853460e-05 2.1853460e-05 2.1853460e-05
1.7444370e-06 1.7444370e-06 1.7444370e-06
2.2916830e-13 2.2916830e-13 2.2916830e-13
5.9482370e-12 5.9482370e-12 5.9482370e-12
1.2286700e-16 1.2286700e-16 1.2286700e-16
3.6030010e-13 3.6030010e-13 3.6030010e-13
5.5508550e-17 5.5508550e-17 5.5508550e-17
1.1504340e-10 1.1504340e-10 1.1504340e-10
7.4884180e-01 7.4884180e-01 7.4884180e-01
0.0000000e+00 0.0000000e+00 0.0000000e+00
0.0000000e+00 0.0000000e+00 0.0000000e+00
0.0000000e+00 0.0000000e+00 0.0000000e+00
4.3699380e-10 4.3699380e-10 4.3699380e-10
2.4445370e-21 2.4445370e-21 2.4445370e-21
-0.028 0.343 0. <--- boundary stationary wrto. blade
1. 1. 1. 1. 1. 0.999 0.995 0.992
0.99100 0.992 0.995 0.999 1. 1. 1. 1.
1. 1. 1. 1. 1. 0.999 0.995 0.992
0.99100 0.992 0.995 0.999 1. 1. 1. 1.
1.
5. 5. 4. 3. 2. 2. 2. 2.
2. 2. 2. 2. 3. 4. 5. 5.
5. 5. 4. 3. 2. 2. 2. 2.
2. 2. 2. 2. 3. 4. 5. 5.

```

HPT1 rotor - Max power – Mixed-out:

```

CNEWT:mid-span of DERA HPT1 rotor:max power condition,mixed-out
4800 0 2 1 1 0 <--- change KNORM=1 for stronger blade bc
1.00000 0.00000 0.50000 0.00200 0.25000
1627730.0 1363.33900 -60.84980 0.00000 361.16470 985627.1 985627.1 956.20700
1138. 1.34 0.0000546 -8863.8 0.019
1 2 3 3 -4
3 0 1 29 1 1 <--- MASKIN=0; code will not read lines after MIN
25 80 3
0.26924 0.27124
1627730.0 1627730.0 1627730.0
1363.339 1363.339 1363.339
-60.850 -60.850 -60.850
0. 0. 0.
361.165 361.165 361.165
1. 1. 1.
1.1291178E-05 1.1291178E-05 1.1291178E-05
7.2902240E-02 7.2902240E-02 7.2902240E-02
0.1480131 0.1480131 0.1480131
2.9883305E-02 2.9883305E-02 2.9883305E-02
8.3788480E-12 8.3788480E-12 8.3788480E-12
3.4125186E-08 3.4125186E-08 3.4125186E-08
3.6788304E-06 3.6788304E-06 3.6788304E-06
4.2947221E-08 4.2947221E-08 4.2947221E-08
1.6948434E-08 1.6948434E-08 1.6948434E-08
3.1493246E-04 3.1493246E-04 3.1493246E-04
5.7360417E-06 5.7360417E-06 5.7360417E-06
1.0588782E-11 1.0588782E-11 1.0588782E-11
1.2943577E-10 1.2943577E-10 1.2943577E-10
2.0222627E-07 2.0222627E-07 2.0222627E-07
9.1435254E-10 9.1435254E-10 9.1435254E-10
2.1843829E-05 2.1843829E-05 2.1843829E-05
1.7563391E-06 1.7563391E-06 1.7563391E-06
1.4487009E-13 1.4487009E-13 1.4487009E-13
8.1400182E-12 8.1400182E-12 8.1400182E-12
1.5103668E-16 1.5103668E-16 1.5103668E-16
3.4998060E-13 3.4998060E-13 3.4998060E-13
4.5071751E-17 4.5071751E-17 4.5071751E-17
7.3819911E-10 7.3819911E-10 7.3819911E-10
0.7488415 0.7488415 0.7488415
0.0000000E+00 0.0000000E+00 0.0000000E+00
0.0000000E+00 0.0000000E+00 0.0000000E+00
0.0000000E+00 0.0000000E+00 0.0000000E+00
5.7222255E-10 5.7222255E-10 5.7222255E-10
2.4445346E-21 2.4445346E-21 2.4445346E-21
.-0.028 0.343 0. <--- boundary stationary wrto. blade
1. 1. 1. 1. 1. 0.999 0.995 0.992
0.99100 0.992 0.995 0.999 1. 1. 1. 1.
1. 1. 1. 1. 1. 0.999 0.995 0.992
0.99100 0.992 0.995 0.999 1. 1. 1. 1.
1.
5. 5. 4. 3. 2. 2. 2. 2.
2. 2. 2. 2. 3. 4. 5. 5.
5. 5. 4. 3. 2. 2. 2. 2.
2. 2. 2. 2. 3. 4. 5. 5.

```

[illegible]

3.6740560E-08 3.7039767E-08 3.7281342E-08 3.7219986E-08 3.6967498E-08 3.6469722E-08 3.5309451E-08 3.3929308E-08
3.2220627E-08 3.1432577E-08 3.1552902E-08 3.1978402E-08 3.2603269E-08 3.3260385E-08 3.3813600E-08 3.4291738E-08
3.4642331E-08 3.4864049E-08 3.5017839E-08 3.5132846E-08 3.5351533E-08 3.5603954E-08 3.6222523E-08 3.6740560E-08
3.7039767E-08 3.7281342E-08 3.7219986E-08 3.6967498E-08 3.6469722E-08 3.5309451E-08 3.3929308E-08 3.2220627E-08
3.1432577E-08 3.1552902E-08 3.1978402E-08 3.2603269E-08 3.3260385E-08 3.3813600E-08 3.4291738E-08 3.4642331E-08
3.6878900E-06 3.7080213E-06 3.7277736E-06 3.7479838E-06 3.7766963E-06 3.8073647E-06 3.8308082E-06 3.8246800E-06
3.7690451E-06 3.6930851E-06 3.6311205E-06 3.6818206E-06 3.6812374E-06 3.6729106E-06 3.6689327E-06 3.6743286E-06
3.4920339E-06 3.6311205E-06 3.6818206E-06 3.6812374E-06 3.6729106E-06 3.6689327E-06 3.6743286E-06 3.6878900E-06
3.7080213E-06 3.7277736E-06 3.7479838E-06 3.7766963E-06 3.8073647E-06 3.8308082E-06 3.8246800E-06 3.7690451E-06
3.6930851E-06 3.6294911E-06 3.5229465E-06 3.3766549E-06 3.2804493E-06 3.2578806E-06 3.3545979E-06 3.4920339E-06
3.6311205E-06 3.6818206E-06 3.6812374E-06 3.6729106E-06 3.6689327E-06 3.6743286E-06 3.6878900E-06 3.7080213E-06
3.7277736E-06 3.7479838E-06 3.7766963E-06 3.8073647E-06 3.8308082E-06 3.8246800E-06 3.7690451E-06 3.6930851E-06
3.6294911E-06 3.5229465E-06 3.3766549E-06 3.2804493E-06 3.2578806E-06 3.3545979E-06 3.4920339E-06 3.6311205E-06
3.6818206E-06 3.6812374E-06 3.6729106E-06 3.6689327E-06 3.6743286E-06 3.6878900E-06 3.7080213E-06 3.7277736E-06
3.6930851E-06 3.6294911E-06 3.5229465E-06 3.3766549E-06 3.2804493E-06 3.2578806E-06 3.3545979E-06 3.4920339E-06
4.2494400E-08 4.2789645E-08 4.3188823E-08 4.3644891E-08 4.4264530E-08 4.4912680E-08 4.5437244E-08 4.5387788E-08
4.4586922E-08 4.3546491E-08 4.2736072E-08 4.1526559E-08 4.3552703E-08 4.3883513E-08 4.4264530E-08 4.4912680E-08
4.0514640E-08 4.2704330E-08 4.3773599E-08 4.3552703E-08 4.3883513E-08 4.4264530E-08 4.4912680E-08 4.5437244E-08
4.2789645E-08 4.3188823E-08 4.3644891E-08 4.4264530E-08 4.4912680E-08 4.5437244E-08 4.5387788E-08 4.586922E-08
4.3546491E-08 4.2736072E-08 4.1526559E-08 4.3552703E-08 4.3883513E-08 4.4264530E-08 4.4912680E-08 4.5437244E-08
4.2704330E-08 4.3773599E-08 4.3552703E-08 4.3883513E-08 4.4264530E-08 4.4912680E-08 4.5437244E-08 4.5387788E-08
4.3188823E-08 4.3644891E-08 4.4264530E-08 4.4912680E-08 4.5437244E-08 4.5387788E-08 4.586922E-08 4.3546491E-08
4.2736072E-08 4.1526559E-08 3.9883513E-08 3.8735799E-08 3.8232551E-08 3.8949119E-08 4.0514640E-08 4.2704330E-08
4.3773599E-08 4.3552703E-08 4.3050069E-08 4.2603554E-08 4.2413847E-08 4.2494400E-08 4.2789645E-08 4.3188823E-08
1.4940000E-08 1.5278168E-08 1.5490873E-08 1.5513094E-08 1.5253305E-08 1.4886596E-08 1.4851887E-08 1.5485478E-08
1.8140504E-08 2.1484439E-08 2.4347309E-08 2.9846094E-08 2.846094E-08 2.780012E-08 2.780012E-08 2.780012E-08
2.3321989E-08 1.4368399E-08 1.1843122E-08 1.2080676E-08 1.2080676E-08 1.2080676E-08 1.2080676E-08 1.2080676E-08
1.5278168E-08 1.5490873E-08 1.5513094E-08 1.5253305E-08 1.4886596E-08 1.4851887E-08 1.5485478E-08 1.5485478E-08
2.1484439E-08 2.4347309E-08 2.9846094E-08 2.846094E-08 2.780012E-08 2.780012E-08 2.780012E-08 2.780012E-08
1.4368399E-08 1.1843122E-08 1.2080676E-08 1.2080676E-08 1.2080676E-08 1.2080676E-08 1.2080676E-08 1.2080676E-08
1.5490873E-08 1.5513094E-08 1.5253305E-08 1.4886596E-08 1.4851887E-08 1.5485478E-08 1.5485478E-08 1.5485478E-08
2.4347309E-08 2.9846094E-08 2.846094E-08 2.780012E-08 2.780012E-08 2.780012E-08 2.780012E-08 2.780012E-08
1.1843122E-08 1.2080676E-08 1.2080676E-08 1.2080676E-08 1.2080676E-08 1.2080676E-08 1.2080676E-08 1.2080676E-08
3.1502400E-04 3.1496899E-04 3.1461182E-04 3.1451682E-04 3.1442564E-04 3.1439556E-04 3.1446591E-04 3.1467016E-04
3.1475565E-04 3.1467365E-04 3.1505820E-04 3.1505820E-04 3.1505820E-04 3.1505820E-04 3.1505820E-04 3.1505820E-04
3.1485724E-04 3.1500566E-04 3.1496590E-04 3.1493705E-04 3.1493705E-04 3.1493705E-04 3.1493705E-04 3.1493705E-04
3.1499689E-04 3.1496590E-04 3.1461182E-04 3.1451682E-04 3.1442564E-04 3.1439556E-04 3.1446591E-04 3.1467016E-04
3.1467365E-04 3.1461182E-04 3.1451682E-04 3.1442564E-04 3.1439556E-04 3.1446591E-04 3.1467016E-04 3.1467365E-04
3.1500566E-04 3.1505820E-04 3.1505820E-04 3.1505820E-04 3.1505820E-04 3.1505820E-04 3.1505820E-04 3.1505820E-04
3.1496590E-04 3.1493705E-04 3.1493705E-04 3.1493705E-04 3.1493705E-04 3.1493705E-04 3.1493705E-04 3.1493705E-04
3.1461182E-04 3.1451682E-04 3.1442564E-04 3.1439556E-04 3.1446591E-04 3.1467016E-04 3.1467365E-04 3.1500566E-04
3.1505820E-04 3.1506870E-04 3.1506562E-04 3.1505710E-04 3.1504266E-04 3.1502400E-04 3.1502400E-04 3.1502400E-04
5.6239200E-06 5.6602822E-06 5.7030755E-06 5.7473146E-06 5.7861705E-06 5.8216338E-06 5.8648701E-06 5.9257070E-06
5.9992466E-06 6.0721584E-06 6.1363353E-06 6.2009919E-06 6.2247980E-06 6.2046267E-06 6.0865673E-06 5.9306476E-06
5.7684544E-06 5.6547121E-06 5.6017010E-06 5.5844275E-06 5.5824495E-06 5.5869516E-06 5.5995508E-06 5.6239200E-06
5.6602822E-06 5.7030755E-06 5.7473146E-06 5.7861705E-06 5.8216338E-06 5.8648701E-06 5.9257070E-06 5.9992466E-06
5.0721584E-06 6.1363353E-06 6.2009919E-06 6.2247980E-06 6.2046267E-06 6.0865673E-06 5.9306476E-06 5.7684544E-06
5.6547121E-06 5.6017010E-06 5.5844275E-06 5.5824495E-06 5.5869516E-06 5.5995508E-06 5.6239200E-06 5.9992466E-06
5.7030755E-06 5.7473146E-06 5.7861705E-06 5.8216338E-06 5.8648701E-06 5.9257070E-06 5.9992466E-06 5.6602822E-06
6.1363353E-06 6.2009919E-06 6.2247980E-06 6.2046267E-06 6.0865673E-06 5.9306476E-06 5.7684544E-06 5.6547121E-06
5.6017010E-06 5.5844275E-06 5.5824495E-06 5.5869516E-06 5.5995508E-06 5.6239200E-06 5.9992466E-06 5.6602822E-06
9.9303600E-12 1.0133041E-11 1.0315558E-11 1.0459090E-11 1.0512444E-11 1.0515709E-11 1.0654593E-11 1.1131837E-11
1.1930260E-11 1.2833108E-11 1.3693774E-11 1.4720614E-11 1.5492479E-11 1.6275552E-11 1.5740753E-11 1.4153022E-11
1.1850625E-11 9.8119282E-12 8.9716894E-12 8.9745790E-12 8.9745790E-12 8.9745790E-12 8.9745790E-12 8.9745790E-12
1.0133041E-11 1.0315558E-11 1.0459090E-11 1.0512444E-11 1.0515709E-11 1.0654593E-11 1.1131837E-11 1.1930260E-11
1.2833108E-11 1.3693774E-11 1.4720614E-11 1.5492479E-11 1.6275552E-11 1.5740753E-11 1.4153022E-11 1.1850625E-11
9.8119282E-12 8.9716894E-12 8.9745790E-12 8.9745790E-12 8.9745790E-12 8.9745790E-12 8.9745790E-12 8.9745790E-12
1.0135558E-11 1.0459090E-11 1.0512444E-11 1.0515709E-11 1.0654593E-11 1.1131837E-11 1.1930260E-11 1.2833108E-11
1.3693774E-11 1.4720614E-11 1.5492479E-11 1.6275552E-11 1.5740753E-11 1.4153022E-11 1.1850625E-11 9.8119282E-12
8.9716894E-12 8.9745790E-12 8.9745790E-12 8.9745790E-12 8.9745790E-12 8.9745790E-12 8.9745790E-12 8.9745790E-12
1.2691400E-10 1.2515727E-10 1.2381082E-10 1.2254941E-10 1.2080821E-10 1.1883032E-10 1.1807289E-10 1.2019209E-10
1.2517224E-10 1.3132024E-10 1.3749699E-10 1.4588913E-10 1.5407723E-10 1.6582781E-10 1.6942488E-10 1.6411289E-10
1.5083575E-10 1.3571490E-10 1.2835028E-10 1.2782938E-10 1.2876088E-10 1.2905563E-10 1.2839354E-10 1.2691400E-10
1.2515727E-10 1.2381082E-10 1.2254941E-10 1.2080821E-10 1.1883032E-10 1.1807289E-10 1.2019209E-10 1.2517224E-10
1.3132024E-10 1.3749699E-10 1.4588913E-10 1.5407723E-10 1.6582781E-10 1.6942488E-10 1.6411289E-10 1.5083575E-10
1.3571490E-10 1.2835028E-10 1.2782938E-10 1.2876088E-10 1.2905563E-10 1.2839354E-10 1.2691400E-10 1.2515727E-10
1.2381082E-10 1.2254941E-10 1.2080821E-10 1.1883032E-10 1.1807289E-10 1.2019209E-10 1.2517224E-10 1.3132024E-10
1.3749699E-10 1.4588913E-10 1.5407723E-10 1.6582781E-10 1.6942488E-10 1.6411289E-10 1.5083575E-10 1.3571490E-10
1.2835028E-10 1.2782938E-10 1.2876088E-10 1.2905563E-10 1.2839354E-10 1.2691400E-10 1.2515727E-10 1.3132024E-10
1.7317200E-07 1.7721829E-07 1.7970502E-07 1.8004258E-07 1.7648628E-07 1.7095664E-07 1.7075896E-07 1.8447604E-07
2.1490865E-07 2.5504971E-07 2.9995857E-07 3.7428040E-07 4.5420162E-07 5.7189776E-07 5.6724403E-07 5.5990030E-07
2.9083002E-07 1.7581928E-07 1.4185696E-07 1.4128161E-07 1.4811355E-07 1.5722138E-07 1.6620917E-07 1.7317200E-07
1.7721829E-07 1.7970502E-07 1.8004258E-07 1.7648628E-07 1.7095664E-07 1.7075896E-07 1.8447604E-07 2.1490865E-07
2.5504971E-07 2.9995857E-07 3.7428040E-07 4.5420162E-07 5.7189776E-07 5.6724403E-07 5.5990030E-07 2.9083002E-07
1.7581928E-07 1.4185696E-07 1.4128161E-07 1.4811355E-07 1.5722138E-07 1.6620917E-07 1.7317200E-07 1.7721829E-07
1.7970502E-07 1.8004258E-07 1.7648628E-07 1.7095664E-07 1.7075896E-07 1.8447604E-07 2.1490865E-07 2.5504971E-07
2.9995857E-07 3.7428040E-07 4.5420162E-07 5.7189776E-07 5.6724403E-07 5.5990030E-07 2.9083002E-07 1.7581928E-07
1.4185696E-07 1.4128161E-07 1.4811355E-07 1.5722138E-07 1.6620917E-07 1.7317200E-07 1.7721829E-07 1.7970502E-07
7.5791800E-10 7.8111140E-10 7.9861544E-10 8.0693481E-10 8.0693481E-10 7.9701261E-10 7.7744679E-10 7.8280420E-10
1.0077276E-09 1.2096770E-09 1.4373165E-09 1.8106757E-09 2.032795E-09 2.6948357E-09 2.1152827E-09 2.152827E-09
1.3072919E-09 7.7766358E-10 6.2276265E-10 6.1713629E-10 6.4497725E-10 6.8376725E-10 7.2404147E-10 7.5791800E-10
7.8111140E-10 7.9861544E-10 8.0693481E-10 8.0693481E-10 7.9701261E-10 7.7744679E-10 7.8280420E-10 8.5455809E-10
1.2096770E-09 1.4373165E-09 1.8106757E-09 2.032795E-09 2.6948357E-09 2.1152827E-09 2.152827E-09 1.3072919E-09
7.7766358E-10 6.2276265E-10 6.1713629E-10 6.4497725E-10 6.8376725E-10 7.2404147E-10 7.5791800E-10 7.8111140E-10
7.9861544E-10 8.0693481E-10 7.9701261E-10 7.7744679E-10 7.8280420E-10 8.5455809E-10 1.0077276E-09 1.2096770E-09

204

[illegible]

HPT1 - Max power - Mass averaged:

1	21	29	0	287.03	0	
	1.17883E-05	0.00000E+00				
	7.29015E-02	0.00000E+00				
	1.48014E-01	2.33000E-01				
	2.98833E-02	0.00000E+00				
	7.87784E-12	0.00000E+00				
	2.61288E-08	0.00000E+00				
	3.74385E-06	0.00000E+00				
	5.41438E-08	0.00000E+00				
	6.67006E-09	0.00000E+00				
	3.15494E-04	0.00000E+00				
	4.99679E-06	0.00000E+00				
	6.03887E-12	0.00000E+00				
	7.81056E-11	0.00000E+00				
	7.87986E-08	0.00000E+00				
	3.09774E-10	0.00000E+00				
	2.18535E-05	0.00000E+00				
	1.74444E-06	0.00000E+00				
	2.29168E-13	0.00000E+00				
	5.94824E-12	0.00000E+00				
	1.22867E-16	0.00000E+00				
	3.60300E-13	0.00000E+00				
	5.55086E-17	0.00000E+00				
	1.15043E-10	0.00000E+00				
	7.48842E-01	7.67000E-01				
	0.00000E+00	0.00000E+00				
	0.00000E+00	0.00000E+00				
	0.00000E+00	0.00000E+00				
	4.36994E-10	0.00000E+00				
	2.44454E-21	0.00000E+00				
	1359.795	1570803	175.9363	0.0038	0	1
	1359.712	1570423	176.2318	0.0038	0	1
	1358.812	1566410	179.302	0.0038	0	1
	1349.544	1526507	214.2155	0.003799999	0	1
	1338.676	1484815	253.0134	0.003790001	0	1
	1324.634	1431395	279.816	0.003800001	0	1
	1307.769	1368246	285.5765	0.003799999	0	1
	1298.097	1332669	257.3565	0.003800001	0	1
	1289.669	1303722	232.7334	0.003799997	0	1
	1285.294	1293009	207.5762	0.003790003	0	1
	1280.689	1258006	215.10745	0.00227	0	1
	1271.736	1209131	233.2347	0.00228	0	1
	1253.796	1148566	294.5791	0.00227	0	1
	1247.374	1131973	338.2817	0.00228	0	1
	1236.726	1098380	369.9686	0.00227	0	1
	1218.939	1042952	394.7301	0.00228	0	1
	1194.913	969092.2	405.5363	0.00228	0	1
	1183.045	926285.8	383.9227	0.00227	0	1
	1181.315	917795.9	352.4142	0.00228	0	1
	1195.526	959228.8	300.664	0.00197	0	1
	1202.61	980842.3	271.0783	0	0	1

HPT1 - Max power - High temperature streamline:

1	80	29	0	287.03	0	
	1.17883E-05	0.00000E+00				
	7.29015E-02	0.00000E+00				
	1.48014E-01	2.33000E-01				
	2.98833E-02	0.00000E+00				
	7.87784E-12	0.00000E+00				
	2.61288E-08	0.00000E+00				
	3.74385E-06	0.00000E+00				
	5.41438E-08	0.00000E+00				
	6.67006E-09	0.00000E+00				
	3.15494E-04	0.00000E+00				
	4.99679E-06	0.00000E+00				
	6.03887E-12	0.00000E+00				
	7.81056E-11	0.00000E+00				
	7.87986E-08	0.00000E+00				
	3.09774E-10	0.00000E+00				
	2.18535E-05	0.00000E+00				
	1.74444E-06	0.00000E+00				
	2.29168E-13	0.00000E+00				
	5.94824E-12	0.00000E+00				
	1.22867E-16	0.00000E+00				
	3.60300E-13	0.00000E+00				
	5.55086E-17	0.00000E+00				
	1.15043E-10	0.00000E+00				
	7.48842E-01	7.67000E-01				
	0.00000E+00	0.00000E+00				
	0.00000E+00	0.00000E+00				
	0.00000E+00	0.00000E+00				
	4.36994E-10	0.00000E+00				
	2.44454E-21	0.00000E+00				
	1361.67	1579350	163.6325233	0.000974026	0	1
	1361.731133	1579629.425	163.2297162	0.000974026	0	1
	1361.859356	1580212.748	162.3276685	0.000974026	0	1
	1362.045129	1581059.69	161.0120533	0.000974026	0	1
	1362.3448	1582430.668	158.8705417	0.000974026	0	1
	1362.716561	1584132.707	156.1941047	0.000974026	0	1
	1363.187816	1586296.968	152.6077004	0.000974026	0	1
	1363.702964	1588664.787	148.6079543	0.000974026	0	1
	1364.254994	1591211.35	144.1493071	0.000974026	0	1
	1364.740035	1593429.721	139.7613897	0.000974026	0	1
	1365.013192	1594685.8	136.381452	0.000974026	0	1
	1364.936523	1594337.736	134.8354564	0.000974026	0	1
	1364.452676	1592293.788	135.5192932	0.000974026	0	1
	1363.734687	1589264.619	137.8009499	0.000974026	0	1
	1362.954266	1585520.713	140.9655827	0.000974026	0	1
	1362.143905	1581204.741	144.7854538	0.000974026	0	1
	1361.31015	1576323.393	149.0393239	0.000974026	0	1
	1360.469281	1571068.214	153.4957755	0.000974026	0	1
	1359.548987	1565302.737	158.1249937	0.000974026	0	1
	1358.541125	1558991.823	162.8804288	0.000974026	0	1
	1357.438706	1552166.183	167.7122939	0.000974026	0	1
	1356.220931	1544789.46	172.5968847	0.000974026	0	1
	1354.876306	1536784.723	177.4999794	0.000974026	0	1
	1353.383465	1528060.375	182.3620107	0.000974026	0	1
	1351.828607	1518645.336	187.0398626	0.000974026	0	1
	1350.198608	1508591.203	191.3673109	0.000974026	0	1
	1348.521538	1497951.842	195.1452903	0.000974026	0	1
	1346.643097	1486807.582	198.2114491	0.000974026	0	1
	1344.40452	1474694.669	200.5048012	0.000974026	0	1
	1341.584896	1460743.398	202.3211892	0.000974026	0	1
	1337.945957	1444059.825	204.1661148	0.000974026	0	1
	1333.002734	1422694.55	207.2876771	0.000974026	0	1

1326.192181	1393886.381	213.7535496	0.000974026	0	1
1319.047329	1365927.603	228.3462013	0.000974026	0	1
1320.246711	1373860.776	216.0797396	0.000974026	0	1
1301.253438	1347200.356	214.4186074	0.000974026	0	1
1294.163824	1327025.625	219.0556362	0.000974026	0	1
1289.593153	1311139.441	220.4491074	0.000974026	0	1
1286.663243	1300574.15	220.1306449	0.000974026	0	1
1284.582895	1293575.863	218.4710914	0.000778679	0	1
1282.58151	1249358.725	218.6341176	0.000583333	0	1
1283.826663	1254086.8	219.2939185	0.000583333	0	1
1284.724178	1257542.561	219.5469849	0.000583333	0	1
1285.955472	1262300.125	218.0146573	0.000583333	0	1
1287.513907	1268338.567	214.8767426	0.000583333	0	1
1289.34823	1275488.125	210.4504239	0.000583333	0	1
1291.30807	1283159.944	205.4279798	0.000583333	0	1
1292.910141	1289454.385	201.5639105	0.000583333	0	1
1294.101112	1294101.381	199.6967323	0.000583333	0	1
1294.815722	1296849.155	199.901098	0.000583333	0	1
1294.303468	1294999.942	203.5542228	0.000583333	0	1
1293.404184	1291706.919	208.5842319	0.000583333	0	1
1292.227073	1287430.792	213.9890612	0.000583333	0	1
1290.823817	1282214.178	219.7755159	0.000583333	0	1
1289.183985	1276026.816	225.650816	0.000583333	0	1
1287.383554	1269183.12	231.5872877	0.000583333	0	1
1285.405252	1261622.65	237.5970562	0.000583333	0	1
1283.251739	1253352.085	243.6246136	0.000583333	0	1
1280.934675	1244372.688	249.6141627	0.000583333	0	1
1278.448822	1234636.376	255.5826876	0.000583333	0	1
1275.752764	1224062.804	261.5443532	0.000583333	0	1
1272.774086	1212436.959	267.5323968	0.000583333	0	1
1269.377606	1199319.479	273.7337962	0.000583333	0	1
1265.572569	1184454.479	280.3494671	0.000583333	0	1
1261.28942	1167675.024	287.5356723	0.000583333	0	1
1256.353664	1148599.814	295.4885152	0.000583333	0	1
1250.646129	1127118.716	304.1021445	0.000583333	0	1
1244.318943	1103821.814	313.0604302	0.000583333	0	1
1237.33245	1078615.991	322.4144125	0.000583333	0	1
1229.14201	1049886.253	332.8202322	0.000583333	0	1
1218.730098	1014461.748	346.5393325	0.000583333	0	1
1205.731857	971575.4713	366.4237725	0.000583333	0	1
1192.502914	928452.9769	393.2397397	0.000583333	0	1
1188.169418	912710.0383	416.661042	0.000583333	0	1
1216.456088	999538.5689	366.9117658	0.000583333	0	1
1221.600443	1024556.716	335.9278348	0.000583333	0	1
1217.887545	1020755.464	321.0972363	0.000583333	0	1
1213.432511	1007409.083	315.0504912	0.000583333	0	1
1209.427894	994491.3791	311.2279984	0.000583333	0	1
1205.671597	984280.3104	307.8753852	0	0	1

HPT1 - Max power - Low temperature streamline:

1	80	29	0	287.03	0	
	1.17883E-05	0.00000E+00				
	7.29015E-02	0.00000E+00				
	1.48014E-01	2.33000E-01				
	2.98833E-02	0.00000E+00				
	7.87784E-12	0.00000E+00				
	2.61288E-08	0.00000E+00				
	3.74385E-06	0.00000E+00				
	5.41438E-08	0.00000E+00				
	6.67006E-09	0.00000E+00				
	3.15494E-04	0.00000E+00				
	4.99679E-06	0.00000E+00				
	6.03887E-12	0.00000E+00				
	7.81056E-11	0.00000E+00				
	7.87986E-08	0.00000E+00				
	3.09774E-10	0.00000E+00				
	2.18535E-05	0.00000E+00				
	1.74444E-06	0.00000E+00				
	2.29168E-13	0.00000E+00				
	5.94824E-12	0.00000E+00				
	1.22867E-16	0.00000E+00				
	3.60300E-13	0.00000E+00				
	5.55086E-17	0.00000E+00				
	1.15043E-10	0.00000E+00				
	7.48842E-01	7.67000E-01				
	0.00000E+00	0.00000E+00				
	0.00000E+00	0.00000E+00				
	0.00000E+00	0.00000E+00				
	4.36994E-10	0.00000E+00				
	2.44454E-21	0.00000E+00				
	1361.493333	1578546.667	164.839656	0.000974026	0	1
	1361.466192	1578425.56	164.5952474	0.000974026	0	1
	1361.604002	1579053.754	163.5284478	0.000974026	0	1
	1361.804629	1579966.982	162.0800594	0.000974026	0	1
	1362.145143	1581521.66	159.5112592	0.000974026	0	1
	1362.594095	1583581.799	156.0765876	0.000974026	0	1
	1363.232964	1586517.578	150.9349891	0.000974026	0	1
	1364.042053	1590234.226	144.1284106	0.000974026	0	1
	1365.162053	1595407.78	134.1615632	0.000974026	0	1
	1366.795742	1602985.596	118.3095485	0.000974026	0	1
	1369.272409	1614682.489	89.43887755	0.000974026	0	1
	1364.526187	1584822.24	51.07783472	0.000974026	0	1
	1291.527273	1329161.844	315.6673148	0.000974026	0	1
	1277.678082	1299682.65	377.7369451	0.000974026	0	1
	1275.978669	1326068.804	370.1731122	0.000974026	0	1
	1269.402691	1309584.362	387.5991185	0.000974026	0	1
	1257.998873	1285392.64	403.5493714	0.000974026	0	1
	1245.793181	1258396.257	417.5255673	0.000974026	0	1
	1232.620969	1227732.865	429.6271387	0.000974026	0	1
	1218.498533	1193735.771	438.8576732	0.000974026	0	1
	1203.778588	1157823.321	441.8781725	0.000974026	0	1
	1189.737367	1125553.566	434.522286	0.000974026	0	1
	1177.237046	1099213.408	417.5474688	0.000974026	0	1
	1167.504991	1083412.816	388.1184497	0.000974026	0	1
	1163.923057	1089289.441	341.2596273	0.000974026	0	1
	1168.342227	1125630.029	290.5231776	0.000974026	0	1
	1172.833301	1169261.064	253.0616594	0.000974026	0	1
	1173.29684	1204656.195	231.0850281	0.000974026	0	1
	1167.346347	1218667.702	219.5558085	0.000974026	0	1
	1159.752545	1222097.051	209.8811117	0.000974026	0	1
	1153.419329	1226853.325	199.6633722	0.000974026	0	1
	1146.829021	1232944.565	188.3923005	0.000974026	0	1

1143.312018	1243698.304	175.4889752	0.000974026	0	1
1140.402407	1258885.435	161.0597535	0.000974026	0	1
1140.036382	1281944.708	145.2191088	0.000974026	0	1
1175.145197	1335021.695	90.38037157	0.000974026	0	1
1211.306202	1369922.242	147.4152696	0.000974026	0	1
1207.12102	1337729.59	165.8133053	0.000974026	0	1
1206.773496	1319203.566	175.0043011	0.000974026	0	1
1208.699917	1307136	180.816468	0.000778679	0	1
1287.330753	1267688.4	212.7221961	0.000583333	0	1
1287.762684	1269355.101	211.6905576	0.000583333	0	1
1288.820598	1273488.41	206.779503	0.000583333	0	1
1290.589866	1280431.457	197.7692586	0.000583333	0	1
1293.468976	1291761.396	182.5206961	0.000583333	0	1
1297.547167	1307914.898	158.9508226	0.000583333	0	1
1303.602496	1332182.473	118.4879717	0.000583333	0	1
1164.931084	870116.5997	253.5501099	0.000583333	0	1
1144.175412	853904.2104	385.1477051	0.000583333	0	1
1131.419472	839969.4267	445.4349092	0.000583333	0	1
1123.69347	834659.5046	481.7317531	0.000583333	0	1
1116.675521	828255.7264	508.2110508	0.000583333	0	1
1109.91928	820438.2077	530.0886496	0.000583333	0	1
1102.738785	810998.8817	545.8099993	0.000583333	0	1
1098.641442	799476.4425	558.8569498	0.000583333	0	1
1094.594253	784471.2937	571.6215983	0.000583333	0	1
1083.994215	761175.8426	585.1416047	0.000583333	0	1
1073.370783	736268.411	594.5327905	0.000583333	0	1
1062.381619	710342.4874	599.7291891	0.000583333	0	1
1051.045407	682847.2009	599.3197894	0.000583333	0	1
1039.160949	654660.4653	595.8591248	0.000583333	0	1
1031.110655	631251.7175	582.3609096	0.000583333	0	1
1026.345079	616296.2965	560.2919372	0.000583333	0	1
1028.250405	616917.7426	525.6422008	0.000583333	0	1
1040.345257	643772.7946	476.6042655	0.000583333	0	1
1058.673726	689551.6292	422.8428595	0.000583333	0	1
1078.47177	746780.4128	375.6378799	0.000583333	0	1
1092.282331	793869.6333	337.067325	0.000583333	0	1
1100.246523	828547.8406	306.7501579	0.000583333	0	1
1104.8363	855583.6909	284.8229632	0.000583333	0	1
1106.83783	876502.0781	269.4715436	0.000583333	0	1
1105.5863	886148.2441	257.312107	0.000583333	0	1
1105.345968	893562.7729	244.0794738	0.000583333	0	1
1105.586062	913599.3989	229.8527779	0.000583333	0	1
1106.31671	929963.5037	214.9652901	0.000583333	0	1
1106.954414	941075.4732	202.9952434	0.000583333	0	1
1175.93931	1076786.092	54.5923099	0.000583333	0	1
1185.101995	1075679.495	120.8449247	0.000583333	0	1
1180.331047	1046363.434	160.4974738	0.000583333	0	1
1174.886129	1023109.349	179.9368539	0	0	1

HPT1 exit to nozzle exit - Max power - Mass Averaged:

1	39	29	0	287.03	0
1.1183140e-05	0.000000E+00				
7.2902410e-02	0.000000E+00				
1.4801330e-01	0.000000E+00				
2.9883340e-02	0.000000E+00				
9.6843060e-12	0.000000E+00				
4.4202050e-08	0.000000E+00				
3.4493320e-06	0.000000E+00				
3.7568700e-08	0.000000E+00				
3.8295280e-08	0.000000E+00				
3.1464130e-04	0.000000E+00				
5.9002840e-06	0.000000E+00				
1.4215190e-11	0.000000E+00				
1.5348320e-10	0.000000E+00				
4.8974110e-07	0.000000E+00				
2.1678720e-09	0.000000E+00				
2.1842190e-05	0.000000E+00				
1.7583280e-06	0.000000E+00				
9.7461800e-14	0.000000E+00				
1.0319860e-11	0.000000E+00				
1.9406000e-16	0.000000E+00				
3.2799880e-13	0.000000E+00				
4.1740790e-17	0.000000E+00				
8.1290550e-10	0.000000E+00				
7.4884160e-01	0.000000E+00				
0.0000000e+00	0.000000E+00				
0.0000000e+00	0.000000E+00				
0.0000000e+00	0.000000E+00				
7.1511560e-10	0.000000E+00				
2.4445390e-21	0.000000E+00				
1202.61	980842.3	260	0.02	0	1
1184.993301	955524.7629	264.378224	0.02	0	1
1146.54476	831071.8	283.547	0.02	0	1
1111.539513	723225.8061	303.839296	0.02	0	1
1079.720221	630506.8605	324.569528	0.02	0	1
1050.839058	551500.6221	345.052112	0.02	0	1
1024.657707	484858.3293	364.601464	0.02	0	1
1000.94736	429296.8	382.532	0.02	0	1
979.4887209	383598.4317	398.158136	0.02	0	1
960.0720028	346611.2013	410.794288	0.02	0	1
942.4969292	317248.6653	419.754872	0.02	0	1
926.5727337	294489.9597	424.354304	0.02	0	1
912.11816	277379.8	423.907	0.02	0	1
898.961462	265028.4813	417.727376	0.02	0	1
886.9404038	256611.8781	405.129848	0.02	0	1
875.9022595	251371.4445	385.428832	0.02	0	1
865.7038134	248614.2141	357.938744	0.02	0	1
856.21136	247712.8	321.974	0.02	0	1
847.3007039	248105.3949	276.849016	0.02	0	1
838.8571599	249295.7709	247.8614208	0.02	0	1
830.7755529	250853.2797	239.9685248	0.02	0	1
822.9602179	252412.8525	232.1420512	0.02	0	1
815.325	253675	224.382	0.02	0	1
807.7932547	254405.8125	216.6883712	0.02	0	1
800.2978473	254436.9597	209.0611648	0.02	0	1
792.7811535	253665.6909	201.5003808	0.02	0	1
785.1950591	252054.8349	194.0060192	0.02	0	1
777.50096	249632.8	186.57808	0.02	0	1
769.6697622	246493.5741	179.2165632	0.02	0	1
761.6818819	242796.7245	171.9214688	0.02	0	1
753.5272454	238767.3981	164.6927968	0.02	0	1
745.2052892	234696.3213	157.5305472	0.02	0	1
736.72496	230939.8	145.4	0.02	0	1
728.1047145	227919.7197	148.9824	0.01	0	1
723.7504913	226835.616	176.7896	0.01	0	1
719.3725196	226123.5453	230.0912	0.01	0	1
714.9757813	225854.6875	315	0.01	0	1
710.5658524	226104.3213	437.6288	0.01	0	1
706.1489037	226951.824	604.0904	0	0	1

APPENDIX F

MEDIA CONTAINING SUPPLEMENTAL DATA

Several of the computational results obtained in this research are time dependent and thus are best presented with an animation. The attached Compact Disc (CD) contains several figures which were referenced in this thesis. The figures were formatted using HTML which can be viewed from a typical web browser such as Netscape Communicator 4.7 or Internet Explorer 5.0. To view these figures simply insert the CD into a personal computer, launch the web browser, and open the file "appendix_f.html."

An index of the figures is given below for convenience:

4 Validation

4.4 Convergence Criteria Study

4.4.3 Results

Figure F.1 Convergence time evolution for mass fraction of O

Figure F.2 Convergence time evolution for mass fraction of OH

Figure F.3 Convergence time evolution for mass fraction of SO₃

5 Modeling the NASA/DERA Engine Test

5.4 High Fidelity Modeling

5.4.2 High Fidelity Modeling Results

Figure F.4 Static temperature for max power wake model case

Figure F.5 Mass fraction of SO₃ for max power wake model case

Figure F.6 Mass fraction of SO₃ for max power wake model case (full stage view)

Figure F.7 Static temperature for non-uniform max power wake model case

Figure F.8 Mass fraction of SO₃ for non-uniform max power wake model case

Appendix A Princeton VPFR Validation Modeling

"Unsteady Non-Reacting Flow Solution"

Figure F.9 Initial transient

Figure F.10 One vortex shedding cycle

Finally, the files "SMThesis.doc" and "SMThesis.pdf" is contains the text of this thesis in Microsoft Word 97 and Adobe PDF format, respectively.

REFERENCES

- [1] Lukachko, S.P. Research on the Science and Politics of the Atmospheric Effects of Aviation Debate. S.M. Thesis. Massachusetts Institute of Technology. 1997.
- [2] Penner, J.E., D.H. Lister, D.J. Griggs, D.J. Dokken, and M. McFarland. Aviation and the Global Atmosphere. New York: Cambridge University Press, 1999.
- [3] Penner, J.E., D.H. Lister, D.J. Griggs, D.J. Dokken, and M. McFarland. Summary for Policymakers: Aviation and the Global Atmosphere. A special report of IPCC Working Groups I and III: Published for the Intergovernmental Panel on Climate Change.
- [4] GAO/RCED-00-57. Aviation and the Environment: Aviation's Effects on the Global Atmosphere are Potentially Significant and Expected to Grow. United States General Accounting Office: Report to the Honorable James L. Oberstar, Ranking Democratic Member, Committee on Transportation and Infrastructure, House of Representative, February, 2000.
- [5] <http://hyperion.gsfc.nasa.gov/AEAP/1385links.html>
- [6] <http://hyperion.gsfc.nasa.gov/AEAP/1400links.html>
- [7] Kerrebrock, J.L. Aircraft Engines and Gas Turbines, 2nd Ed.. Cambridge, MA: The MIT Press, 1992. Chapter 4.
- [8] <http://hyperion.gsfc.nasa.gov/AEAP/aesa.html>
- [9] <http://hyperion.gsfc.nasa.gov/AEAP/1381links.html>
- [10] Howard, R.P., et al. "Experimental Characterization of Gas Turbine Emissions at Simulated Flight Altitude Conditions." AEDC-TR-96-3. September 1996.
- [11] ICAO, International Civil Aviation Organization. ICAO Engine Exhaust Emissions Data Bank, ICAO Doc 9646-AN/943. 1st ed. : 1995.
- [12] Lukachko, S.P., I.A. Waitz, R.C. Miake-Lye, R.C. Brown, M.R. Anderson, and W.N. Dawes. "Simulation of Post-Combustor Chemical Evolution in a Gas Turbine Engine." As submitted to Journal of Propulsion and Power. 1998.
- [13] Miake-Lye, R.C., M. Martinez-Sanchez, R.C. Brown, C.E. Kolb. "Plume and wake-dynamics, mixing, and chemistry behind a high speed civil transport aircraft." Journal of Aircraft. 30. July-August 1993: pp. 467-479.
- [14] Brown, R.C., R.C. Miake-Lye, M.R. Anderson, C.E. Kolb, and T.J. Resch. "Aerosol dynamics in near field aircraft plumes." Journal of Geophysical Research. 101(D17). October 20, 1996: pp.22939-22953.
- [15] Schumann, U., P. Konopka, R. Baumann, R. Busen, T. Gerz, H. Schlager, P. Schulte, and H. Volkert. "Estimation of diffusion parameters of aircraft exhaust plumes near the tropopause from nitric oxide and turbulence measurements." Journal of Geophysical Research. 100(D7). July 20, 1995: pp.14147-14162.
- [16] Anderson, M.R., R.C. Miake-Lye, R.C. Brown, and C.E. Kolb. "Calculation of exhaust plume structure and emissions of the ER-2 aircraft in the stratosphere." Journal of Geophysical Research. 101. February 20, 1996: pp. 4025-4032.
- [17] Quackenbush, T.R., M.E. Teske, and A.J. Bilanin. "Computation of Wake/Exhaust Mixing Downstream of Advanced Transport Aircraft." AIAA-93-2944. Presented at AIAA 24th Fluid Dynamics Conference. Orlando, Florida. July 6-9, 1993.

- [18] Miake-Lye, R.C., R.C. Brown, M.R. Anderson, and C.E. Kolb. "Calculations of Condensation and Chemistry in an Aircraft Contrail." In *Impact of Emissions from Aircraft and Spacecraft Upon the Atmosphere*, Proceedings. U. Schumann and D. Wurzel, eds. Koln, Germany. April 18-20, 1994.
- [19] Schumann, U., AERONOX: The impact of NO_x Emissions from Aircraft Upon the Atmosphere at Flight Altitudes 8-15km: Final Report to the Commission of European Communities. Brussels, Belgium: EC-DLR, August 1995.
- [20] National Research Council. *A Review of NASA's Atmospheric Effects of Stratospheric Aircraft Project*. Washington DC: National Academy Press, 1999.
- [21] <http://hyperion.gsfc.nasa.gov/AEAP/97NRA.html>
- [22] <http://hyperion.gsfc.nasa.gov/AEAP/1333links.html>
- [23] Mueller, M.A., R.A. Yetter, F.L. Dryer. "Kinetic Modeling of the CO/H₂O/O₂/NO/SO₂ System: Implication for High-Pressure Fall-off in the SO₂ + O (+M) = SO₃ (+M) Reaction." *International Journal of Chemical Kinetics* 32. January 2000: pp. 317-339.
- [24] Glarborg, P., D. Kubel, K. Dam-Johansen, H-M. Chiang and J.W. Bozzelli. "Impact of SO₂ and NO on CO oxidation under Post-Flame Conditions." *International Journal of Chemical Kinetics* 28. March 1996: pp. 773-790.
- [25] DeGraaff, D.B., E.P. Zimmitti, F.L. Dryer. *A Study of the Mixing Characteristics of the Variable Pressure Flow Reactor: Final Report. Undergraduate Independent Work. Princeton University. 1993.*
- [26] Held, T.H. *The Oxidation of Methanol, Isobutene and Methyl tertiary-Butyl Ether. PhD. Thesis. Princeton University. 1993.*
- [27] Veermersch, M.L. *A Variable Pressure Flow Reactor for Chemical Kinetic Studies: Hydrogen, Methane, and Butane Oxidation at 1 to 10 Atmospheres and 880 to 1040 K. PhD. Thesis. Princeton University. 1991.*
- [28] Lukachko, S.P., I.A. Waitz, R.C. Miake-Lye, R.C. Brown, and M.R. Anderson. "Production of Sulfate Aerosol Precursors in the Turbine and Exhaust Nozzle of an Aircraft Engine." *Journal of Geophysical Research* 103 (D13). July 20, 1998: pp. 16159-16174.
- [29] Tremmel, H.G., and U. Schumann. "Model Simulations of Fuel Sulfur Conversion Efficiencies in an Aircraft Engine: Dependence on Reaction Rate Constants and Initial Species Mixing Ratios" *Aerosp. Sci. Technol* 3. 1999: pp. 17-430.
- [30] Brown, R.C. et al. "Aircraft Exhaust Sulfur Emissions." *Geophysical Research Letters* 23. December 1, 1996: pp. 3603-3606.
- [31] Lukachko, S. Personal Communication, 1998-2000.
- [32] Waitz, I.A. Personal Communication, 1998-2000.
- [33] Wilson, Chris. Personal Communications, June 2000.
- [34] Clague, Andrew or Whiteman, Mike. *Internal Project Memorandum, DERA and MIT/ARI Proprietary, 1998-2000.*
- [35] Caleb Dhanasekaran and Albert Demarange. Personal Communications, January/March 1999.
- [36] Mattingly, J.D. *Elements of Gas Turbine Propulsion*. New York: McGraw-Hill, Inc., 1996.
- [37] Horlock, J.H. *Axial Flow Turbines : Fluid Mechanics and Thermodynamics*. Malabar, Florida: Krieger Publishing Company, 1985.
- [38] Munson, B.R., D.F. Young, and T.H. Okiishi. *Fundamentals of Fluid Mechanics, 2nd Ed.* New York: John Wiley and Sons, Inc., 1994.

- [39] Fox and Kline, S.J. "Flow Patterns in Curvilinear Subsonic Diffusers." *Transactions of the ASME*. Series E, 1962.
- [40] Idelchik, I.E. *Handbook of Hydraulic Resistance*, 3rd Ed. Bergell House, 1996.
- [41] Runstadler, P.W., F.X. Dolan, and R.C. Dean. *Diffuser Data Book Creare Technical Note TN-186*. New York: Creare, Inc., 1975.
- [42] Bury, M.E. *Influence of Reynolds Number and Blade Geometry on Low Pressure Turbine Performance*. S.M. Thesis. Massachusetts Institute of Technology. 1997.
- [43] Guenette, G.R. Jr. *A Fully Scaled Short Duration Turbine Experiment*. PhD. Thesis. Massachusetts Institute of Technology. 1985.
- [44] O'Sullivan, M.N. *A Computational Study of the Effects of Viscosity on Lobed Mixer Flowfields*. S.M. Thesis. Massachusetts Institute of Technology. 1993.
- [45] Dietz, H. "Linux Parallel Processing HOWTO." V980105. January 5, 1998.
- [46] Gropp, W., and E. Lusk. *User's Guide for mpich, A Portable Implementation of MPI*. Chicago: University of Chicago Argonne National Laboratory, Mathematics and Computer Science Division, 1996. ANL/MCS-TM-ANL-96/6.
- [47] Gropp, W., and E. Lusk. *Installation Guide to mpich, A Portable Implementation of MPI*. Chicago: University of Chicago Argonne National Laboratory, Mathematics and Computer Science Division, 1996. ANL/MCS-TM-ANL-96/5.
- [48] Lukachko, S. *CNEWT Primer*. November 1998. Unpublished Work.
- [49] Dawes, W.N. *The Solution-Adaptive 3D Navier-Stokes Solver "NEWT": User's Manual*. Cambridge, U.K.: Whittle Laboratory, 199x.
- [50] Dawes, W.N., *Advanced Numerical Methods: Solution of the Navier-Stokes Equations*. Cambridge, U.K.: Whittle Laboratory, 199x.
- [51] Dawes, W.N., *A Computer Program for the Analysis of Three Dimensional Viscous Compressible Flow in Turbomachinery Blade Rows*. Cambridge, U.K.: Whittle Laboratory, 199x.
- [52] Dawes, W.N. "The Practical Application of Solution-Adaptation to the Numerical Simulation of Complex Turbomachinery Problems." *Prog. Aerospace Sci.* Vol. 29. 1992: pp.221-269.
- [53] Yetter, R.A., F.L. Dryer, M.A. Mueller, and J. Scire. *A Study of Hot Section Chemical Kinetics for Gas Turbine Emissions Predictions*. Final Technical Research Report for Combustion Technology Branch. NASA-Lewis Research Center, OH, 1998.
- [54] Mueller, M.A., R.A. Yetter, and F.L. Dryer. *Experimental Studies and Modeling of the Kinetic Interactions of CO, NOx, and SO2 between $.5 \leq P \leq 10$ atm and $950 \leq T \leq 1070$ K*. 1999 AEAP Conference.
- [55] Hunter, S.C. "Formation of SO₃ in Gas Turbines." *Transactions of the ASME*. 104. January 1982: pp.44-51.
- [56] Harris, B.W. "Conversion of Sulfur Dioxide to Sulfur Trioxide in Gas Turbine Exhaust." *Journal of Engineering for Gas Turbines and Power*. 112. October 1990: pp.585-589.
- [57] Fahey, D.W., E.R. Keim, K.A. Boering, C.A. Brock, J.C. Wilson, H.H. Jonsson, S. Anthony, T.F. Hanisco, P.O. Wennberg, R.C. Miake-Lye, R.J. Salawitch, N. Louisnard, E.L. Woodbridge, R.S. Gao, S.G. Donnelly, R.C. Wamsley, L.A. Del Negro, S. Solomon, B.C. Daube, S.C. Wofsy, C.R. Webster, R.D. May, K.K. Kelly, M. Loewenstein, J.R. Podolske, K.R. Chan. "Emission Measurements of the Concorde Supersonic Aircraft in the Lower Stratosphere." *Science*. 270. October 6, 1995: pp. 70-74.

- [58] Brown, R.C. and R.C. Maie-Lye. "Heterogeneous Reactions in Aircraft Gas Turbine Engines." To be submitted to *Geophysical Research Letters*.
- [59] Penner, S.S. *Similarity Analysis for Chemical Reactors and The Scaling of Liquid Fuel Rocket Engines*. Washington, D.C.: Office of Ordnance Research, 19xx.
- [60] Spalding, D.B. "The Art of Partial Modeling": *9th International Symposium on Combustion: Colloquium on Modeling Principles*. pp. 833-843.
- [61] Brown, P.N., G. D. Byrne, and A.C. Hindmarsh. "VODE: A Variable-Coefficient ODE Solver." *SIAM Journal Sci. Stat. Comput.* Vol. 10, No. 5. September 1989: pp. 1038-1051.
- [62] Byrne, G.D. and A.M. Dean. "The Numerical Solution of Some Kinetics Models with VODE and Chemkin II." *Computers Chem.* Vol. 17, No. 3. 1993: pp. 297-302. s
- [63] MIT-ARI Intra-Engine Trace Species Chemistry Research Plan. October 1998-March 1999.
- [64] Lee, J.J. Historical and Future Trends in Aircraft Performance, Cost, and Emissions. S.M. Thesis. Massachusetts Institute of Technology. 2000.
- [65] Kirk, D. Personal Communication, 2000.
- [66] *Unstructured Mesh Generation and Visualization Package*. Cambridge, U.K.: Whittle Laboratory. Unpublished Work.
- [67] Brown, R., Maie-Lye, R., Zhang, J. Personal Communication, 1998-2000.
- [68] Kee, R.J., F.M. Rupley, and J.A. Miller. "Chemkin-II: A Fortran Chemical Kinetics Package for the Analysis of Gas-Phase Chemical Kinetics." *SAND89-8009*. Sandia National Laboratories. March 1991.
- [69] Dawes, W.N. Personal Communication, 1998-2000.
- [70] Darmonfal, D. Personal Communication, 1999.
- [71] Haimes, B. "VISUAL3 User's & Programmer's Manual." Massachusetts Institute of Technology. 1996.